SPECTROSCOPY, REACTIONS AND DECAY MECHANISMS OF MESONS WITH HEAVY QUARKS

JORGE SEGOVIA GONZÁLEZ

UNIVERSIDAD DE SALAMANCA
Departamento de Física Fundamental

Marzo 2012

D. DAVID RODRÍGUEZ ENTEM, PROFESOR TITULAR DEL ÁREA DE FÍSICA ATÓMICA, MOLECULAR Y NUCLEAR, Y MIEMBRO DEL DEPARTAMENTO DE FÍSICA FUNDAMENTAL,

Autoriza la presentación de la tesis doctoral titulada *'Spectroscopy, reactions and decay mechanisms of mesons with heavy quarks'*, realizada bajo su dirección por **D. Jorge Segovia González.**

En Salamanca, a 15 de Marzo de 2012

El Director

Fdo.: David Rodríguez Entem

El Doctorando

Fdo.: Jorge Segovia González

Agradecimientos

Son muchos los que se merecen mi agradecimiento por su colaboración de una u otra forma en la elaboración de este trabajo de tesis. Muchas gracias a todos ellos, en especial...

- A mi director de tesis, David R. Entem, que me has 'reñido' cuando no sabía algo pero que te has esforzado tantísimo, profesional y personalmente, en enseñármelo que espero que al final este trabajo te devuelva en parte tu sacrificio. Ha sido un gran placer trabajar a tu lado y no me gustaría que dejáramos de colaborar en un futuro. Y a Francisco Fernández, por su dedicación tan comprometida e intensa. Te considero como uno más de abordo en este viaje y me has enseñado algo muy importante, el trabajo duro y la experiencia te hacen ser mejor científico.
- A los profesores que me han brindado la oportunidad de conocer su punto de vista sobre la física y de trabajar con ellos. A veces ha sido como un soplo de aire fresco... ellos son Eef van Beveren, Enrique Ruiz Arriola, Eliecer Hernández y Conrado Albertus.
- Al Departamento de Física Fundamental, y en especial al Grupo de Física Nuclear, por su trato cordial, por ayudarme siempre que lo he necesitado y por dejarme trabajar de la forma más cómoda posible.
- A los marsopas y demás especies como la marmota, por haberme acompañado en mi día a día durante estos años. Hemos compartido comedores, bares, aficiones y demás actividades necesarias para poder desconectar de vez en cuando de este trabajo tan absorbente.
- Y por supuesto a mi familia, mis padres y mis hermanos, quienes conocen más de cerca lo que ha influido este trabajo en mi vida. Gracias por vuestro apoyo incondicional, os debo todo lo que soy.

Creo que la mejor enseñanza solo puede hacerse
cuando hay una relación individual directa entre
un estudiante y un buen profesor: una situación
en la que el estudiante discute las ideas, piensa
sobre las cosas y habla sobre las cosas.

Richard P. Feynman, Junio de 1963.

A mis padres y mis hermanos.

SPECTROSCOPY, REACTIONS AND DECAY MECHANISMS OF MESONS WITH HEAVY QUARKS

Jorge Segovia González

University of Salamanca, 2012

The main motivation of this work has been the description of the heavy quark systems within the framework of a constituent quark model. The difficulties to solve nonperturbative QCD make phenomenological models a useful tool to approach the data and, at the same time, to learn about the theory.

The investigation of properties of the heavy mesons has allowed us to understand the model applicability and to generate possible improvements. The properties studied are the meson spectra and the electromagnetic, strong and weak decays.

- **Published papers:**

1. **Is chiral symmetry restored in the excited meson spectrum?** J. Segovia, D.R. Entem and F. Fernández. Physics Letters B **662**, 33 (2008).
2. $\mathbf{J^{PC} = 1^{--}}$ **hidden charm resonances**. J. Segovia, A.M. Yasser, D.R. Entem and F. Fernández. Physical Review D **78**, 114033 (2008).
3. $\mathbf{D_{s1}(2536)^+}$ **decays and the properties of P-wave charmed strange mesons**. J. Segovia, A.M. Yasser, D.R. Entem and F. Fernández. Physical Review D **80**, 054017 (2009).
4. **Coupled channel approach to the structure of the X(3872)**. P.G. Ortega, J. Segovia, D.R. Entem and F. Fernández. Physical Review D **81**, 054023 (2010).
5. **Charmonium narrow resonances in the string breaking region**. J. Segovia, D.R. Entem and F. Fernández. Journal of Physics G: Nucl. Part. Phys. **37**, 075010 (2010).
6. **A very broad X(4260) and the resonance parameters of the** ψ**(3D) vector charmonium state**. Eef van Beveren, George Rupp and J. Segovia. Physical Review Letters **105**, 102001 (2010).
7. **Charmonium resonances in** $\mathbf{e^+e^-}$ **exclusive reactions around the** ψ**(4415) region**. J. Segovia, D.R. Entem and F. Fernández. Physical Review D **83**, 114018 (2011).
8. **Semileptonic B and** $\mathbf{B_s}$ **decays into orbitally excited charmed mesons**. J. Segovia, C. Albertus, D.R. Entem, F. Fernández, E. Hernández and M.A. Pérez-García. Physical Review D **84**, 094029 (2011).
9. **Renormalization approach to constituent quark models of quarkonium**. J. Segovia, D.R. Entem, F. Fernández and E. Ruiz-Arriola. Physical Review D **85**, 074001 (2012).

- **Papers in progress:**

1. **Scaling of the** $\mathbf{^3P_0}$ **strength in heavy meson strong decays**. J. Segovia, D.R. Entem and F. Fernández. In preparation.
2. **Strong Charmonium decays in a microscopic model**. J. Segovia, D.R. Entem and F. Fernández. In preparation.
3. **Renormalized Quarkonium**. J. Segovia, D.R. Entem, F. Fernández and E. Ruiz Arriola. In preparation.
4. **Nonleptonic** $\mathbf{B \to D^{(*)}D_{sJ}^{(*)}}$ **decays and the nature of the orbitally excited charmed-strange mesons**. J. Segovia, C. Albertus, E. Hernández, F. Fernández and D.R. Entem. In preparation.

Contents

List of Tables

List of Figures

Chapter 1

Introduction

The theory that describes the strong interaction is Quantum Chromodynamics (QCD). It was proposed in the 1970s and was widely accepted after the discovery of asymptotic freedom in 1973 as it offered a satisfying explanation to some of the puzzling experimental results at the time. However, QCD has remained only partially solved until today due to the non-Abelian structure of the gauge group which generates it. The main problem is that a perturbative understanding can only be properly done at very high energies where the quark-gluon coupling constant becomes small enough. In the low-energy region one has to develop nonperturbative methods of limited applicability or to model the theory to describe the phenomenology. Among them one has constituent quark models, numerical techniques in a discrete lattice space, Lattice QCD, or other approaches that build an Effective Field Theory taking some limit of QCD and generate from it a systematic expansion, Chiral Perturbation Theory, Heavy Quark Effective Field Theory, Non-Relativistic QCD or $1/N_c$ approaches.

The difficulties to solve QCD make phenomenological models incorporating the basic properties of the original theory a useful tool to approach the data and, at the same time, to learn about the theory. Among them, constituent quark models have surprisingly described quite well hadrons as composite objects made of constituent valence quarks. The quark model of hadrons was first introduced in 1964 by Gell-Mann [1] and, independently, by Zweig [2]. There was no universal agreement if the quarks were real particles or merely mathematical objects until 1967 when the situation changed due to an electron-proton deep inelastic scattering experiment performed by Friedman, Kendall and Taylor at the Stanford Linear Accelerator Center (SLAC). They found that the scattering rate deviated from Rutherford formula for the scattering between point particles, proving the proton was formed by three point-like particles.

Before 1974 it was possible to understand the experimental data using only three different types of quarks (and the corresponding antiquarks), up (u), down (d) and strange (s). Then very narrow hadron resonances were discovered simultaneously at Brookhaven National Laboratory [3] and SLAC [4]. The states were interpreted as a bound state of a new heavy quark, the charm quark (c). In 1977 another heavy meson named Υ was discovered at Fermilab in the 9.5 GeV region [5], a discovery that leads to the bottom quark (b). The top quark (t), was discovered in 1995 at Fermilab [6] with a mass around 175 GeV, although no meson containing a t quark has ever been detected [1].

[1] Due to the large weak decay rate, $t \to bW^+$, it is not expected that the top quark appears as a constituent in bound states.

The scientific community has witnessed what is called the golden age for heavy quarkonium physics, dawned a decade ago and initiated by the confluence of exciting theoretical advances in QCD and an explosion of related experimental activity. Focusing on the charmonium sector, it is important to remark that since its discovery in 1974 [3, 4], the charmonium system has become the prototypical "hydrogen atom" of meson spectroscopy [7–10]. The experimentally clear spectrum of relatively narrow states below the open-charm threshold of 3.73 GeV can be identified with the $1S$, $1P$, and $2S$ $c\bar{c}$ levels predicted by potential models, which incorporate a color Coulomb term at short distances and a confining term at large distances. Spin-dependent interquark forces are evident in the splittings of states within these multiplets. Discussions of the theoretical importance and experimental status of heavy quarkonium, including recent experimental results for charmonium, have been given by Quigg [11], Galik [12], the CERN Quarkonium Working Group [13], Seth [14–16], and Swarnicki [17].

Concerning charmonium one open topic remains its spectroscopy. In this respect the B-factories have contributed to the study of the missing $c\bar{c}$ states [18] but also to find unanticipated states. The most important experiments are BaBar [19], Belle [20], BES [21], CLEO [22] and LHCb [23], but there are also some future projects as the PANDA experiment at FAIR [24].

Within the conventional $c\bar{c}$ states they have contributed with the discovery of the long missing 2^1S_0 η_c' state performed by the Belle Collaboration [25], which has since been confirmed by BaBar [26], and has also been observed by CLEO in $\gamma\gamma$ collisions [27]. There has also been experimental activity in the spin-singlet P-wave sector, with recent reports on the observation of the elusive 1^1P_1 h_c state by CLEO [14, 28]. The surprisingly large cross sections for double charmonium production in e^+e^- reported by Belle [29–31] suggest that it may be possible to study $C = (+)$ $c\bar{c}$ states in e^+e^- without using the higher-order $O(\alpha^4)$ two-photon annihilation process. Finally, one of the great current interests in $c\bar{c}$ spectroscopy is the search for $\psi_2(1^3D_2)$ and $\eta_{c2}(1^1D_2)$ states, which are expected to be quite narrow due to the absence of open-charm decay modes.

On the other hand, since the discovery of the unexpected and still-fascinating $X(3872)$ by Belle [32] and CDF [33] in B decays to $J/\psi\pi^+\pi^-$, the interest of charmonium has been focused on the namely XYZ charmonium-like states that appear to lie outside the quark model. Despite of many of these states still need experimental confirmation, there has been a huge theoretical effort to describe these states as quark-gluon hybrids, mesonic molecules and tetraquarks.

Another important topic is the Lorentz nature of the confinement. This is tested by the multiplet splittings of orbitally excited $c\bar{c}$ states in naive quark models. With a pure scalar confinement, as is normally assumed, there is no spin-spin hyperfine interaction at $\mathcal{O}(v^2/c^2)$. Therefore the mass of the spin-singlet $^1P_1$ h_c state is degenerated with the corresponding triplet center-of-gravity (c.o.g.) of the ^3P_J χ_{cJ} states. However, in the original Cornell model [34] was assumed that the confinement acts as the static term of a Lorentz vector structure, which breaks the degeneracy of the $^1P_1$ and the ^3P_J center-of-gravity. Another possibility is that confinement may have a more complicated Lorentz structure being a mixture of a scalar and a vector contributions [35]. Of course these simple potential model considerations may be complicated by mass shifts due to other effects, such as couplings to open-flavor channels.

Li *et al.* [36] have shown that a screened linear confinement potential gives similar global features to those of a coupled channel calculation based on the Cornell potential and therefore describes, in an effective way, the effects of dynamical light quark pair creation. However, it seems evident the great influence that lead a meson-meson threshold on the nearby mesons. The mixing between quark model $q\bar{q}$ basis states and two-meson continuum has been cited as a possible reason for the low masses of the recently discovered $D^*_{s0}(2317)$ and $D_{s1}(2460)$ states [37, 38]. The effects of unquenching the quark model by including meson loops can presumably be studied effectively in the $c\bar{c}$ system, in which the experimental spectrum of states is relatively unambiguous. The success of the $q\bar{q}$ quark model is surprising, in view of the probable importance of corrections to the valence approximation; the range of the validity of the naive quenched $q\bar{q}$ quark model is an interesting and open question [39].

In the end, the heavy quarkonium physics is of great interest to the scientific community and its relative simple structure makes it an ideal system to learn more about QCD. The main motivation of this work is the description of heavy meson properties within the framework of a constituent quark model. The meson properties studied include meson spectra and electromagnetic, strong and weak decays. This will allow us to understand the model applicability and to generate possible improvements.

The thesis is organized as follows. After the introduction, we describe in Chapter two the basic properties of QCD and how they are implemented into the constituent quark model. There is a detailed description of all different terms of the interacting potential. To find new physics it is very important to test the theoretical model with as many as possible known states. It allows us to clearly understand the strengths and weaknesses of the model and thus to extract later reliable predictions. Moreover, it is widely believed that confinement is flavor independent. Based on these two cornerstones, in this Chapter, we develop a reparametrization of the model to describe the spectrum of light mesons up to the recent highly excited states reported by the Crystal Barrel Collaboration. This constrains the model parameters and allows us to carry out predictions within the heavy quark sector.

In Chapter three we focus on the heavy quark sector. Introducing the meson spectra we calculate the radiative decays. It includes leptonic, $E1$ and $M1$ decay rates and the decays into two and three photons. We present the experimental analysis of higher multipole contributions to the radiative decays between spin-triplet charmonium states. It allows us to discuss about the phenomenological mixing between $J^{PC} = 1^{--}$ charmonium states proposed by other groups to explain the leptonic widths. Once the meson spectra has been presented, certain modifications to the model are suggested. We study firstly the influence of the Lorentz structure of the confinement in the meson spectra. Second, the incorporation of the one-loop QCD corrections to the spin-dependent terms of the one-gluon exchange potential. This is motivated by the fact that in the one-loop computation there is a spin-dependent term which affects only to mesons with different flavor quarks. And finally, the application of a renormalization technique with boundary conditions to disentangle the physics of the ground state to that of the excited states. This involves the elimination of the *ad hoc* cutoffs of the model, providing information on the way the original model takes into account the unknown short-distance dynamics. Once the regulators are eliminated, a study of the properties of the heavy mesons with respect some parameters with physical meaning

is also included.

Chapter four is devoted to the development of a microscopic decay model to explain the open-flavor strong decays of heavy mesons. We begin with the $^3P_0$ model, the strength γ of the decay interaction is regarded as a free parameter and it is fitted to the data. We propose a scale-dependent strength, γ, given by a global fit of the total decay widths of mesons which belong to charmed, charmed-strange, hidden charm and hidden bottom sectors. Once we have got experience in that model, we will perform a calculation of meson strong decays in terms of quark and gluon degrees of freedom to address a more fundamental description of the decay mechanism. Results and applications of both models concerning different heavy quark sectors are included.

In Chapter five we study the spin-nonflip dipion transitions between triplet charmonium states and also between triplet bottomonium states. To do that we will follow the QCD multipole expansion method in which is necessary to develop a model of hybrid mesons. Many XYZ mesons have been discovered in hadronic transitions that can be analyzed from a theoretical point of view to facilitate possible assignments.

Chapter six is devoted to the semileptonic and nonleptonic decays of B mesons. The B-factories have become a fundamental tool to find new heavy hadrons. The experimental data concerning the properties of these new heavy hadrons are usually accompanied of information about the weak decay of meson B. Moreover, we will see, on one hand, that the theoretical analysis of the semileptonic B decays into orbitally excited charmed mesons, that include both weak and strong decays, offers the possibility for a stringent test of meson models. On the other hand, the B nonleptonic decays into $D^{(*)}D_{sJ}$ channels provide information about the structure of the D_{sJ} mesons.

Finally, we give the conclusions in Chapter seven.

Chapter 2

Review of the constituent quark model

QCD is generally regarded as the non-Abelian gauge theory that describes quark and gluon physics. It is very successful at high energies since perturbative calculations are allowed and some non trivial and unexpected properties of QCD have been well understood and confirmed experimentally.

However, the nonperturbative regime of QCD, where the hadron properties are involved, remains to be understood. For instance, a rigorous proof is still lacking that QCD works as a microscopic theory of strong interactions that gives rise to the phenomenological properties of hadron spectra as spontaneous chiral symmetry breaking or quark confinement.

The main problem is that perturbation theory cannot be applied to low energy scales and other methods should be developed to deal with. One of them is to use phenomenological models, but there are more as Lattice gauge theories, the Dyson-Schwinger formalism, Light-cone QCD and Effective Field Theories.

The phenomenological models incorporate the main properties of QCD. Among them, constituent quark models describe quite well mesons and baryons as composite objects made of constituent valence quarks. Their electromagnetic, strong and weak decays have been studied offering explanations and raising questions that have made the understanding of theory and experiment to advance. In conclusion, constituent quark models offer one of the most complete descriptions of hadron properties.

2.1 Main properties of Quantum Chromodynamics

2.1.1 Gauge invariance: non-Abelian theories

One can infer the structure of Quantum Chromodynamics from local gauge invariance where the group of phase transformations on the quark color fields is $SU(3)$ [40]. The free Lagrangian is

$$\mathcal{L}_0 = \bar{\psi}_j(i\gamma^\mu\partial_\mu - m)\psi_j, \tag{2.1}$$

where $j = 1$, 2 and 3 denotes the color index. For simplicity, we show just one quark flavor.

Let us explore the consequences of requiring $\mathcal{L}_0$ to be invariant under local phase transformations of the form

$$\psi(x) \to U\psi(x) \equiv e^{i\alpha_a(x)T_a}\psi(x), \tag{2.2}$$

where U is an arbitrary 3×3 unitary matrix for which we give a general parametrization. A summation over the repeated suffix a is implied. T_a with $a = 1, \ldots, 8$ are a set of linearly independent, traceless, hermitian 3×3 matrices, and α_a are the group parameters. The matrices $\lambda_a/2$, where

$$\lambda_1 = \begin{pmatrix} 0 & 1 & 0 \\ 1 & 0 & 0 \\ 0 & 0 & 0 \end{pmatrix}, \qquad \lambda_2 = \begin{pmatrix} 0 & -i & 0 \\ i & 0 & 0 \\ 0 & 0 & 0 \end{pmatrix}, \qquad \lambda_3 = \begin{pmatrix} 1 & 0 & 0 \\ 0 & -1 & 0 \\ 0 & 0 & 0 \end{pmatrix},$$
$$\lambda_4 = \begin{pmatrix} 0 & 0 & 1 \\ 0 & 0 & 0 \\ 1 & 0 & 0 \end{pmatrix}, \qquad \lambda_5 = \begin{pmatrix} 0 & 0 & -i \\ 0 & 0 & 0 \\ i & 0 & 0 \end{pmatrix}, \qquad \lambda_6 = \begin{pmatrix} 0 & 0 & 0 \\ 0 & 0 & 1 \\ 0 & 1 & 0 \end{pmatrix}, \tag{2.3}$$
$$\lambda_7 = \begin{pmatrix} 0 & 0 & 0 \\ 0 & 0 & -i \\ 0 & i & 0 \end{pmatrix}, \qquad \lambda_8 = \sqrt{\frac{1}{3}} \begin{pmatrix} 1 & 0 & 0 \\ 0 & 1 & 0 \\ 0 & 0 & -2 \end{pmatrix},$$

are the conventional choice of the T_a matrices.

The group is non-Abelian since not all the generators T_a commute with each other. It is easy to show that the commutator of any two is a linear combination of all the T's

$$[T_a, T_b] = i f_{abc} T_c, \tag{2.4}$$

where f_{abc} are real constants, called the structure constants of the group.

To impose $SU(3)$ local gauge invariance on the Lagrangian, Eq. (2.1), it is sufficient to consider infinitesimal phase transformations

$$\begin{aligned} \psi(x) &\to [1 + i\alpha_a(x) T_a]\, \psi(x), \\ \partial_\mu \psi &\to (1 + i\alpha_a T_a)\partial_\mu \psi + i T_a \psi \partial_\mu \alpha_a. \end{aligned} \tag{2.5}$$

The last term spoils the invariance of $\mathcal{L}$. However, we can introduce (eight) gauge fields G^a_μ, each transforming as

$$G^a_\mu \to G^a_\mu - \frac{1}{g_s}\partial_\mu \alpha_a - f_{abc}\alpha_b G^c_\mu, \tag{2.6}$$

where the last term is introduced to achieve gauge invariance of $\mathcal{L}$ when the group of transformations is non-Abelian, and form a covariant derivative

$$D_\mu = \partial_\mu + i g_s T_a G^a_\mu. \tag{2.7}$$

We then make the replacement $\partial_\mu \to D_\mu$ in Lagrangian, Eq. (2.1), and obtain

$$\mathcal{L} = \bar{\psi}(i\gamma^\mu \partial_\mu - m)\psi - g_s(\bar{\psi}\gamma^\mu T_a \psi) G^a_\mu. \tag{2.8}$$

Finally, we may add to $\mathcal{L}$ a gauge invariant kinetic energy term for each of G^a_μ fields. The final gauge invariant QCD Lagrangian is then

$$\mathcal{L} = \bar{\psi}(i\gamma^\mu \partial_\mu - m)\psi - g_s(\bar{\psi}\gamma^\mu T_a \psi) G^a_\mu - \frac{1}{4} G^a_{\mu\nu} G^{\mu\nu}_a, \tag{2.9}$$

where

$$G^a_{\mu\nu} = \partial_\mu G^a_\nu - \partial_\nu G^a_\mu - g_s f_{abc} G^b_\mu G^c_\nu. \tag{2.10}$$

The Eq. (2.9) is the Lagrangian for interacting colored quarks ψ and vector gluons G_μ, with coupling specified by g_s, which follows simply for demanding that the Lagrangian be invariant under local color phase transformations to the quark fields. Since we can arbitrarily vary the phase of the three quark color fields, it is not surprising that eight vector gluon fields (G^a_μ with $a = 1, \ldots, 8$) are needed to compensate all possible phase changes. Local gauge invariance requires the gluons to be massless

The kinetic energy term in $\mathcal{L}$ is not purely kinetic but includes an induced self-interaction between gauge bosons, last term in Eq. (2.10), which diagrammatically represents three and four gluon vertices and reflects the fact that gluons themselves carry color charge. This arises on account of the non-Abelian character of the gauge group. The gauge invariance uniquely determines the structure of these gluon self-coupling terms. There is only one coupling g_s.

2.1.2 Chiral symmetry and its spontaneous breaking

As the masses of the u and d quarks are quite small compared to $\Lambda_{\rm QCD}$ and the typical hadronic scale of 1 GeV, one can take the chiral limit which consists on neglecting the mass of the quarks. We define the right and left-handed components of quark fields

$$\begin{aligned} \psi_R &= \frac{1}{2}(1+\gamma_5)\psi, \\ \psi_L &= \frac{1}{2}(1-\gamma_5)\psi. \end{aligned} \tag{2.11}$$

If there is no interaction, the right and left-handed components of the quark field get decoupled, as it is seen from the kinetic energy term of the quark field in Eq. (2.9)

$$i\bar{\psi}\gamma^\mu\partial_\mu\psi = i\bar{\psi}_L\gamma^\mu\partial_\mu\psi_L + i\bar{\psi}_R\gamma^\mu\partial_\mu\psi_R. \tag{2.12}$$

In QCD the quark-gluon interaction term of the Lagrangian is a vectorial coupling which does not mix the right and left-handed components of quark fields. Hence in the chiral limit the right and left-handed components of quarks are completely decoupled in the QCD Lagrangian. Then, assuming only one flavor of quarks such a Lagrangian is invariant under two independent global variations of phases of the left-handed and right-handed quark

$$\begin{aligned} \psi_R &\to \exp(i\theta_R)\psi_R, \\ \psi_L &\to \exp(i\theta_L)\psi_L. \end{aligned} \tag{2.13}$$

Such a transformation can be identically rewritten in terms of the vectorial and axial transformations

$$\begin{aligned} \psi &\to \exp(i\theta_V)\psi, \\ \psi &\to \exp(i\theta_A\gamma_5)\psi. \end{aligned} \tag{2.14}$$

The symmetry group of these phase transformations is

$$U(1)_L \times U(1)_R = U(1)_A \times U(1)_V. \tag{2.15}$$

Consider now the chiral limit for two flavors, u and d. The quark-gluon interaction Lagrangian is insensitive to the specific flavor of quarks. For example, one can

substitute the u and d quarks by properly normalized orthogonal linear combinations of u and d quarks (*i.e.* one can perform a rotation in the isospin space) and nothing will change. Since the left and right-handed components are completely decoupled, one can perform two independent isospin rotations of the left and right-handed components

$$\begin{aligned} \psi_R &\to \exp\left(i\frac{\theta_R^a \tau^a}{2}\right)\psi_R, \\ \psi_L &\to \exp\left(i\frac{\theta_L^a \tau^a}{2}\right)\psi_L, \end{aligned} \tag{2.16}$$

where τ^a are the isospin Pauli matrices and the angles θ_L^a and θ_R^a parametrize rotations of the left and right-handed components, respectively. These rotations leave the QCD Lagrangian invariant. The symmetry group of these transformations

$$SU(2)_L \times SU(2)_R, \tag{2.17}$$

is called chiral symmetry.

Actually in this case the Lagrangian is also invariant under the variation of the common phase of the left-handed u_L and d_L quarks, which is the $U(1)_L$ symmetry and similarly for the right-handed quarks. Hence the total chiral symmetry group of the QCD Lagrangian is

$$U(2)_L \times U(2)_R = SU(2)_L \times SU(2)_R \times U(1)_V \times U(1)_A. \tag{2.18}$$

If one includes into this consideration the next flavors, the respective chiral symmetry is strongly explicitly broken due the quark mass.

Generally if the Hamiltonian of a system is invariant under some transformation group G, it is expected that one can find states which are simultaneously eigenstates of the Hamiltonian and of the Casimir operators of the group, C_i. If the ground state of the theory, the vacuum, is invariant under the same group, *i.e.* if for all $U \in G$

$$U\left|0\right\rangle = \left|0\right\rangle, \tag{2.19}$$

then eigenstates of this Hamiltonian corresponding to excitations above the vacuum can be grouped into degenerate multiplets corresponding to the particular representations of G. This mode of symmetry is usually referred to as the Wigner-Weyl mode. Conversely, if Eq. (2.19) does not hold, the excitations do not generally form degenerate multiplets. This situation is called spontaneous symmetry breaking.

If chiral $SU(2)_L \times SU(2)_R$ symmetry were realized in the Wigner-Weyl mode, then the excitations would be grouped into representations of the chiral group. This feature is definitely not observed for the low-lying states in hadron spectra. This means that the Eq. (2.19) does not apply; the continuous chiral symmetry of the QCD Lagrangian is spontaneously (dynamically) broken in the vacuum and according to the Goldstone theorem there exist a boson, which couples to the fermions of the theory, for each group generator which fails to annihilate the vacuum.

2.1.3 Asymptotic freedom

In a non-Abelian gauge theory such as Quantum Chromodynamics, the gluons also carry color charge. As a consequence, a virtual gluon emitted from a quark does

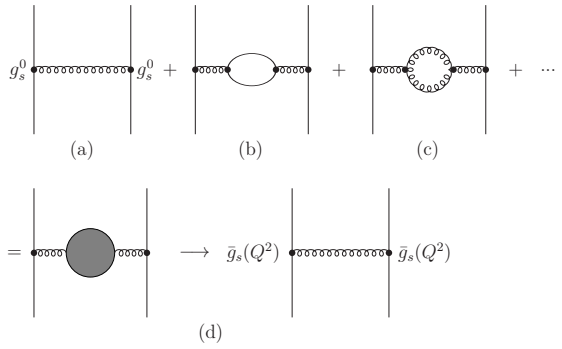

Figure 2.1. Diagrams which contribute to second order in g_s^0 to the running coupling constant $\bar{g}_s(Q^2)$.

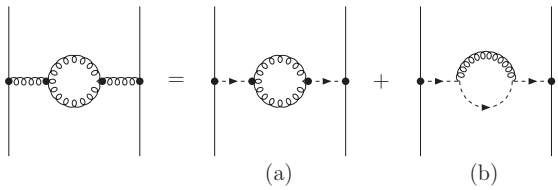

Figure 2.2. Decomposition of the two gluon loop in Coulomb gauge into transverse components (wiggly lines) and "Coulomb" components (arrow lines). Only the self energy diagram (b) gives anti-screening.

not only see the color charge of another quark (diagram (a) in Fig. 2.1) and of a virtual quark-antiquark pair (diagram (b)), but also the color charge of virtual gluons (diagram (c)). The combined effect of the Feynman diagrams in Fig. 2.1 yields the effective coupling constant [41]

$$\alpha_s(Q^2) = \frac{g_s^2(Q^2)}{4\pi} = \alpha_s^{(0)}\left[1 - \frac{2}{3}n_f\frac{\alpha_s^{(0)}}{4\pi}\ln\frac{\Lambda^2}{Q^2} + 11\frac{\alpha_s^{(0)}}{4\pi}\ln\frac{\Lambda^2}{Q^2}\right], \tag{2.20}$$

where $\alpha_s^{(0)} = (g_s^0)^2/4\pi$, g_s^0 is the bare quark-gluon coupling constant, n_f is the number of quark flavors which contribute at the corresponding energy, Q^2 is the space-like momentum transfer carried by the virtual gluon, and Λ is a cutoff parameter. The second term is the contribution of the virtual quark-antiquark pairs. It is negative and leads to charge screening. The third term comes from the virtual gluon loop. It is positive and gives anti-screening. The appearance of these two competing terms of opposite sign is a peculiarity of non-Abelian gauge theories.

The anti-screening mechanism works only for loops of massless gauge bosons. For these bosons the longitudinal and the time-like components do not correspond to the propagation of physical particles. One of these components can be eliminated using current conservation, but one unphysical component is left over. In Coulomb gauge the gluon propagators in diagram (c) of Fig. 2.1 [42, 43] can be decomposed into the unphysical "Coulomb" part and a transversal part, which yields the two diagrams shown in Fig. 2.2. The transversal gluon loop (diagram (a) in Fig. 2.2) leads to charge screening, as do all physical intermediate states, while the loop in diagram (b), which consists of a "Coulomb" gluon and a transversal gluon, gives anti-screening. Thus the

last term in Eq. (2.20) is actually the sum of two terms

$$-\frac{\alpha_s^{(0)}}{4\pi}\ln\frac{\Lambda^2}{Q^2}, \tag{2.21}$$

for diagram (a) and

$$+\frac{12\alpha_s^{(0)}}{4\pi}\ln\frac{\Lambda^2}{Q^2}, \tag{2.22}$$

for diagram (b) in Fig. 2.2. The anti-screening due to the unphysical component is twelve times stronger than the charge screening due to the two transversal components [42–44].

The cutoff parameter and the bare coupling constant in Eq. (2.20) can be eliminated by renormalization group techniques. For a qualitative discussion of the results we may use a short cut, and differentiate Eq. (2.20) with respect to $\ln Q^2$. The resulting equation does not contain the cutoff any more and $\alpha_s^{(0)}$ is replaced by the cutoff-independent quantity $\bar{\alpha}_s(Q^2)$. Hence one arrives at the differential equation [45, 46]

$$\frac{d\bar{\alpha}_s(Q^2)}{d\ln Q^2} = -(11-\frac{2}{3}n_f)\frac{\bar{\alpha}_s^2(Q^2)}{4\pi}. \tag{2.23}$$

This equation can be integrated to give [45, 47, 48] the running strong fine structure constant

$$\bar{\alpha}_s(Q^2) = \frac{\bar{\alpha}_s(Q_0^2)}{1+(11-2n_f/3)[\bar{\alpha}_s(Q_0^2)/4\pi]\ln(Q^2/Q_0^2)}. \tag{2.24}$$

Here Q_0^2 is a suitable reference momentum transfer where the coupling constant is known from experiment. While the effective quark-gluon coupling constant may be rather large at small energies, and hence perturbation theory does not hold in this regime, Eq. (2.24) tells us that the coupling constant decreases with increasing energy. In particular, in the limit of very high momentum transfers one obtains

$$\bar{\alpha}_s(Q^2) \simeq \left(\frac{33-2n_f}{12\pi}\ln\frac{Q^2}{Q_0^2}\right)^{-1} \xrightarrow[Q^2\to\infty]{} 0 \text{ for } n_f \le 16. \tag{2.25}$$

Now Eq. (2.25) is the essence of asymptotic freedom. It allows us to justify the quark parton picture, which describes high energy hadron phenomena in terms of free point-like constituents. Furthermore, the corrections to this picture may be calculated using perturbation theory, because at large Q^2 the effective coupling constant $\bar{\alpha}_s(Q^2)$ is small. Incidentally, the restriction $n_f \le 16$ in Eq. (2.25) gives an upper limit on the number of quark flavors which are allowed if asymptotic freedom holds in the very high energy domain. Since the logarithm varies very slowly, Eq. (2.25) really only holds for extremely high energies.

The expression for $\bar{\alpha}_s(Q^2)$, Eq. (2.24), depends on the arbitrary renormalization point Q_0^2. It is possible to express $\bar{\alpha}_s(Q^2)$ by the renormalization group invariant parameter Λ', which is characteristic for the strength of the coupling constant and can be determined from experiment.

In the derivation of Eq. (2.24) only the one-loop corrections in Fig 2.1 were taken into account. Its validity for small Q^2 depend on the magnitude of higher-order loop corrections.

2.1.4 Confinement

The hadron spectrum found in nature consists of color singlet combinations of color non singlet objects: the quarks and gluons. Unlike atomic physics, where electrons can readily be separated from atoms, there is no color charge version of ionization in hadronic physics. Every attempt to kick a quark free from a hadron, via high energy collisions, only results in the production of more color singlet hadrons; a non singlet particle is never produced. Particle and nuclear physicists have become accustomed to this fact, which is often referred to as color confinement, but after nearly forty years of intense effort this very basic feature of hadronic physics still has no generally agreed upon explanation.

An indication for permanent quark confinement comes from the fact that the running coupling constant of QCD grows as one approaches the region of low momentum transfer, long distances. This means that the strength of the force which binds quarks increases making impossible to separate them. The weak point in this argument is that it is precisely in that limit where the perturbative calculations are unreliable.

Since the problem of confinement appears as a nonperturbative phenomenon, it has also been investigated in the framework of lattice gauge theories. These theories have their own definition of confinement. Field theory is said to exhibit confinement if the interaction potential between quarks, which corresponds to the Wilson loop calculated on the lattice, has asymptotic linear behaviour at large distances (a review of potentials from Lattice QCD can be found *e.g.* in Ref. [49]). Moreover, there are exact inequalities for the Wilson loop exploiting reflection positivity [50, 51], namely

$$V'(r) > 0, \qquad V''(r) \leq 0, \tag{2.26}$$

where the latter identity is saturated by the linear potential.

A remarkable pattern emerges in the hadronic spectrum when the spin of mesons and baryons is plotted against their squared mass. In such plots the mesons and baryons of given flavor quantum numbers seem to lie on nearly parallel straight lines, known as linear Regge trajectories.

Suppose that we picture a meson as a straight line of length $L = 2R$, with mass per unit length σ. The line rotates about a perpendicular axis through its midpoint, such that the endpoints of the line are moving at the speed of light, $v(R) = c = 1$. Then for the energy in the rest frame, *i.e.* the mass, of the spinning stick we have

$$m = \text{Energy} = 2\int_0^R \gamma\sigma\, dr = 2\int_0^R \frac{\sigma\, dr}{\sqrt{1-v^2(r)}} = 2\int_0^R \frac{\sigma\, dr}{\sqrt{1-r^2/R^2}} = \pi\sigma R, \tag{2.27}$$

and for the angular momentum

$$J = 2\int_0^R \gamma\sigma r v(r)\, dr = 2\int_0^R \frac{\sigma r v(r)\, dr}{\sqrt{1-v^2(r)}} = \frac{2}{R}\int_0^R \frac{\sigma r^2\, dr}{\sqrt{1-r^2/R^2}} = \frac{1}{2}\pi\sigma R^2. \tag{2.28}$$

Comparing the two expressions, we see that

$$J = \frac{1}{2\pi\sigma} m^2 = \alpha\, m^2. \tag{2.29}$$

The constant α is known as the Regge slope.

The spinning stick model is, of course, only a caricature of the real situation. In fact the various Regge trajectories do not pass through the origin, and have slightly different slopes. To make the model more realistic, one might want to relax the requirement of rigidity, and allow the stick to fluctuate in transverse directions. This line of thought leads to string theory. However, since QCD is the theory of quarks and gluons, the question to be answered is how a stick-like or string-like object actually emerges from that theory.

One possible answer is via the formation of a color electric flux-tube. We imagine that the color electric field running between a static quark and antiquark is, for some reason, squeezed into a cylindrical region, whose cross-sectional area is nearly constant as quark-antiquark separation L increases. In that case, the energy stored in the color electric field will grow linearly with quark separation, *i.e.*

$$\text{Energy} = \sigma\, L \quad \text{with} \quad \sigma = \int d^2x_\perp \frac{1}{2}\vec{E}^a \cdot \vec{E}^a, \tag{2.30}$$

where the integration is over a cross-section of the flux-tube. This means that there will be a linearly rising potential energy associated with static sources, and an infinite energy is required to separate these charges an infinite distance.

2.2 Constituent quark model

Spontaneous chiral symmetry breaking of the QCD Lagrangian together with the perturbative one-gluon exchange and the nonperturbative confining interaction are the main pieces of the potential models. Using this idea, Vijande *et al.* [52] developed a model of the quark-quark interaction which is able to describe meson phenomenology from the light to the heavy quark sector.

We have adopted this model and fine tune its parameters to reproduce the higher excited light mesons despite of our study is focused on the heavy quark sector. The reason for that lies in the fact that it is widely believed that confinement is flavor independent. Therefore the interactions, which largely determine the high energy quarkonium spectrum, should be constrained by the light quark sector.

The dynamics of the light quark sector is characterized by the spontaneous chiral symmetry breaking. It makes that the nearly massless current light quarks (u and d) acquire a dynamical momentum-dependent mass, namely, the constituent mass, and that they interact through Goldstone bosons. This feature divides the quarks into two different sectors, light quarks (u, d and s) where the chiral symmetry is spontaneously broken, and the heavy quarks (c and b) where the symmetry is explicitly broken.

Therefore, for the light sector hadrons can be described as systems of confined constituent quarks (antiquarks) interacting through gluons and Goldstone-boson exchanges, whereas for the heavy sector hadrons are systems of confined current quarks interacting through gluon exchanges.

2.2.1 Goldstone-boson exchanges potential

The picture of the QCD vacuum as a dilute medium of instantons [53, 54] explains nicely the spontaneous breaking of chiral symmetry at some momentum scale. Quarks

interact with fermion zero modes of the individual instantons in the medium. Therefore, the light quark propagator gets modified and quarks acquire a momentum dependent mass, which drops to zero for momenta higher than the inverse of the average instanton size $\bar{\rho}$.

The momentum dependent mass acts as a natural cutoff of the theory. In the domain of momenta $k < 1/\bar{\rho}$, a simple Lagrangian invariant under chiral transformations can be derived as [53, 54]

$$\mathcal{L} = \bar{\psi}\left(i\gamma^{\mu}\partial_{\mu} - MU^{\gamma_5}\right)\psi, \tag{2.31}$$

where $U^{\gamma_5} = \exp\left(i\pi^a\lambda^a\gamma_5/f_\pi\right)$, π^a denotes the pseudoscalar fields $(\vec{\pi}, K_i, \eta_8)$ with $i = 1, \ldots, 4$, λ^a are the $SU(3)$ flavor matrices, f_π is the pion decay constant and $M(q^2)$ is the constituent quark mass. An expression of the constituent quark mass can be obtained from the theory, but we use the parametrization $M(q^2) = m_q F(q^2)$ with

$$F(q^2) = \left[\frac{\Lambda^2}{\Lambda^2 + q^2}\right]^{\frac{1}{2}}, \tag{2.32}$$

where Λ determines the scale at which chiral symmetry is broken. Besides the constituent quark mass one obtains terms in which the quarks interact through Goldstone bosons. The Lagrangian in Eq. (2.31) is invariant under chiral rotations since the rotation of the quark fields can be compensated renaming the boson fields. U^{γ_5} can be expanded in terms of boson fields as

$$U^{\gamma_5} = 1 + \frac{i}{f_\pi}\gamma^5\lambda^a\pi^a - \frac{1}{2f_\pi^2}\pi^a\pi^a + \ldots \tag{2.33}$$

The first term generates the constituent quark mass and the second one gives rise to a one-boson exchange interaction between quarks. The main contribution of the third term comes from the two-pion exchange which can be simulated by means of a scalar exchange potential. Inserting Eqs. (2.32) and (2.33) in Eq. (2.31), one obtains the simplest Lagrangian invariant under the chiral transformation $SU(3)_L \otimes SU(3)_R$ with a scale dependent constituent quark mass, containing $SU(3)$ scalar and pseudoscalar potentials. The nonrelativistic reduction of this Lagrangian has been performed for the study of nuclear forces in Refs. [55, 56]. The different terms of the potential contain central and tensor or central and spin-orbit contributions that will be grouped. Therefore, the chiral part of the quark-quark interaction can be expressed as follows

$$V_{\rm qq}\left(\vec{r}_{ij}\right) = V_{\rm qq}^{\rm C}\left(\vec{r}_{ij}\right) + V_{\rm qq}^{\rm T}\left(\vec{r}_{ij}\right) + V_{\rm qq}^{\rm SO}\left(\vec{r}_{ij}\right), \tag{2.34}$$

where C stands for central, T for tensor and SO for spin-orbit potentials. The central part presents four different contributions

$$V_{\rm qq}^{\rm C}\left(\vec{r}_{ij}\right) = V_{\sigma}^{\rm C}\left(\vec{r}_{ij}\right) + V_{\pi}^{\rm C}\left(\vec{r}_{ij}\right) + V_{K}^{\rm C}\left(\vec{r}_{ij}\right) + V_{\eta}^{\rm C}\left(\vec{r}_{ij}\right), \tag{2.35}$$

given by

$$
\begin{aligned}
V_\sigma^{\rm C}(\vec{r}_{ij}) =& -\frac{g_{ch}^2}{4\pi}\frac{\Lambda_\sigma^2}{\Lambda_\sigma^2-m_\sigma^2}m_\sigma\left[Y(m_\sigma r_{ij})-\frac{\Lambda_\sigma}{m_\sigma}Y(\Lambda_\sigma r_{ij})\right],\\
V_\pi^{\rm C}(\vec{r}_{ij}) =& \frac{g_{ch}^2}{4\pi}\frac{m_\pi^2}{12m_im_j}\frac{\Lambda_\pi^2}{\Lambda_\pi^2-m_\pi^2}m_\pi\left[Y(m_\pi r_{ij})-\frac{\Lambda_\pi^3}{m_\pi^3}Y(\Lambda_\pi r_{ij})\right]\times\\
&\times(\vec{\sigma}_i\cdot\vec{\sigma}_j)\sum_{a=1}^{3}(\lambda_i^a\cdot\lambda_j^a),\\
V_K^{\rm C}(\vec{r}_{ij}) =& \frac{g_{ch}^2}{4\pi}\frac{m_K^2}{12m_im_j}\frac{\Lambda_K^2}{\Lambda_K^2-m_K^2}m_K\left[Y(m_K r_{ij})-\frac{\Lambda_K^3}{m_K^3}Y(\Lambda_K r_{ij})\right]\times\\
&\times(\vec{\sigma}_i\cdot\vec{\sigma}_j)\sum_{a=4}^{7}(\lambda_i^a\cdot\lambda_j^a),\\
V_\eta^{\rm C}(\vec{r}_{ij}) =& \frac{g_{ch}^2}{4\pi}\frac{m_\eta^2}{12m_im_j}\frac{\Lambda_\eta^2}{\Lambda_\eta^2-m_\eta^2}m_\eta\left[Y(m_\eta r_{ij})-\frac{\Lambda_\eta^3}{m_\eta^3}Y(\Lambda_\eta r_{ij})\right]\times\\
&\times(\vec{\sigma}_i\cdot\vec{\sigma}_j)\left[\cos\theta_p\left(\lambda_i^8\cdot\lambda_j^8\right)-\sin\theta_p\right],
\end{aligned}
\tag{2.36}
$$

where $Y(x)$ is the standard Yukawa function defined by $Y(x)=e^{-x}/x$. We consider the physical η meson instead of the octet one and so we introduce the angle θ_p. The λ^a are the $SU(3)$ flavor Gell-Mann matrices, m_i is the quark mass and m_π, m_K and m_η are the masses of the $SU(3)$ Goldstone bosons, taken at their experimental values. m_σ is determined through the PCAC relation $m_\sigma^2\simeq m_\pi^2+4m_{u,d}^2$ [57]. Finally, the chiral coupling constant, g_{ch}, is determined from the πNN coupling constant through

$$
\frac{g_{ch}^2}{4\pi}=\frac{9}{25}\frac{g_{\pi NN}^2}{4\pi}\frac{m_{u,d}^2}{m_N^2},
\tag{2.37}
$$

which assumes that flavor $SU(3)$ is an exact symmetry only broken by the different mass of the strange quark.

There are three different contributions to the tensor potential

$$
V_{\rm qq}^{\rm T}(\vec{r}_{ij})=V_\pi^{\rm T}(\vec{r}_{ij})+V_K^{\rm T}(\vec{r}_{ij})+V_\eta^{\rm T}(\vec{r}_{ij}),
\tag{2.38}
$$

each term given by

$$
\begin{aligned}
V_\pi^{\rm T}(\vec{r}_{ij}) =& \frac{g_{ch}^2}{4\pi}\frac{m_\pi^2}{12m_im_j}\frac{\Lambda_\pi^2}{\Lambda_\pi^2-m_\pi^2}m_\pi\left[H(m_\pi r_{ij})-\frac{\Lambda_\pi^3}{m_\pi^3}H(\Lambda_\pi r_{ij})\right]S_{ij}\sum_{a=1}^{3}(\lambda_i^a\cdot\lambda_j^a),\\
V_K^{\rm T}(\vec{r}_{ij}) =& \frac{g_{ch}^2}{4\pi}\frac{m_K^2}{12m_im_j}\frac{\Lambda_K^2}{\Lambda_K^2-m_K^2}m_K\left[H(m_K r_{ij})-\frac{\Lambda_K^3}{m_K^3}H(\Lambda_K r_{ij})\right]S_{ij}\sum_{a=4}^{7}(\lambda_i^a\cdot\lambda_j^a),\\
V_\eta^{\rm T}(\vec{r}_{ij}) =& \frac{g_{ch}^2}{4\pi}\frac{m_\eta^2}{12m_im_j}\frac{\Lambda_\eta^2}{\Lambda_\eta^2-m_\eta^2}m_\eta\left[H(m_\eta r_{ij})-\frac{\Lambda_\eta^3}{m_\eta^3}H(\Lambda_\eta r_{ij})\right]S_{ij}\left[\cos\theta_p\left(\lambda_i^8\cdot\lambda_j^8\right)-\sin\theta_p\right],
\end{aligned}
\tag{2.39}
$$

where $S_{ij}=3(\vec{\sigma}_i\cdot\hat{r}_{ij})(\vec{\sigma}_j\cdot\hat{r}_{ij})-\vec{\sigma}_i\cdot\vec{\sigma}_j$ is the quark tensor operator and $H(x)=(1+3/x+3/x^2)Y(x)$.

Finally, the spin-orbit potential only presents a contribution coming from the scalar part of the interaction

$$V_{\rm qq}^{\rm SO}(\vec{r}_{ij}) = V_{\sigma}^{\rm SO}(\vec{r}_{ij}) = -\frac{g_{ch}^2}{4\pi}\frac{m_\sigma^3}{2m_i m_j}\frac{\Lambda_\sigma^2}{\Lambda_\sigma^2 - m_\sigma^2}\left[G(m_\sigma r_{ij}) - \frac{\Lambda_\sigma^3}{m_\sigma^3}G(\Lambda_\sigma r_{ij})\right](\vec{L}\cdot\vec{S}). \tag{2.40}$$

In the last equation $G(x)$ is the function $(1+1/x)Y(x)/x$.

2.2.2 One-gluon exchange potential

Beyond the chiral symmetry breaking scale one expects the dynamics to be governed by QCD perturbative effects. There are consequences of the gluon fluctuations around the instanton vacuum and we take it into account through the one-gluon exchange (OGE) potential. Following de Rújula *et al.* [58] the OGE is a standard color Fermi-Breit interaction obtained from the vertex Lagrangian given by Eq. (2.9).

The nonrelativistic reduction of the OGE diagram for point-like quarks presents an hyperfine interaction which contains a delta function in configuration space. This contact term is normally smeared to make it nonperturbatively tractable [59]. We have regularized it in a suitable way by replacing the Dirac delta function by a Yukawa form

$$\delta(\vec{r}_{ij}) \to \frac{1}{4\pi r_0^2}\frac{e^{-r_{ij}/r_0}}{r_{ij}}, \tag{2.41}$$

where $r_0(\mu) = \hat{r}_0\frac{\mu_{nn}}{\mu_{ij}}$ with $\hat{r}_0$ as a model parameter and μ_{ij} the reduced mass of quarks with n referred to light u and d quarks. As a consequence, the central part of the OGE reads

$$V_{\rm OGE}^{\rm C}(\vec{r}_{ij}) = \frac{1}{4}\alpha_s(\vec{\lambda}_i^c\cdot\vec{\lambda}_j^c)\left[\frac{1}{r_{ij}} - \frac{1}{6m_i m_j}(\vec{\sigma}_i\cdot\vec{\sigma}_j)\frac{e^{-r_{ij}/r_0(\mu)}}{r_{ij}r_0^2(\mu)}\right], \tag{2.42}$$

with $\vec{\lambda}^c$ being the $SU(3)$ color matrices and α_s is the quark-gluon coupling constant.

The non-central terms of the OGE behave as $1/r^3$. Therefore, these contributions are singulars and it is necessary to introduce phenomenological regulators to treat them exactly, obtaining tensor and spin-orbit potentials of the form

$$\begin{aligned}
V_{\rm OGE}^{\rm T}(\vec{r}_{ij}) &= -\frac{1}{16}\frac{\alpha_s}{m_i m_j}(\vec{\lambda}_i^c\cdot\vec{\lambda}_j^c)\left[\frac{1}{r_{ij}^3} - \frac{e^{-r_{ij}/r_g(\mu)}}{r_{ij}}\left(\frac{1}{r_{ij}^2} + \frac{1}{3r_g^2(\mu)} + \frac{1}{r_{ij}r_g(\mu)}\right)\right]S_{ij},\\
V_{\rm OGE}^{\rm SO}(\vec{r}_{ij}) &= -\frac{1}{16}\frac{\alpha_s}{m_i^2 m_j^2}(\vec{\lambda}_i^c\cdot\vec{\lambda}_j^c)\left[\frac{1}{r_{ij}^3} - \frac{e^{-r_{ij}/r_g(\mu)}}{r_{ij}^3}\left(1 + \frac{r_{ij}}{r_g(\mu)}\right)\right]\times\\
&\quad\times\left[((m_i+m_j)^2 + 2m_i m_j)(\vec{S}_+\cdot\vec{L}) + (m_j^2 - m_i^2)(\vec{S}_-\cdot\vec{L})\right],
\end{aligned} \tag{2.43}$$

where $r_g(\mu) = \hat{r}_g\frac{\mu_{nn}}{\mu_{ij}}$ with $\hat{r}_g$ as a model parameter and $\vec{S}_\pm = \vec{S}_i \pm \vec{S}_j$.

The wide energy range needed to provide a consistent description of light, strange and heavy mesons requires an effective scale dependent strong coupling constant [60–62]. The freezing of the strong coupling constant at low energies studied in several theoretical approaches [63, 64] has been used in different phenomenological models [65, 66]. The momentum-dependent quark-gluon constant is frozen for each

flavor sector that, as explained in [67], can be assimilated to the reduced mass of the system. As a consequence, we use an effective scale dependent strong coupling constant given by [52]

$$\alpha_s(\mu) = \frac{\alpha_0}{\ln\left(\frac{\mu^2+\mu_0^2}{\Lambda_0^2}\right)}, \tag{2.44}$$

where μ is the reduced mass of the quarks and α_0, μ_0 and Λ_0 are parameters.

2.2.3 Confinement potential

Confinement is one of the crucial aspects of the strong interaction that is widely accepted and incorporated into any QCD based model. Color charges are confined inside hadrons. It is well known that multigluon exchanges produce an attractive linearly rising potential proportional to the distance between quarks. This idea has been confirmed, but not rigorously proved, by quenched lattice gauge Wilson loop calculations for heavy valence quark systems. However, sea quarks are also important ingredients of the strong interaction dynamics. When included in the lattice calculations they contribute to the screening of the rising potential at low momenta and eventually to the breaking of the quark-antiquark binding string. This fact, which has been observed in $n_f = 2$ lattice QCD [68], has been taken into account in our model by including the term

$$V_{\rm CON}^{\rm C}(\vec{r}_{ij}) = \left[-a_c(1-e^{-\mu_c r_{ij}}) + \Delta\right](\vec{\lambda}_i^c \cdot \vec{\lambda}_j^c), \tag{2.45}$$

where a_c, μ_c and Δ are parameters, Δ is a global constant fixing the origin of energies. At short distances this potential presents a linear behaviour with an effective confinement strength $\sigma = \frac{16}{3}a_c\mu_c$ and becomes constant at large distances with a threshold defined by $V_{\rm thr} = \frac{16}{3}(a_c - \Delta)$.

No $q\bar{q}$ bound states can be found for energies higher than the threshold. The system suffers a transition from a color string configuration between two static color sources into a pair of static mesons due to the breaking of the color string and the most favored decay into hadrons.

One important question which has not been properly answered is the Lorentz character of confinement. Analytic techniques [69] and numerical studies using lattice QCD [70] have shown that the confining forces are spin independent apart from the inevitable spin-orbit pseudo-force due to the Thomas precession [71]. However, there is no a clear agreement which is the Lorentz structure of the confinement. We consider a confinement spin-orbit contribution

$$\begin{aligned} V_{\rm CON}^{\rm SO}(\vec{r}_{ij}) = &-(\vec{\lambda}_i^c \cdot \vec{\lambda}_j^c)\frac{a_c\mu_c e^{-\mu_c r_{ij}}}{4m_i^2 m_j^2 r_{ij}}\left[((m_i^2+m_j^2)(1-2a_s)\right. \\ &\left.+4m_i m_j(1-a_s))(\vec{S}_+ \cdot \vec{L}) + (m_j^2-m_i^2)(1-2a_s)(\vec{S}_- \cdot \vec{L})\right], \end{aligned} \tag{2.46}$$

where a_s controls the mixture between the scalar and vector Lorentz structures.

2.2.4 Summary of the potential

Once perturbative (one-gluon exchange) and nonperturbative (confinement and chiral symmetry breaking) aspects of QCD have been considered, one ends up with a quark-

quark interaction of the form (we refer to a light quark, u or d, as n, s is used for the strange quark and Q for the heavy quarks c and b):

$$V_{\rm qq} = \begin{cases} {\rm qq} = {\rm nn} & \Rightarrow V_{\rm CON} + V_{\rm OGE} + V_\pi + V_\sigma + V_\eta, \\ {\rm qq} = {\rm ns} & \Rightarrow V_{\rm CON} + V_{\rm OGE} + V_\sigma + V_K + V_\eta, \\ {\rm qq} = {\rm ss} & \Rightarrow V_{\rm CON} + V_{\rm OGE} + V_\sigma + V_\eta, \\ {\rm qq} = {\rm nQ} & \Rightarrow V_{\rm CON} + V_{\rm OGE}, \\ {\rm qq} = {\rm QQ} & \Rightarrow V_{\rm CON} + V_{\rm OGE}. \end{cases} \tag{2.47}$$

The corresponding $q\bar{q}$ potential is obtained from the qq one as detailed in [72]. In the case of $V_K(\vec{r}_{ij})$, where G-parity is not well defined, the transformation is given by $\lambda_1^a \cdot \lambda_2^a \rightarrow \lambda_1^a \cdot (\lambda_2^a)^T$, which recovers the standard change of sign in the case of the pseudoscalar exchange between two nonstrange quarks.

2.3 Solving the two-body system

The main objective of this work is the study of mesons which contain heavy quarks. After the discovery of the first heavy-quark bound states, the ψ and Υ systems, it was soon realized that a nonrelativistic picture seemed to hold for them. However, it is more difficult to justify the nonrelativistic treatment in the light sector. In Ref. [73] the results of nonrelativistic, semirelativistic and relativistic quark-quark Hamiltonians with a QCD-inspired interactions were compared, concluding that the $q\bar{q}$ spectra are very similar when the model parameters are adjusted.

Therefore, we solve the Schrödinger equation for the relative motion of the $q\bar{q}$ pair with the potential described in Sec. 2.2. We use the Rayleigh-Ritz variational principle which is one of the most extended tools to solve eigenvalue problems due to its simplicity and flexibility. However, it is of great importance how to choose the basis on which to expand the wave function.

Our choice is the Gaussian Expansion Method (GEM) which was proposed by Kamimura in Refs. [74, 75] to carry out non adiabatic three-body calculations of muonic molecules and muon-atomic collisions. Following Ref. [76], we employ Gaussian trial functions whose ranges are in geometric progression. This enables the optimization of ranges employing a small number of free parameters. Moreover, the geometric progression is dense at short distances, so that it allows the accuracy description of the dynamics mediated by short range potentials. The fast damping of the gaussian tail is not a problem, since we can choose the maximal range much longer than the hadronic size. Other feature of this basis is that most matrix elements can be computed analytically.

2.3.1 Gaussian Expansion Method

Let us consider the two-body Schrödinger equation

$$\left[-\frac{\hbar^2}{2\mu}\nabla^2 + V(r) - E \right] \psi_{lm}(\vec{r}) = 0, \tag{2.48}$$

where μ is the reduced mass and $V(r)$ is a central potential. We expand $\psi_{lm}(\vec{r})$ in terms of a set of Gaussian basis functions with given range parameters

$$\begin{aligned}
\psi_{lm}(\vec{r}) &= \sum_{n=1}^{n_{\max}} c_{nl}\phi^{\mathrm{G}}_{nlm}(\vec{r}), \\
\phi^{\mathrm{G}}_{nlm}(\vec{r}) &= \phi^{\mathrm{G}}_{nl}(r)Y_{lm}(\hat{r}), \\
\phi^{\mathrm{G}}_{nl}(r) &= N_{nl}r^l e^{-\nu_n r^2}, \\
N_{nl} &= \left(\frac{2^{l+2}(2\nu_n)^{l+\frac{3}{2}}}{\sqrt{\pi}\,(2l+1)!!}\right)^{\frac{1}{2}},
\end{aligned} \tag{2.49}$$

where N_{nl} is a normalization constant. Note that the set $\left\{\phi^{\mathrm{G}}_{nlm}; n = 1, \ldots, n_{\max}\right\}$ of Gaussian basis functions is a non-orthogonal set.

The set of Gaussian size parameters are in geometric progression

$$\begin{aligned}
\nu_n &= \frac{1}{r_n^2}, \\
r_n &= r_1 a^{n-1},
\end{aligned} \tag{2.50}$$

where the free parameters are $\{n_{\max}, r_1, r_{n_{\max}}\}$ or $\{n_{\max}, r_1, a\}$. The non-orthogonal basis functions $\phi^{\mathrm{G}}_{nl}(r)$ satisfy the condition that the overlap between the nearest neighbors, $\langle\phi^{\mathrm{G}}_{nl}|\phi^{\mathrm{G}}_{n-1l}\rangle$, is a constant independent of n, which is considered to be one of the reasons why the expansion works well.

As we have said above, the expansion coefficients $\{c_{nl}\}$ and the eigenenergies E are determined by Rayleigh-Ritz variational principle, which leads to a generalized matrix eigenvalue problem

$$\sum_{n'=1}^{n_{\max}} \left[(T_{nn'} + V_{nn'}) - EN_{nn'}\right] c_{n'l} = 0, \tag{2.51}$$

the generalization for coupled channels make that the Eq. (2.51) is converted in

$$\sum_{n'=1}^{n_{\max}} \left[(T^{\alpha}_{nn'} - EN^{\alpha}_{nn'})\, c^{\alpha}_{n'l} + \sum_{\alpha'=1}^{\text{num. channels}} V^{\alpha\alpha'}_{nn'} c^{\alpha'}_{n'l} = 0\right], \tag{2.52}$$

where $T^{\alpha}_{n'n}$, $N^{\alpha}_{n'n}$ and $V^{\alpha\alpha'}_{n'n}$ are the matrix elements of the kinetic energy, the normalization and the potential, respectively. $T^{\alpha}_{n'n}$ and $N^{\alpha}_{n'n}$ are diagonal whereas the mixing between different channels is given by $V^{\alpha\alpha'}_{n'n}$.

2.3.2 Complex-range Gaussian basis functions

Despite of the advantages of the expansion in terms of Gaussian basis functions, it is difficult to reproduce highly oscillatory functions or even wave functions with some nodes which are present in few-body systems. Therefore we use a more useful basis functions which satisfy the above requirement, taking Gaussian functions multiplied by cosine and sine functions

$$\begin{aligned}
\phi^{\mathrm{GC}}_{nl}(r) &= N^{\mathrm{GC}}_{nl} r^l e^{-\nu_n r^2} \cos(\alpha\nu_n r^2), \\
\phi^{\mathrm{GS}}_{nl}(r) &= N^{\mathrm{GS}}_{nl} r^l e^{-\nu_n r^2} \sin(\alpha\nu_n r^2).
\end{aligned} \tag{2.53}$$

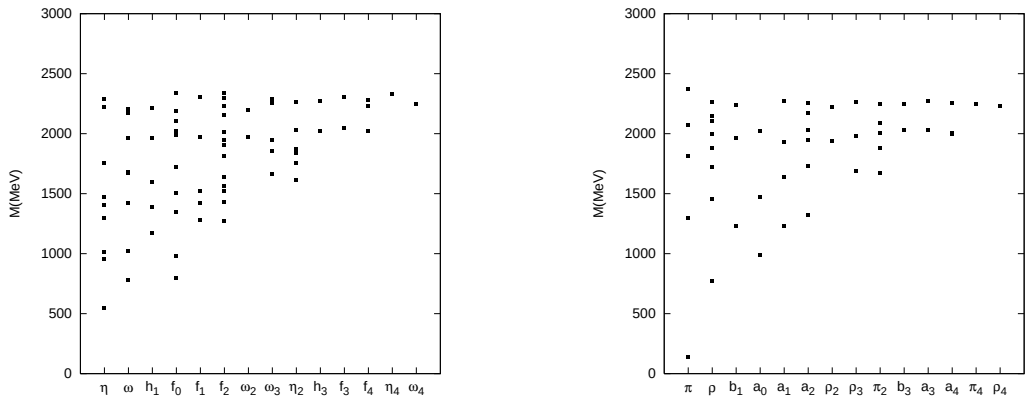

Figure 2.3. Masses, in MeV, of the well established states in Ref. [78] and the analyzed states in Ref. [77] for the light mesons. The left panel shows the $I = 0$ light mesons and the right panel shows the $I = 1$ light mesons.

The Gaussian sizes, ν_n, are taken to form a geometric progression in the same manner as in Eq. (2.50) and the parameter α is a free parameter in principle, but it is taken as $\pi/2$.

The reason why the functions $\phi_{nl}^{\rm GC}(r)$ and $\phi_{nl}^{\rm GS}(r)$ are easy to be used in numerical calculations is that they can be rewritten as

$$\phi_{nl}^{\rm GC}(r) = N_{nl}^{\rm GC} r^l \frac{e^{-\eta_n r^2} + e^{-\eta_n^* r^2}}{2} \qquad n = 1, \ldots, n_{\rm max}, \tag{2.54}$$

$$\phi_{nl}^{\rm GS}(r) = N_{nl}^{\rm GS} r^l \frac{e^{-\eta_n r^2} - e^{-\eta_n^* r^2}}{2i} \qquad n = 1, \ldots, n_{\rm max}, \tag{2.55}$$

with complex size parameters

$$\eta_n = (1 + i\alpha)\nu_n, \qquad \eta_n^* = (1 - i\alpha)\nu_n. \tag{2.56}$$

Some useful formulas involving matrix elements which are calculated within GEM in a complex range can be found in Appendix A.

2.4 Fitting the model parameters

To find new physics it is very important to test the theoretical model with as many as possible known states. It allows us to clearly understand the strengths and weaknesses of the model and thus to extract later reliable predictions.

We perform a study of the light meson spectrum taking into account the new resonances collected in Ref. [77] from the Crystal Barrel and PS172 data. This study implies a continuation of the previous work presented in Ref. [52], extending their thorough study of mesons to the higher excited states of light mesons. This leads to a fine tune of the model parameters, as we will see below.

The Fig. 2.3 shows the masses of all light mesons reported by the Particle Data Group [78] up to 1.9 GeV, and by Ref. [77] in which one can find resonances of light mesons up to 2.4 GeV. A more quantitative presentation of the experimental data

and their comparison with the theoretical predictions can be found in Appendix B, comments are also included.

An extensive spectrum of light non-strange $q\bar{q}$ states up to a mass of 2.4 GeV has emerged from Crystal Barrel and PS172 data on $\bar{p}p \to Resonance \to A + B$ in 17 final states. Crystal Barrel experiment ran at LEAR (CERN). Most of the data were taken during the last four months of LEAR operation, August-December 1996. The corresponding $\bar{p}p$ mass range is from 1962 to 2409 MeV. PS172 experiment ran during 1986 and extended the mass range to 1912 MeV.

All these data have been reviewed with detailed comments on the status of each resonance in Ref. [77]. The most striking feature is that all observed resonances cluster into fairly narrow mass ranges (i) $1590 - 1700$ MeV, (ii) $1930 - 2100$ MeV and (iii) $2240 - 2340$ MeV. It has been interpreted as a signal of an effective chiral symmetry restoration.

Based in that hypothesis, some authors [79–81] suggest that the dynamics of the light mesons is different in the lowest spectrum than in the higher one. The typical scale of chiral symmetry breaking is $\Lambda \sim 1$ GeV. Below this scale the chiral symmetry is known to be realized non-linearly (the Nambu-Goldstone realization), but above this scale the linear (Wigner-Weyl) realization is expected to be restored. The rationale for that is the following: if an hadron is highly excited the typical quark momenta are also high and therefore the quark dynamical mass becomes small, quarks decouple with Goldstone-bosons and the chiral symmetry gets approximately restored.

If the chiral symmetry restoration is realized, hadrons are placed in chiral multiplets. It means that for $q\bar{q}$ mesons one has [79]

- Mesons with $J = 0$:

$$\begin{aligned} &(1/2,1/2)_a : (I, J^{PC}) = (1, 0^{-+}) \leftrightarrow (0, 0^{++}), \\ &(1/2,1/2)_b : (1, 0^{++}) \leftrightarrow (0, 0^{-+}). \end{aligned} \tag{2.57}$$

- Mesons with $J = 2k$, $k = 1, 2, \ldots$:

$$\begin{aligned} (0,0) : (0, J^{--}) &\leftrightarrow (0, J^{++}), \\ (1/2,1/2)_a : (1, J^{-+}) &\leftrightarrow (0, J^{++}), \\ (1/2,1/2)_b : (1, J^{++}) &\leftrightarrow (0, J^{-+}), \\ (0,1) \oplus (1,0) : (1, J^{++}) &\leftrightarrow (1, J^{--}). \end{aligned} \tag{2.58}$$

- Mesons with $J = 2k - 1$, $k = 1, 2, \ldots$:

$$\begin{aligned} (0,0) : (0, J^{++}) &\leftrightarrow (0, J^{--}), \\ (1/2,1/2)_a : (1, J^{+-}) &\leftrightarrow (0, J^{--}), \\ (1/2,1/2)_b : (1, J^{--}) &\leftrightarrow (0, J^{+-}), \\ (0,1) \oplus (1,0) : (1, J^{--}) &\leftrightarrow (1, J^{++}). \end{aligned} \tag{2.59}$$

Above, we have considered only mesons of isospin $I = 0, 1$ and therefore three types of irreducible representations of the parity-chiral group exist. The parity-chiral group is $SU(2)_L \times SU(2)_R \times C_i$ where the group C_i has two elements, the

Quark masses	m_n (MeV)	313
	m_s (MeV)	555
	m_c (MeV)	1763
	m_b (MeV)	5110
Goldstone bosons	m_π (fm^{-1})	0.70
	m_σ (fm^{-1})	3.42
	m_K (fm^{-1})	2.51
	m_η (fm^{-1})	2.77
	Λ_π (fm^{-1})	4.20
	Λ_σ (fm^{-1})	4.20
	Λ_K (fm^{-1})	4.21
	Λ_η (fm^{-1})	5.20
	$g^2_{ch}/4\pi$	0.54
	θ_p ($^\circ$)	-15
One-gluon exchange	α_0	2.118
	Λ_0 (fm^{-1})	0.113
	μ_0 (MeV)	36.976
	$\hat{r}_0$ (fm)	0.181
	$\hat{r}_g$ (fm)	0.259
Confinement	a_c (MeV)	507.4
	μ_c (fm^{-1})	0.576
	Δ (MeV)	184.432
	a_s	0.81

Table 2.1. Model parameters.

identity and the inversion in three-dimensional space. This symmetry group is the symmetry of the QCD Lagrangian neglecting quark masses. The three types of irreducible representations specified by the isospin of the left-handed and right-handed quarks are $(I_L, I_R) = (0,0)$, $(1/2,1/2)$, where there are two independent irreducible representations $(1/2,1/2)_a$ and $(1/2,1/2)_b$, and $(0,1) \oplus (1,0)$.

However, the experimental data shows additional degeneracy, see Fig. 2.3. It can be interpreted as a larger symmetry that includes chiral $SU(2)_L \times SU(2)_R$ and $U(1)_A$ as subgroups, but also other mechanisms with different physics origin can explain it, like the modification of the confinement potential due to the color screening.

We analyze the role played by the screened confining potential as a possible explanation of the observed degeneracy. We have parametrized the behaviour of confinement potential in Eq. (2.45). At short distances this potential presents a linear behaviour while it becomes constant at large distances. It provides a threshold mass characterized by

$$M_{\rm thr} = \frac{16}{3}(a_c - \Delta) + m_q + m_{\bar{q}}, \tag{2.60}$$

which has been fixed phenomenologically.

We have taken, as a reference, the model parameters for the quark-quark interaction of Ref. [52] and perform a fine tune. The most important changes are the parameters of

	Light mesons			Heavy-light mesons				Heavy mesons		
	$I=1$	$I=0$	$I=1/2$	$(n\bar{c})$	$(s\bar{c})$	$(n\bar{b})$	$(s\bar{b})$	$(c\bar{c})$	$(c\bar{b})$	$(b\bar{b})$
Theo.	2.35	2.83	2.59	3.80	4.04	7.15	7.39	5.25	8.60	11.94
Exp.	2.33	2.51	2.49	2.64	2.86	5.74	5.85	4.42	6.28	11.02

Table 2.2. Threshold values, in GeV, for the different quark sectors. Experimental data refer to the highest state which is experimentally known in the corresponding sector [78]. We exclude those states which are quoted as "needs confirmation". The n symbol stands for u or d quark.

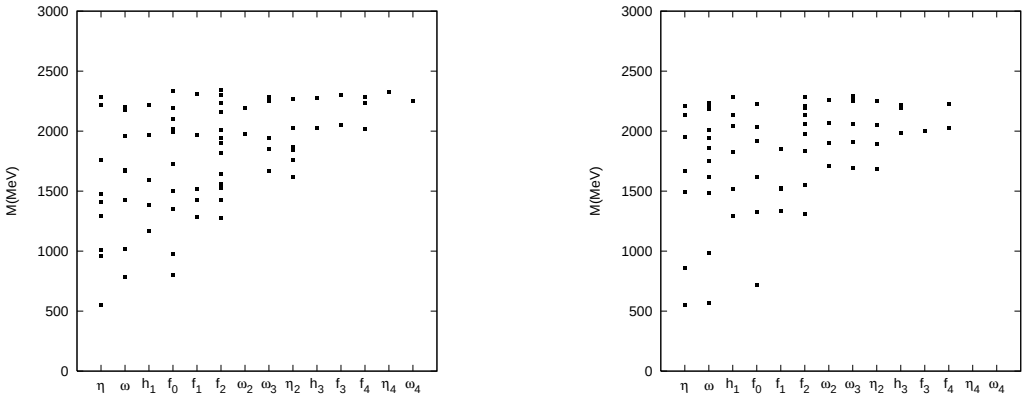

Figure 2.4. The left panel shows the experimental data of $I=0$ light mesons, our theoretical results are shown in the right panel.

the confinement potential which has been tuned to obtain the experimental thresholds. This process has been done keeping constant the product $a_c\mu_c$ to guarantee the good description of the low lying spectrum. The resulting parameters are shown in Table 2.1 and assuming flavor independence of the confinement potential, we show the threshold values for the different quark sectors in Table 2.2. The experimental data are the last states appearing in the Particle Data Group [78] except those which need confirmation. One can see that all the states are included in our theoretical thresholds. This is an important fact which tells us that we are very close to the limit where the meson string breaks and no more states are allowed. We are then in a critical region to understand the properties of the confinement interaction.

In Figures 2.4 and 2.5 we compare our calculation with the light meson spectrum with $I=0$ and $I=1$, respectively. One can see that the pattern of the degeneracy is very well reproduced. The sector $I=1$ is more suitable to single out the effect of the confinement color screening because it is not coupled to the strange sector and no suffers of the presence of glueballs. The theoretical calculation for sector $I=0$ is done in coupled channel calculation where $s\bar{s}$ components have been included. As expected, the degeneracy pattern is well reproduced although the comparison with the experimental data is worse.

It is worth to notice that the results are obtained without changes in the dynamical quark mass. Although the chiral symmetry is still broken, in fact this symmetry breaking is irrelevant because, as one can see in Tables 2.3 and 2.4, the contribution of the Goldstone-bosons is almost negligible compared with that from the confinement

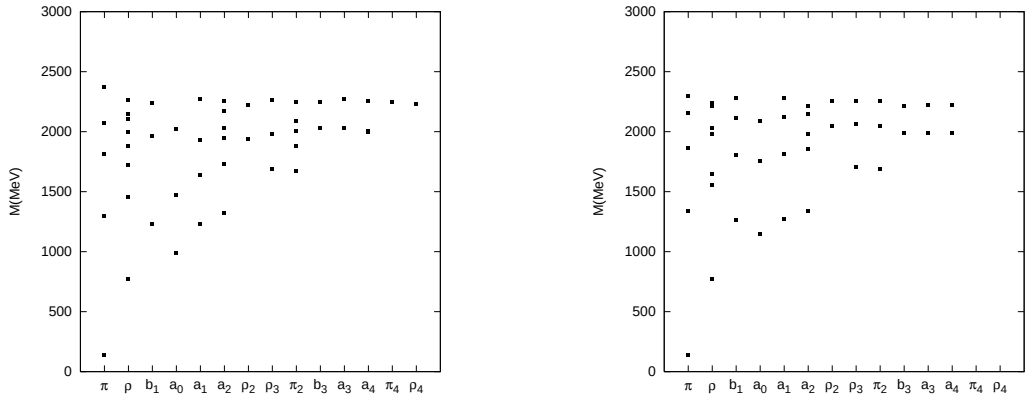

Figure 2.5. The left panel shows the experimental data of $I = 1$ light mesons, our theoretical results are shown in the right panel.

	$\eta_0(4S)$	$\omega_1/\phi_1(4S)$	$\eta_4(1G)$	$\omega_4/\phi_4(1G)$
Goldstone bosons	$+34.14$	-37.73	-0.74	$+1.94$
Confinement	-476.17	-685.85	-447.56	-432.39

Table 2.3. Contribution, in MeV, to the mass of the high excited states from the different potential pieces in the $I = 0$ sector.

	$\pi_0(4S)$	$\rho_1(4S)$	$\pi_4(1G)$	$\rho_4(1G)$
Goldstone bosons	-7.90	-1.46	$+0.18$	-0.64
Confinement	-480.19	-393.29	-445.62	-439.42

Table 2.4. Contribution, in MeV, to the mass of the high excited states from the different potential pieces in the $I = 1$ sector.

potential. Then, apparently, the effect is very similar to the decoupling of the Goldstone bosons from the quark sector.

Although chiral symmetry restoration and our model are able to reproduce degeneracy patterns for the high excited meson states, the physics behind the two approaches is very different. The hypothesis that Goldstone boson decouples from quarks is based on the assumption that increasing the excitation energy of an hadron one also increases the typical momentum of valence quarks. So the wave function range in coordinate space decreases as the excitation energy increases. In our approach, the degeneracy comes about from the gradual decreases of the confinement potential slope and so the wave function range in coordinate space increases as the excitation energy increases.

The differences between the two models can be single out studying the leptonic widths of the excited resonances. These are given by the Van Royen-Weisskopf formula with the QCD correction taken into account [82]. It contains, beside some known quantities, the wave function at the origin. Then, accurate knowledge of the leptonic widths of high meson excitations is of especial importance because the square module of the wave function at the origin $|R_{nS}(0)|^2$, proportional to $\Gamma_{e^+e^-}$, directly provides

	$\psi(nS)$			$\rho(nS)$		
	$2S$	$3S$	$4S$	$2S$	$3S$	$4S$
The.	1.78	1.11	0.78	0.155	0.058	0.026
Exp.	2.33 ± 0.07	0.89 ± 0.08	0.71 ± 0.10	-	-	-

Table 2.5. The leptonic widths, in keV, of higher excited states of ψ and ρ mesons. Experimental data are from Ref. [78] for $\psi(2S)$ and from Ref. [84] for $\psi(3S)$ and $\psi(4S)$.

information about the mechanism which produces the degeneracy.

If Goldstone-bosons decouple from quarks the wave function in coordinate space should decrease as the excitation energy increases and $\Gamma_{e^+e^-}$ should increase accordingly. In our model the behaviour of the wave function at the origin is just the opposite and the leptonic widths will decrease as the excitation energy increases. This behaviour is observed in the leptonic widths of high excitations in heavy quarkonia and explained by the flattening of the confinement potential at distances $r \geq 1.2\,\mathrm{fm}$ [83]. Assuming flavor independence for the confinement, it should also be expected for high excitations in light mesons. In Table 2.5 we show the agreement between our results for the leptonic widths of charmonium and the experimental data. In Table 2.5 we give also our predictions for high excitations of ρ meson. The measurement of these widths in the new PANDA experiment at FAIR may give definitive arguments about the possible effective restoration of chiral symmetry on the high spectrum of light mesons.

Chapter 3

Heavy meson spectroscopy

The discovery of charmonium and bottomonium states in 1970's opened up the possibility to use a nonrelativistic picture of QCD. They can indeed be classified in terms of the quantum numbers of a nonrelativistic bound state. The spacing of the excitations and of the fine and hyperfine splittings has a pattern similar to the ones in positronium, a well studied QED nonrelativistic bound state.

In addition, after the discovery of the $X(3872)$ more and more similar narrow resonances have been discovered and confirmed at electron-positron and proton-antiproton colliders. Some of namely XYZ mesons are in conflict with standard quarkonium interpretations, others fit well within the expected quarkonium levels.

We use the nonrelativistic potential model described above to study the heavy quark sector in order to establish which states can be explained as $q\bar{q}$ pairs and which do not fit in this scheme. In this chapter, we do not only study the energy spectrum but also electromagnetic decay widths.

3.1 Charmonium

In Table 3.1 we compare the calculated spectrum with the experimental data. We have taken into account the possible XYZ assignments predicted by our model. New conventional states have been well established in the PDG [78] during the last years. The h_c is the $^1P_1$ state of charmonium, singlet partner of the long-known χ_{cJ} triplet ^3P_J states. The $\eta_c(2S)$ is the first excitation of the pseudoscalar ground state $\eta_c(1S)$ and the $Z(3930)$ whose assignment as the 2^3P_2 state, $\chi_{c2}(2P)$, seems widely accepted.

3.1.1 The ψ states

In Table 3.2 we compare the calculated spectrum of $J^{PC} = 1^{--}$ $c\bar{c}$ states with the experimental data. The difference with respect Table 3.1 is that we show in Table 3.2 all possible XYZ mesons whose quantum numbers are more likely 1^{--}. The masses are taken from Ref. [78] for the well established states and from their respective original works for XYZ mesons. As one can see, the agreement with the experimental data is remarkable except for three states: the $G(3900)$, $X(4008)$ and $X(4260)$ which do not seem to fit in the $q\bar{q}$ scheme.

The first observation of an unexpected vector charmonium-like state was made by BaBar [89] in ISR production of $X(4260) \to \pi^+\pi^- J/\psi$. Then CLEO [90] and Belle [91] confirmed the BaBar result, but Belle also found a smaller, broader structure at 4008 MeV. BaBar [92] found one more apparent enhancement, $X(4360)$, in $\pi^+\pi^-\psi(2S)$,

State	J^{PC}	n	The. (MeV)	Exp. (MeV)	[78]
η_c	0^{-+}	1	2990	2980.3 ± 1.2	
		2	3643	3637 ± 4	
		3	4054	-	
χ_{c0}	0^{++}	1	3452	3414.75 ± 0.31	
		2	3909	$3915 \pm 3 \pm 2$	[85]
		3	4242	-	
h_c	1^{+-}	1	3515	3525.42 ± 0.29	
		2	3956	-	
		3	4278	-	
ψ	1^{--}	1	3096	3096.916 ± 0.011	
		2	3703	3686.093 ± 0.034	
		3	3796	3775.2 ± 1.7	
		4	4097	4039 ± 1	
		5	4153	4153 ± 3	
		6	4389	$4361 \pm 9 \pm 9$	[86]
		7	4426	4421 ± 4	
		8	4614	4634^{+8+5}_{-7-8}	[87]
		9	4641	$4664 \pm 11 \pm 5$	[86]
χ_{c1}	1^{++}	1	3504	3510.66 ± 0.07	
		2	3947	-	
		3	4272	-	
η_{c2}	2^{-+}	1	3812	-	
		2	4166	-	
		3	4437	-	
χ_{c2}	2^{++}	1	3532	3556.20 ± 0.09	
		2	3969	$3929 \pm 5 \pm 2$	[88]
		3	4043	-	
ψ_2	2^{--}	1	3810	-	
		2	4164	-	
		3	4436	-	

Table 3.1. Masses, in MeV, of charmonium states. We compare with the well established states in Ref. [78] and assign possible XYZ mesons.

which Belle [86] measured with somewhat larger mass and smaller width. Belle also found a second structure near 4660 MeV.

The $e^+e^- \to \Lambda_c^+\Lambda_c^-$ cross section was measured by Belle [87] using ISR and partial reconstruction. A clear peak is evident near the threshold. The nature of this enhancement remains unclear. Although both mass and width of the $X(4630)$ are consistent, see Table 3.2, within errors with those of the $X(4660)$, this could be coincidence and does not exclude other interpretations.

(nL)	States	The. (MeV)	Exp. (MeV)	
(1S)	J/ψ	3096	3096.916 ± 0.011	[78]
(2S)	$\psi(2S)$	3703	3686.09 ± 0.04	[78]
(1D)	$\psi(3770)$	3796	3772 ± 1.1	[78]
	$G(3900)$	-	3943 ± 21	[93, 94]
	$X(4008)$	-	4008 ± 40	[91]
(3S)	$\psi(4040)$	4097	4039 ± 1	[78]
(2D)	$\psi(4160)$	4153	4153 ± 3	[78]
	$X(4260)$	-	4260 ± 10	[89]
(4S)	$\psi(4360)$	4389	$4355^{+9}_{-10} \pm 9$	[86]
(3D)	$\psi(4415)$	4426	4421 ± 4	[78]
(5S)	$X(4630)$	4614	4634^{+8+5}_{-7-8}	[87]
(4D)	$X(4660)$	4641	$4664 \pm 11 \pm 5$	[86]

Table 3.2. Masses, in MeV, of ψ states. (nL) refers to the dominant partial wave.

The $D\bar{D}$ cross sections across the entire charm energy range from Belle [93] and BaBar [94] are consistent with one another. Both observe a structure in the ISR $D\bar{D}$ cross section, known as $G(3900)$, which must be taken into account to describe both the $D\bar{D}$ cross section and R [1] in the region between $\psi(3770)$ and $\psi(4040)$. This structure is qualitatively consistent with the theoretical predictions of the $D\bar{D}$ cross section and the R ratio using the Cornell model and without considering that the $G(3900)$ is a specific $c\bar{c}$ bound state [95]. Another explanation as a hybrid meson is also possible since different approaches of hybrid mesons predict states in this energy region.

We can assign as $q\bar{q}$ structures the $X(4360)$, $X(4630)$ and $X(4660)$ mesons attending to the masses. Throughout this work we will try to explain other properties of the XYZ assignments, as their decays, considering them as quark-antiquark pairs. For those mesons which we suspect more complex structures than $q\bar{q}$, we will give some explanation when possible. The $X(4008)$ resonance needs confirmation according to Ref. [13], a reasonable explanation of the $X(4260)$ is given below and a calculation of hybrid mesons will be discussed in another chapter.

The knowledge of the leptonic width of higher charmonium states is important for several reasons. First of all it allows to test the wave function at very short distances. Moreover it can help to distinguish between conventional $c\bar{c}$ mesons and multiquark structures which have much smaller dielectron widths [96]. The leptonic widths for the predicted states are compared in Table 3.3 with the recent data reported by the BES Collaboration in Ref. [97] and, once again, the agreement is good.

One striking feature of our model is the new assignment of the $\psi(4415)$. Usually this state has been assigned as a $4S$ state. Our particular choice of the potential includes the new $X(4360)$ as a $4S$ state between the well established $\psi(4160)$ and $\psi(4415)$ which are both predicted as D-wave states. Whether or not this assignment is correct can be tested with the e^+e^- leptonic widths. From Table 3.3 one can see that the width of the $4S$ state is 0.78 keV, whereas the experimental value for the $\psi(4415)$ is $\Gamma_{e^+e^-} = 0.35 \pm 0.12$ keV, in excellent agreement with the result for the $3D$ state

[1] R is the ratio between the total e^+e^- annihilation cross section into hadrons and $\sigma(e^+e^- \to \mu^+\mu^-)$.

(nL)	State	$M_{\rm The.}$ (MeV)	$\Gamma_{\rm The.}$ (keV)	$\Gamma_{\rm Exp.}$ (keV)	
$(1S)$	J/ψ	3096	3.93	$5.55 \pm 0.14 \pm 0.02$	[78]
$(2S)$	$\psi(2S)$	3703	1.78	2.33 ± 0.07	[78]
$(1D)$	$\psi(3770)$	3796	0.22	0.22 ± 0.05	[97]
$(3S)$	$\psi(4040)$	4097	1.11	0.83 ± 0.20	[97]
$(2D)$	$\psi(4160)$	4153	0.30	0.48 ± 0.22	[97]
$(4S)$	$X(4360)$	4389	0.78	-	-
$(3D)$	$\psi(4415)$	4426	0.33	0.35 ± 0.12	[97]
$(5S)$	$X(4630)$	4614	0.57	-	-
$(4D)$	$X(4660)$	4641	0.31	-	-

Table 3.3. Leptonic decay widths, in keV, of ψ states.

State	Mass (MeV)	$\mathcal{P}_{^3S_1}$	$\mathcal{P}_{^3D_1}$
J/ψ	3096	99.959	0.041
$\psi(2S)$	3703	99.958	0.042
$\psi(3770)$	3796	0.032	99.968
$\psi(4040)$	4097	99.935	0.065
$\psi(4160)$	4153	0.060	99.940
$\psi(4360)$	4389	99.908	0.092
$\psi(4415)$	4426	0.089	99.911
$\psi(4660)$	4614	99.884	0.116
$\psi(4660)$	4641	0.114	99.886

Table 3.4. The $^3S_1$ and $^3D_1$ channel probability, in (%), of ψ states.

(0.33 keV). The measurement of the leptonic width for the $X(4360)$ is very important and would clarify the situation.

It is generally assumed that the 1^{--} $c\bar{c}$ mesons are a mixture of $^3S_1$ and $^3D_1$ states in order to reproduce the leptonic widths. The mixing angle ranges from $\theta = -17$ [98] to $\theta = +34$ [99]. In our model the mixing is not fitted to the experimental data but driven by the tensor piece of the quark-antiquark interaction. In Table 3.4 we show the different components of these states. One can see that all are almost pure states either $^3S_1$ or $^3D_1$ and we can reasonably reproduce the leptonic widths.

The study of higher multipole contributions to the radiative transitions between spin-triplet states involves an alternative way to disentangle the mixing between S and D-waves in 1^{--} $c\bar{c}$ mesons. The radiative decay sequences

$$e^+e^- \to \psi(2S), \quad \psi(2S) \to \gamma' \, \chi_{(c1,c2)}, \quad \chi_{(c1,c2)} \to \gamma J/\psi, \quad J/\psi \to e^+e^- \text{ or } \mu^+\mu^-, \tag{3.1}$$

has been studied experimentally in Ref. [100]. The electric dipole E1 amplitudes are dominant but higher multipole contributions are allowed.

For the χ_{cJ} $(J = 1, 2)$ sequences, they search for two multipole amplitudes $b_2^{J=1,2}$ and $a_2^{J=1,2}$, where b stands for the amplitude where χ_{cJ} is a reaction product $(\psi' \to \gamma'\chi_{cJ})$ and a stands for the amplitude where χ_{cJ} is the decay particle $(\chi_{cJ} \to \gamma J/\psi)$. In the case χ_{cJ} with $J = 2$, the process has contribution from E3 amplitude but is

Mode	$\Gamma_{\rm The.}$	$\Gamma_{\rm Exp.}$
$\gamma(\gamma J/\psi)_{\chi_{c0}}$	0.156	$0.125 \pm 0.007 \pm 0.013$
$\gamma(\gamma J/\psi)_{\chi_{c1}}$	4.423	$3.56 \pm 0.03 \pm 0.12$
$\gamma(\gamma J/\psi)_{\chi_{c2}}$	2.099	$1.95 \pm 0.02 \pm 0.07$

Table 3.5. Branching fraction for the decay $\psi(2S) \to \gamma(\gamma J/\psi)_{\chi_{cJ}}$. Experimental data are from [102].

considered negligible.

Theoretically, if one defines E1, M2 and E3 to be the electric dipole, magnetic quadrupole and electric octupole amplitudes, respectively. The amplitudes mentioned above are given by [101]

$$\begin{aligned}
a_2^{J=1} &\equiv \frac{M2}{\sqrt{E1^2+M2^2}} = -\frac{E_\gamma}{4m_c}(1+\kappa_c), \\
a_2^{J=2} &\equiv \frac{M2}{\sqrt{E1^2+M2^2+E3^2}} = -\frac{3}{\sqrt{5}}\frac{E_\gamma}{4m_c}(1+\kappa_c), \\
b_2^{J=1} &\equiv \frac{M2}{\sqrt{E1^2+M2^2}} = \frac{E_{\gamma'}}{4m_c}(1+\kappa_c), \\
b_2^{J=2} &\equiv \frac{M2}{\sqrt{E1^2+M2^2+E3^2}} = \frac{3}{\sqrt{5}}\frac{E_{\gamma'}}{4m_c}(1+\kappa_c),
\end{aligned} \tag{3.2}$$

where these expressions are first order contributions in E_γ/m_c or $E_{\gamma'}/m_c$ assuming that the $\psi(1S)$ and $\psi(2S)$ are pure S-wave states (no mixing with D-wave states) and that the χ_{cJ} states are pure P-wave states (no mixing with F-wave states).

We show in Fig. 3.1 the experimental data (solid circles) obtained by the CLEO Collaboration in Ref. [100]. The rest of the data are previous to Ref. [100]. Our theoretical estimations assuming $m_c = 1763\,\text{MeV}$ and $\kappa_c = 0$ are represented by a vertical solid line. The same theoretical estimations considering a c-quark mass ($m_c = 1.5\,\text{GeV}$) closer to the PDG value are represented by a vertical dashed line as given in Ref. [100]. The last experimental measurements and the theoretical estimations agrees well. In some sense it indicates us that the mixing between S and D-waves in the 1^{--} $c\bar{c}$ states is small. Note that the mixture in our model is given by the tensor piece. Its contribution is small for the 1^{--} channel, but also in others as the 2^{++} channel where the mixing is between the P and F-waves.

The mixing between $L = J-1$ and $L = J+1$ partial waves of a state with $J \neq 0$ and $S = 1$ is provided by the tensor term of our OGE potential. This tensor force is small enough to have almost purely one orbital state component.

To end the above discussion, the formula for the E1 transitions, Eq. (C.2), can be used to calculate the branching fraction of the process $\psi(2S) \to J/\psi\gamma\gamma$ trough $\gamma\chi_{cJ}$. In Table 3.5 we compare our results with those of Ref. [102]. We reproduce not only the tendency of the experimental data but the agreement of the absolute value is also good.

Finally in Tables 3.6, 3.7, 3.8 and 3.9 we quote the E1 and M1 radiative transitions. The results are in general agreement with the scarce experimental results. CLEO has recently reported [103, 104] results on $\psi(3770) \to \gamma\chi_{cJ}$ with $J = 0, 1$ and upper limit for $J = 2$. Also upper limits are placed on the decays $\psi(4040) \to \gamma\chi_{cJ}$ and

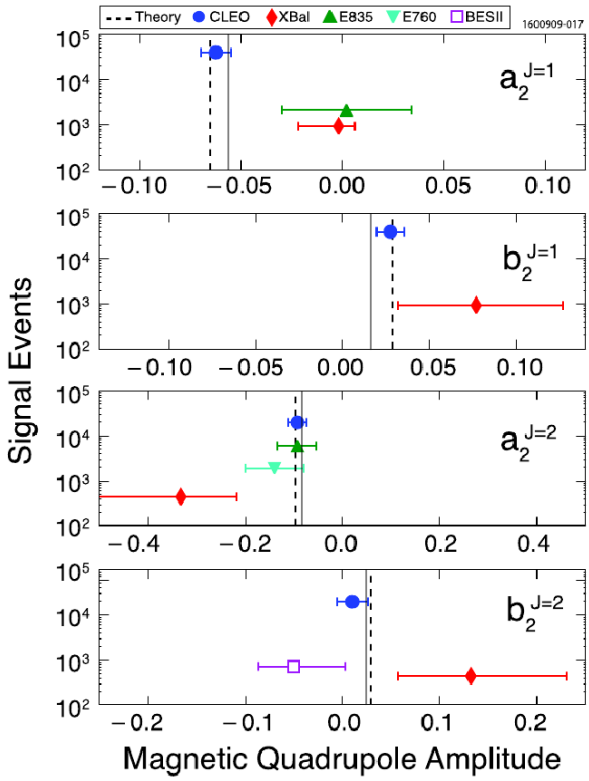

Figure 3.1. Figure from Ref. [100]. Experimental values of the magnetic quadrupole amplitudes obtained by the CLEO Collaboration and their comparison with previous experimental data and theoretical expectations.

$\psi(4160) \to \gamma\chi_{cJ}$. Our results slightly overestimate the experimental results which may indicate that coupled-channel corrections may be significant in this case.

The $J/\psi \to 3\gamma$ width

The CLEO Collaboration has recently measured the branching ratio of the $J/\psi \to 3\gamma$ decay using $\psi(2S) \to \pi^+\pi^- J/\psi$ events acquired with the CLEO-c detector operating at the CESR e^+e^- collider. A signal of 6σ significance was found with branching fraction $\mathcal{B}_{3\gamma} = (1.2 \pm 0.3 \pm 0.2) \times 10^{-5}$ [105]. This value is almost a factor 5 below the one expected from the $J/\psi \to e^+e^-$ decay ignoring QCD corrections which suggests that these corrections can be large. Then the understanding of this disagreement is very important because it can shed some light on the knowledge of the behavior of QCD loop expansion when its coefficients are large.

The expression for the width of the $J/\psi \to 3\gamma$ can be calculated in the formalism developed by Glover and Morgan for one boson decay to three photons [106]. The calculation is analogous to the decay of the orthopositronium (o-Ps) to three photons which has the same quantum numbers. This rate has been extensively studied in the past mainly due to the discrepancies that, from time to time, appeared between the successive improvements of the experimental data and the theoretical corrections. The

Initial meson	Final meson	$\Gamma_{\text{The.}}$ (keV)	$\mathcal{B}_{\text{The.}}$	$\mathcal{B}_{\text{Exp.}}$
$\psi(2^3S_1)$	$\chi_{c0}(1^3P_0)$	31.9	11.2×10^{-2}	$(9.62 \pm 0.31) \times 10^{-2}$
	$\chi_{c1}(1^3P_1)$	35.4	12.5×10^{-2}	$(9.20 \pm 0.40) \times 10^{-2}$
	$\chi_{c2}(1^3P_2)$	30.1	10.6×10^{-2}	$(8.74 \pm 0.35) \times 10^{-2}$
$\psi(1^3D_1)$	$\chi_{c0}(1^3P_0)$	252.3	9.6×10^{-3}	$(7.3 \pm 0.9) \times 10^{-3}$
	$\chi_{c1}(1^3P_1)$	99.1	3.8×10^{-3}	$(2.9 \pm 0.6) \times 10^{-3}$
	$\chi_{c2}(1^3P_2)$	3.6	1.4×10^{-4}	$< 9.0 \times 10^{-4}$
$\psi(3^3S_1)$	$\chi_{c0}(1^3P_0)$	16.8	-	-
	$\chi_{c1}(1^3P_1)$	18.2	2.3×10^{-2}	$< 1.1 \times 10^{-2}$
	$\chi_{c2}(1^3P_2)$	14.8	1.9×10^{-4}	$< 1.7 \times 10^{-2}$
	$\chi_{c0}(2^3P_0)$	10.7	-	-
	$\chi_{c1}(2^3P_1)$	14.0	-	-
	$\chi_{c2}(2^3P_2)$	48.5	-	-
$\psi(2^3D_1)$	$\chi_{c0}(1^3P_0)$	165.0	-	-
	$\chi_{c1}(1^3P_1)$	60.3	5.9×10^{-4}	$< 7 \times 10^{-3}$
	$\chi_{c2}(1^3P_2)$	1.6	1.5×10^{-5}	$< 1.3 \times 10^{-2}$
	$\chi_{c0}(2^3P_0)$	144.2	-	-
	$\chi_{c1}(2^3P_1)$	93.5	-	-
	$\chi_{c2}(2^3P_2)$	6.8	-	-

Table 3.6. E1 radiative transitions of ψ states. The branching fraction $\mathcal{B}_{\text{The.}}$ is calculated using the experimental value for the total width. The experimental data are from [78].

theoretical result from o-Ps decay can be written as

$$\Gamma_0 = \frac{16}{9}\frac{(\pi^2 - 9)}{m^2}\alpha^3 e^6 |\phi(0)|^2. \tag{3.3}$$

This formula coincides with the old Ore and Powell [107] expression if one takes for the wave function at the origin the hydrogen-like wave function value.

To obtain the $J/\psi \to 3\gamma$ width from Eq. (3.3) one has to use $e_Q = +2/3$ instead of $e = -1$ and multiply by a factor 3 to take into account the three quark colors, leading to the final expression

$$\Gamma_0(J/\psi \to 3\gamma) = \frac{4}{3\pi}\frac{(\pi^2 - 9)}{m_Q^2}\alpha^3 e_Q^6 |R_{1S}(0)|^2, \tag{3.4}$$

where we have separated the radial part from the total wave function. Using the wave function calculated by the constituent quark model we obtain $\mathcal{B}_{3\gamma} = 3.4 \times 10^{-5}$ where we have used the experimental value for the total width. This theoretical estimation is almost three times the experimental result.

One-loop QCD corrections can be adapted from the expressions for o-Ps decay. This correction has been calculated in Ref. [108] using the formalism of Ref. [106] in the framework of the nonrelativistic QED. We show the diagrams that enter in the one-loop correction to the decay amplitude in Fig. 3.2, where the photon which gives

Initial meson	Final meson	$\Gamma_{\text{The.}}$ (keV)
$\psi(4^3S_1)$	$\chi_{c0}(1^3P_0)$	21.6
	$\chi_{c1}(1^3P_1)$	28.9
	$\chi_{c2}(1^3P_2)$	29.4
	$\chi_{c0}(2^3P_0)$	24.0
	$\chi_{c1}(2^3P_1)$	41.8
	$\chi_{c2}(2^3P_2)$	81.7
	$\chi_{c0}(3^3P_0)$	27.2
	$\chi_{c1}(3^3P_1)$	51.6
	$\chi_{c2}(3^3P_2)$	68.4
$\psi(3^3D_1)$	$\chi_{c0}(1^3P_0)$	120.6
	$\chi_{c1}(1^3P_1)$	43.0
	$\chi_{c2}(1^3P_2)$	0.9
	$\chi_{c0}(2^3P_0)$	107.2
	$\chi_{c1}(2^3P_1)$	58.0
	$\chi_{c2}(2^3P_2)$	2.7
	$\chi_{c0}(3^3P_0)$	93.7
	$\chi_{c1}(3^3P_1)$	63.1
	$\chi_{c2}(3^3P_2)$	2.6

Table 3.7. E1 radiative transitions of ψ states (Continuation I).

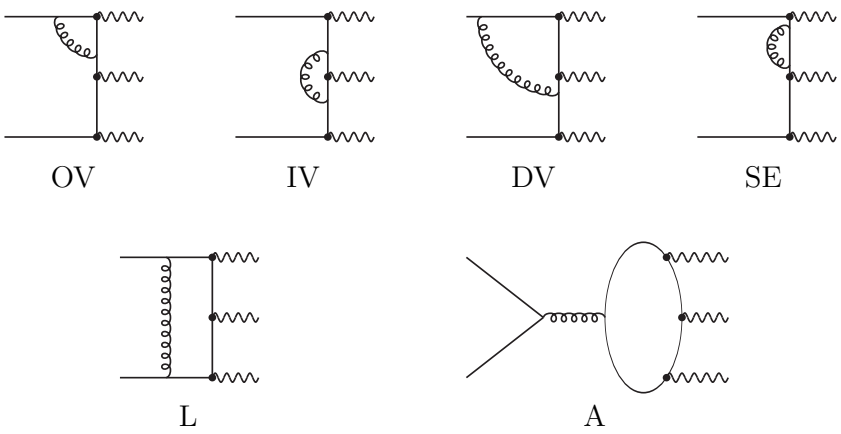

Figure 3.2. One-loop diagrams that contribute to the decay amplitude at first order in α_s.

the radiative correction has been changed by a gluon. Following [108] we refer to the six diagrams as the outer vertex (OV), inner vertex (IV), double vertex (DV), self-energy (SE), ladder (L), and annihilation vertex (A). The separated contributions of each diagram can be found in [108]. Collecting all the contributions together we arrive for the orthopositronium at

$$\Gamma = \Gamma_0 \left[1 + A\left(\frac{\alpha}{\pi}\right)\right], \tag{3.5}$$

Initial meson	Final meson	$\Gamma_{\text{The.}}$ (keV)
$\psi(5^3S_1)$	$\chi_{c0}(1^3P_0)$	19.5
	$\chi_{c1}(1^3P_1)$	27.2
	$\chi_{c2}(1^3P_2)$	29.4
	$\chi_{c0}(2^3P_0)$	22.1
	$\chi_{c1}(2^3P_1)$	39.4
	$\chi_{c2}(2^3P_2)$	72.0
	$\chi_{c0}(3^3P_0)$	22.4
	$\chi_{c1}(3^3P_1)$	39.2
	$\chi_{c2}(3^3P_2)$	47.0
	$\chi_{c0}(4^3P_0)$	22.9
	$\chi_{c1}(4^3P_1)$	43.0
	$\chi_{c2}(4^3P_2)$	56.9
$\psi(4^3D_1)$	$\chi_{c0}(1^3P_0)$	100.1
	$\chi_{c1}(1^3P_1)$	36.6
	$\chi_{c2}(1^3P_2)$	0.7
	$\chi_{c0}(2^3P_0)$	94.4
	$\chi_{c1}(2^3P_1)$	50.1
	$\chi_{c2}(2^3P_2)$	1.9
	$\chi_{c0}(3^3P_0)$	82.6
	$\chi_{c1}(3^3P_1)$	49.2
	$\chi_{c2}(3^3P_2)$	1.5
	$\chi_{c0}(4^3P_0)$	72.1
	$\chi_{c1}(4^3P_1)$	51.2
	$\chi_{c2}(4^3P_2)$	2.0

Table 3.8. E1 radiative transitions of ψ states (Continuation II).

where the best value for A is given by [108] and is $A = -10.286606$.

To adapt these diagrams to the QCD case one has to include a factor $\lambda_c/2$ in each vertex diagram which contributes with a global factor 4/3. Furthermore, the diagram (A) does not contribute to the QCD case due to color conservation. Summing up all the contributions one arrives at the expression

$$\Gamma = \Gamma_0 \left[1 + A_{\text{QCD}} \left(\frac{\alpha_s}{\pi}\right)\right], \tag{3.6}$$

with $A_{\text{QCD}} = -12.630$.

Now, using the value of the $\alpha_s(m_c^2)$ coupling constant at the charm quark mass ($\alpha_s = 0.288$) the first correction to the width cancels with the zeroth order approximation given a theoretical prediction compatible with zero.

Because of the strong cancellation between the first two terms in Eq. (3.6), the most important contribution to the decay rate comes from the $\left(\frac{\alpha_s}{\pi}\right)^2$ term. This correction has two different sources. The first one arises when we square the one-loop corrections to the annihilation amplitude. The second one corresponds to the leading order two-loop corrections. This part cannot be straightforwardly deduced from the two-loop

Initial meson	Final meson	$\Gamma_{\text{The.}}$ (keV)	$\mathcal{B}_{\text{The.}}$	$\mathcal{B}_{\text{Exp.}}$
$\psi(1^3S_1)$	$\eta_c(1^1S_0)$	2.1	2.2×10^{-2}	$(1.7 \pm 0.4) \times 10^{-2}$
$\psi(2^3S_1)$	$\eta_c(1^1S_0)$	10.8	3.8×10^{-2}	$(3.4 \pm 0.5) \times 10^{-3}$
	$\eta_c(2^1S_0)$	0.2	5.5×10^{-4}	$< 8.0 \times 10^{-4}$
$\psi(3^3S_1)$	$\eta_c(1^1S_0)$	12.2	-	-
	$\eta_c(2^1S_0)$	2.0	-	-
	$\eta_c(3^1S_0)$	4.6×10^{-3}	-	-
$\psi(4^3S_1)$	$\eta_c(1^1S_0)$	16.7	-	-
	$\eta_c(2^1S_0)$	5.3	-	-
	$\eta_c(3^1S_0)$	1.4	-	-
	$\eta_c(4^1S_0)$	4.7×10^{-2}	-	-
$\psi(5^3S_1)$	$\eta_c(1^1S_0)$	16.7	-	-
	$\eta_c(2^1S_0)$	6.1	-	-
	$\eta_c(3^1S_0)$	2.3	-	-
	$\eta_c(4^1S_0)$	0.7	-	-
	$\eta_c(5^1S_0)$	2.3×10^{-2}	-	-

Table 3.9. M1 radiative transitions of ψ states. The branching fraction $\mathcal{B}_{\text{The.}}$ is calculated using the experimental value for the total width. The experimental data are from [78].

QED corrections due to the non-Abelian character of QCD. However, we can naively estimate the first contribution as

$$B_{1,\text{QCD}} = \left(\frac{A_{\text{QCD}}}{2}\right)^2. \tag{3.7}$$

In the o-Ps case Burichenko has shown [109] that this estimate is in fact a lower bound for the contribution under consideration. Thus we estimate the $J/\psi \to 3\gamma$ decay rate as

$$\Gamma(J/\psi \to 3\gamma) = 3.17 \times 10^{-3} \left[1 - 12.630 \left(\frac{\alpha_s}{\pi}\right) + 39.879 \left(\frac{\alpha_s}{\pi}\right)^2\right], \tag{3.8}$$

expressed in keV. With this new correction the theoretical value is now $\mathcal{B}_{3\gamma} = 0.6 \times 10^{-5}$ lower than the experimental data but near the experimental error bar.

This result shows the importance of the high order corrections in this particular decay. The leading order of the two-loop corrections, which are almost of the same size as the one coming from the square of one-loop corrections in the orthopositronium decay [110] should contribute to obtain more precise results.

Non-resonant explanation for the $X(4260)$ structure

The $X(4260)$ $J^{PC} = 1^{--}$ charmonium enhancement was discovered in $\pi^+\pi^- J/\psi$ by the BaBar Collaboration [89]. It was later confirmed and also seen in $\pi^0\pi^0 J/\psi$ as well as $K^+K^- J/\psi$ by CLEO [104], and finally by Belle in $\pi^+\pi^- J/\psi$ [91].

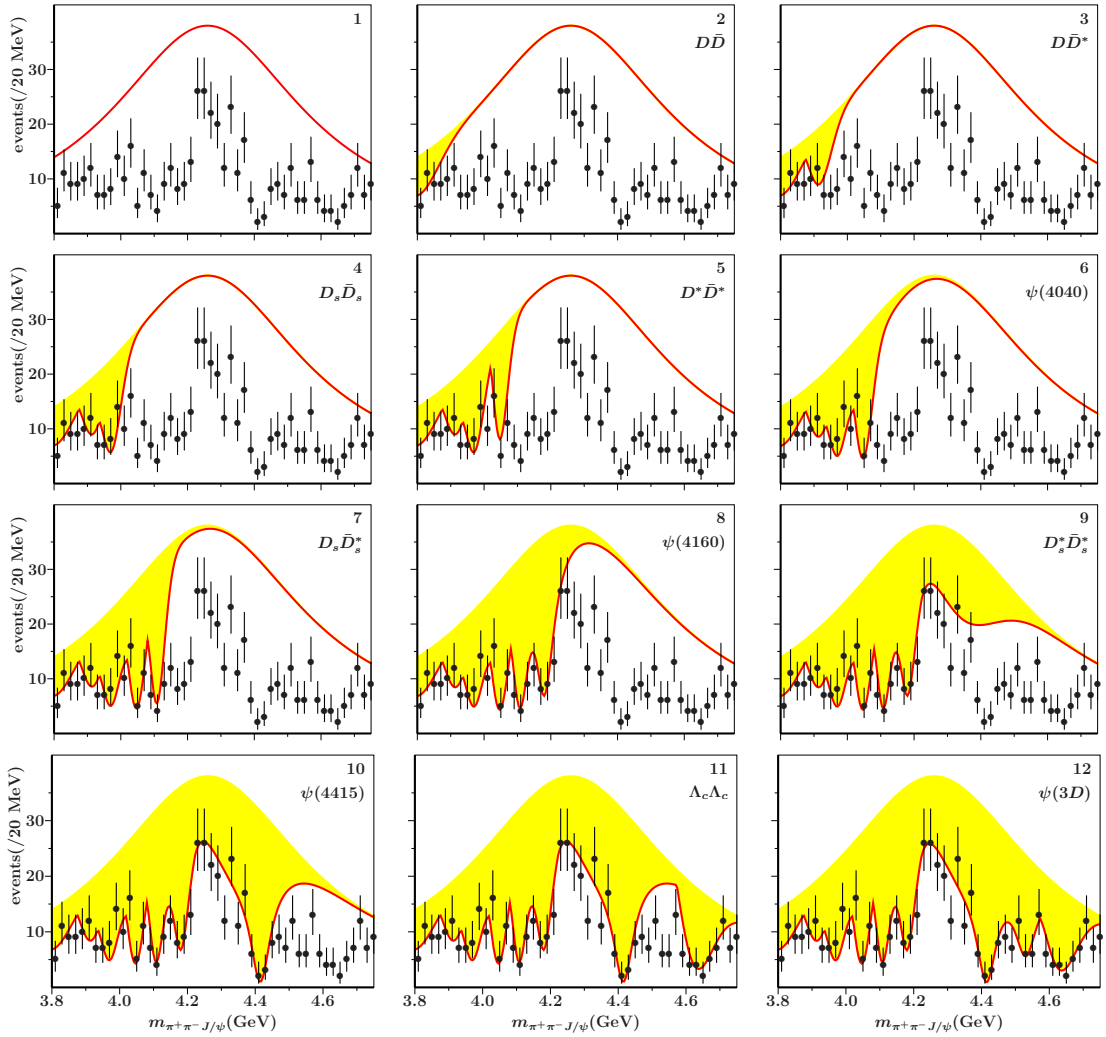

Figure 3.3. A stepwise study of how the presumed $X(4260)$ signal in $e^+e^- \to \pi^+\pi^- J/\psi$ [89] is depleted by OZI-allowed processes.

The experimental observation of the completely unexpected $X(4260)$ resonance has stimulated extensive interest among theorists and experimentalists. In the past years, different theoretical interpretations were proposed to understand its underlying structure, which can be categorized in two groups, *i.e.* an exotic state and a conventional charmonium. Although there already exist many theoretical explanations, we cannot give a definite solution. This has sparked our interest in further investigating $X(4260)$ under a framework different from these existing theoretical explanations.

In Ref. [112] Eef van Beveren and George Rupp, with my collaboration, discuss the shape of the $X(4260)$ observed in the Okubo-Zweig-Iizuka (OZI)-forbidden process $e^+e^- \to \pi^+\pi^- J/\psi$, in particular, at and near vector charmonium resonances as well as open-charm threshold enhancements. The model used differs from that presented in this work and so the predicted masses for charmonium resonances are also slightly different. The reader is referred to [112] and references therein for further details.

The most interesting and puzzling aspect of all experimental data related with

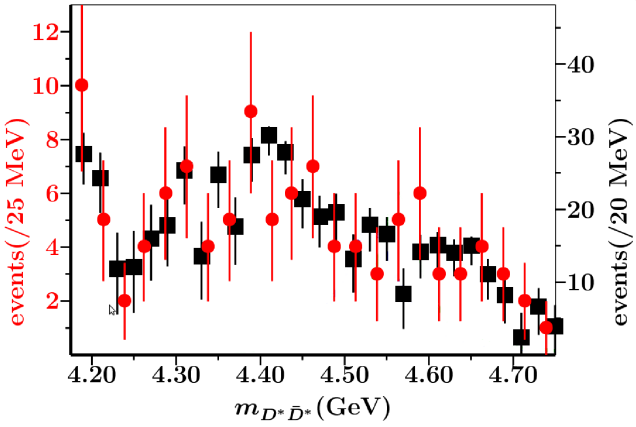

Figure 3.4. BaBar data for $e^+e^- \to D^*\bar{D}^*$ [111], (●), and the missing signal in $e^+e^- \to \pi^+\pi^- J/\psi$ [89], (■), due to OZI-allowed decay processes as shown in panel (12) of Fig. 3.3. The annotations at the vertical axis on the left-hand side refer to the data of Ref. [111], while those on the right-hand side concern the data of Ref. [89]. The missing signal is adjusted in magnitude so as to be compared with the $e^+e^- \to D^*\bar{D}^*$ data.

the $X(4260)$ resonance, in particular, the initial-state radiation events for $e^+e^- \to \gamma_{\rm ISR}\pi^+\pi^- J/\psi$ collected by BaBar detector in the invariant-mass spectrum of $\pi^+\pi^- J/\psi$, is the depletion of the signal exactly at the mass of the $\psi(4415)$ resonance. Our interpretation of the enhancement at $X(4260)$ observed in $e^+e^- \to \pi^+\pi^- J/\psi$ is that near a $c\bar{c}$ resonance its decay into open-charm mesons dominates and hence depletes the $\pi^+\pi^- J/\psi$ signal. Actually, panel (9) of Fig. 3.3 shows the lack of signal just above all open-charm thresholds and also at the vector charmonium resonances in the relevant invariant-mass region.

The original signal (panel (1) of Fig. 3.3) from which we have eliminated in a stepwise fashion the depletions due to the $c\bar{c}$ resonances and the open-charm thresholds (remaining panels in Fig. 3.3) is the very broad $X(4260)$ structure. It does not seem to classify itself as a 1^{--} $c\bar{c}$ resonance rather as a non-resonant structure.

In order to judge whether our presumed shape of the $X(4260)$ enhancement makes any sense, we compare it to production data for open-charm pairs. To that end, in Fig. 3.4 we depict, in one and the same figure, BaBar production data [111] for the open-charm reaction $e^+e^- \to D^*\bar{D}^*$ (●), as well as the differences (■) between the presumed shape of the $X(4260)$ enhancement and the experimental data, also by BaBar [89], for $e^+e^- \to \pi^+\pi^- J/\psi$. We have indicated in Fig. 3.4 how the magnitudes of the two signals are adjusted, due to different experimental efficiencies for the two processes, in order to be comparable. As a matter of fact, close to the $D^*\bar{D}^*$ threshold (at 4.02 GeV) we cannot really compare the two data sets, because the phase space factors of $\pi^+\pi^- J/\psi$ and $D^*\bar{D}^*$ are very different at that energy. However, from roughly 4.2 GeV upwards we may to some extent ignore phase space effects.

One observes in Fig. 3.4 that indeed the OZI-allowed signal of $e^+e^- \to D^*\bar{D}^*$ is in very good agreement with the signal stemming from the missing signal in $e^+e^- \to \pi^+\pi^- J/\psi$ reaction, both sharing in detail their maxima and minima as a function of the invariant mass.

3.1.2 The η_c states

Here we discuss the $^1S_0$ singlet $c\bar{c}$ states. The $\eta_c(1S)$ is the lowest state of charmonium. The model predicts a mass of 2990 MeV in good agreement with the experimental one. The splitting between 1^1S_0 and 1^3S_1 is given by the Dirac delta term of the OGE potential. This splitting is measured experimentally to be 116.6 ± 1.2 MeV which is in reasonable agreement with our prediction of 106 MeV. The $\eta_c(1S)$ decays only into mesons via weak interaction or annihilates into two photons due to its even C-parity. The decay of η_c into two photons is given by the wave function at the origin and our prediction is 7.77×10^{-4} for its branching fraction. It is 12 times larger than the experimental value, $(6.3 \pm 2.9) \times 10^{-5}$. Theoretically one can suppose that the wave function at the origin of 1^1S_0 and 1^3S_1 is the same and predicts the ratio between $1^1S_0 \to 2\gamma$ and $J/\psi \to e^+e^-$ decay rates where the value of the wave function at the origin cancels. The theoretical ratio obtained is 1.6 with $\alpha_s \sim 0.3$ and the experimental one is 1.21 ± 0.22 [78]. This indicates that η_c and J/ψ may have a similar value of the wave function at the origin. It is not the case in our model because the range of the η_c wave function is small and it peaks up its value at the origin, increasing the theoretical values of annihilation rates.

The search for a reproducible $\eta_c(2S)$ signal has a long history. Recently, Belle [25] found a signal in $B \to K\eta_c(2S)$ in the exclusive $\eta_c(2S) \to K^0_S K^-\pi^+$ decay mode (a favorite all-charged final state for $\eta_c(1S)$), at $3654 \pm 6 \pm 8$ MeV. Since then, measurements of $\eta_c(2S)$ in that mass region have been reported by BaBar [26], CLEO [27], and Belle [113] in $\gamma\gamma$-fusion to $K\bar{K}\pi$ final states and by BaBar [114] and Belle [115] in double charmonium production.

Our predicted mass for the $\eta_c(2S)$ is shown in Table 3.1 as 3643 MeV. It is in very good agreement with the experimental data. The updated ratio into two photons of the $\eta_c(2S)$ is $< 5 \times 10^{-4}$ [78]. Our result is 1.28×10^{-3}, 2.5 times larger than the experimental upper bound. As one can see, the effect of the high value at the origin for the wave function is reduced as we go up in the spectrum.

The $\eta_c(3S)$ is the first state which can decay into open-charm mesons, being its mass 4054 MeV. We will study later the strong decays into open-charm mesons. We also calculate the partial width of the $\eta_c(3S)$ into two photons and our prediction is 17.0 keV.

For completeness, we give the decay rates for different E1 and M1 transitions of the n^1S_0 states in Table 3.10.

3.1.3 The h_c states

Two experiments reported the observation of the $h_c(1P)$ in 2005. CLEO [116, 117] obtained a 6σ statistical significance in the isospin-forbidden decay chain $e^+e^- \to \psi(2S) \to \pi^0 h_c$, $h_c \to \gamma\eta_c(1S)$. E835 [118] found a 3σ evidence in $p\bar{p} \to h_c$, $h_c \to \gamma\eta_c(1S)$, $\eta_c(1S) \to \gamma\gamma$.

The precision measurement of its mass was reported by CLEO in 2008 [119], $3525.28 \pm 0.19 \pm 0.12$ MeV. Later, BES III [120] has confirmed this with a mass of $3525.40 \pm 0.13 \pm 0.18$ MeV. The measurement of the h_c mass is important since lattice data show a vanishing long-range component of the spin-spin potential. Thus, this part of the potential appears to be entirely dominated by its short-range, delta-like term,

Initial meson	Final meson	$\Gamma_{\rm The.}$ (keV)
$\eta_c(2^1S_0)$	$h_c(1^1P_1)$	42.41
	$\psi(1^3S_1)$	3.90
$\eta_c(3^1S_0)$	$h_c(1^1P_1)$	9.12
	$h_c(2^1P_1)$	67.21
	$\psi(1^3S_1)$	4.16
	$\psi(2^3S_1)$	1.02

Table 3.10. E1 and M1 radiative transitions of η_c states.

n	$m(h_c)$ (MeV)	$\langle m(n^3P_J)\rangle_{\rm The.}$ (MeV)	$\langle m(n^3P_J)\rangle_{\rm Exp.}$ (MeV)
1	3515	3513	3525.30 ± 0.20
2	3956	3955	-
3	4278	4278	-

Table 3.11. The theoretical masses, in MeV, of the ground state and the first two excitations of h_c, compared with the spin-averaged centroid, in MeV, of the corresponding triplet P-wave states. We compare with the experimental data [78].

suggesting that the $^1P_1$ should be close to the center-of-gravity of the ^3P_J system

$$\langle m(1^3P_J)\rangle \equiv \frac{m_{\chi c0} + 3m_{\chi c1} + 5m_{\chi c2}}{9}. \tag{3.9}$$

This makes the hyperfine mass splitting, $\Delta m_{hf}[h_c(1P)] = \langle m(1^3P_J)\rangle - m[h_c(1P)]$, an important measurement of the spin-spin interaction. The centroid of the 1^3P_J states is known to be [78] 3525.30 ± 0.04 MeV and then the hyperfine splitting is $+0.02 \pm 0.23$ MeV from CLEO and -0.10 ± 0.22 MeV from BES III.

Table 3.1 shows the masses for the three excitations of the singlet $^1P_1$ and the triplet ^3P_J mesons. In Table 3.11 we show the comparison between the centroid of ^3P_J states and the corresponding h_c mass for the ground state and the first two excitations, showing that our spin-spin interaction is negligible for these channels and it is in perfect agreement with the lattice expectations and the experimental measurements for the ground state.

Focusing our interest on h_c we have calculated other properties of that state. Table 3.12 shows the E1 and M1 radiative decays into those states which are allowed by phase space requirements. These numerical results can be useful for future experimental searches.

The decay chain $\psi(2S) \to \pi^0 h_c(1P)$, $h_c(1P) \to \gamma\eta_c(1S)$ was first observed by CLEO [117, 119] and later confirmed with higher statistics by BESIII [120]. BESIII has also measured $\mathcal{B}(\psi(2S) \to \pi^0 h_c(1P))$ allowing the extraction of $\mathcal{B}(h_c(1P) \to \gamma\eta_c(1S))$. This paper also gives the total width of $h_c(1P)$ and it allows us to calculate the theoretical estimation of the $h_c(1P) \to \gamma\eta_c(1S)$ branching fraction. It is in good agreement with the experimental data, as shown in Table. 3.12. Other M1 radiative decays appear very small.

Initial meson	Final meson	$\Gamma_{\text{The.}}$ (keV)	$\Gamma_{\text{Exp.}}$ (keV)
$h_c(1^1P_1)$	$\eta_c(1^1S_0)$	353.41	(394.20 ± 294.40) [120]
$h_c(2^1P_1)$	$\eta_c(1^1S_0)$	175.42	-
	$\eta_c(2^1S_0)$	197.35	-
	$\eta_{c2}(1^1D_2)$	53.64	-
	$\chi_{c0}(1^3P_0)$	1.20	-
	$\chi_{c1}(1^3P_1)$	0.39	-
	$\chi_{c2}(1^3P_2)$	0.010	-
$h_c(3^1P_1)$	$\eta_c(1^1S_0)$	115.62	
	$\eta_c(2^1S_0)$	139.19	-
	$\eta_c(3^1S_0)$	144.34	-
	$\eta_{c2}(1^1D_2)$	25.80	-
	$\eta_{c2}(2^1D_2)$	65.46	-
	$\chi_{c0}(1^3P_0)$	1.24	-
	$\chi_{c1}(1^3P_1)$	0.48	-
	$\chi_{c2}(1^3P_2)$	0.02	-
	$\chi_{c0}(2^3P_0)$	0.50	-
	$\chi_{c1}(2^3P_1)$	0.26	-
	$\chi_{c2}(2^3P_2)$	0.02	-

Table 3.12. E1 and M1 radiative transitions of h_c states.

3.1.4 The χ_{cJ} states

Although they cannot be produced directly in e^+e^- collisions, radiative decays of the $\psi(2S)$ into χ_{cJ} states occur with a branching ratio of about 27% [78] and provide large χ_{cJ} samples that have proven to be a very clean environment for studies of the χ_{cJ} states. According with Table 3.1 the long known 1^3P_J states are in agreement with the model predictions.

The mean $2P$ multiplet mass is predicted to be near 3.95 GeV. Although no $2P$ $c\bar{c}$ state has been clearly seen experimentally, there are reports from the different Collaborations which claim enhancements in that energy region. We have the $X(3872)$, $X(3915)$, $Y(3940)$, $X(3940)$ and $Z(3930)$.

The $X(3872)$ is one of the most studied and well established of those states. It was first discovered by the Belle Collaboration in the $J/\psi\pi\pi$ invariant mass spectrum of the decay $B^+ \to K^+\pi^+\pi^- J/\psi$ [32]. Its existence was soon confirmed by BaBar [121], CDF [33] and D0 [122]. The world average mass is $M_X = 3871.2 \pm 0.5$ MeV and its width $\Gamma_X < 2.3$ MeV. The measurements of the $X(3872) \to \gamma J/\psi$ decay [123, 124] implies an even C-parity. Moreover, the angular correlation between final state particles in the $X(3872) \to \pi^+\pi^- J/\psi$ decay measured by Belle [123] and CDF [125] indicates that the most likely quantum numbers should be $J^{PC} = 1^{++}$ but cannot totally exclude the $J^{PC} = 2^{-+}$ combination.

The $X(3872)$ mass is difficult to reproduce by the standard quark models, see

Initial meson	Final meson	$\Gamma_{\text{The.}}$ (keV)	$\Gamma_{\text{Exp.}}$ (keV)
$\chi_{c0}(1^3P_0)$	$\psi(1^3S_1)$	127.18	121.80 ± 12.50
$\chi_{c0}(2^3P_0)$	$\psi(1^3S_1)$	32.35	-
	$\psi(2^3S_1)$	150.56	-
	$\psi(1^3D_1)$	50.50	-
	$h_c(1^1P_1)$	0.35	-
$\chi_{c0}(3^3P_0)$	$\psi(1^3S_1)$	12.43	-
	$\psi(2^3S_1)$	52.96	-
	$\psi(1^3D_1)$	14.98	-
	$\psi(3^3S_1)$	221.34	-
	$\psi(2^3D_1)$	36.68	-
	$h_c(1^1P_1)$	0.39	-
	$h_c(2^1P_1)$	0.17	-

Table 3.13. E1 and M1 radiative transitions of χ_{c0} states. The experimental data are from [78].

Table 3.1. Moreover no four-quark bound state configurations have been found in this mass region [126, 127]. The $X(3872)$ mass is extremely close to the D^0D^{*0} threshold so it appears as a natural candidate to an even C-parity D^0D^{*0} molecule. This structure will also explain the large isospin violation. The molecular interpretation runs into trouble when it tries to explain the high $\gamma\psi'$ decay rate. This puzzling situation suggests for the $X(3872)$ state a combination of a $2P$ $c\bar{c}$ state and a weakly-bound D^0D^{*0} molecule. In Ref. [128] we have performed a coupled channel calculation of the 1^{++} $c\bar{c}$ sector including $q\bar{q}$ and $q\bar{q}q\bar{q}$ configurations. Two and four quark configurations are coupled using the $^3P_0$ model which will be introduced in the following Chapter. The elusive $X(3872)$ meson appears as a new state with a high probability for the DD^* molecular component. The original $c\bar{c}(2^3P_1)$ state acquires a sizable DD^* component and can be identified with the $X(3940)$.

The $Y(3940) \to \omega J/\psi$ enhancement was initially found by Belle [129] in $B^+ \to K^+Y(3940)$ decays. It was confirmed by BaBar [130] with more statistics, albeit with somewhat smaller mass. But Belle [85] also found a statistically compelling resonant structure $X(3915)$ in $\gamma\gamma$ fusion decaying to $\omega J/\psi$. It shares the same production and decay signature as that of BaBar's $Y(3940)$, which has mass and width consistent with the $X(3915)$. An interpretation of these two states as the same appears as a widely accepted idea and the name which is conserved is $X(3915)$. We only know at the moment that this state has an even C-parity. If $X(3915)$ was a $c\bar{c}$ state, the most probable quantum numbers would be 0^{++}. The mass predicted for the 2^3P_0 is 3909, in very good agreement with the experimental measurement. One can find in Table 3.13 its E1 and M1 radiative decays.

In 2005 Belle [88] observed an enhancement in the $D\bar{D}$ mass spectrum from $e^+e^- \to e^+e^-D\bar{D}$ events with a statistical significance of 5.3σ. It was initially dubbed the $Z(3930)$, but since then it has been widely (if not universally) accepted as the $\chi_{c2}(2P)$. There is some Lattice calculations [131] which suggest that the $\chi_{c2}(2P)$ and

Initial meson	Final meson	$\Gamma_{\text{The.}}$ (keV)	$\Gamma_{\text{Exp.}}$ (keV)
$\chi_{c1}(1^3P_1)$	$\psi(1^3S_1)$	264.40	302.72 ± 21.68
$\chi_{c1}(2^3P_1)$	$\psi(1^3S_1)$	94.06	-
	$\psi(2^3S_1)$	194.94	-
	$\psi(1^3D_1)$	22.60	-
	$\psi_2(1^3D_2)$	36.55	-
	$h_c(1^1P_1)$	0.04	-
$\chi_{c1}(3^3P_1)$	$\psi(1^3S_1)$	53.63	-
	$\psi(2^3S_1)$	102.26	-
	$\psi(1^3D_1)$	9.48	-
	$\psi_2(1^3D_2)$	16.83	-
	$\psi(3^3S_1)$	241.72	-
	$\psi(2^3D_1)$	19.26	-
	$\psi_2(2^3D_2)$	44.86	-
	$h_c(1^1P_1)$	0.06	-
	$h_c(2^1P_1)$	0.04	-
$\chi_{c2}(1^3P_2)$	$\psi(1^3S_1)$	323.26	380.25 ± 29.77
$\chi_{c2}(2^3P_2)$	$\psi(1^3S_1)$	130.52	-
	$\psi(2^3S_1)$	212.28	-
	$\psi(1^3D_1)$	0.83	-
	$\psi_2(1^3D_2)$	9.39	-
	$h_c(1^1P_1)$	0.52	-
$\chi_{c2}(1^3F_2)$	$\psi(1^3D_1)$	345.08	-
	$\psi_2(1^3D_2)$	45.76	-

Table 3.14. E1 and M1 radiative transitions of χ_{c1} and χ_{c2} states. The experimental data are from [78].

the 1^3F_2 state could be quite close in mass, so that perhaps the $Z(3930)$ is not the 2^3P_2 but rather the 1^3F_2. Our constituent quark model predicts a mass for the 2^3P_2 and 1^3F_2 of 3969 MeV and 4043 MeV, respectively. Therefore the mass splitting is 74 MeV, so we do not predict states nearby degenerated and assign the $Z(3930)$ as the 2^3P_2 state.

The next states in mass for the χ_{cJ} mesons are 3^3P_0, 3^3P_1 and 1^3F_2. The $3P$ states have an expected mean multiplet mass of about 4.3 GeV according with our model.

All E1 and M1 radiative decays of the states commented above as a $c\bar{c}$ meson can be found in Tables 3.13 and 3.14.

3.1.5 D-wave states with $J = 2$

Since the 1^3D_2 and 1^1D_2 states do not have allowed open-flavor decay modes, these states are difficult to observe. One possibility is that the 1^3D_2 may be found in $E1$

Initial meson	Final meson	$\Gamma_{\rm CQM}$ (keV)
$\eta_{c2}(1^1D_2)$	$h_c(1^1P_1)$	276.95
$\eta_{c2}(2^1D_2)$	$h_c(1^1P_1)$	114.66
	$h_c(2^1P_1)$	211.78
$\eta_{c2}(3^1D_2)$	$h_c(1^1P_1)$	69.34
	$h_c(2^1P_1)$	124.56
	$h_c(3^1P_1)$	155.78

Table 3.15. E1 radiative transitions of η_{c2} states.

Initial meson	Final meson	$\Gamma_{\rm CQM}$ (keV)
$\psi_2(1^3D_2)$	$\chi_{c1}(1^3P_1)$	224.10
	$\chi_{c2}(1^3P_2)$	53.74
$\psi_2(2^3D_2)$	$\chi_{c1}(1^3P_1)$	95.44
	$\chi_{c2}(1^3P_2)$	19.92
	$\chi_{c1}(2^3P_1)$	164.35
	$\chi_{c2}(2^3P_2)$	47.92
	$\chi_{c2}(1^3F_2)$	3.88
$\psi_2(3^3D_2)$	$\chi_{c1}(1^3P_1)$	58.17
	$\chi_{c2}(1^3P_2)$	11.42
	$\chi_{c1}(2^3P_1)$	99.61
	$\chi_{c2}(2^3P_2)$	25.00
	$\chi_{c1}(3^3P_1)$	120.52
	$\chi_{c2}(1^3F_2)$	1.96

Table 3.16. E1 radiative transitions of ψ_2 states.

transitions from the 2^3P_2 state since this has been recently well established in the PDG and its production comes from $\gamma\gamma$ fusion. However, it appears difficult to get a signal of 1^1D_2 because this state need parent states which have not been seen at the moment. Tables 3.15 and 3.16 show the E1 radiative decays which can be useful to the experimentalists for future searches.

3.2 Charmed and charmed-strange mesons

The spectra of charmed and charmed-strange mesons contain a number of long known and well established states [78], all of them are low-lying states. The high excited states have been difficult to find due to the poor statistics and their relatively large widths.

We find as well established states in the charmed sector, the S-wave states of quantum numbers $J^P = 0^-$ and 1^- which are the D and D^* mesons, respectively. Also the P-wave states with quantum numbers 0^+ ($D_0^*(2400)$), 1^+ ($D_1(2420)$ and $D_1(2430)$) and 2^+ ($D_2^*(2460)$) are given in Ref. [78]. In addition, the PDG lists the $D^*(2640)$

meson seen in Z-decays [132] which lacks confirmation.

In the case of the charmed-strange sector the scheme is very similar, the S-wave states of quantum numbers $J^P = 0^-$ and 1^- are the D_s and D_s^*, and the P-wave states are $D_{s0}^*(2317)$, $D_{s1}(2460)$, $D_{s1}(2536)$ and $D_{s2}^*(2573)$ with quantum numbers 0^+, 1^+, 1^+ and 2^+, respectively.

However, in the last years several new resonances have been observed and their quantum numbers are a matter of active discussion.

The BaBar Collaboration have performed a study of the $D^+\pi^-$, $D^0\pi^+$ and $D^{*+}\pi^-$ systems in inclusive $e^+e^- \to c\bar{c}$ reactions to find new excited D mesons [133]. The $D(2550)$, $D^*(2600)$, $D_J(2750)$ and $D_J^*(2760)$ mesons have been observed.

The $D(2550)$ is considered the singlet 2^1S_0 state due to its helicity-angle distribution [133]. By the same reasoning, the resonance $D^*(2600)$ is consistent with the excited 2^3S_1 state. The $D_J^*(2760)$ signal observed in $D^+\pi^-$ is very close in mass to the signal $D_J(2750)$ observed in $D^{*+}\pi^-$. The quantum numbers of the resonances $D_J(2750)$ and $D_J^*(2760)$ are not clear but the 2^- and 3^- possibilities are given as the most probables.

In addition there are a number of D_s states which have been observed more recently. These are the $D_{s1}^*(2710)$, observed by both BaBar [134, 135] and Belle [136], the $D_{sJ}^*(2860)$ [134, 135], the $D_{sJ}(3040)$ [135] and an unconfirmed state previously observed by SELEX [137], the $D_{sJ}(2632)$. While the $D_{s1}^*(2710)$ is commonly believed to have quantum numbers $J^P = 1^-$, there are several possibilities for the other states which are not ruled out by experiment. The $D_{sJ}^*(2860)$ is most often identified with a 3^- state, while some still argue the possibility of a 0^+ identification. The $D_{sJ}(3040)$ is commonly interpreted as either 1^+ or 2^- state.

Table 3.17 shows the current status of charmed and charmed-strange mesons with some of their properties. The model prediction in both sectors is shown in Table 3.18 up to $J = 3$ and for the first four excitations.

A simple analysis about the properties of hadrons containing a single heavy quark $Q = c$, b can be carried out in the $m_Q \to \infty$ limit. In such a limit, the heavy quark acts as a static color source for the rest of the hadron, its spin s_Q is decoupled from the total angular momentum of the light degrees of freedom j_q, and they are separately conserved. Hadrons can be classified according to the values of j_q and of the total spin $\vec{J} = \vec{j}_q + \vec{s}_Q$. In particular, heavy mesons can be organized in doublets, each one corresponding to a particular value of j_q and parity. The members of each doublet differ for the orientation of s_Q with respect to j_q and, in the heavy quark limit, are degenerated. Mass degeneracy is broken at order $1/m_Q$.

For $Q\bar{q}$ states, one can write $\vec{j}_q = \vec{s}_q + \vec{l}$, where s_q is the light antiquark spin and l is the orbital angular momentum of the light degrees of freedom relative to the heavy quark. The lowest lying $Q\bar{q}$ mesons correspond to $l = 0$ (S-wave states of the quark model) with $j_q^P = \frac{1}{2}^-$. This doublet comprises two states with spin-parity $J^P = (0^-, 1^-)$. For $l = 1$ (P-wave states of the quark model), it could be either $j_q^P = \frac{1}{2}^+$ or $j_q^P = \frac{3}{2}^+$, the two corresponding doublets having $J^P = (0^+, 1^+)$ and $J^P = (1^+, 2^+)$. The mesons with $l = 2$ (D-wave states) are collected either in the $j_q^P = \frac{3}{2}^-$ doublet, consisting of states with $J^P = (1^-, 2^-)$, or in the $j_q^P = \frac{5}{2}^-$ with $J^P = (2^-, 3^-)$, and so on.

Meson	J^P	Mass (MeV)	Width (MeV)	Seen in
D^0	0^-	1864.91 ± 0.17	1.60×10^{-9}	K^-X and $\bar{K}^0X + K^0X$
$D^\pm$	0^-	1869.5 ± 0.4	6.33×10^{-10}	K^-X and $\bar{K}^0X + K^0X$
D^{*0}	1^-	2006.97 ± 0.16	< 2.1	$D^0\pi^0$ and $D^0\gamma$
$D^{*\pm}$	1^-	2010.25 ± 0.14	$96 \pm 4 \pm 22$ keV	$D^0\pi^+$, $D^+\pi^0$ and $D^+\gamma$
D_0^{*0}	0^+	2318 ± 29	267 ± 40	$D^+\pi^-$
$D_0^{*\pm}$	0^+	$2403 \pm 14 \pm 35$	$283 \pm 24 \pm 34$	$D^0\pi^+$
$D_1(2420)^0$	1^+	2422.3 ± 1.3	20.4 ± 1.7	$D^{*+}\pi^-$, $D^0\pi^+\pi^-$, $D_0^{*+}\pi^-$
$D_1(2420)^\pm$	1^+	2423.4 ± 3.1	25 ± 6	$D^{*0}\pi^+$, $D^+\pi^+\pi^-$, $D_0^{*0}\pi^+$
$D_1(2430)^0$	1^+	$2427 \pm 26 \pm 25$	$384^{+107}_{-75} \pm 74$	$D^{*+}\pi^-$
$D_2^*(2460)^\pm$	2^+	$2460.1^{+2.6}_{-3.5}$	37 ± 6	$D^0\pi^+$ and $D^{*0}\pi^+$
$D_2^*(2460)^0$	2^+	2460.9 ± 1.3	49.0 ± 1.4	$D^+\pi^-$ and $D^{*+}\pi^-$
$D(2550)^0$	0^-	$2539.4 \pm 4.5 \pm 6.8$	$130 \pm 12 \pm 13$	$D^*\pi$
$D^*(2600)^0$	1^-	$2608.7 \pm 2.4 \pm 2.5$	$93 \pm 6 \pm 13$	$D\pi/D^*\pi$
$D_J(2750)^0$	2^-, 3^-	$2752.4 \pm 1.7 \pm 2.7$	$71 \pm 6 \pm 11$	$D^*\pi$
$D_J^*(2760)^0$	2^-, 3^-	$2763.3 \pm 2.3 \pm 2.3$	$60.9 \pm 5.1 \pm 3.6$	$D\pi$

Meson	J^P	Mass (MeV)	Width (MeV)	Seen in
$D_s^\pm$	0^-	1969.0 ± 1.4	-	$K^*\bar{K}^*$
$D_s^{*\pm}$	1^-	2112.3 ± 0.5	< 1.9	$D_s^+\gamma$
$D_{s0}^*(2317)^\pm$	0^+	2318.0 ± 1.0	< 3.8	$D_s^+\pi^0$
$D_{s1}(2460)^\pm$	1^+	2459.6 ± 0.9	< 3.5	$D_s^{*+}\pi^0$
$D_{s1}(2536)^\pm$	1^+	2535.12 ± 0.25	< 2.3	D^*K
$D_{s2}^*(2573)^\pm$	2^+	2572.6 ± 0.9	20 ± 5	D^0K^+
$D_{s1}^*(2710)^\pm$	1^-	$2710 \pm 2^{+12}_{-7}$	$149 \pm 7^{+39}_{-52}$	$B^+ \to \bar{D}^0 D_{s1} \to \bar{D}^0 D^0 K^+$
$D_{sJ}^*(2860)^\pm$	3^-, 0^+	$2862 \pm 2^{+5}_{-2}$	$48 \pm 3 \pm 6$	DK
$D_{sJ}(3040)^\pm$	1^+, 2^-	$3044 \pm 8^{+30}_{-5}$	$239 \pm 35^{+46}_{-42}$	D^*K

Table 3.17. Charmed and charmed-strange mesons well established in PDG [78] and the latest experimental data which have been taken from Refs. [133] (charmed mesons) and [135] (charmed-strange mesons).

The two states D and D^* (D_s and D_s^*) can be identified with the members of the lowest lying $j_q^P = \frac{1}{2}^-$ doublet. Our mass prediction is in good agreement with the experimental measurements in both charmed and charmed-strange sectors.

In the infinite heavy quark mass limit the strong decays of the $D_J\,(j_q = 3/2)$ proceed only through D-waves, while the $D_J\,(j_q = 1/2)$ decays happen only through S-waves [138]. The D-wave decay is suppressed by the barrier factor which behaves as q^{2L+1} where q is the relative momentum of the two decaying mesons. Therefore, the states decaying through D-waves are expected to be narrower than those decaying via S-waves. Our assignment in Table 3.18 for the 2^+ state and one of the low lying 1^+ states corresponding to the doublet $j_q^P = \frac{3}{2}^+$ follows the reasoning above and so the 1^+ states which belong to that doublet are the assignments $D_1(2420)$ and $D_{s1}(2536)$.

		Charmed mesons		Charmed-strange mesons	
J^P	n	Mass (MeV)	Assignment	Mass (MeV)	Assignment
0^-	1	1896	D	1984	D_s
	2	2695	$D(2550)$	2729	
	3	3154		3178	
	4	3448		3487	
0^+	1	2516	$D_0^*(2400)$	2510	$D_{s0}^*(2317)$
	2	3033		3025	
	3	3366		3376	
	4	3582		3625	
1^+	1	2466	$D_1(2420)$	2554	$D_{s1}(2536)$
	2	2596	$D_1(2430)$	2593	$D_{s1}(2460)$
	3	3008		3056	$D_{sJ}(3040)$
	4	3079		3077	$D_{sJ}(3040)$
1^-	1	2017	D^*	2110	D_s^*
	2	2756	$D^*(2600)$	2797	$D_{s1}^*(2710)$
	3	2935		2915	$D_{sJ}^*(2860)$
	4	3193		3224	
2^-	1	2812	$D_J(2750)$	2886	
	2	2973		2948	
	3	3227		3278	
	4	3323		3317	
2^+	1	2513	$D_2^*(2460)$	2591	$D_{s2}^*(2573)$
	2	3037		3081	
	3	3220		3196	
	4	3372		3417	
3^+	1	3090		3151	
	2	3244		3216	
	3	3409		3464	
	4	3503		3507	
3^-	1	2847	$D_J^*(2760)$	2911	$D_{sJ}^*(2860)$
	2	3249		3296	
	3	3443		3428	
	4	3511		3569	

Table 3.18. Masses, in MeV, of charmed and charmed-strange mesons. We show our assignment for the new mesons.

We cannot explain the mass of the doublet $j_q^P = \frac{1}{2}^+$ corresponding to the ground state of the 0^+ meson and the remainder of the 1^+ mesons. Lattice calculations of charmed and charmed-strange mesons present the same features as those of the phenomenological models (for a review of that results one can read Ref. [139]). We

will study the inclusion of one-loop corrections to the Fermi-Breit spin dependent OGE potential. These terms improve the agreement for the 0^+ state, we postpone this discussion for a later Section. It is also important for the states which belong to the doublet $j_q^P = \frac{1}{2}^+$, and in particular for the charmed-strange sector, the coupling between $q\bar{q}$ and non-$q\bar{q}$ structures in the 1^+ channel, this discussion is left over for a later Section.

Concerning the new discovered mesons, the assignment is not justified if one attends only to the masses, see Table 3.18. This has been done following their strong decays which will be studied later.

3.3 Bottomonium

The bound states of the $b\bar{b}$ system are the heaviest and most compact bound states of a quark and an antiquark in nature. They were discovered as spin triplet states called $\Upsilon(1S)$, $\Upsilon(2S)$ and $\Upsilon(3S)$ by the E288 Collaboration at Fermilab in 1977 in proton scattering on Cu and Pb targets studying muon pairs in a regime of invariant masses larger than 5 GeV [5, 141]. Later, they were better resolved and studied at various e^+e^- storage rings. Six triplet-P states, $\chi_b(2P_J)$ and $\chi_b(1P_J)$ with $J = 0$, 1, 2, were discovered in radiative decays of the $\Upsilon(3S)$ and $\Upsilon(2S)$ in 1982 [142, 143] and 1983 [144, 145], respectively.

Despite such early measurements during the next thirty years there were no new contributions to the spectrum of bottomonium. This was largely because the B-factories were not usually considered ideal facilities for the study of the bottomonium spectrum since their energy was tuned to the peak of the $\Upsilon(4S)$ resonance, which decays in almost 100% of cases to a $B\bar{B}$ pair. However, during the last years both BaBar and Belle Collaborations have reported data samples at various energies in the bottomonium region that made possible discoveries like the η_b [146], and the $h_b(1P)$ and $h_b(2P)$ [140].

The world average masses reported in Ref. [78] and our model predictions are collected in Table 3.19. In general the experimental data and our theoretical results are in good agreement.

3.3.1 The Υ states

The predicted masses of the narrow $\Upsilon(1S)$, $\Upsilon(2S)$ and $\Upsilon(3S)$ resonances are in reasonable agreement with the values from PDG. They are below the open-bottom threshold (10.56 GeV) and thus the electromagnetic transitions involve an important contribution to the total decay width. Table 3.20 shows the E1 and M1 electromagnetic transitions of $\Upsilon(1S)$, $\Upsilon(2S)$ and $\Upsilon(3S)$ states, the predictions agree with the experimental data. As expected the M1 radiative decays for $b\bar{b}$ mesons are very small.

The current generation of B-factories have scanned the energy range above open-bottom threshold. BaBar [148] performed a comprehensive scan between 10.54 and 11.2 GeV, followed by an eight-point scan in the proximity of the $\Upsilon(6S)$ peak. Belle [149] acquired nine points over $10.80 - 11.02$ GeV, as well as spread over seven additional points more focused on the $\Upsilon(5S)$ peak. Both scans suggest that the simple Breit-Wigner parametrization, previously used to model the peaks observed in the CLEO [150] and CUSB [151] scans, is not good enough for the description

State	J^{PC}	n	The. (MeV)	Exp. (MeV)	[78]
η_b	0^{-+}	1	9455	9390.9 ± 2.8	
		2	9990	-	
		3	10330	-	
χ_{b0}	0^{++}	1	9855	$9859.44 \pm 0.42 \pm 0.31$	
		2	10221	$10232.5 \pm 0.4 \pm 0.5$	
		3	10500	-	
h_b	1^{+-}	1	9879	$9898.25 \pm 1.06^{+1.03}_{-1.07}$	[140]
		2	10240	$10259.76 \pm 0.64^{+1.43}_{-1.03}$	[140]
		3	10516	-	
Υ	1^{--}	1	9502	9460.30 ± 0.26	
		2	10015	10023.26 ± 0.31	
		3	10117	-	
		4	10349	10355.2 ± 0.5	
		5	10414	-	
		6	10607	10579.4 ± 1.2	
		7	10653	-	
		8	10818	10865 ± 8	
		9	10853	-	
		10	10995	11019 ± 8	
		11	11023	-	
χ_{b1}	1^{++}	1	9874	$9892.78 \pm 0.26 \pm 0.31$	
		2	10236	$10255.46 \pm 0.22 \pm 0.50$	
		3	10513	-	
η_{b2}	2^{-+}	1	10123	-	
		2	10419	-	
		3	10658	-	
χ_{b2}	2^{++}	1	9886	$9912.21 \pm 0.26 \pm 0.31$	
		2	10246	$10268.65 \pm 0.22 \pm 0.50$	
		3	10315	-	
		4	10521	-	
		5	10569	-	
Υ_2	2^{--}	1	10122	10163.7 ± 1.4	
		2	10418	-	
		3	10657	-	

Table 3.19. Masses, in MeV, of bottomonium states. We compare with the well established states in Ref. [78].

of the complex dynamics in the proximity of the $B^{(*)}\bar{B}^{(*)}$ and $B_s^{(*)}\bar{B}_s{}^{(*)}$ thresholds. The new data points on $R_b = \sigma(b\bar{b})/\sigma(\mu\mu)$ are better modeled assuming a flat $b\bar{b}$ continuum contribution which interferes constructively with the $5S$ and $6S$ Breit-

Initial meson	Final meson	$\Gamma_{\rm The.}$ (keV)	$\mathcal{B}_{\rm The.}$	$\mathcal{B}_{\rm Exp.}$
$\Upsilon(1S)$	$\eta_b(1S)$	0.014	2.59×10^{-4}	-
$\Upsilon(2S)$	$\chi_{b0}(1P)$	1.09	3.41×10^{-2}	$(3.8 \pm 0.4) \times 10^{-2}$
	$\chi_{b1}(1P)$	1.84	5.75×10^{-2}	$(6.9 \pm 0.4) \times 10^{-2}$
	$\chi_{b2}(1P)$	2.08	6.50×10^{-2}	$(7.15 \pm 0.35) \times 10^{-2}$
	$\eta_b(1S)$	0.059	1.85×10^{-3}	$(1.1 \pm 0.4^{+0.7}_{-0.5}) \times 10^{-3}$ [147]
	$\eta_b(2S)$	0.0015	4.69×10^{-5}	-
$\Upsilon(3S)$	$\chi_{b0}(1P)$	0.15	7.38×10^{-3}	$(3.0 \pm 1.1) \times 10^{-3}$
	$\chi_{b1}(1P)$	0.16	7.87×10^{-3}	$< 1.7 \times 10^{-3}$
	$\chi_{b2}(1P)$	0.08	3.94×10^{-3}	$< 19.0 \times 10^{-3}$
	$\chi_{b0}(2P)$	1.21	5.95×10^{-2}	$(5.9 \pm 0.6) \times 10^{-2}$
	$\chi_{b1}(2P)$	2.13	10.48×10^{-2}	$(12.6 \pm 1.2) \times 10^{-2}$
	$\chi_{b2}(2P)$	2.56	12.60×10^{-2}	$(13.1 \pm 1.6) \times 10^{-2}$
	$\eta_b(1S)$	0.059	29.04×10^{-4}	$(5.1 \pm 0.7) \times 10^{-4}$
	$\eta_b(2S)$	0.012	5.91×10^{-4}	$< 6.2 \times 10^{-4}$
	$\eta_b(3S)$	0.00066	3.25×10^{-5}	-

Table 3.20. E1 and M1 radiative transitions of $\Upsilon(1S)$, $\Upsilon(2S)$ and $\Upsilon(3S)$ states. The experimental data are from Ref. [78].

Υ	The.	BaBar [148]	Belle [149]	PDG2010 [78]
$5S$	10818	10876 ± 2	10879 ± 3	10865 ± 8
$6S$	10995	10996 ± 2	-	11019

Table 3.21. New masses, in MeV, reported by BaBar and Belle for $\Upsilon(5S)$ and $\Upsilon(6S)$ and the comparison with the model prediction.

Wigner resonances, and a second flat contribution which adds incoherently. Such fits alter the PDG results on the $5S$ and $6S$ peaks. Table 3.21 compares the theoretical prediction with the new parameters reported by BaBar and Belle and the PDG values for the $5S$ and $6S$ resonances.

The Υ family can be studied easily via e^+e^- annihilation as they have the same quantum numbers of the emitted virtual photon. However, their production rate in this reaction is related with their leptonic widths. They are smaller than the ψ states and for D-wave states are negligible. This is the reason why there is no experimental confirmation of the $^3D_1$ states. Potential model predicts that these states are close to their S-wave partner. In our model this feature is highlighted due to the linear screened confining interaction. Table 3.22 shows our prediction for the leptonic widths of $J^{PC} = 1^{--}$ $b\bar{b}$ states.

Additional insight can be provided by the exclusive decomposition of the two-body (e.g. $B\bar{B}$, $B\bar{B}^*$, $B^*\bar{B}^*$) and other decay modes. Results from e^+e^- collisions have been given by Belle [152] and they will be studied later.

(nL)	States	$M_{\text{The.}}$ (MeV)	$\Gamma_{\text{The.}}$ (keV)	$\Gamma_{\text{Exp.}}$ (keV)
$(1S)$	$\Upsilon(1S)$	9502	0.71	1.340 ± 0.018
$(2S)$	$\Upsilon(2S)$	10015	0.37	0.612 ± 0.011
$(1D)$		10117	0.14×10^{-2}	-
$(3S)$	$\Upsilon(3S)$	10349	0.27	0.443 ± 0.008
$(2D)$		10414	0.25×10^{-2}	-
$(4S)$	$\Upsilon(10580)$	10607	0.21	0.272 ± 0.029
$(3D)$		10653	0.31×10^{-2}	-
$(5S)$	$\Upsilon(10860)$	10818	0.18	0.31 ± 0.07
$(4D)$		10853	0.36×10^{-2}	0.31 ± 0.07
$(6S)$	$\Upsilon(11020)$	10995	0.15	0.130 ± 0.030
$(5D)$		11023	0.38×10^{-2}	-

Table 3.22. Leptonic decay widths, in keV, of Υ states. The experimental data are from [78].

Initial meson	Final meson	$\Gamma_{\text{The.}}$ (keV)
$\eta_b(2S)$	$h_b(1P)$	2.20
$\eta_b(3S)$	$h_b(1P)$	0.008
	$h_b(2P)$	2.61

Table 3.23. E1 radiative transitions of η_b states.

3.3.2 The η_b states

The BaBar Collaboration have succeeded in observing the $\eta_b(1S)$ in 2008 [146]. The η_b remained elusive because branching fractions for transitions from the $\Upsilon(nS)$ states are small and no low-multiplicity decay modes, analogous to $\eta_c(1S) \to K\bar{K}\pi$, appear to exist for η_b. This makes the decay $\Upsilon(nS) \to \gamma\eta_b$ the most suitable for searching but this is also non-trivial.

The hyperfine mass-splitting of singlet-triplet states, $\Delta m_{hf}[\eta_b(1S)] = m(1^3S_1) - m(1^1S_0)$, probes the spin-dependence of bound-state energy levels and imposes constraints on theoretical descriptions. It is given experimentally by

$$\Delta m_{hf}[\eta_b(1S)] = 69.6 \pm 2.9\,\text{MeV}, \tag{3.10}$$

although the masses of the 1^1S_0 and 1^3S_1 states are not so well reproduced by the model, the splitting between them is good.

The η_b states and their E1 radiative decays are shown in Tables 3.19 and 3.23, respectively.

3.3.3 The h_b and χ_{bJ} states

Belle [140] has very recently reported a large cross section for $e^+e^- \to \pi^+\pi^- h_b(1P)$ or $\pi^+\pi^- h_b(2P)$ at the center-of-mass energy of $\Upsilon(5S)$. This is reminiscent of CLEO's observation of a large cross section for $e^+e^- \to \pi^+\pi^- h_c$ at $\sqrt{s} = 4170\,\text{MeV}$ [153]. The masses of the $h_b(1P)$ and $h_b(2P)$ [140], as well as the $h_c(1P)$ discovered earlier,

n	$m(h_b)$ (MeV)	$\langle m(n^3P_J)\rangle_{\text{The.}}$ (MeV)	$\langle m(n^3P_J)\rangle_{\text{Exp.}}$ (MeV)
1	9879	9879	9899.87 ± 0.27
2	10240	10240	10260.24 ± 0.36
3	10516	10516	-

Table 3.24. The theoretical masses, in MeV, of the ground state and the first two excitations of h_b, compared with the spin-averaged centroid, in MeV, of the corresponding triplet P-wave states. We compare with the experimental data [78].

are very close to the spin-weighted average of the corresponding ^3P_J states, indicating small hyperfine splitting in P-wave mesons as expected in the naive quark model.

The centroid of the n^3P_J states with $n = 1, 2$ is known to be, respectively, 9899.87 ± 0.27 MeV and 10260.24 ± 0.36 MeV [78]. The hyperfine splittings measured by the Belle Collaboration [140] are $\Delta m_{hf}[h_b(1P)] = +1.6 \pm 1.5$ MeV and $\Delta m_{hf}[h_b(2P)] = +0.5^{+1.6}_{-1.2}$ MeV which are compatible with zero.

Table 3.19 shows the masses for three excitations of the singlet $^1P_1$ and the triplet ^3P_J mesons. They are in reasonable agreement with the experimental data. In Table 3.24 we show the comparison between the centroid of ^3P_J states and the corresponding h_b mass for the ground state and the first two excitations, showing that our spin-spin interaction is negligible. For completeness, we show the E1 radiative transitions in Table 3.25.

The $\chi_b(nP)$ states have been recently produced in proton-proton collisions at the LHC at $\sqrt{s} = 7$ TeV and recorded by the ATLAS detector [154]. These states have been reconstructed through their radiative decays to $\Upsilon(1S, 2S)$ with $\Upsilon \to \mu^+\mu^-$. In addition to the mass peaks corresponding to the decay modes $\chi_b(1P, 2P) \to \Upsilon(1S)\gamma$, a new structure centered at a mass of $(10.530 \pm 0.005 \pm 0.009)$ GeV has been also observed, in both the $\Upsilon(1S)\gamma$ and $\Upsilon(2S)\gamma$ decay modes. This structure has been interpreted as the $\chi_b(3P)$ system. One can see in Table 3.19 that our mass prediction for the triplet $\chi_{bJ}(3P)$ states is in very good agreement with the experimental one. We give in Table 3.25 their E1 decays into the different Υ states.

3.3.4 D-wave states with $J = 2$

Based on 122×10^6 $\Upsilon(3S)$ events, the BaBar Collaboration have attempted to measure the $\Upsilon(1^3D_J)$ bottomonium multiplet through the $\Upsilon(3S) \to \gamma\gamma\Upsilon(1^3D_J) \to \gamma\gamma\pi^+\pi^-\Upsilon(1S)$ decay chain [155]. The process $\Upsilon(1^3D_J) \to \pi^+\pi^-\Upsilon(1S)$ is of interest because looking at the distribution of the differential decay width with respect the invariant mass of the $\pi^+\pi^-$, one can distinguish the orbital angular momentum of the initial meson. The BaBar Collaboration has only provided the mass of the $J = 2$ member of the $\Upsilon(1^3D_J)$ triplet due to their significances (5.8σ for this state) with a value of $10164.5 \pm 0.8 \pm 0.5$ MeV. We predict a mass of 10122 MeV, lower than the experimental data but in reasonable agreement considering the uncertainties in the naive quark model. The members of the triplet are expected to be within 10 MeV or less according to our model and others as Ref. [156]. The model predicts the next excitations of the triplet in 10.42 GeV and 10.65 GeV energy regions.

It is expected that in the same energy range of the 1^3D_2 appears the 1^1D_2 state,

Initial meson	Final Meson	$\Gamma_{\text{The.}}$ (keV)	$\mathcal{B}_{\text{The.}}$	$\mathcal{B}_{\text{Exp.}}$
$h_b(1P)$	$\eta_b(1S)$	45.33	-	-
$h_b(2P)$	$\eta_b(1S)$	15.36	-	-
	$\eta_b(2S)$	19.40	-	-
$h_b(3P)$	$\eta_b(1S)$	8.16	-	-
	$\eta_b(2S)$	7.29	-	-
	$\eta_b(3S)$	12.27	-	-
$\chi_{b0}(1P)$	$\Upsilon(1S)$	28.07	-	$< 6 \times 10^{-2}$
$\chi_{b1}(1P)$	$\Upsilon(1S)$	35.66	-	$(35 \pm 8) \times 10^{-2}$
$\chi_{b2}(1P)$	$\Upsilon(1S)$	39.15	-	$(22 \pm 4) \times 10^{-2}$
$\chi_{b0}(2P)$	$\Upsilon(1S)$	5.44	-	$(9 \pm 6) \times 10^{-3}$
	$\Upsilon(2S)$	12.80	-	$(4.6 \pm 2.1) \times 10^{-2}$
$\chi_{b1}(2P)$	$\Upsilon(1S)$	9.13	-	$(8.5 \pm 1.3) \times 10^{-2}$
	$\Upsilon(2S)$	15.89	-	$(21 \pm 4) \times 10^{-2}$
$\chi_{b2}(2P)$	$\Upsilon(1S)$	11.38	-	$(7.1 \pm 1.0) \times 10^{-2}$
	$\Upsilon(2S)$	17.50	-	$(16.2 \pm 2.4) \times 10^{-2}$
$\chi_{b0}(3P)$	$\Upsilon(1S)$	1.99	-	-
	$\Upsilon(2S)$	2.99	-	-
	$\Upsilon(3S)$	8.50	-	-
$\chi_{b1}(3P)$	$\Upsilon(1S)$	4.17	-	-
	$\Upsilon(2S)$	4.58	-	-
	$\Upsilon(3S)$	9.62	-	-
$\chi_{b2}(3P)$	$\Upsilon(1S)$	5.65	-	-
	$\Upsilon(2S)$	5.62	-	-
	$\Upsilon(3S)$	10.38	-	-

Table 3.25. E1 radiative transitions of h_b and χ_{bJ} states. The experimental data are from [78].

η_{b2}. Unfortunately there are no data about the 1^1D_2 state. One possibility to find this state is studying the decays of the very recently discovered $h_b(2P)$ because the E1 transition $h_b(2P) \to \gamma\eta_{b2}(1D)$ is allowed. Our prediction is 5.26 keV.

3.4 Bottom, bottom-strange and bottom-charmed mesons

The B-factories have reached a kinematically clean environment of B meson decays providing an excellent opportunity to search for new states. Most of the hadronic B decays involve a $b \to c$ transition at the quark level, and so they have been used to search for new, conventional or unexpected, charmonium and charmed mesons and to study their properties in detail.

The experimental data concerning the properties of the new hidden or open-charm mesons are usually accompanied of information about the weak decay of meson B. Within the constituent quark model, we will have to deal with observables which involve weak decays of B mesons and thus these mesons should be well described by the model.

Until a couple of years ago, excited meson states containing b quarks have not been

Particle	J^P	The. (MeV)	Exp. (MeV) [78]
$B^{\pm}$	0^-	5275	5279.1 ± 0.4
B^0			5279.5 ± 0.5
B^*	1^-	5317	5325.1 ± 0.5
$B_1(5721)^0$	1^+	5776	5723.4 ± 2.0
$B_2^*(5747)^0$	2^+	5794	5743 ± 5
$B_J^*(5732)$	$\begin{bmatrix}0^+\\1^+\end{bmatrix}$	$\begin{bmatrix}5885\\5914\end{bmatrix}$	5698 ± 8
B_s^0	0^-	5348	5366.0 ± 0.9
B_s^*	1^-	5393	5415.8 ± 1.5
$B_{s1}(5830)^0$	1^+	5841	5829.4 ± 0.7
$B_{s2}^*(5840)^0$	2^+	5856	5839.7 ± 0.6
$B_{sJ}^*(5850)$	$\begin{bmatrix}0^+\\1^+\end{bmatrix}$	$\begin{bmatrix}5851\\5883\end{bmatrix}$	5853 ± 15
$B_c^{\pm}$	0^-	6275	6277 ± 6

Table 3.26. Masses of B, B_s and B_c states. We compare with the well established states in Ref. [78].

studied well. Only the stable 0^- ground states B^+, B^0 and B_s^0 and the excited 1^- state B^* had been firmly established. On Table 3.26 we give the mass predictions for these states which are in very good agreement with those from the PDG.

The B-factories can produce the B_s^* by running on the $\Upsilon(5S)$ resonance, i.e. $\Upsilon(5S) \to B_s^* \bar{B}_s^*$. The CLEO [157, 158] and Belle [159] Collaborations have isolated B_s^* states. The average of the two measurements about the B_s^* mass and the mass splitting between B_s^* and B_s mesons (including an older CUSB2 measurement [160]) are $M(B_s^*) = 5412.8 \pm 0.9\,\text{MeV}$ and $\Delta M(B_s^* - B_s) = 46.7 \pm 1.0\,\text{MeV}$, respectively. These are in good agreement with our values 5393 MeV and 45 MeV.

Focusing on the orbitally excited mesons, the doublet $j_q^P = \frac{3}{2}^+$ is well established in the PDG. The mesons which belong to this doublet are $B_1(5721)$ and $B_2^*(5747)$ within the B sector, and $B_{s1}(5830)$ and $B_{s2}^*(5840)$ within the B_s sector. The predicted masses are in good agreement with the experimental ones. There are no experimental evidences of the mesons which belong to the doublet $j_q^P = \frac{1}{2}^+$. These states should have quantum numbers 0^+ and 1^+. Also, following HQS, these mesons are expected to be broad and this may be the reason why they have not been seen so far. The PDG provides one state whose quantum numbers are not well established in the bottom and bottom-strange sectors, we are referring to the $B_J^*(5732)$ and $B_{sJ}^*(5850)$ mesons. The mass is nearby degenerated with the doublet $j_q^P = \frac{3}{2}^+$ and we have assigned this meson to our theoretical doublet $j_q^P = \frac{1}{2}^+$, as one can see in Table 3.26.

The B_c is the heaviest of the ground state b-flavored mesons, and the most difficult to produce: it was observed for the first time in the semileptonic mode by CDF in 1998 [161], but its mass was accurately determined only in 2006, from the fully reconstructed mode $B_c^+ \to J/\psi\pi^+$ [162]. The agreement between our prediction and the experimental data is good.

3.5 Lorentz structure of the confinement

The interquark potential depends on the Lorentz nature of the interaction and so assumptions for it are needed. Although it seems clear the Lorentz structure of the Goldstone-boson and the OGE potentials, the Lorentz character of the confinement has not yet established firmly. In this section we study the influence of the Lorentz structure of the confinement in the previously presented spectra, to do that we focus on some physical observables which are more sensible to this effect.

One of the most experimental evidences in the heavy quark sector which favors the scalar structure of the confinement is the measurement, compatible with zero, of the hyperfine mass splitting between the $^1P_1$ state and the center-of-gravity (c.o.g.) of the corresponding triplet ^3P_J states. Within the charmonium sector, the $\Delta m_{hf}[h_c(1P)] = \langle m(1^3P_J)\rangle - m[h_c(1P)]$ has been measured to be $+0.02 \pm 0.23\,\text{MeV}$ from CLEO [119], and $-0.10 \pm 0.22\,\text{MeV}$ from BES III [120]. In the case of the bottomonium sector, the Belle Collaboration [140] has reported $\Delta m_{hf}[h_b(1P)] = +1.6 \pm 1.5\,\text{MeV}$ and $\Delta m_{hf}[h_b(2P)] = +0.5^{+1.6}_{-1.2}\,\text{MeV}$.

A hyperfine mass splitting between the $^1P_1$ and the c.o.g of the triplet ^3P_J states compatible with zero means that the interquark potential has a vanishing long-range component of the spin-spin contribution. At large distances, the confinement potential is dominant. If it had a vector Lorentz structure, it would present a spin-spin contribution, proportional to the Laplacian of its central term, that does not behave as a delta-like term. Only the short range of the interquark potential, the coulomb term of the OGE potential, has a spin-spin contribution proportional to a delta function.

In the case of a scalar Lorentz confinement, there is no magnetic field to influence the quark spin and the only spin-orbit interaction is the kinematic Thomas precession term. The Thomas type spin-orbit interaction partially cancels that of the short range one-gluon exchange, in agreement with the observed spectrum. Sophisticated QCD calculations predict spin-dependent [163] and spin-independent [164] relativistic corrections of the long-range potential. The spin dependence is just the Thomas type spin-orbit interaction. Moreover, Lattice QCD simulations study the spin-dependent terms of the potential finding that they can be associated with the Thomas interaction [165]. However, the spin-independent corrections differ from those of scalar confinement [166].

Our confining potential has a mixture of scalar and vector Lorentz structures which was fixed in Ref. [52] to reproduce the masses of $a_0(980)$, $a_1(1260)$ and $a_2(1320)$ mesons. The model parameter which controls the mixture is a_s. In Ref. [52] its value was 0.78 and with the fine tuned model is 0.81. The value of a_s indicates that our confinement is dominantly scalar.

We have considered that the central part of the scalar and vector Lorentz structures of the confinement are the same

$$V_{\text{CON}}^{\text{C,scalar}}(\vec{r}_{ij}) = V_{\text{CON}}^{\text{C,vector}}(\vec{r}_{ij}) = \left[-a_c(1 - e^{-\mu_c r_{ij}}) + \Delta\right](\vec{\lambda}_i^c \cdot \vec{\lambda}_j^c). \tag{3.11}$$

There are different spin-dependent corrections related with the scalar or vector Lorentz character of the confinement. We have both corrections weighed by the model parameter a_s. For the scalar potential we calculate the spin-orbit contribution as

follows

$$V_{\rm CON}^{\rm SO,scalar}(\vec{r}_{ij}) = -\frac{1}{4m_i^2m_j^2}\frac{1}{r}\frac{dV_{\rm CON}^{\rm C,scalar}(\vec{r}_{ij})}{dr_{ij}}\left[(m_i^2+m_j^2)(\vec{S}_+\cdot\vec{L})+(m_j^2-m_i^2)(\vec{S}_-\cdot\vec{L})\right], \tag{3.12}$$

whereas for the vector one, there are spin-spin, tensor and spin-orbit contributions which are calculated as

$$\begin{aligned}
V_{\rm CON}^{\rm SS,vector}(\vec{r}_{ij}) =& \frac{1}{6m_im_j}(\vec{\sigma}_i\cdot\vec{\sigma}_j)\nabla^2 V_{\rm CON}^{\rm C,vector}(\vec{r}_{ij}),\\
V_{\rm CON}^{\rm T,vector}(\vec{r}_{ij}) =& \frac{1}{12m_im_j}\left(\frac{1}{r}\frac{dV_{\rm CON}^{\rm C,vector}(\vec{r}_{ij})}{dr_{ij}}-\frac{d^2V_{\rm CON}^{\rm C,vector}(\vec{r}_{ij})}{dr_{ij}^2}\right)S_{ij},\\
V_{\rm CON}^{\rm SO,vector}(\vec{r}_{ij}) =& \frac{1}{4m_i^2m_j^2}\frac{1}{r}\frac{dV^{\rm C,vector}(\vec{r}_{ij})}{dr_{ij}}\times\\
&\times\left[((m_i+m_j)^2+2m_im_j)(\vec{S}_+\cdot\vec{L})+(m_j^2-m_i^2)(\vec{S}_-\cdot\vec{L})\right].
\end{aligned} \tag{3.13}$$

So that the different contributions of our confinement potential are

$$\begin{aligned}
V_{\rm CON}^{\rm C}(\vec{r}_{ij}) =& \left[-a_c(1-e^{-\mu_c r_{ij}})+\Delta\right](\vec{\lambda}_i^c\cdot\vec{\lambda}_j^c),\\
V_{\rm CON}^{\rm SO}(\vec{r}_{ij}) =& -(\vec{\lambda}_i^c\cdot\vec{\lambda}_j^c)\frac{a_c\mu_c e^{-\mu_c r_{ij}}}{4m_i^2m_j^2r_{ij}}\left[((m_i^2+m_j^2)(1-2a_s)\right.\\
&\left.+4m_im_j(1-a_s))(\vec{S}_+\cdot\vec{L})+(m_j^2-m_i^2)(1-2a_s)(\vec{S}_-\cdot\vec{L})\right],\\
V_{\rm CON}^{\rm T}(\vec{r}_{ij}) =& -(\vec{\lambda}_i^c\cdot\vec{\lambda}_j^c)\frac{a_c\mu_c e^{-\mu_c r_{ij}}}{12m_im_jr_{ij}}(1-a_s)(1+\mu_c r_{ij})S_{ij},\\
V_{\rm CON}^{\rm SS}(\vec{r}_{ij}) =& -(\vec{\lambda}_i^c\cdot\vec{\lambda}_j^c)\frac{a_c\mu_c e^{-\mu_c r_{ij}}}{6m_im_jr_{ij}}(1-a_s)(2-\mu_c r_{ij})(\vec{\sigma}_i\cdot\vec{\sigma}_j).
\end{aligned} \tag{3.14}$$

We show in Fig. 3.5 different observables related with meson spectra as a function of a_s. The observables are calculated using the constituent quark model taking into account the central and spin-orbit contributions of Eq. (3.14) (solid line) and including also the tensor and spin-spin terms coming from the vector nature of the confinement (dashed line).

We have in panel (a) $m(J/\psi)-m(\eta_c(1S))$, in panel (b) $m(\psi(2S))-m(\eta_c(2S))$, in panel (c) $\langle m(\chi_{cJ}(1P))\rangle - m[h_c(1P)]$ and in panel (d) $\langle m(\chi_{cJ}(2P))\rangle - m[h_c(2P)]$. All these observables are in the charmonium sector and they are more sensitive to the spin-spin contribution of the potential. One can see that we need a dominantly scalar confinement to reproduce simultaneously the different observables and that, within this assumption, the inclusion of the tensor and spin-spin terms coming from the vector nature of the confinement produces differences of $5-10\,$MeV. Panels (e), (f), (g) and (h) are referred to the same observables but in the bottomonium sector, the same conclusion of the charmonium sector can be derived also in this case. The mass of the $D_{s0}^*(2317)$, $D_{s1}(2460)$ and $D_{s1}(2536)$ mesons are shown in panels (i), (j) and (k), respectively. The inclusion of the tensor and spin-spin terms coming from the vector nature of the confinement produces a negligible effect. It is interesting to note

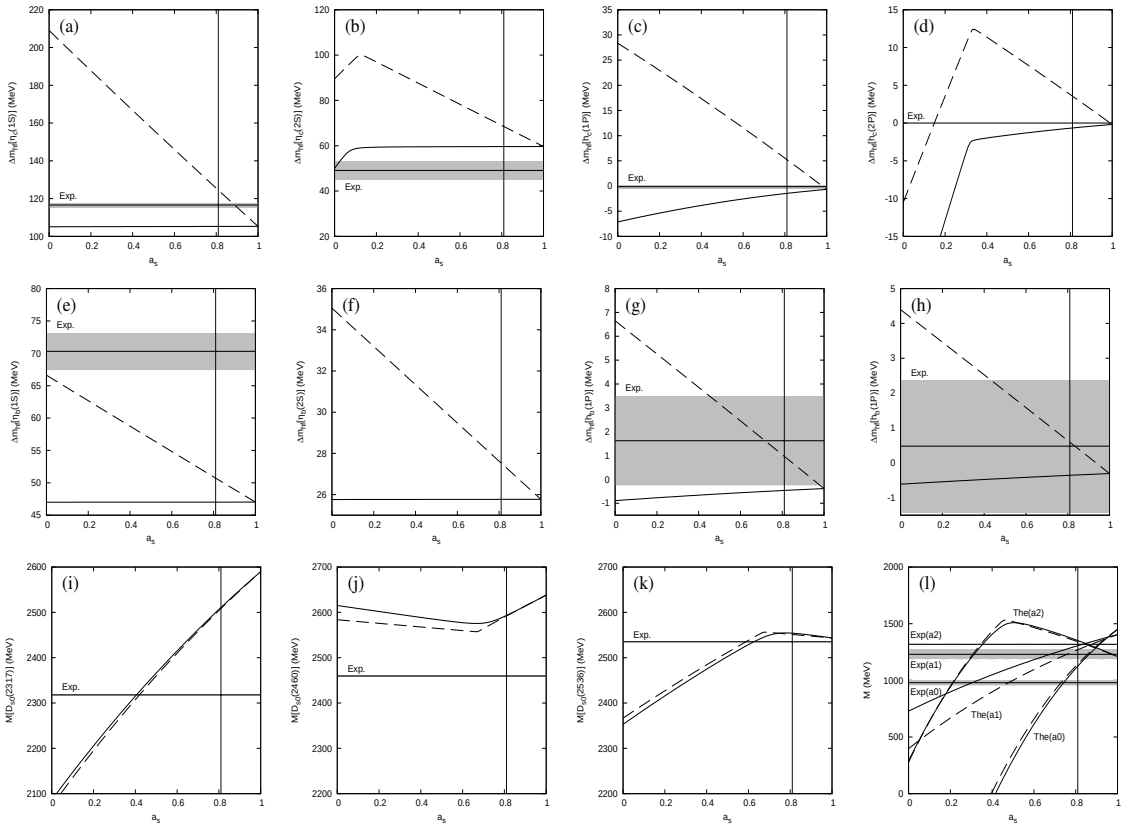

Figure 3.5. We show as a function of a_s the following observables: **(a):** $m(J/\psi) - m(\eta_c(1S))$, **(b):** $m(\psi(2S)) - m(\eta_c(2S))$, **(c):** $\langle m(\chi_{cJ}(1P))\rangle - m[h_c(1P)]$, **(d):** $\langle m(\chi_{cJ}(2P))\rangle - m[h_c(2P)]$, **(e):** $m(\Upsilon(1S)) - m(\eta_b(1S))$, **(f):** $m(\Upsilon(2S)) - m(\eta_b(2S))$, **(g):** $\langle m(\chi_{bJ}(1P))\rangle - m[h_b(1P)]$, **(h):** $\langle m(\chi_{bJ}(2P))\rangle - m[h_b(2P)]$, **(i):** Mass of $D^*_{s0}(2317)$, **(j):** Mass of $D_{s1}(2460)$, **(k):** Mass of $D_{s1}(2536)$, **(l):** Masses of $a_0(980)$, $a_1(1260)$ and $a_2(1320)$ mesons. The solid line is the constituent quark model taking into account the central and spin-orbit contributions. The dashed line reflects that we include also the tensor and spin-spin contributions coming from the vector nature of the confinement. The vertical solid line indicates our value of a_s.

that while the mass of the $D^*_{s0}(2317)$ meson is sensible to the Lorentz structure of the confinement potential, we never reach an agreement with the experimental situation for the masses of the $D_{s1}(2460)$ and $D_{s1}(2536)$ mesons, whatever be the value of a_s. Finally, in panel (l) are drawn the masses of $a_0(980)$, $a_1(1260)$ and $a_2(1320)$ mesons. Again, the inclusion of the tensor and spin-spin terms coming from the vector nature of the confinement produces a negligible effect. A dominantly scalar confining interaction is needed to explain the masses of the $a_0(980)$, $a_1(1260)$ and $a_2(1320)$ mesons.

We conclude that the confinement interaction is dominantly scalar and the inclusion of the tensor and spin-spin terms coming from the vector nature of the confinement does not affect the global description of the spectrum in the different sectors.

3.6 One-loop QCD corrections to the OGE potential

The spectra of charmed and charmed-strange sectors are not so well reproduced theoretically. There are some inconsistencies with experiment, mainly in the charmed-

		Charmed mesons		Charmed-strange mesons	
Contribution	Parameters	Set I	Set II	Set I	Set II
Mass	m_q (MeV)	313	313	555	555
	m_c (MeV)	1763	1763	1763	1763
OGE	α_0	2.118	2.118	2.118	2.118
	Λ_0 (fm^{-1})	0.113	0.113	0.113	0.113
	μ_0 (MeV)	36.976	36.976	36.976	36.976
	$\hat{r}_0$ (fm)	0.181	0.149	0.181	0.158
	$\hat{r}_g$ (fm)	0.259	0.259	0.259	0.177
Confinement	a_c (MeV)	507.4	464.4	507.4	507.4
	μ_c (fm^{-1})	0.576	0.630	0.576	0.576
	Δ (MeV)	184.432	184.432	184.432	184.432
	a_s	0.81	0.78	0.81	0.81

Table 3.27. The two sets of model parameters.

strange sector due to the fact that the mass splittings between the $D^*_{s0}(2317)$, $D_{s1}(2460)$ and $D_{s1}(2536)$ mesons are difficult to reproduce with quark models and also with Lattice QCD calculations [167]. For instance, one would expect that the mesons $D^*_{s0}(2317)$ and $D_{s1}(2460)$, which belong to the doublet $j^P_q = \frac{1}{2}^+$, are nearby degenerated. This feature is almost fulfilled with the other P-wave doublet $j^P_q = \frac{3}{2}^+$, the $D_{s1}(2536)$ and $D^*_{s2}(2573)$ mesons. In principle and depending on the mass of the $D^*_0(2400)$ meson, the charmed sector follows the expectations and the mass splittings are small between $D^*_0(2400)$, $D_1(2420)$, $D_1(2430)$ and $D^*_2(2460)$.

The strong interest on the charmed-strange meson spectroscopy was originated by the discovery of the $D^*_{s0}(2317)$ meson by the BaBar Collaboration [37]. It was seen in the isospin violating $D_s\pi$ decay mode in $K\bar{K}\pi\pi$ and $K\bar{K}\pi\pi\pi$ mass distributions. The CLEO Collaboration, motivated by the recent discovery of BaBar, found later the missing meson of the doublet, $D_{s1}(2460)$, decaying into $D^*_s\pi^0$ channel. Potential models, in particular our potential model, predict usually the ground state of the 0^+ and 1^+ $c\bar{s}$ mesons above the DK and D^*K thresholds, respectively. The experiment tell us that the mass of the state is below the corresponding threshold, which has important consequences on the width of the state.

The interpretation of the $D^*_{s0}(2317)$ as a multiquark state (e.g. [168, 169]), in particular as a DK molecule, has several attractive features. This is supported by its isospin violating discovery mode and the proximity of the S-wave DK threshold. The same occurs for the $D_{s1}(2460)$ as a D^*K molecule. However, if the $D_s\pi^0$ mode dominates the total width of the $D^*_{s0}(2317)$, the measured product of branching ratios [170]

$$\mathcal{B}(B^0 \to D^*_{s0}(2317)K) \times \mathcal{B}(D^*_{s0}(2317) \to D_s\pi^0) = (4.4 \pm 0.8 \pm 1.1) \times 10^{-5} \qquad (3.15)$$

implies that the $\mathcal{B}(B^0 \to D^*_{s0}(2317)K) \sim 10^{-5}$. Other similar branching ratios of the B meson decays into well established D_s mesons can be seen in Ref. [78], e.g. $\mathcal{B}(B^0 \to D^-_s K^+) = (2.2 \pm 0.5) \times 10^{-5}$, all of them are of the same order of magnitude than the previous one and this is consistent with the $D^*_{s0}(2317)$ being a canonical 0^+

		Charmed mesons					Charmed-strange mesons				
J^P	n	Set I		Set II			Set I		Set II		
		α_s	α_s^2	α_s	α_s^2		α_s	α_s^2	α_s	α_s^2	
0^-	1	1896	1896	1867	1867	D	1984	1984	1969	1969	D_s
	2	2695	2695	2646	2646	$D(2550)$	2729	2729	2720	2720	
	3	3154	3154	3075	3075		3178	3178	3173	3173	
	4	3448	3448	3334	3334		3487	3487	3483	3483	
0^+	1	2516	2362	2464	2368	$D_0^*(2400)$	2510	2383	2473	2318	$D_{s0}^*(2317)$
	2	3033	2925	2960	2896		3025	2934	2995	2883	
	3	3366	3292	3262	3221		3376	3310	3353	3271	
	4	3582	3533	3442	3419		3625	3576	3608	3548	
1^+	1	2466	2499	2450	2482	$D_1(2420)$	2554	2560	2555	2560	$D_{s1}(2535)$
	2	2596	2535	2548	2492	$D_1(2430)$	2593	2570	2588	2564	$D_{s1}(2460)$
	3	3008	3033	2955	2979		3056	3061	3056	3059	$D_{sJ}(3040)$
	4	3079	3030	3006	2963		3077	3058	3073	3054	$D_{sJ}(3040)$
1^-	1	2017	2014	2006	2005	D^*	2110	2104	2109	2102	D_s^*
	2	2756	2754	2715	2715	$D^*(2600)$	2797	2794	2796	2792	$D_{s1}^*(2710)$
	3	2935	2905	2869	2851		2915	2890	2913	2893	$D_{sJ}^*(2860)$
	4	3193	3191	3117	3117		3224	3221	3224	3221	
2^-	1	2812	2822	2784	2793	$D_J(2750)$	2886	2888	2886	2888	
	2	2973	2962	2908	2899		2948	2943	2948	2943	
	3	3227	3234	3158	3165		3278	3280	3278	3281	
	4	3323	3313	3228	3221		3317	3313	3317	3313	
2^+	1	2513	2544	2497	2516	$D_2^*(2460)$	2591	2609	2594	2608	$D_{s2}^*(2573)$
	2	3037	3059	2983	2996		3081	3094	3084	3093	
	3	3220	3207	3136	3129		3196	3184	3196	3186	
	4	3372	3387	3279	3287		3417	3427	3419	3427	
3^+	1	3090	3094	3045	3049		3151	3151	3151	3152	
	2	3244	3240	3161	3158		3216	3215	3216	3215	
	3	3409	3412	3321	3323		3464	3464	3464	3464	
	4	3503	3500	3386	3384		3507	3506	3507	3506	
3^-	1	2847	2863	2819	2828	$D_J^*(2760)$	2911	2922	2911	2920	$D_{sJ}^*(2860)$
	2	3249	3260	3179	3185		3296	3304	3296	3302	
	3	3443	3437	3340	3336		3428	3421	3428	3423	
	4	3511	3518	3398	3402		3569	3575	3569	3574	

Table 3.28. Masses, in MeV, of charmed and charmed-strange mesons. The predictions are without (α_s) and with (α_s^2) one-loop corrections of the OGE potential. A possible assignment of the new mesons is also included. We show the results for two sets of parameters, Table 3.27.

$c\bar{s}$ meson. For this reason it is important to exhaust possible canonical $c\bar{s}$ descriptions before resorting to more exotic models.

The quark model explanation of the P-wave mass splittings lies on the spin-dependent interactions. The spin-dependence of our constituent quark model is based on the Fermi-Breit reduction of the OGE interaction supplemented with the spin-dependence due to the confinement interaction. This dependence is common with other quark models. The incorporation of the one-loop QCD corrections to the spin-dependent terms of the OGE potential was proposed by Lakhina *et al.* in Ref. [171]. It was motivated by the fact that in the one-loop computation there is a spin-dependent term which affects only to mesons with different flavor quarks [172].

We want to see what happens if we incorporate these corrections to our potential. The net result is a quark-antiquark interaction that can be written as:

$$V(\vec{r}_{ij}) = V_{\rm OGE}(\vec{r}_{ij}) + V_{\rm CON}(\vec{r}_{ij}) + V_{\rm OGE}^{\rm 1-loop}(\vec{r}_{ij}), \tag{3.16}$$

where $V_{\rm OGE}$ and $V_{\rm CON}$ have been already defined and will be treated nonperturbatively. The $V_{\rm OGE}^{\rm 1-loop}$ is the one-loop correction to the OGE potential and presents singular contributions. In order to avoid *ad hoc* cutoffs, this part of the potential is treated perturbatively.

As in the case of $V_{\rm OGE}$ and $V_{\rm CON}$, we write the $V_{\rm OGE}^{\rm 1-loop}$ as follows:

$$V_{\rm OGE}^{\rm 1-loop}\left(\vec{r}_{ij}\right) = V_{\rm OGE}^{\rm 1-loop,C}\left(\vec{r}_{ij}\right) + V_{\rm OGE}^{\rm 1-loop,T}\left(\vec{r}_{ij}\right) + V_{\rm OGE}^{\rm 1-loop,SO}\left(\vec{r}_{ij}\right), \tag{3.17}$$

where C stands for central, T for tensor and SO for spin-orbit potentials. These contributions are given by [171]

$$\begin{aligned}
&V_{\rm OGE}^{\rm 1-loop,C}(\vec{r}_{ij}) = 0,\\
&V_{\rm OGE}^{\rm 1-loop,T}(\vec{r}_{ij}) = \frac{C_F}{4\pi}\frac{\alpha_s^2}{m_i m_j}\frac{1}{r^3}S_{ij}\left[\frac{b_0}{2}\left(\ln(\mu r_{ij}) + \gamma_E - \frac{4}{3}\right) + \frac{5}{12}b_0 - \frac{2}{3}C_A\right.\\
&\qquad\qquad\left. + \frac{1}{2}\left(C_A + 2C_F - 2C_A\left(\ln(\sqrt{m_i m_j}\, r_{ij}) + \gamma_E - \frac{4}{3}\right)\right)\right],\\
&V_{\rm OGE}^{\rm 1-loop,SO}(\vec{r}_{ij}) = \frac{C_F}{4\pi}\frac{\alpha_s^2}{m_i^2 m_j^2}\frac{1}{r^3}\times\\
&\times\left\{(\vec{S}_+\cdot\vec{L})\Big[\left((m_i+m_j)^2 + 2m_i m_j\right)\left(C_F + C_A - C_A\left(\ln(\sqrt{m_i m_j}\, r_{ij}) + \gamma_E\right)\right)\right.\\
&\qquad + 4m_i m_j\left(\frac{b_0}{2}\left(\ln(\mu r_{ij}) + \gamma_E\right) - \frac{1}{12}b_0 - \frac{1}{2}C_F - \frac{7}{6}C_A + \frac{C_A}{2}\left(\ln(\sqrt{m_i m_j}\, r_{ij}) + \gamma_E\right)\right)\\
&\qquad \left. + \frac{1}{2}(m_j^2 - m_i^2)C_A\ln\left(\frac{m_j}{m_i}\right)\Big]\right.\\
&+(\vec{S}_-\cdot\vec{L})\Big[(m_j^2 - m_i^2)\left(C_F + C_A - C_A\left(\ln(\sqrt{m_i m_j}\, r_{ij}) + \gamma_E\right)\right)\\
&\qquad \left. + \frac{1}{2}(m_i + m_j)^2 C_A\ln\left(\frac{m_j}{m_i}\right)\Big]\right\},
\end{aligned} \tag{3.18}$$

where $C_F = 4/3$, $C_A = 3$, $b_0 = 9$, $\gamma_E = 0.5772$ and the scale $\mu \sim 1\,\text{GeV}$.

These additional terms do not destroy the agreement in the $Q\bar{Q}$ spectra. Table 3.27 shows the two sets of model parameters which have been considered (Set I is the original one). The masses of charmed and charmed-strange mesons predicted by the constituent quark model without and with one-loop corrections to the OGE potential are shown in Table 3.28.

We conclude that the 0^+ states are more sensitive to the inclusion of the one-loop corrections to the OGE potential. This feature is fulfilled in both charmed and charmed-strange sectors. It allows us to explain the lower mass of the $D^*_{s0}(2317)$ meson within our constituent quark model. If the mass of the $D^*_0(2400)$ was lower than the expected one, this mass would be explained also. This effect does not solve the puzzle of the 1^+ mesons, which may be an indication that in the 1^+ $c\bar{s}$ sector the effects of the meson-meson continuum are important.

Finally, the work presented here may explain the difficulty in accurately computing the mass of the $D^*_0(2400)$ and $D^*_{s0}(2317)$ in lattice simulations. According to the Ref. [171], the rationale for that is the following: if the extended quark model is correct, it implies that important mass and spin-dependent interactions are presented in the one-loop level OGE quark interaction. It is possible that current lattice computations are not sufficiently sensitive to the ultraviolet behaviour of QCD to capture this physics. The problem is exacerbated by the nearby, and presumably strongly coupled, DK continuum; which requires simulations sensitive to the infrared behaviour of QCD.

3.7 Renormalization approach to the CQM

We have already mentioned that after the discovery of the first heavy-quark bound states, the ψ and Υ systems, it was soon realized that a nonrelativistic picture seemed to hold for them. Potential models, which incorporate OGE interaction at short distances and confinement at large distances, describe well the spectrum of charmonium and bottomonium systems when one solves the bound state problem with the Schrödinger equation.

In the nonrelativistic framework, the OGE potential is singular at the origin. A potential is said to be singular at $r = 0$ if

$$\lim_{r\to 0} r^2 V(r) = \pm\infty. \tag{3.19}$$

A singular potential is called repulsively or attractively singular according to whether the limiting value in Eq. (3.19) is, respectively, $+\infty$ or $-\infty$, regardless of whether the potential maintains one sign for $r > 0$. The basic feature of an attractive singular potential is seen to lie in the fact that physical processes are not uniquely determined. This gives rise to the possibility of imposing unusual or unconventional boundary conditions in physical problems as a means of representing particular physical processes. In contrast to the attractive potential, the repulsive case poses no problem as regards physical interpretation. The solutions to physical problems are uniquely given.

The presence of the OGE short-distance singularities motivates the introduction of phenomenological gluonic form factors in potential models (see e.g. [173] for an early proposal). This triggers an unpleasant short-distance sensitivity and, as we will show, it mainly hides the fact that the ground state is actually being used as an input rather than a prediction.

We want to address the question on how much can we deduce for the spectrum of 1^{--} $c\bar{c}$ meson from the knowledge of the potential at long distances in a way that our ignorance at short distances needs not play a crucial role. This allows to disentangle the physics of the ground state to that of the excited states. The method which we will be using is based on renormalization ideas. The presence of long-range confining forces suggests pursuing the calculations in coordinate space. One of the advantages of the coordinate space treatment of renormalization is that it can directly be extended to other singular cases such as the multigluon exchange potentials.

There is the added difficulty that we have coupled second order differential equations in the $J^{PC} = 1^{--}$ channel. Then one has four independent solutions, which according to their singularity structure correspond to either two regular and two irregular solutions at infinity or three regular and one irregular solution at the origin. The normalization of the wave functions of the 1^{--} $c\bar{c}$ states eliminates all constants for a given J/ψ binding energy, which instead of being predicted has to be treated as an independent parameter.

Actually, our original motivation for the present study was to analyze the role of regulators within the constituent quark model described before. However, our ideas can be generally extended to any quark model and shed some light on their predictive power.

3.7.1 The uncoupled $J^{PC} = 1^{--}$ $c\bar{c}$ system

Let us consider the standard nonrelativistic Schrödinger equation for bound states in S-waves

$$-u_n''(r) + U(r)u_n(r) = -\kappa^2 u_n(r), \tag{3.20}$$

where $U(r) = 2\mu V(r)$ is the reduced potential, $\kappa^2 = 2\mu(V_{\rm thr} - E_n)$ with $V_{\rm thr} = \frac{16}{3}(a_c - \Delta)$, $u_n(r)$ is the reduced wave function ($R_n(r) = u_n(r)/r$) which vanishes at long distances and the energy is defined with respect to the $q - \bar{q}$ threshold, $E_n = M_n - m_q - m_{\bar{q}}$.

Anticipating our discussion we will assume for definiteness a short-distance auxiliary cutoff, r_c, below which the potential vanishes. This cutoff is just a parameter which will ultimately be removed while keeping some physical condition fixed. Typically the range taken will be $r_c = 0.3 - 0.01\,$fm. In our case we will choose to fix the ground state energy to the experimental value. In the numerical application we will be concerned with the residual cutoff dependence of observables induced by such a procedure.

Using the standard trick of multiplying Eq. (3.20) by $u_m(r)$ and subtracting the similar equation with $n \leftrightarrow m$, we get for two different energies $E_n \neq E_m$ the orthogonality relation between their bound state wave functions

$$u_n'(r_c)u_m(r_c) - u_n(r_c)u_m'(r_c) = 2\mu(E_n - E_m)\int_{r_c}^{\infty} u_n(r)u_m(r)\,dr. \tag{3.21}$$

Note that usually the regularity condition at the origin, $u_n(r_c) = 0$ for $r_c \to 0$, is imposed. Whence orthogonality of wave functions with different energies holds. However, this is not the only solution to the orthogonality requirement. Instead the

common boundary condition, we may as well take

$$\frac{u'_m(r_c)}{u_m(r_c)} = \frac{u'_n(r_c)}{u_n(r_c)}, \tag{3.22}$$

for any two states, meaning that the logarithmic derivative at short distances becomes state independent. In particular, choosing the ground state as a reference state we get the condition

$$\frac{u'_0(r_c)}{u_0(r_c)} = \frac{u'_n(r_c)}{u_n(r_c)}. \tag{3.23}$$

How can this logarithmic derivative be determined? If we know the energy of the ground state and the potential we may integrate from the long distance region inward to deduce $u'_0(r_c)/u_0(r_c)$. Once this number is known, we may use Eq. (3.23) to integrate out the excited state and the corresponding bound state energy can be fixed by requiring the wave function to vanish at large distances[2]. Thus, such a procedure allows to treat the ground state energy, E_0, as an independent variable from the potential $V(r)$ and still deduce wave functions and the excited spectrum. There is of course the question on how to interpret the short-distance cutoff, r_c. In principle one may look for stability at scales below the relevant sizes. Actually, varying the cutoff in this region is a way of assessing theoretical uncertainties[3]. However, there are situations where the limit $r_c \to 0$ is rather smooth and induces moderate changes in observables.

A good feature of the present approach is that since wave functions are matched at short distances the resulting energies are largely independent on the short distance behaviour of the potential.

The previous discussion has been conducted for S-waves and regular potentials, i.e. fulfilling $\lim_{r\to 0} r^2|V(r)| < \infty$. Higher partial waves cannot be renormalized in this fashion as short distances are dominated by the centrifugal barrier. This also has the benefit of diminishing the dependence on the short-distance potential since the short-distance behaviour of the wave function, $u(r) \sim r^{l+1}$, is not controlled by the potential.

The case of singular potentials has also been discussed at length (see e.g. Refs. [175–177] regarding nuclear or atomic systems). The relation to momentum space renormalization and the corresponding Lagrangian counterterms is discussed in Ref. [178]. The irrelevance of form factors is analyzed in Refs. [177, 179].

The treatment of the potential in this framework has the advantage to reduce the number of model parameters. This allows us to study in a cleaner way the existence of correlations between physical observables and model parameters which have a direct physical interpretation.

Our first aim is to reanalyze the calculation of the $J^{PC} = 1^{--}$ $c\bar{c}$ spectrum. While the tensor force induces a mixing between S and D-waves we will, in a first step,

[2]There is of course the subtlety that if we include exactly the origin the radial wave function does not provide a three-dimensional solution of the Schrödinger equation as it generates a $\delta(\vec{x})$ term [174]. As has been discussed at length in previous works [175–177] we can take any arbitrarily small (but non-vanishing) short-distance cutoff $r > r_c > 0$ which in the limit $r_c \to 0^+$ generates a well defined result. In all our discussions we assume this limiting procedure.

[3]In a model where phenomenological form factors are implemented *ad hoc*, just to prevent singularities, the assessment of theoretical errors could be done by choosing all possible regularization functions, unless the form factor is known from first principles.

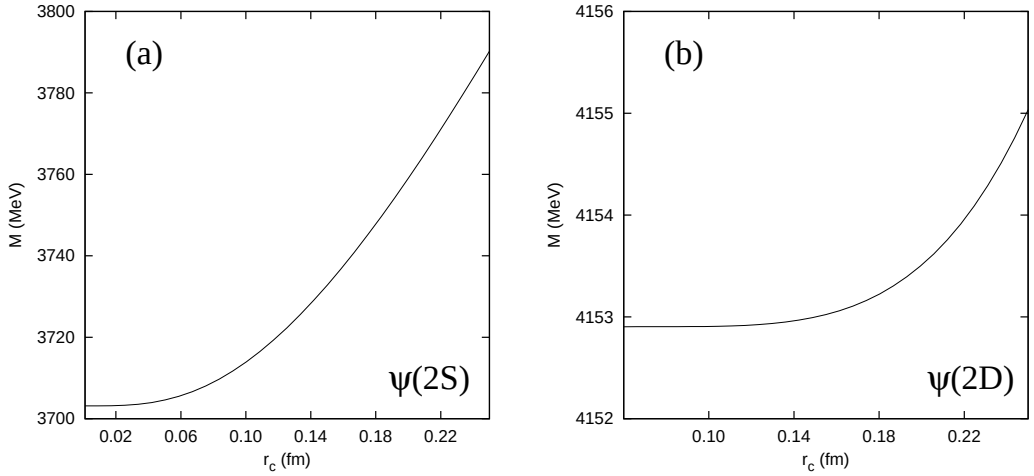

Figure 3.6. Dependence of the mass, in MeV, on the short distance cutoff, r_c, in fm, for the excited 1^{--} charmonium states 2^3S_1 (left panel) and 2^3D_1 (right panel).

State	n	$M_{\rm RSC}$ (MeV)	$M_{\rm CQM}$ (MeV)	$M_{\rm Exp.}$ (MeV)	Ref.
$^3S_1$	1	$3096^\dagger$	3096	3096.916 ± 0.011	[78]
	2	3703	3703	3686.093 ± 0.034	[78]
	3	4097	4097	4039.6 ± 4.3	[78]
	4	4389	4389	$4361 \pm 9 \pm 9$	[86]
	5	4614	4614	4634^{+8+5}_{-7-8}	[87]
$^3D_1$	1	$3796^\dagger$	3796	3772.92 ± 0.35	[78]
	2	4153	4153	4153 ± 3	[78]
	3	4426	4426	4421 ± 4	[78]
	4	4641	4641	$4664 \pm 11 \pm 5$	[86]

Table 3.29. Masses, in MeV, of uncoupled $J^{PC} = 1^{--}$ $c\bar{c}$ states within the renormalization scheme (RSC) and potential model with form factors (CQM). The symbol † indicates that the state has been fixed.

neglect such a mixing. This implies that both ground states are completely unrelated and renormalization is pursued independently. As expected, the masses in this scheme depend on the short-distance cutoff, r_c. Fig. 3.6 shows this dependence for the first excitations of S and D-wave states. One can see that at some value of r_c the masses do not depend on the short-distance cutoff.

In Table 3.29 the masses predicted by the renormalized model and the standard constituent quark model (with form factors) are displayed. We find a perfect agreement between both schemes. This provides confidence on the way the original model took into account the unknown short-distance dynamics, on the one hand, and also on the irrelevance of those form factors for excited states as long as the ground state mass is fixed.

As it becomes clear from the expressions of the potential, the perturbative and non-perturbative contributions dominate at short and large distances respectively. Therefore, we want to study now the dependence of the mass with respect to two

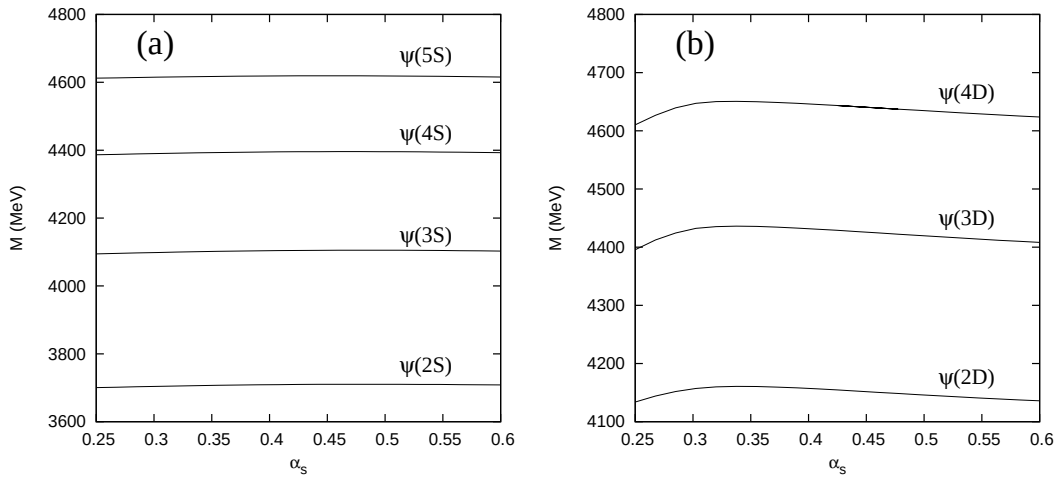

Figure 3.7. Mass, in MeV, dependence on the strong coupling constant of excited $J^{PC} = 1^{--}$ $c\bar{c}$ states.

important model parameters, the strong coupling constant, α_s, and our effective string tension of the confinement potential, σ, featuring those short and long distance effects.

The dependence on α_s can be seen in Fig. 3.7 for S and D-wave states. For S-wave states the mass changes about 15 MeV meaning a 0.4% change in the total mass and we see a flattening behaviour along the considered range of α_s. We find a similar trend for the D-wave states, although in this case the change in mass is larger than in the case of S-wave states, the picture shows again a rather clear plateau.

We now turn to the mass dependence on the effective string tension of our confinement potential, fixing the threshold. Fig. 3.8 shows such a dependence for the S and D-wave states. The range for the effective string tension is in percentage level equal than the range of the strong coupling constant and we can see that the masses change on the hundreds of MeV. We can conclude that at least the masses of excited states are dominated by the confinement potential as long as the ground state mass is kept to its physical value.

It is interesting to see what is the renormalized model sensitivity to the parameters. Of course, at this level one should envisage the possibly non-negligible contribution of the missing mesonic thresholds and the induced mass shift. To this end we fit the model parameters from the experimental masses of 1^{--} $c\bar{c}$ states [78] and estimate their theoretical uncertainties as well as an educated mass-shift guess. The way to perform the first task is of course debatable. This requires some compromise as to what are the errors attached to the masses within the present framework. Naively one would just take the quoted PDG errors on the experimental masses. Meson-meson thresholds which have not been taken into account may affect more significantly the higher excited states via a subthreshold induced mass shift, which we take as a systematic error of the model.

We decide to make a χ^2 fit using as fitting parameters the quark mass, m_c, a_c and μ_c related with the confinement strength and the strong coupling constant, α_s. We

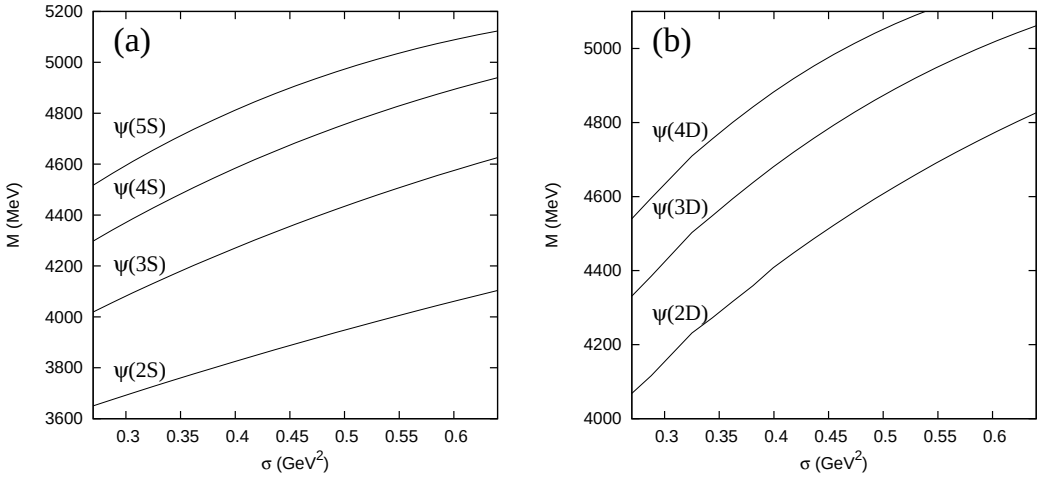

Figure 3.8. Dependence of the $J^{PC} = 1^{--}$ $c\bar{c}$ masses, in MeV, on the effective string tension of our confinement potential, $\sigma = -a_c\,\mu_c\,(\vec{\lambda}_i^c \cdot \vec{\lambda}_j^c)$, in GeV^2.

define the

$$\chi^2(\vec{p}) = \sum_i \frac{(M_{\text{Exp.}}(i) - M_{\text{The.}}(i,\vec{p}))^2}{\sigma^2_{\text{Exp.}}(i)}, \tag{3.24}$$

where $\vec{p}$ represents our model parameters and the experimental data are taken as $M_{\psi(2S)} = 3686.093 \pm 0.143\,\text{MeV}$, $M_{\psi(3S)} = 4039.6 \pm 42.25\,\text{MeV}$ and $M_{\psi(4S)} = 4361 \pm 37\,\text{MeV}$, where the errors are taken as the half-width of the state, as our educated guess. By minimizing the χ^2 function we obtain the theoretical uncertainties from the corresponding covariance matrix at the minimum. The outcoming values for the parameters are

$$\begin{aligned} m_c &= 1862 \pm 12.6\,\text{MeV} \quad (0.68\,\%), \\ a_c &= 524 \pm 43\,\text{MeV} \quad (8.2\,\%), \\ \mu_c &= 88 \pm 7.2\,\text{MeV} \quad (8.2\,\%), \\ \alpha_s &= 0.41 \pm 0.14 \quad (34\,\%), \end{aligned} \tag{3.25}$$

where we put in parenthesis the relative uncertainties in percentage. Here we clearly see that the highest uncertainty corresponds to the value of the strong coupling constant. This rather large insensitivity to the otherwise too large α_s is a rewarding feature of the renormalization approach. Actually, quite natural values of α_s are obtained. The spectrum at the χ^2-minimum is given by

$$\begin{aligned} \psi(2S) &= 3687 \pm 80\,\text{MeV}, \\ \psi(3S) &= 4108 \pm 79\,\text{MeV}, \\ \psi(4S) &= 4348 \pm 80\,\text{MeV}, \\ \psi(5S) &= 4586 \pm 66\,\text{MeV}. \end{aligned} \tag{3.26}$$

We now focus on the leptonic widths of S-wave states given by the Eq. (C.10). This will illustrate the interesting subject of the wave function renormalization. Decay

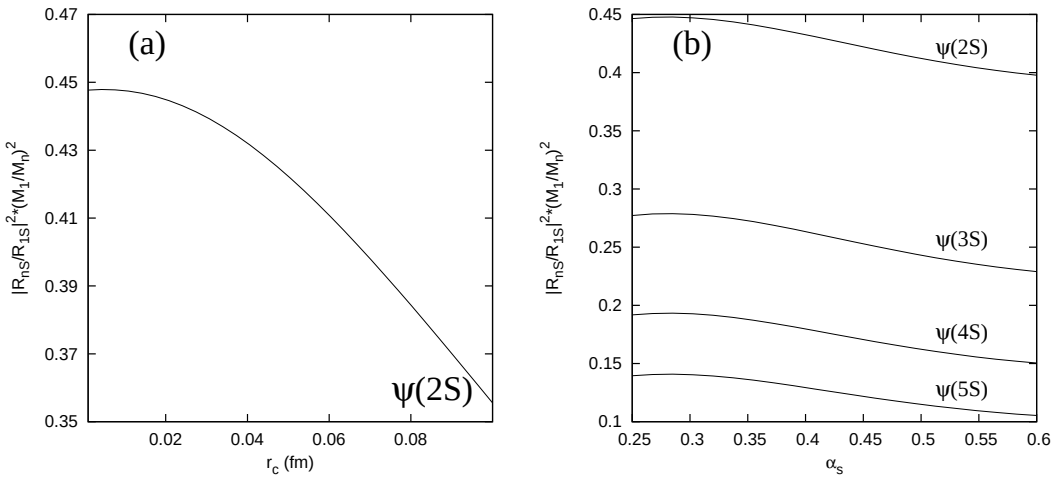

Figure 3.9. Left picture shows the dependence of the ratio $\mathcal{R}$ for $\psi(2S)$ with respect to the short-distance cutoff, r_c. Right picture shows the dependence of the ratio $\mathcal{R}$ for the 1^{--} S-wave $c\bar{c}$ states on the strong coupling constant, α_s.

widths depend on the value of the wave function at short distances. Of course while the decay may be triggered by a short-distance operator, we may predict decay ratios as

$$\mathcal{R} = \frac{\Gamma\left(n^3S_1 \to e^+e^-\right)}{\Gamma\left(1^3S_1 \to e^+e^-\right)} = \frac{|R_{nS}(0)|^2}{|R_{1S}(0)|^2}\frac{M_1^2}{M_n^2}. \tag{3.27}$$

This corresponds in practice to implement a common wave function renormalization which factors out in the ratio.

Fig. 3.9(a) shows the dependence of $\mathcal{R}$ with respect to the short-distance cutoff for the first excitation of S-wave states. At some range of r_c, the ratio does not depend on its value. Fig. 3.9(b) shows the dependence of the ratio for the S-wave states along the range of strong coupling constant used for the mass study. We find a stronger dependence on the strong coupling constant as expected since the leptonic decay width is a short range observable.

We have studied the leptonic widths taking into account momentum dependent effects, Eq. (C.12). These tend to diminish the absolute value of the leptonic decay rate but in the study of ratios between them the difference with respect the original results, Eq. (C.10), is negligible.

It is straightforward to extend the previous analysis on the leptonic widths to the $\psi(nS) \to 3g$ and $\psi(nS) \to 3\gamma$ cases. Using the usual formulas which describe these processes, one can see that the ratios from excited states to the ground state are process independent and identical to the corresponding leptonic decay widths discussed above

$$\frac{\Gamma\left(n^3S_1 \to 3g\right)}{\Gamma\left(1^3S_1 \to 3g\right)} = \frac{\Gamma\left(n^3S_1 \to 3\gamma\right)}{\Gamma\left(1^3S_1 \to 3\gamma\right)} = \frac{\Gamma\left(n^3S_1 \to e^+e^-\right)}{\Gamma\left(1^3S_1 \to e^+e^-\right)}. \tag{3.28}$$

This obviously allows to predict the excited state decay widths from the experimental ground state decay widths. The results are presented in Table 3.30.

	$\psi(nS) \to e^+e^-$		$\psi(nS) \to 3g$		$\psi(nS) \to 3\gamma$	
$\psi(nS)$	$\Gamma_{\rm The.}$ (keV)	$\Gamma_{\rm Exp.}$ (keV)	$\Gamma_{\rm The.}$ (keV)	$\Gamma_{\rm Exp.}$ (keV)	$\Gamma_{\rm The.}$ (eV)	$\Gamma_{\rm Exp.}$ (eV)
$1S$	input	5.55 ± 0.14	input	59.5 ± 2.0	input	1.11 ± 0.37
$2S$	2.49 ± 0.06	2.33 ± 0.07	26.7 ± 0.9	30.3 ± 4.9	0.49 ± 0.18	-
$3S$	1.55 ± 0.04	0.86 ± 0.07	16.6 ± 0.6	-	0.31 ± 0.11	-
$4S$	1.08 ± 0.03	-	11.5 ± 0.4	-	0.21 ± 0.08	-
$5S$	0.78 ± 0.02	-	8.4 ± 0.3	-	0.16 ± 0.06	-

Table 3.30. Absolute annihilation rates for excited 1^{--} S-wave $c\bar{c}$ states. We use the ground state experimental width as input. The quoted errors reflect the uncertainty stemming from the ground state only.

3.7.2 The coupled $J^{PC} = 1^{--}$ $c\bar{c}$ system

Our previous discussion of renormalization was undertaken without taking into account the role played by the tensor force. In the channel $J^{PC} = 1^{--}$, these states are a combination of S and D-wave components due to the tensor force contribution. As we will see below, this tensor force is small enough to have almost pure S and D orbital state components. The interesting aspect of our discussion below is that using just one renormalization condition we can predict all S and D-wave mesons, i.e. we reduce the number of renormalization conditions.

The radial Schrödinger equation for the $^3S_1 - {}^3D_1$ coupled channel reads in our unregulated model

$$\begin{aligned} &-u''(r) + U_S(r)u(r) + U_{SD}(r)w(r) = -\kappa^2 u(r), \\ &-w''(r) + U_{SD}(r)u(r) + \left[U_D(r) + \frac{6}{r^2}\right] w(r) = -\kappa^2 w(r), \end{aligned} \tag{3.29}$$

with U_S, U_D and U_{SD} are the different contributions of the reduced potential, $U(r) = 2\mu V(r)$, where the $^3S_1 - {}^3D_1$ coupled channel potential is given by

$$\begin{aligned} V_S(r) &= -\frac{4\alpha_s}{3r} + \frac{16}{3}\left[a_c(1 - e^{-\mu_c r}) - \Delta\right], \\ V_D(r) &= -\frac{4\alpha_s}{3r} + \frac{16}{3}\left[a_c(1 - e^{-\mu_c r}) - \Delta\right] - \frac{8a_c\mu_c e^{-\mu_c r}}{m_c^2 r}(3 - 4a_s) - \frac{20}{3}\frac{\alpha_s}{m_c^2}\frac{1}{r^3}, \\ V_{SD}(r) &= \frac{2\sqrt{2}}{3}\frac{\alpha_s}{m_c^2}\frac{1}{r^3}. \end{aligned} \tag{3.30}$$

Obviously, in order to describe a bound state we seek for normalizable solutions

$$\int_0^\infty \left[u^2(r) + w^2(r)\right] = 1, \tag{3.31}$$

which impose conditions on the wave functions both at infinity as well as at the origin.

The set of equations (3.29) must be accompanied by asymptotic conditions at infinity. We have a screened confining potential at large distances for both channels. Once we have discarded the irregular function at long distances, the wave functions at

infinity have the following behaviour

$$\begin{aligned} u(r) &\rightarrow A_S\, e^{-\kappa r}, \\ w(r) &\rightarrow A_D \left(1 + \frac{3}{\kappa r} + \frac{3}{(\kappa r)^2}\right) e^{-\kappa r}, \end{aligned} \tag{3.32}$$

where A_S is the normalization factor and the asymptotic D/S ratio parameter is defined by $\eta = A_D/A_S$. Ideally, one would integrate the Schrödinger equation taking its solutions at infinity, Eq. (3.32), which depend on the bound state energy and η. The singular structure of the problem at short distances requires a specific analysis of the coupled equations as it has been done extensively elsewhere [179] and we adapt it for our particular case in Appendix D. The result amounts to integrate from infinity for the physical value of $M_{J/\psi}$ and η. Generally, the solutions diverge strongly at the origin, so that the normalization of the state is precluded. However, there is a particular value of η which guarantees that the wave function becomes normalizable. Then, if one imposes the regularity condition at the origin one will determine η and therefore the wave function of the bound state. In practice, however, the converging solution is rather elusive since integrated-in solutions quickly run into diverging solution due to the round-off errors and dominate over the converging solution.

According to Ref. [179] one may proceed as follows. One can impose different auxiliary short-distance boundary conditions corresponding to a choice of regular solutions at the origin

$$\begin{aligned} u(r_c) &= 0 \quad \text{(BC1)}, \\ u'(r_c) &= 0 \quad \text{(BC2)}, \\ w(r_c) &= 0 \quad \text{(BC3)}, \\ w'(r_c) &= 0 \quad \text{(BC4)}, \\ u(r_c) - \sqrt{2}\, w(r_c) &= 0 \quad \text{(BC5)}, \\ u'(r_c) - \sqrt{2}\, w'(r_c) &= 0 \quad \text{(BC6)}. \end{aligned} \tag{3.33}$$

All of these boundary conditions must predict the same value of η at some value of the cutoff radius, r_c. The precise convergence value corresponds to the particular choice. As in Ref. [180] we find a better convergence for the boundary conditions BC5 and BC6 for larger cutoff radii, which improves the numerical results.

To calculate the D/S asymptotic ratio, η, it is convenient to use the superposition principle of boundary conditions to write

$$\begin{aligned} u(r) &= u_S(r) + \eta u_D(r), \\ w(r) &= w_S(r) + \eta w_D(r), \end{aligned} \tag{3.34}$$

where (u_S, w_S) and (u_D, w_D) correspond to the boundary conditions at infinity, Eq. (3.32) with $A_S = 1$ and $A_D = 0$ and with $A_S = 0$ and $A_D = 1$, respectively. Through that decomposition the boundary conditions, BC1-BC6, can be rewritten as algebraic expressions for η. For instance, if we use the BC6 boundary condition we get

$$\eta = -\frac{u'_S(r_c) - \sqrt{2}\, w'_S(r_c)}{u'_D(r_c) - \sqrt{2}\, w'_D(r_c)}. \tag{3.35}$$

Once η has been calculated, the wave function of the bound state is completely determined by the normalization factor A_S

$$\begin{aligned} u(r) &= A_S(u_S + \eta\, u_D), \\ w(r) &= A_S(w_S + \eta\, w_D), \end{aligned} \tag{3.36}$$

in which A_S is obtained normalizing the wave function to one

$$A_S^2 \int_0^\infty [(u_S + \eta\, u_D)^2 + (w_S + \eta\, w_D)^2] dr = 1. \tag{3.37}$$

The above procedure can be undertaken for the ground state of the system if its energy is known. Now, if we want to calculate the excited states of the system we must impose the orthogonality condition between wave functions of states with different energy together with the regularity condition at the origin.

Thus, given the ground state and one excited state, the orthogonality condition can be written as

$$\int_0^\infty dr\, [u_0(r)u_m(r) + w_0(r)w_m(r)] = 0, \tag{3.38}$$

where it is useful to rewrite the above expression through a Lagrange identity

$$[u_0' u_m - u_0 u_m' + w_0' w_m - w_0 w_m'] \Big|_0^\infty = 0. \tag{3.39}$$

Note that any individual term in the integrand is actually divergent, because of the dominance of the singular solutions at the origin. At very short distances, the orthogonality between wave functions and the regularity condition of them have been imposed at a certain cutoff radius, r_c. Of course, we always check that the numerical calculation is stable against suitable changes of the short-distance cutoff so that the range $r_c \sim 0.01 - 0.3\,\mathrm{fm}$ is sufficient. In that case, the orthogonality condition, Eq. (3.39), can be written as

$$u_0'(r_c)u_m(r_c) + w_0'(r_c)w_m(r_c) = u_0(r_c)u_m'(r_c) + w_0(r_c)w_m'(r_c), \tag{3.40}$$

and combining this expression with the corresponding one of the boundary conditions, Eq. (3.33), we obtain in the case of the boundary condition BC6

$$\frac{w_m'(r_c)}{\sqrt{2}\, u_m(r_c) + w_m(r_c)} = \frac{w_0'(r_c)}{\sqrt{2}\, u_0(r_c) + w_0(r_c)}, \tag{3.41}$$

and similarly for all other auxiliary boundary conditions. Obviously in this case the D/S mixing of the excited state is determined from the requirement of regularity at the origin

$$\eta_m = -\frac{u_{S,m}'(r_c) - \sqrt{2}\, w_{S,m}'(r_c)}{u_{D,m}'(r_c) - \sqrt{2}\, w_{D,m}'(r_c)}. \tag{3.42}$$

Results on the mass, the asymptotic D/S ratio parameter and D-wave probability are presented in Table 3.31. The comparison between renormalization scheme and constituent quark model with form factors is given in Table 3.32. One can see that the agreement is completely satisfactory. Essentially, this proves that the form factors only provide the correct mass of J/ψ. Once this is fixed the rest of the excited states with either S or D-wave character are predicted. For completeness, Fig. 3.10 shows the S and D-waves of the different states.

State	Mass (MeV)	η	$\mathcal{P}_D$ (%)
J/ψ	$3096^\dagger$	-0.0117	0.146
$\psi(2S)$	3703	$+0.0112$	0.221
$\psi(1D)$	3796	-13.2229	99.852
$\psi(3S)$	4098	$+0.0349$	0.446
$\psi(2D)$	4152	-10.3577	99.606
$\psi(4S)$	4389	$+0.0563$	0.758
$\psi(3D)$	4425	-8.8022	99.279
$\psi(5S)$	4614	$+0.0775$	1.109
$\psi(4D)$	4640	-7.4616	98.924

Table 3.31. Mass, in MeV, the asymptotic D/S ratio parameter and D-wave probability, in %, of $J^{PC} = 1^{--}$ $c\bar{c}$ states including S-D mixture. We take the ground state of the original model, $M_{J/\psi} = 3096^\dagger$, as input.

		Renormalized scheme			Form factors scheme			Exp. data
State	n	$\mathcal{P}_{^3S_1}$ (%)	$\mathcal{P}_{^3D_1}$ (%)	M (MeV)	$\mathcal{P}_{^3S_1}$ (%)	$\mathcal{P}_{^3D_1}$ (%)	M (MeV)	M (MeV)
J/ψ	1	99.85	0.15	$3096^\dagger$	99.96	0.04	3096	3096.916 ± 0.011
$\psi(2S)$	2	99.78	0.22	3703	99.96	0.04	3703	3686.093 ± 0.034
$\psi(3770)$	3	0.15	99.85	3796	0.03	99.97	3796	3772.92 ± 0.35
$\psi(4040)$	4	99.55	0.45	4098	99.94	0.06	4097	4039.6 ± 4.3
$\psi(4150)$	5	0.39	99.61	4152	0.06	99.94	4153	4153 ± 3
$X(4360)$	6	99.24	0.76	4389	99.91	0.09	4389	$4361 \pm 9 \pm 9$
$\psi(4415)$	7	0.72	99.28	4426	0.09	99.91	4426	4421 ± 4
$X(4630)$	8	98.89	1.11	4614	99.88	0.12	4614	4634^{+8+5}_{-7-8}
$X(4660)$	9	1.08	98.92	4640	0.11	99.89	4641	$4664 \pm 11 \pm 5$

Table 3.32. Comparison of different properties of $J^{PC} = 1^{--}$ $c\bar{c}$ states between the renormalization scheme and the constituent quark model with form factors, considering coupled channels in both cases. The symbol † indicates that the state has been fixed.

3.7.3 Generalization of the renormalization procedure

Once we have presented the renormalization ideas applied to our potential model and we have studied the case of $J^{PC} = 1^{--}$ $c\bar{c}$ states, we extend the study to the whole spectrum of charmonium. For completeness, the bottomonium spectrum is also presented.

Not always we can apply the renormalization procedure. It depends on the character of the potential at short distances. The study of the solutions at the origin and the regularity conditions gives the free parameters of the regularized theory. We can find different cases:

- In the case of an uncoupled channel with a singular attractive potential, the renormalization procedure implies to fix an observable. On the contrary, if the potential is repulsive we do not have this freedom.
- In the case of a coupled channel, the number of free parameters depends on

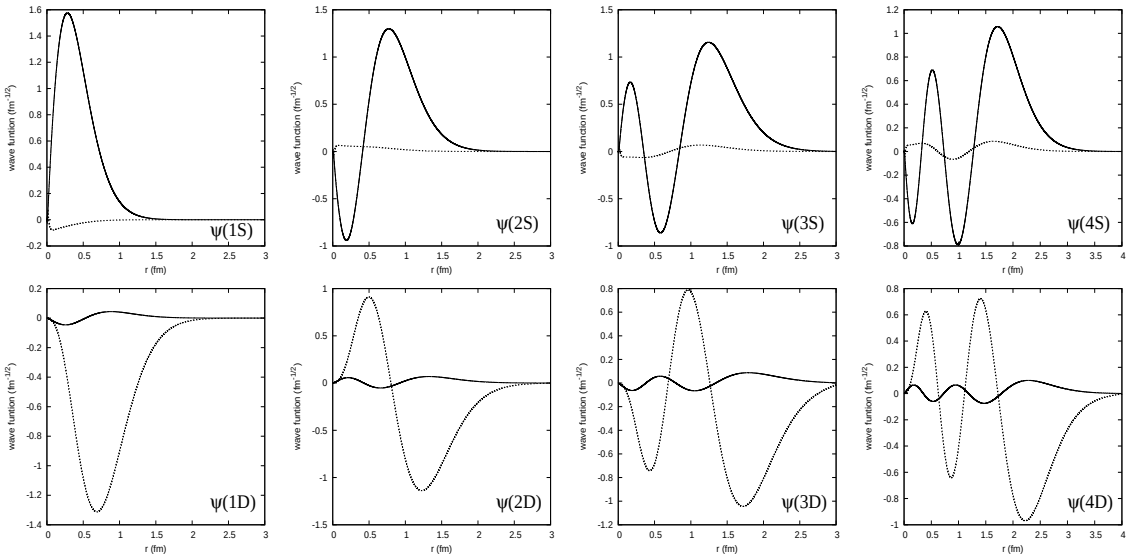

Figure 3.10. S and D-wave functions of the different states of the $J^{PC} = 1^{--}$ $c\bar{c}$ states calculated through the coupled renormalized model.

the values of the potential near the origin. Two attractive eigenvalues indicate the need to establish three observables, one attractive eigenvalue requires one parameter and finally, with two repulsive eigenvalues no parameter can be fix.

Focusing on the charmonium and bottomonium sectors, we continue working in the nonrelativistic framework. The dynamics of the system is given by the Schrödinger equation and the reduced one for every case can be written as

- Singlet channel ($S = 0$, $L = J$)

$$-u_n''(r) + \left[U_{J,J}^{0J}(r) + \frac{J(J+1)}{r^2}\right] u_n(r) = -\kappa^2 u_n(r), \tag{3.43}$$

- Triplet uncoupled channel ($S = 1$, $L = J$)

$$-u_n''(r) + \left[U_{J,J}^{1J}(r) + \frac{J(J+1)}{r^2}\right] u_n(r) = -\kappa^2 u_n(r), \tag{3.44}$$

- Triplet coupled channel ($S = 1$, $L = J \pm 1$)

$$\begin{aligned} -u_n''(r) + \left[U_{J-1,J-1}^{1J}(r) + \frac{(J-1)J}{r^2}\right] u_n(r) + U_{J-1,J+1}^{1J}(r) w_n(r) = -\kappa^2 u_n(r), \\ -w_n''(r) + U_{J+1,J-1}^{1J}(r) u_n(r) + \left[U_{J+1,J+1}^{1J}(r) + \frac{(J+1)(J+2)}{r^2}\right] w_n(r) = -\kappa^2 w_n(r). \end{aligned} \tag{3.45}$$

At short distances the dominant contributions of the potential are the tensor and

the spin-orbit terms of the OGE. These contributions when $r \to 0$ can be written as

$$\begin{aligned} V_{OGE}^{T}(r \to 0) &= \frac{1}{3}\frac{\alpha_s}{m^2}\frac{1}{r^3}\langle S_{12}\rangle\,, \\ V_{OGE}^{SO}(r \to 0) &= \frac{6}{3}\frac{\alpha_s}{m^2}\frac{1}{r^3}\langle \vec{L}\cdot\vec{S}\rangle\,. \end{aligned} \tag{3.46}$$

We need to know their character for the different cases:

- Singlet channel ($S = 0$, $L = J$). We have $\langle S_{12}\rangle = 0$ and $\langle \vec{L}\cdot\vec{S}\rangle = 0$ showing that the potential is regular and there is no observable free parameters. For the $^1S_0$ channel we must take into account that the potential has an attractive Dirac delta function and thus it is singular. In this case, we have to set an observable for a regularized solution.

- Triplet uncoupled channel ($S = 1$, $L = J$). We have $\langle S_{12}\rangle = +2$ and $\langle \vec{L}\cdot\vec{S}\rangle = -1$, thus the potential is singular attractive and an observable have to be fixed for a regularized solution.

- Triplet coupled channel ($S = 1$, $L = J\pm 1$). If we denote $L = J-1$ and $L' = J+1$, we will have

$$\begin{aligned} \langle {}^3L_J|S_{12}|{}^3L'_J\rangle &= \frac{6\sqrt{J(J+1)}}{2J+1}, \\ \langle {}^3L_J|S_{12}|{}^3L_J\rangle &= -\frac{2(J-1)}{2J+1}, \\ \langle {}^3L'_J|S_{12}|{}^3L'_J\rangle &= -\frac{2(J+2)}{2J+1}, \\ \langle {}^3L_J|\vec{L}\cdot\vec{S}|{}^3L_J\rangle &= J-1, \\ \langle {}^3L'_J|\vec{L}\cdot\vec{S}|{}^3L'_J\rangle &= -(J+2), \end{aligned} \tag{3.47}$$

  and diagonalizing the matrix of the potential we find the eigenvalues

$$E(J) = -10 \pm 6\sqrt{1+J+J^2} \tag{3.48}$$

  with $J \geq 1$. We always have one attractive and one repulsive eigenvalue and it requires one parameter.

Tables 3.33 and 3.34 shows the renormalized charmonium and bottomonium spectrum, respectively. We denote this calculation as RSC(1) and it is showed in column 5. For the channels in which the ground state can be fixed, we take the original value provided by the constituent quark model with form factors (CQM). Column 4 shows the masses predicted by CQM. The comparison between RSC(1) and CQM must be done taking the mass of the ground state predicted by the original model as a parameter, this is why we denote this calculation as RSC(1). RSC(2) in column 6 is the renormalized calculation where the experimental ground state is used when possible. The symbol † indicates that the mass of the ground state has been established as a parameter in RSC(1) and RSC(2). When the potential is regular or singular repulsive, we cannot fix the mass of the ground state and the symbol † does not appear.

Particle	J^{PC}	n	CQM (MeV)	RSC(1) (MeV)	RSC(2) (MeV)	Exp. [78] (MeV)
η_c	0^{-+}	1	2991	2991†	2980.3†	2980.3 ± 1.2
		2	3643	3640	3634	3637 ± 4
		3	4054	4050	4046	
χ_{c0}	0^{++}	1	3452	3452†	3414.75†	3414.75 ± 0.31
		2	3909	3910	3872	$3915 \pm 3 \pm 2$ [88]
		3	4242	4243	4209	
h_c	1^{+-}	1	3515	3516	3516	3525.42 ± 0.29
		2	3956	3957	3957	
		3	4278	4279	4279	
ψ	1^{--}	1	3096	3096†	3096.916†	3096.916 ± 0.011
		2	3703	3703	3704	3686.093 ± 0.034
		3	3796	3796	3796	3775.2 ± 1.7
		4	4097	4097	4098	4039 ± 1
		5	4153	4153	4152	4153 ± 3
		6	4389	4389	4390	$4361 \pm 9 \pm 9$ [86]
		7	4426	4426	4425	4421 ± 4
		8	4614	4614	4615	4634^{+8+5}_{-7-8} [87]
		9	4641	4641	4640	$4664 \pm 11 \pm 5$ [86]
χ_{c1}	1^{++}	1	3504	3504†	3510.66	3510.66 ± 0.07
		2	3947	3947	3955	
		3	4272	4272	4278	
η_{c2}	2^{-+}	1	3812	3812	3812	
		2	4166	4166	4166	
		3	4437	4437	4437	
χ_{c2}	2^{++}	1	3531	3531†	3556.20†	3556.20 ± 0.09
		2	3969	3968	3974	$3929 \pm 5 \pm 2$
		3	4043	4043	4043	
ψ_2	2^{--}	1	3810	3810†	3810†	
		2	4164	4164	4164	
		3	4436	4436	4436	

Table 3.33. Masses, in MeV, of charmonium states calculated within the constituent quark model with form factors (CQM), the renormalized quarkonium model where the ground states have been fixed to the values predicted by CQM (RSC(1)) and the renormalized quarkonium model where the ground states have been fixed to the experimental data (RSC(2)). The symbol † means that the ground state is a parameter in the renormalization scheme. We compare with the well established states in Ref. [78] and assign possible XYZ mesons.

The agreement between predicted masses in RSC(2) and the experimental data is good. The renormalization procedure allows to avoid unpleasant regulators that

Particle	J^{PC}	n	CQM (MeV)	RSC(1) (MeV)	RSC(2) (MeV)	Exp. [78] (MeV)
η_b	0^{-+}	1	9455	$9455^{\dagger}$	$9390.3^{\dagger}$	9390.9 ± 2.8
		2	9990	9989	9957	
		3	10330	10329	10306	
χ_{b0}	0^{++}	1	9855	$9855^{\dagger}$	$9859.44^{\dagger}$	$9859.44 \pm 0.42 \pm 0.31$
		2	10221	10221	10226	$10232.5 \pm 0.4 \pm 0.5$
		3	10500	10500	10505	
h_b	1^{+-}	1	9879	9879	9879	$9898.25 \pm 1.06^{+1.03}_{-1.07}$
		2	10240	10241	10241	$10259.76 \pm 0.64^{+1.43}_{-1.03}$
		3	10516	10516	10516	
Υ	1^{--}	1	9502	$9502^{\dagger}$	$9460.3^{\dagger}$	9460.30 ± 0.26
		2	10015	10015	9992	10023.26 ± 0.31
		3	10117	10117	10117	
		4	10349	10349	10331	10355.2 ± 0.5
		5	10414	10414	10414	
		6	10607	10607	10592	10579.4 ± 1.2
		7	10653	10653	10653	
		8	10818	10818	10805	10865 ± 8
		9	10853	10853	10853	
		10	10995	10995	10984	11019 ± 8
		11	11023	11023	11023	
χ_{b1}	1^{++}	1	9874	$9874^{\dagger}$	$9892.78^{\dagger}$	$9892.78 \pm 0.26 \pm 0.31$
		2	10236	10236	10254	$10255.46 \pm 0.22 \pm 0.50$
		3	10513	10513	10527	
η_{b2}	2^{-+}	1	10123	10123	10123	
		2	10419	10419	10419	
		3	10658	10658	10658	
χ_{b2}	2^{++}	1	9886	$9886^{\dagger}$	$9912.21^{\dagger}$	$9912.21 \pm 0.26 \pm 0.31$
		2	10246	10246	10248	$10268.65 \pm 0.22 \pm 0.50$
		3	10315	10315	10315	
Υ_2	2^{--}	1	10122	$10122^{\dagger}$	$10163.7^{\dagger}$	10163.7 ± 1.4
		2	10418	10418	10418	
		3	10657	10657	10657	

Table 3.34. Masses, in MeV, of bottomonium states calculated within the constituent quark model with form factors (CQM), the renormalized quarkonium model where the ground states have been fixed to the values predicted by CQM (RSC(1)) and the renormalized quarkonium model where the ground states have been fixed to the experimental data (RSC(2)). The symbol † means that the ground state is a parameter in the renormalization scheme. We compare with the well established states in Ref. [78].

State	$\Gamma_{\rm CQM}$	$\mathcal{B}_{\rm CQM}$	$\Gamma_{\rm Exp.}$	$\mathcal{B}_{\rm Exp.}$
$\eta_c(1S)$	22.23	7.77×10^{-4}	$6.7^{+0.9}_{-0.8}$	$(6.3 \pm 2.9) \times 10^{-5}$
$\eta_c(2S)$	17.95	1.28×10^{-3}	1.3 ± 0.6	$< 5 \times 10^{-4}$
$\eta_c(3S)$	16.98	-	-	-

Table 3.35. Annihilation rates of the η_c states into two photons, in keV, calculated with the constituent quark model with form factors (CQM).

triggers unwanted short-distance sensitivities. The only prize to pay is to treat the mass of the ground state, which is very well known experimentally, as a parameter. Indeed the use of regulators mainly hides the fact that the ground state is actually being used as an input rather than a prediction for the potential models.

Focusing on the CQM and RSC(1) calculations, one can see that the agreement is completely satisfactory. It provides confidence on the way the original model took into account the unknown short-distance dynamics.

3.7.4 Study of the $\eta_c \to \gamma\gamma$ decay

The $\eta_c(1S)$ was seen long time ago, but the $\eta_c(2S)$ is the subject of numerous experimental studies since it was observed in 2002 by the Belle Collaboration [25]. The $\gamma\gamma$-fusion to $K\bar{K}\pi$ final states is one of the most favorite reactions to find the $\eta_c(2S)$ state, there are data from BaBar [26], CLEO [27] and Belle [113]. This reaction allows to measure the 2γ decay width of the $\eta_c(2S)$. In fact, the PDG [78] reports $\Gamma_{\gamma\gamma}(\eta_c(1S)) = 6.7^{+0.9}_{-0.8}\,\text{keV}$ and $\Gamma_{\gamma\gamma}(\eta_c(2S)) = 1.3 \pm 0.6\,\text{keV}$ based mainly on the work published by the CLEO Collaboration [27]. The CLEO Collaboration have reported also the branching ratio

$$\mathcal{R} = \frac{\Gamma(\eta_c(2S) \to \gamma\gamma)}{\Gamma(\eta_c(1S) \to \gamma\gamma)} \frac{\mathcal{B}(\eta_c(2S) \to K_S K\pi)}{\mathcal{B}(\eta_c(1S) \to K_S K\pi)} = 0.18 \pm 0.05 \pm 0.02. \tag{3.49}$$

The OGE potential has a spin-spin contact hyperfine interaction which is proportional to a Dirac delta function. We have regularized it in a suitable way by replacing the Dirac delta function by a Yukawa form within the constituent quark model with form factors. This term allows us to determine the hyperfine splittings between the n^1S_0 and n^3S_1 states. They have been measured experimentally for the ground and the first excitation to be $m(J/\psi) - m(\eta_c(1S)) = 116.6 \pm 1.2\,\text{MeV}$ and $m(\psi(2S)) - m(\eta_c(2S)) = 49.1 \pm 4.0\,\text{MeV}$. We obtain reasonable values of 106 MeV and 60 MeV, respectively.

Despite of the good description of masses, we have seen that the two photon annihilation rates of the η_c states are in strongly disagreement with the experimental data when they are calculated with the constituent quark model with form factors, see Table 3.35. This is because the spin-spin interaction for the $^1S_0$ channel is attractive and to give a good description of the mass, we have reduced artificially the range of the wave function peaking up its value at the origin.

The calculation of the annihilation rates of the η_c states into 2γ within the renormalization scheme provides another opportunity to address the interesting issue

	CQM	RSC(1)	RSC(2)	Exp.
$\widetilde{\mathcal{R}}(2S) \times \widetilde{\mathcal{B}}$	0.15 ± 0.10	0.10 ± 0.07	0.10 ± 0.07	$0.18 \pm 0.05 \pm 0.02$
$\widetilde{\mathcal{R}}(3S)$	0.42	0.22	0.21	-

Table 3.36. The CLEO branching ratio calculated in the CQM with form factors (CQM) and in the renormalization scheme taking as an input the ground state mass predicted by CQM (RSC(1)) and its experimental value (RSC(2)). We give also the $\widetilde{\mathcal{R}}(3S)$ ratio, which provides a 2γ decay rate for the $\eta_c(3S)$.

State	$\mathcal{R}_{\rm CQM}$	$\mathcal{R}_{\rm RSC(1)}$	$\mathcal{R}_{\rm RSC(2)}$	$\mathcal{R}_{\rm Exp.}$
$\Upsilon(2S)$	0.52	0.5228	0.4850	0.457 ± 0.010
$\Upsilon(3S)$	0.38	0.3780	0.3426	0.331 ± 0.007
$\Upsilon(4S)$	0.30	0.2984	0.2670	0.203 ± 0.022
$\Upsilon(5S)$	0.25	0.2452	0.2174	0.231 ± 0.052
$\Upsilon(6S)$	0.21	0.2059	0.1814	0.097 ± 0.002

Table 3.37. The ratio $\mathcal{R}$ for 1^{--} S-wave $b\bar{b}$ states calculated within the CQM with form factors (CQM) and within the renormalization scheme taking as an input the ground state mass predicted by CQM (RSC(1)) and its experimental value (RSC(2)). The experimental data are taken from Ref. [78].

of the wave function renormalization. We may predict decay ratios as

$$\widetilde{\mathcal{R}} = \frac{\Gamma\left(n^1S_0 \to \gamma\gamma\right)}{\Gamma\left(1^1S_0 \to \gamma\gamma\right)} = \frac{|R_{nS}(0)|^2}{|R_{1S}(0)|^2}\frac{M_1^2}{M_n^2}, \tag{3.50}$$

where the two photon decay rate of a n^1S_0 state is given by Eq. (C.21) without the approximation $M_n \sim 2m_c$.

To compare our theoretical result with the branching ratio reported by CLEO, Eq. (3.49), we need the additional information

$$\widetilde{\mathcal{B}} = \frac{\mathcal{B}(\eta_c(2S) \to K_S K\pi)}{\mathcal{B}(\eta_c(1S) \to K_S K\pi)} = 0.27 \pm 0.18, \tag{3.51}$$

that has been taken from PDG [78]. Table 3.36 shows our theoretical result for the CLEO branching ratio calculated in the constituent quark model with form factors (CQM) and in the renormalization scheme taking as an input the ground state mass predicted by CQM (RSC(1)) and its experimental value (RSC(2)). We give also in the Table 3.36 the $\widetilde{\mathcal{R}}(3S)$ ratio, which provides a 2γ decay rate for the $\eta_c(3S)$ in the order of $(0.2 - 0.4) \times \Gamma_{\gamma\gamma}(\eta_c(1S))$.

We conclude that despite of our prediction of the absolute values for the two photon decay widths of $\eta_c(1S)$ and $\eta_c(2S)$ are in strong disagreement with the experimental data, the constituent quark model predicts a ratio between them in good agreement with the CLEO branching ratio. As the experimental errors are still large, the renormalization approach obtains also a reasonable ratio. In view of what we have for the masses and the ratios, we predict that in $\gamma\gamma$-fusion to $K\bar{K}\pi$ final states should be traces of the $\eta_c(3S)$ in the energy region of 4.05 GeV with a strength production $\Gamma_{\gamma\gamma}(\eta_c(3S)) = (0.2 - 0.4) \times \Gamma_{\gamma\gamma}(\eta_c(1S))$.

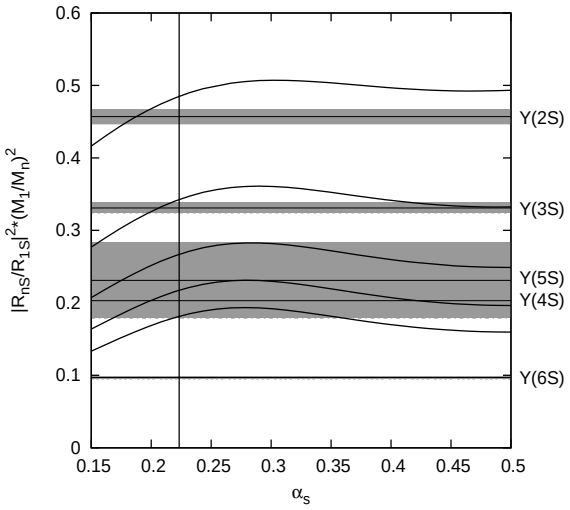

Figure 3.11. The dependence of the ratio $\mathcal{R}$ for the 1^{--} S-wave $b\bar{b}$ states on the strong coupling constant, α_s.

3.7.5 Study of the leptonic decay widths of S-wave Υ states

The renormalization approach can be applied to the calculation of the leptonic widths of 1^{--} S-wave states of bottomonium. As in the case of 1^{--} S-wave states of charmonium, we predict decay ratios, $\mathcal{R}$, given by Eq. (3.27) which means that a common wave function renormalization is implemented and factors out in the ratio.

We show our results for the ratio $\mathcal{R}$ in Table 3.37. Column 2 are the theoretical values calculated with the quark model with form factors (CQM) and columns 3 and 4 are the values calculated within the renormalization approach when the mass of the ground state is fixed to the CQM prediction (RSC(1)) and to the experimental value (RSC(2)), respectively.

One can see that we obtain similar results within the CQM and the RSC(1). Our values in these two schemes are in reasonable agreement with the experimental ones. However, RSC(2) improves the results, bringing them closer to the experimental values. In fact, the theoretical ratios, $\mathcal{R}$, for the $\Upsilon(2S)$ and $\Upsilon(3S)$ states are close to the experimental ones. For the $\Upsilon(4S)$ and $\Upsilon(5S)$ resonances we obtain a reasonable agreement between theory and experiment, note that the experimental pattern seems to change for these two states. In the case of the $\Upsilon(6S)$ resonance our value is higher than the experimental one. Remind that the open-bottom threshold, 10.56 GeV, is located just bellow the mass of the $\Upsilon(4S)$ state.

Figure. 3.11 shows the dependence of the ratio for the S-wave states along the range of strong coupling constant, α_s. The range is in percentage level equal than in the case of the 1^{--} S-wave charmonium states. The vertical line indicates our value for α_s in the bottomonium sector. We find a stronger dependence on the strong coupling constant as expected since the leptonic decay width is a short range observable.

Chapter 4

Strong decays of heavy mesons

Meson strong decay is a complex nonperturbative process that has not yet been described from first principles of QCD. This is a rather poorly understood area of hadronic physics and it is unfortunate because decay widths comprise a large portion of our knowledge of the strong interaction.

Several phenomenological models have been developed to deal with this topic, like the $^3P_0$ model [181–183], the flux-tube model [173, 184, 185], or microscopic models (see Refs. [34, 95, 186, 187]). The difference between the two approaches lies on the description of the $q\bar{q}$ creation vertex. While the $^3P_0$ and the flux-tube models assume that the $q\bar{q}$ pair is created from the vacuum, in the microscopic decay models the $q\bar{q}$ pair is created from the interquark interactions which determine the spectrum.

Focusing on the microscopic decay models presented in Refs. [34, 186] and [187], the main ingredients are the one-gluon exchange and the linear confinement. The difference between them lies in the Lorentz structure of the confinement, being vector for Refs. [34, 186] and scalar for Ref. [187]. Phenomenology suggests that confinement has to be dominantly scalar in order to reproduce the hyperfine splittings observed in Quarkonium, as seen in Sec 3.5. Strong decays may provide some information about the Lorentz structure.

Inspired on Refs. [34, 186, 187] we explore a microscopic decay model assuming that the interquark interactions which cause the strong decays are the contributions of our potential model, the one-gluon exchange and the screened linear confinement. We study the possible influence of the mixture of scalar and vector Lorentz structures in the confinement.

4.1 The $^3P_0$ decay model

The $^3P_0$ model was first proposed by Micu [181]. The meson decay process $A \to B + C$ is described by the $^3P_0$ model assuming that a quark-antiquark pair is created with vacuum quantum numbers, $J^{PC} = 0^{++}$. The strength γ of the decay interaction is regarded as a free constant and is fitted to the data.

Le Yaouanc *et al.* applied subsequently the $^3P_0$ model to meson [182] and baryon [183] open-flavor strong decays in a series of publications in the 1970s. They also evaluated strong decay partial widths of the three charmonium states $\psi(3770)$, $\psi(4040)$ and $\psi(4415)$ in the $^3P_0$ model [188, 189].

The $^3P_0$ model, which has since been applied extensively to the decays of light mesons and baryons, was originally adopted largely due to its success in the prediction

of the D/S amplitude ratio in the decay $b_1 \to \omega\pi$. Another success of the decay model is that it predicts a zero branching fraction $\mathcal{B}(\pi_2(1670) \to b_1\pi)$ and the experimental upper limit is $< 1.9 \times 10^{-3}$ at 97.7% confidence level. It would not be necessarily negligible in a different decay model or if final state interactions were important.

Recent variants of the $^3P_0$ model modify the pair production vertex [190] or modulate the spatial dependence of the pair-production amplitude to simulate a gluonic flux-tube [184]. The latter is the flux-tube decay model and gives very similar predictions to the $^3P_0$ one.

4.1.1 Transition operator

The interaction Hamiltonian involving Dirac quark fields that describes the production process is given by

$$H_I = \sqrt{3}\, g_s \int d^3x\, \bar{\psi}(\vec{x})\psi(\vec{x}), \tag{4.1}$$

where we have introduced for convenience the numerical factor $\sqrt{3}$, which will be canceled with the color factor. As in Ref. [187], we want to keep the relation of g_s with the dimensionless constant giving the strength of the quark-antiquark pair creation from the vacuum as $\gamma = g_s/2m$, being m the mass of the created quark (antiquark).

If we write the Dirac fields in second quantization as

$$\begin{aligned}
\psi(\vec{x}) &= \sum_{\nu} \int \frac{d^3p_\nu}{(2\pi)^{3/2}} \sqrt{\frac{m_\nu}{E_{\vec{p}_\nu}}} \left[a_\nu(\vec{p}_\nu) u_\nu(\vec{p}_\nu) e^{+i\vec{p}_\nu\cdot\vec{x}} + b^\dagger_\nu(\vec{p}_\nu) v_\nu(\vec{p}_\nu) e^{-i\vec{p}_\nu\cdot\vec{x}} \right], \\
\bar{\psi}(\vec{x}) &= \sum_{\mu} \int \frac{d^3p_\mu}{(2\pi)^{3/2}} \sqrt{\frac{m_\mu}{E_{\vec{p}_\mu}}} \left[b_\mu(\vec{p}_\mu) \bar{v}_\mu(\vec{p}_\mu) e^{+i\vec{p}_\mu\cdot\vec{x}} + a^\dagger_\mu(\vec{p}_\mu) \bar{u}_\mu(\vec{p}_\mu) e^{-i\vec{p}_\mu\cdot\vec{x}} \right],
\end{aligned} \tag{4.2}$$

where μ (ν) are the spin, flavor and color quantum numbers of the quark (antiquark), the interaction Hamiltonian is given by

$$\begin{aligned}
H_I =& \sqrt{3}\, g_s \sum_{\mu,\nu} \int d^3p_\mu d^3p_\nu \sqrt{\frac{m_\mu m_\nu}{E_{\vec{p}_\mu} E_{\vec{p}_\nu}}} \\
& \Big[+ b_\mu(\vec{p}_\mu) a_\nu(\vec{p}_\nu) \bar{v}_\mu(\vec{p}_\mu) u_\nu(\vec{p}_\nu) \delta^{(3)}(\vec{p}_\mu + \vec{p}_\nu) + b_\mu(\vec{p}_\mu) b^\dagger_\nu(\vec{p}_\nu) \bar{v}_\mu(\vec{p}_\mu) v_\nu(\vec{p}_\nu) \delta^{(3)}(\vec{p}_\mu - \vec{p}_\nu) \\
& + a^\dagger_\mu(\vec{p}_\mu) a_\nu(\vec{p}_\nu) \bar{u}_\mu(\vec{p}_\mu) u_\nu(\vec{p}_\nu) \delta^{(3)}(\vec{p}_\mu - \vec{p}_\nu) + a^\dagger_\mu(\vec{p}_\mu) b^\dagger_\nu(\vec{p}_\nu) \bar{u}_\mu(\vec{p}_\mu) v_\nu(\vec{p}_\nu) \delta^{(3)}(\vec{p}_\mu + \vec{p}_\nu) \Big],
\end{aligned} \tag{4.3}$$

where we have integrated in x to get the δ-functions. The only contribution of the interaction Hamiltonian which creates a $(\mu\nu)$ quark-antiquark pair is the fourth one. Therefore the transition operator can be written as

$$T = \sqrt{3}\, g_s \sum_{\mu,\nu} \int d^3p_\mu d^3p_\nu \sqrt{\frac{m_\mu m_\nu}{E_{\vec{p}_\mu} E_{\vec{p}_\nu}}} a^\dagger_\mu(\vec{p}_\mu) b^\dagger_\nu(\vec{p}_\nu) \bar{u}_\mu(\vec{p}_\mu) v_\nu(\vec{p}_\nu) \delta^{(3)}(\vec{p}_\mu + \vec{p}_\nu). \tag{4.4}$$

The nonrelativistic reduction of Eq. (4.4), see Appendix E, gives

$$T = -\sqrt{3} \sum_{\mu,\nu} \int d^3p_\mu d^3p_\nu \delta^{(3)}(\vec{p}_\mu + \vec{p}_\nu) \frac{g_s}{2m_\mu} \sqrt{2^5\pi} \left[\mathcal{Y}_1\left(\frac{\vec{p}_\mu - \vec{p}_\nu}{2} \right) \otimes \left(\frac{1}{2}\frac{1}{2} \right) 1 \right]_0 a^\dagger_\mu(\vec{p}_\mu) b^\dagger_\nu(\vec{p}_\nu), \tag{4.5}$$

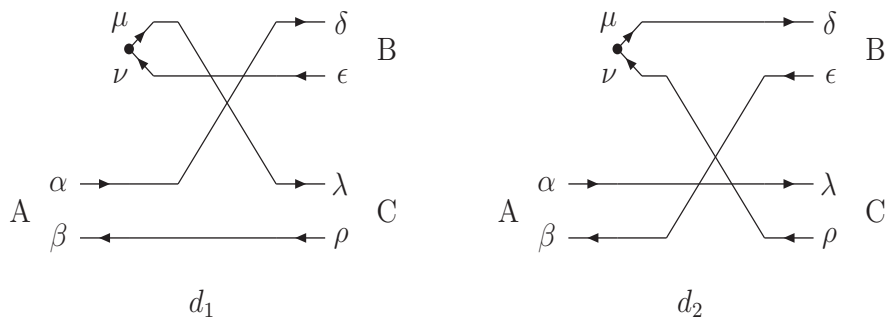

Figure 4.1. Diagrams that contribute to the decay width through the $^3P_0$ model.

where the spin of the quark and antiquark is coupled to one. The $\mathcal{Y}_{lm}(\vec{p}) = p^l Y_{lm}(\hat{p})$ is the solid harmonic defined in function of the spherical harmonic. The factor $\sqrt{2^5\pi}$ can be absorbed in the definition of $\gamma' = (g_s/2m_\mu)\sqrt{2^5\pi}$. The strength of the decay interaction is considered as a free parameter of the $^3P_0$ model which is ultimately fixed by the experimental data. Our final expression for the transition operator is

$$T = -\sqrt{3}\,\gamma' \sum_{\mu,\nu} \int d^3p_\mu d^3p_\nu \delta^{(3)}(\vec{p}_\mu + \vec{p}_\nu) \left[\mathcal{Y}_1\left(\frac{\vec{p}_\mu - \vec{p}_\nu}{2}\right) \otimes \left(\frac{1}{2}\frac{1}{2}\right) 1\right]_0 a^\dagger_\mu(\vec{p}_\mu) b^\dagger_\nu(\vec{p}_\nu). \tag{4.6}$$

4.1.2 Transition amplitude

We are interested on the transition amplitude for the reaction $(\alpha\beta)_A \to (\delta\epsilon)_B + (\lambda\rho)_C$. The meson A is formed by a quark α and antiquark β. At some point it is created a $(\mu\nu)$ quark-antiquark pair. The created $(\mu\nu)$ pair together with the $(\alpha\beta)$ pair in the original meson regroups in the two outgoing mesons via a quark rearrangement process. These final mesons are meson B which is formed by the quark-antiquark pair $(\delta\epsilon)$ and meson C with $(\lambda\rho)$ quark-antiquark pair.

We work in the center-of-mass reference system of meson A, thus we have $\vec{K}_A = \vec{K}_0 = 0$ with $\vec{K}_A$ and $\vec{K}_0$ the total momentum of meson A and of the system BC with respect to a given reference system. We can factorize the matrix element as follow

$$\langle BC|T|A\rangle = \delta^{(3)}(\vec{K}_0)\mathcal{M}_{A\to BC}. \tag{4.7}$$

The initial state in second quantization is

$$|A\rangle = \int d^3p_\alpha d^3p_\beta \delta^{(3)}(\vec{K}_A - \vec{P}_A)\phi_A(\vec{p}_A) a^\dagger_\alpha(\vec{p}_\alpha) b^\dagger_\beta(\vec{p}_\beta)\,|0\rangle\,, \tag{4.8}$$

where α (β) are the spin, flavor and color quantum numbers of the quark (antiquark). The wave function $\phi_A(\vec{p}_A)$ denotes a meson A in a color singlet with an isospin I_A with proyection M_{I_A}, a total angular momentum J_A with proyection M_A, J_A is the coupling of angular momentum L_A and spin S_A. The $\vec{p}_\alpha$ and $\vec{p}_\beta$ are the momentum of quark and antiquark, respectively. The $\vec{P}_A$ and $\vec{p}_A$ are the total and relative momentum of the

$(\alpha\beta)$ quark-antiquark pair within the meson A. The final state is more complicated than the initial one because it is a two-meson state. It can be written as

$$
\begin{aligned}
|BC\rangle =& \frac{1}{\sqrt{1+\delta_{BC}}} \int d^3K_B d^3K_C \sum_{m,M_{BC}} \langle J_{BC}M_{BC}lm|J_TM_T\rangle\, \delta^{(3)}(\vec{K}-\vec{K}_0)\delta(k-k_0) \\
& \frac{Y_{lm}(\hat{k})}{k} \sum_{M_B,M_C,M_{I_B},M_{I_C}} \langle J_BM_BJ_CM_C|J_{BC}M_{BC}\rangle\, \langle I_BM_{I_B}I_CM_{I_C}|I_AM_{I_A}\rangle \\
& \int d^3p_\delta d^3p_\epsilon d^3p_\lambda d^3p_\rho \delta^{(3)}(\vec{K}_B-\vec{P}_B)\delta^{(3)}(\vec{K}_C-\vec{P}_C) \\
& \phi_B(\vec{p}_B)\phi_C(\vec{p}_C)a^\dagger_\delta(\vec{p}_\delta)b^\dagger_\epsilon(\vec{p}_\epsilon)a^\dagger_\lambda(\vec{p}_\lambda)b^\dagger_\rho(\vec{p}_\rho)\,|0\rangle\,,
\end{aligned}
\tag{4.9}
$$

where we have followed the notation of meson A for the mesons B and C. We assume that the final state of mesons B and C is a spherical wave with angular momentum l. The relative and total momentum of mesons B and C are $\vec{k}_0$ and $\vec{K}_0$. The total spin J_{BC} is obtained coupling the total angular momentum of mesons B and C, and J_T is the coupling of J_{BC} and l.

The $^3P_0$ model takes into account only diagrams in which the $(\mu\nu)$ quark-antiquark pair separates into the different final mesons. This was originally motivated by the experiment and it is known as the Okubo-Zweig-Iizuka (OZI)-rule [191–193] which tells us that the disconnected diagrams are more suppressed than the connected ones. The diagrams that can contribute to the decay width through the $^3P_0$ model are shown in Fig. 4.1, we have two cases:

- Case in which $\alpha=\mu=\bar{\beta}$. The two diagrams, d_1 and d_2, contribute to the decay amplitude. The contribution of diagram d_1 is $M_{A\to BC}$ and the contribution from diagram d_2 can be calculated from the amplitude of the d_1 diagram changing meson B and C ($M_{A\to CB}$), so the total amplitude is given by

$$
\mathcal{M}_{A\to BC} = M_{A\to BC} + (-1)^{I_B+I_C-I_A+J_B+J_C-J_{BC}+l} M_{A\to CB}. \tag{4.10}
$$

- Other case. Only one of the two diagrams contribute to the amplitude

$$
\mathcal{M}_{A\to BC} = M_{A\to BC}. \tag{4.11}
$$

When the initial A meson has definite C-parity we have to use final states with definite C-parity. If $\mathcal{C}B = C$ the state has definite C-parity and the amplitude is given by the above rules. If $\mathcal{C}B \neq C$ then the appropriate C-parity combination has to be taken and this gives a factor $\sqrt{2}$ in the amplitude (or the amplitude cancels for the wrong C-parity, see Section E.5).

For illustration we build the result for diagram d_1. The amplitude $M_{A\to BC}$ is a product of a Fermi signature phase, a color factor, a flavor factor and a spin-space overlap integral

$$
M_{A\to BC} = \mathcal{I}_{\text{signature}} \times \mathcal{I}_{\text{color}} \times \mathcal{I}_{\text{flavor}} \times \mathcal{I}_{\text{spin-space}}. \tag{4.12}
$$

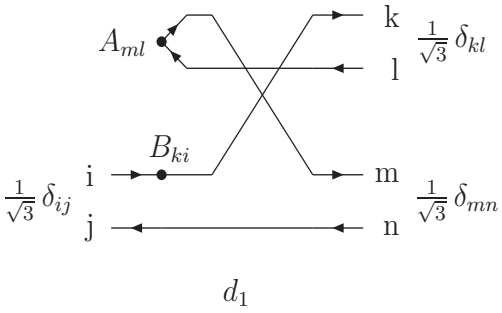

Figure 4.2. Color factor of diagram d_1.

Fermi signature phase, $\mathcal{I}_{\rm signature}$

The matrix element $\langle BC|T|A\rangle$ contains creation and destruction operators. The Fermi signature arises from the ordering of the quark and antiquark operators. It may be read off from the diagram as the number of line crossings, in the case of diagram d_1 we have

$$\mathcal{I}_{\rm signature} = (-1)^3 = -1. \tag{4.13}$$

Color factor, $\mathcal{I}_{\rm color}$

We show in Fig 4.2 the color wave functions for the initial and final mesons and the color operators. We have

$$\begin{aligned}
\mathcal{I}_{\rm color} &= \frac{1}{3^{\frac{3}{2}}}\sum_{i,j}\sum_{k,l}\sum_{m,n}\delta_{ij}\delta_{kl}\delta_{mn}\delta_{jn}A_{ml}B_{ki} \\
&= \frac{1}{3^{\frac{3}{2}}}\sum_{j,l,n}\delta_{jn}A_{nl}B_{lj} \\
&= \frac{1}{3^{\frac{3}{2}}}\sum_{l,n}A_{nl}B_{ln} \\
&= \frac{1}{3^{\frac{3}{2}}}Tr(AB),
\end{aligned} \tag{4.14}$$

where the operators are $A = I$ and $B = I$, and we arrive at

$$\mathcal{I}_{\rm color} = \frac{1}{\sqrt{3}}. \tag{4.15}$$

This factor is canceled with the numerical one that we have introduced *ad hoc* in Eq. (4.1).

Flavor factor, $\mathcal{I}_{\rm flavor}$

For the flavor sector we have

$$\mathcal{I}_{\rm flavor} = (-1)^{t_\alpha+t_\beta+I_A}\sqrt{(2I_B+1)(2I_C+1)}\begin{Bmatrix} t_\beta & I_C & t_\mu \\ I_B & t_\alpha & I_A \end{Bmatrix}, \tag{4.16}$$

where t_ξ is the isospin of a given quark or antiquark ξ. Note that the isospin operator in the creation vertex is $u\bar{u} + d\bar{d} + s\bar{s}$.

Spin-space overlap integral, $\mathcal{I}_{\rm spin-space}$

The spin-space overlap integral for the diagram d_1 reads as follow

$$\begin{aligned}\mathcal{I}_{\rm spin-space} = &-\sqrt{3}\,\gamma' \frac{1}{\sqrt{1+\delta_{BC}}} \int d^3K_B d^3K_C d^3p_\alpha d^3p_\beta d^3p_\mu d^3p_\nu \delta^{(3)}(\vec{K}-\vec{K}_0) \\ &\delta^{(3)}(\vec{K}_B-\vec{P}_B)\delta^{(3)}(\vec{K}_C-\vec{P}_C)\delta^{(3)}(\vec{p}_\mu+\vec{p}_\nu)\delta^{(3)}(\vec{P}_A)\frac{\delta(k-k_0)}{k} \\ &\langle\{[[\phi_B(\vec{p}_B)(s_\alpha s_\nu)S_B]\,J_B\,[\phi_C(\vec{p}_C)(s_\mu s_\beta)S_C]\,J_C]\,J_{BC}Y_l(\hat{k})\}\,J_T| \\ &\{[\phi_A(\vec{p}_A)(s_\alpha s_\beta)S_A]\,J_A\,[\mathcal{Y}_1\left(\frac{\vec{p}_\mu-\vec{p}_\nu}{2}\right)(s_\mu s_\nu)1]\,0\}\,J_A\rangle\,,\end{aligned} \tag{4.17}$$

where s_ξ is the spin of a given quark or antiquark ξ. One can decouple the spin and angular momentum terms through Eq. (E.8) such that the Eq. (4.17) can be written as

$$\mathcal{I}_{spin-space} = -\sqrt{3}\,\gamma' \frac{1}{\sqrt{1+\delta_{BC}}} \sum_{L_{BC},L,S} \mathcal{J}(A\to BC)\mathcal{E}(A\to BC), \tag{4.18}$$

where

$$\begin{aligned}\mathcal{J}(A\to BC) =&\delta_{J_TJ_A}\,(-1)^{L_A+J_A+J_{BC}+l+L+S_C}\sqrt{(2J_B+1)(2J_C+1)(2J_{BC}+1)(2L_{BC}+1)} \\ &\sqrt{(2S_A+1)(2S_B+1)(2S_C+1)}(2L+1)(2S+1)\begin{Bmatrix} S_A & L_A & J_A \\ L & S & 1\end{Bmatrix} \\ &\begin{Bmatrix} S & L_{BC} & J_{BC} \\ l & J_T & L\end{Bmatrix}\begin{Bmatrix} 1/2 & 1/2 & S_B \\ 1/2 & 1/2 & S_C \\ S_A & 1 & S\end{Bmatrix}\begin{Bmatrix} L_B & S_B & J_B \\ L_C & S_C & J_C \\ L_{BC} & S & J_{BC}\end{Bmatrix},\end{aligned}$$

$$\begin{aligned}\mathcal{E}(A\to BC) = &\int d^3K_B d^3K_C d^3p_\alpha d^3p_\beta d^3p_\mu d^3p_\nu \delta^{(3)}(\vec{K}-\vec{K}_0) \\ &\delta^{(3)}(\vec{K}_B-\vec{P}_B)\delta^{(3)}(\vec{K}_C-\vec{P}_C)\delta^{(3)}(\vec{p}_\mu+\vec{p}_\nu)\delta^{(3)}(\vec{P}_A)\frac{\delta(k-k_0)}{k} \\ &\langle\{[\phi_B(\vec{p}_B)\phi_C(\vec{p}_C)]\,L_{BC}Y_l(\hat{k})\}\,L|\,\{\phi_A(\vec{p}_A)\mathcal{Y}_1\left(\frac{\vec{p}_\mu-\vec{p}_\nu}{2}\right)\}\,L\rangle\,.\end{aligned} \tag{4.19}$$

The analytical expression for $\mathcal{E}(A\to BC)$ has been given in Ref. [194] when the radial wave function of the mesons involved in the reaction is expanded in terms of Gaussian basis functions. Details of the formalism following Ref. [194] can be found in Appendix E. We will calculate de different matrix elements that appear in the microscopic decay model in the same way.

4.2 The microscopic decay model

The microscopic decay models are an attempt to describe the strong decays in terms of quark and gluon degrees of freedom. They assume that the strong decays are driven

by the same interquark Hamiltonian which determines the spectrum.

However, there has been little previous work in this area. Two different examples are the study of open-charm decays of $c\bar{c}$ resonances by Eichten *et al.* in their original work [34, 95] and in its updated version [186], and the study of a few strong decays in the light sector by Ackleh *et al.* [187].

In Refs. [34, 95, 186] the pair production amplitude transforms as the time component of a Lorentz vector and it is given by the linear confining term of the potential model. The wave function of the charmonium states is the solution for the potential model while the wave function of the open-charm mesons is approximated by a Gaussian function. They performed a coupled channel calculation between $c\bar{c}$ and meson-meson sectors. The decay rates into some open-charm channels and the total decay width are given for $\psi(3770)$, $\psi(4040)$ and $\psi(4160)$ resonances.

Ackleh *et al.* in Ref. [187] assumes that the $q\bar{q}$ pair production is driven by the one-gluon exchange and the scalar linear confining interactions. Meson wave functions are those of a simple harmonic oscillator which allow them to obtain analytical expressions for the decay rates. They applied the model to the light quark sector.

Inspired in the last references, our microscopic decay model, which will be applied to the heavy quark sector, takes the one-gluon exchange and the confining potentials as the kernels of the interaction Hamiltonian that determines the strong decays. Our confinement is a screened linear potential with a mixture of scalar and vector Lorentz structures. The wave function of mesons are the solutions of the Schrödinger equation with the potential model using the Gaussian expansion method.

4.2.1 Transition operator

The one-gluon exchange and the confinement interactions are the only non zero contributions in our model. Their associated decay amplitudes are undoubtedly all present and should be added coherently. Therefore, the current-current interactions can be written in the generic form as [187]

$$H_I = \frac{1}{2}\int d^3x d^3y\, J^a(\vec{x}) K(|\vec{x}-\vec{y}|) J^a(\vec{y}). \tag{4.20}$$

The current J^a in Eq. (4.20) is assumed to be a color octet. The currents, J, with the color dependence $\lambda^a/2$ factored out and the kernels, $K(r)$, for the interactions are

- Currents

$$J(\vec{x}) = \bar{\psi}(\vec{x})\,\Gamma\,\psi(\vec{x}) = \begin{cases} \bar{\psi}(\vec{x})\,\mathcal{I}\,\psi(\vec{x}) & \text{Scalar Lorentz current,} \\ \bar{\psi}(\vec{x})\,\gamma^0\,\psi(\vec{x}) & \text{Static part of vector Lorentz current,} \\ \bar{\psi}(\vec{x})\,\vec{\gamma}\,\psi(\vec{x}) & \text{Spatial part of vector Lorentz current.} \end{cases} \tag{4.21}$$

- Kernels

$$K(r) = \begin{cases} -4a_s\left[-a_c(1-e^{-\mu_c r})+\Delta\right] & \text{Confining interaction,} \\ +\frac{\alpha_s}{r} & \text{Color Coulomb OGE,} \\ -\frac{\alpha_s}{r} & \text{Transverse OGE.} \end{cases} \tag{4.22}$$

For the Lorentz vector structure of the confinement we use

$$K(r) = \pm 4(1-a_s)\left[-a_c(1-e^{-\mu_c r})+\Delta\right], \tag{4.23}$$

where $\pm$ refers to static and transverse terms, respectively. Following Ref. [187], we refer to this general type of interaction as a JKJ decay model, and to the specific cases considered here as sKs, j^0Kj^0 and j^TKj^T interactions.

The interaction Hamiltonian in function of the Dirac quark fields in second quantization, see Eq. (4.2), is given by

$$\begin{aligned}
H_I =& \frac{1}{2}\int d^3x d^3y \\
& \left\{\left[\int \frac{d^3p_1}{(2\pi)^{3/2}}\sqrt{\frac{m_1}{E_{\vec{p}_1}}}\sum_{r_1}\left[b_{r_1}(\vec{p}_1)\bar{v}_{r_1}(\vec{p}_1)e^{+i\vec{p}_1\cdot\vec{x}}+a^\dagger_{r_1}(\vec{p}_1)\bar{u}_{r_1}(\vec{p}_1)e^{-i\vec{p}_1\cdot\vec{x}}\right]\right]\right. \\
& \left.\Gamma\left[\int \frac{d^3p_2}{(2\pi)^{3/2}}\sqrt{\frac{m_2}{E_{\vec{p}_2}}}\sum_{r_2}\left[a_{r_2}(\vec{p}_2)u_{r_2}(\vec{p}_2)e^{+i\vec{p}_2\cdot\vec{x}}+b^\dagger_{r_2}(\vec{p}_2)v_{r_2}(\vec{p}_2)e^{-i\vec{p}_2\cdot\vec{x}}\right]\right]\right\} \\
& K(|\vec{x}-\vec{y}|) \\
& \left\{\left[\int \frac{d^3p_3}{(2\pi)^{3/2}}\sqrt{\frac{m_3}{E_{\vec{p}_3}}}\sum_{r_3}\left[b_{r_3}(\vec{p}_3)\bar{v}_{r_3}(\vec{p}_3)e^{+i\vec{p}_3\cdot\vec{y}}+a^\dagger_{r_3}(\vec{p}_3)\bar{u}_{r_3}(\vec{p}_3)e^{-i\vec{p}_3\cdot\vec{y}}\right]\right]\right. \\
& \left.\Gamma\left[\int \frac{d^3p_4}{(2\pi)^{3/2}}\sqrt{\frac{m_4}{E_{\vec{p}_4}}}\sum_{r_4}\left[a_{r_4}(\vec{p}_4)u_{r_4}(\vec{p}_4)e^{+i\vec{p}_4\cdot\vec{y}}+b^\dagger_{r_4}(\vec{p}_4)v_{r_4}(\vec{p}_4)e^{-i\vec{p}_4\cdot\vec{y}}\right]\right]\right\}.
\end{aligned} \tag{4.24}$$

If one considers only the contributions in which a quark-antiquark pair is created, the interaction Hamiltonian reduces to the following transition operator

$$\begin{aligned}
T = & \int d^3x d^3y \,\frac{1}{2}\,K(|\vec{x}-\vec{y}|)\int \frac{d^3p_1 d^3p_2 d^3p_3 d^3p_4}{(2\pi)^6}\sqrt{\frac{m_1m_2m_3m_4}{E_{\vec{p}_1}E_{\vec{p}_2}E_{\vec{p}_3}E_{\vec{p}_4}}}\sum_{r_1}\sum_{r_2}\sum_{r_3}\sum_{r_4} \\
& \Big[+b_{r_1}(\vec{p}_1)b^\dagger_{r_2}(\vec{p}_2)a^\dagger_{r_3}(\vec{p}_3)b^\dagger_{r_4}(\vec{p}_4)\left[\bar{v}_{r_1}(\vec{p}_1)\Gamma v_{r_2}(\vec{p}_2)\right]\left[\bar{u}_{r_3}(\vec{p}_3)\Gamma v_{r_4}(\vec{p}_4)\right]e^{+i(\vec{p}_1-\vec{p}_2)\cdot\vec{x}}e^{-i(\vec{p}_3+\vec{p}_4)\cdot\vec{y}} \\
& + a^\dagger_{r_1}(\vec{p}_1)a_{r_2}(\vec{p}_2)a^\dagger_{r_3}(\vec{p}_3)b^\dagger_{r_4}(\vec{p}_4)\left[\bar{u}_{r_1}(\vec{p}_1)\Gamma u_{r_2}(\vec{p}_2)\right]\left[\bar{u}_{r_3}(\vec{p}_3)\Gamma v_{r_4}(\vec{p}_4)\right]e^{-i(\vec{p}_1-\vec{p}_2)\cdot\vec{x}}e^{-i(\vec{p}_3+\vec{p}_4)\cdot\vec{y}} \\
& + a^\dagger_{r_1}(\vec{p}_1)b^\dagger_{r_2}(\vec{p}_2)b_{r_3}(\vec{p}_3)b^\dagger_{r_4}(\vec{p}_4)\left[\bar{u}_{r_1}(\vec{p}_1)\Gamma v_{r_2}(\vec{p}_2)\right]\left[\bar{v}_{r_3}(\vec{p}_3)\Gamma v_{r_4}(\vec{p}_4)\right]e^{-i(\vec{p}_1+\vec{p}_2)\cdot\vec{x}}e^{+i(\vec{p}_3-\vec{p}_4)\cdot\vec{y}} \\
& + a^\dagger_{r_1}(\vec{p}_1)b^\dagger_{r_2}(\vec{p}_2)a^\dagger_{r_3}(\vec{p}_3)a_{r_4}(\vec{p}_4)\left[\bar{u}_{r_1}(\vec{p}_1)\Gamma v_{r_2}(\vec{p}_2)\right]\left[\bar{u}_{r_3}(\vec{p}_3)\Gamma u_{r_4}(\vec{p}_4)\right]e^{-i(\vec{p}_1+\vec{p}_2)\cdot\vec{x}}e^{-i(\vec{p}_3-\vec{p}_4)\cdot\vec{y}}\Big],
\end{aligned} \tag{4.25}$$

where the first term is equal to the third one. This can be seen exchanging the $\vec{x}$ and $\vec{y}$ variables in the first term and then, changing $1 \leftrightarrow 3$ and $2 \leftrightarrow 4$ particles taking into account the anti-commutation rules of the creation and destruction operators to arrive at the third term. This is possible because the kernel depends on $\vec{x}$ and $\vec{y}$ as $|\vec{x}-\vec{y}|$. The same occurs with the second and fourth terms. Therefore we have a factor two

and we can write the transition operator as

$$T = \int d^3x d^3y\, K(|\vec{x}-\vec{y}|) \int \frac{d^3p_1 d^3p_2 d^3p_3 d^3p_4}{(2\pi)^6} \sqrt{\frac{m_1 m_2 m_3 m_4}{E_{\vec{p}_1} E_{\vec{p}_2} E_{\vec{p}_3} E_{\vec{p}_4}}} \sum_{r_1,r_2,r_3,r_4}$$
$$\Big[+a^\dagger_{r_1}(\vec{p}_1) b^\dagger_{r_2}(\vec{p}_2) a^\dagger_{r_3}(\vec{p}_3) a_{r_4}(\vec{p}_4) \left[\bar{u}_{r_1}(\vec{p}_1)\Gamma v_{r_2}(\vec{p}_2)\right] \left[\bar{u}_{r_3}(\vec{p}_3)\Gamma u_{r_4}(\vec{p}_4)\right] e^{-i(\vec{p}_1+\vec{p}_2)\cdot\vec{x}} e^{-i(\vec{p}_3-\vec{p}_4)\cdot\vec{y}}$$
$$+a^\dagger_{r_1}(\vec{p}_1) b^\dagger_{r_2}(\vec{p}_2) b_{r_3}(\vec{p}_3) b^\dagger_{r_4}(\vec{p}_4) \left[\bar{u}_{r_1}(\vec{p}_1)\Gamma v_{r_2}(\vec{p}_2)\right] \left[\bar{v}_{r_3}(\vec{p}_3)\Gamma v_{r_4}(\vec{p}_4)\right] e^{-i(\vec{p}_1+\vec{p}_2)\cdot\vec{x}} e^{+i(\vec{p}_3-\vec{p}_4)\cdot\vec{y}} \Big] , \tag{4.26}$$

where the first and second terms refer to the $q\bar{q}$ pair creation from the quark line and from the antiquark line, respectively. The diagram representation of these two terms can be seen in Fig. 4.3, diagrams d_{1q} and $d_{1\bar{q}}$. For illustration we build the result from the diagram d_{1q}, the transition operator is

$$T = \int d^3x d^3y\, K(|\vec{x}-\vec{y}|) \int \frac{d^3p_1 d^3p_2 d^3p_3 d^3p_4}{(2\pi)^6} \sqrt{\frac{m_1 m_2 m_3 m_4}{E_{\vec{p}_1} E_{\vec{p}_2} E_{\vec{p}_3} E_{\vec{p}_4}}} \sum_{r_1,r_2,r_3,r_4}$$
$$\left[\, a^\dagger_{r_1}(\vec{p}_1) b^\dagger_{r_2}(\vec{p}_2) a^\dagger_{r_3}(\vec{p}_3) a_{r_4}(\vec{p}_4) \left[\bar{u}_{r_1}(\vec{p}_1)\Gamma v_{r_2}(\vec{p}_2)\right] \left[\bar{u}_{r_3}(\vec{p}_3)\Gamma u_{r_4}(\vec{p}_4)\right] e^{-i(\vec{p}_1+\vec{p}_2)\cdot\vec{x}} e^{-i(\vec{p}_3-\vec{p}_4)\cdot\vec{y}} \,\right] . \tag{4.27}$$

The calculation of the diagram $d_{1\bar{q}}$ can be followed from that of the diagram d_{1q}. If the initial meson is formed by a quark and an antiquark with equal masses, the contribution of both diagrams to the decay rate is the same and they contribute constructively.

Now we can integrate in $\vec{x}$ and $\vec{y}$

$$T = \int d^3p_1 d^3p_2 d^3p_3 d^3p_4\, K(|\vec{Q}|)\, \delta^{(3)}(\vec{p}_1+\vec{p}_2+\vec{p}_3-\vec{p}_4) \sqrt{\frac{m_1 m_2 m_3 m_4}{E_{\vec{p}_1} E_{\vec{p}_2} E_{\vec{p}_3} E_{\vec{p}_4}}}$$
$$\sum_{r_1,r_2,r_3,r_4} \left[a^\dagger_{r_1}(\vec{p}_1) b^\dagger_{r_2}(\vec{p}_2) a^\dagger_{r_3}(\vec{p}_3) a_{r_4}(\vec{p}_4) \left[\bar{u}_{r_1}(\vec{p}_1)\Gamma v_{r_2}(\vec{p}_2)\right] \left[\bar{u}_{r_3}(\vec{p}_3)\Gamma u_{r_4}(\vec{p}_4)\right] \right] , \tag{4.28}$$

where $\vec{Q} = \vec{p}_1 + \vec{p}_2 = \vec{p}_4 - \vec{p}_3$ is the momentum transferred, and the δ-function implies the momentum conservation.

4.2.2 Transition amplitude

We are interested on the transition amplitude for the reaction $(\alpha\beta)_A \to (\delta\epsilon)_B + (\lambda\rho)_C$. In the center-of-mass reference system of meson A one has $\vec{K}_A = \vec{K}_0 = 0$ and the matrix element factorizes as follow

$$\langle BC|T|A\rangle = \delta^{(3)}(\vec{K}_0)\mathcal{M}_{A\to BC}, \tag{4.29}$$

where the initial and final states are defined in Eqs. (4.8) and (4.9).

The diagrams that contribute to the reaction and are allowed by the transition operator are shown in Fig. 4.3. Two of them are coming from the quark line, d_{1q} and d_{2q}, and take into account the different rearrangement of the quarks and antiquarks in the final mesons. The other two diagrams are referred to the antiquark line, $d_{1\bar{q}}$ and $d_{2\bar{q}}$. As in the case of the $^3P_0$ model, we have different cases:

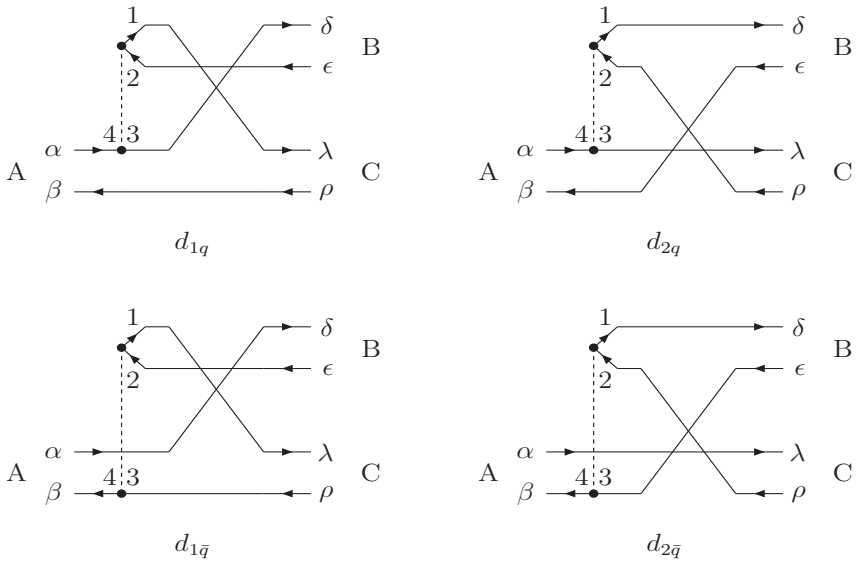

Figure 4.3. Diagrams that contribute to the decay width through the microscopic model.

- Case in which $\alpha = \mu = \bar{\beta}$. The two diagrams, d_{1q} and d_{2q}, contribute to the decay amplitude. The contribution of diagram d_{1q} is $M_{A\to BC}$ and the contribution from diagram d_{2q} can be calculated from the amplitude of the d_{1q} diagram changing meson B and C ($M_{A\to CB}$), so the total amplitude is given by

$$\mathcal{M}_{A\to BC} = M_{A\to BC} + (-1)^{I_B+I_C-I_A+J_B+J_C-J_{BC}+l} M_{A\to CB}. \tag{4.30}$$

- Other case. Only one of the two diagrams contribute to the amplitude

$$\mathcal{M}_{A\to BC} = M_{A\to BC}. \tag{4.31}$$

If the quark and antiquark in the original meson are the same then the contribution of diagram d_{1q} (d_{2q}) is equal to the diagram $d_{1\bar{q}}$ ($d_{2\bar{q}}$) and both contribute constructively. In other case they have to be calculated separately.

When the initial A meson has definite C-parity one has to take it into account in the same way as already mentioned in the $^3P_0$ model.

For illustration we build the result from the diagram d_{1q} ($M_{A\to BC}$). The amplitude is a product of a Fermi signature phase, a color factor, a flavor factor and a spin-space overlap integral

$$M_{A\to BC} = \mathcal{I}_{\text{signature}} \times \mathcal{I}_{\text{color}} \times \mathcal{I}_{\text{flavor}} \times \mathcal{I}_{\text{spin-space}}. \tag{4.32}$$

Fermi signature phase, $\mathcal{I}_{\text{signature}}$

The Fermi signature can be read off from the diagram as the number of line crossings because it arises from the ordering of the quark and antiquark operators. In the case of d_{1q} diagram we have

$$I_{\text{signature}} = (-1)^3 = -1. \tag{4.33}$$

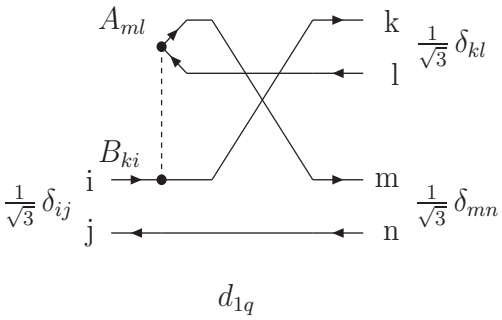

Figure 4.4. Color factor of diagram d_{1q}.

Color factor, $\mathcal{I}_{\text{color}}$

Fig 4.4 shows the color wave functions for the initial and final mesons and the color operators which appear in the vertex. We have

$$\begin{aligned}\mathcal{I}_{\text{color}} &= \frac{1}{3^{\frac{3}{2}}}\sum_{i,j}\sum_{k,l}\sum_{m,n}\delta_{ij}\delta_{kl}\delta_{mn}\delta_{jn}A_{ml}B_{ki} \\ &= \frac{1}{3^{\frac{3}{2}}}\sum_{j,l,n}\delta_{jn}A_{nl}B_{lj} \\ &= \frac{1}{3^{\frac{3}{2}}}\sum_{l,n}A_{nl}B_{ln} \\ &= \frac{1}{3^{\frac{3}{2}}}Tr(AB),\end{aligned} \tag{4.34}$$

where the operators are $A = B = \frac{\lambda^a}{2}$ with a sum over the color index, a, and we arrive at

$$\mathcal{I}_{\text{color}} = +\frac{2^2}{3^{\frac{3}{2}}}. \tag{4.35}$$

Flavor factor, $\mathcal{I}_{\text{flavor}}$

The isospin operator for this decay mechanism is the same as in the $^3P_0$ model, therefore the flavor factor is

$$\mathcal{I}_{\text{flavor}} = (-1)^{t_\alpha+t_\beta+I_A}\sqrt{(2I_B+1)(2I_C+1)}\begin{Bmatrix} t_\beta & I_C & t_\mu \\ I_B & t_\alpha & I_A \end{Bmatrix}, \tag{4.36}$$

where t_ξ is the isospin of a given quark or antiquark ξ.

Spin-space overlap integral, $\mathcal{I}_{\rm spin-space}$

The spin-space overlap integral for the diagram d_{1q}: $1 \leftrightarrow \mu$, $2 \leftrightarrow \nu$, $3 \leftrightarrow \delta'$ and $4 \leftrightarrow \alpha'$, reads as follow

$$\begin{aligned}
\mathcal{I}_{\rm spin-space} =& \frac{1}{\sqrt{1+\delta_{BC}}} \sum_{m,M_{BC},M_B,M_C} \langle J_{BC}M_{BC}lm|J_TM_T\rangle \langle J_BM_BJ_CM_C|J_{BC}M_{BC}\rangle \\
& \int d^3K_B d^3K_C d^3p_\delta d^3p_\epsilon d^3p_\lambda d^3p_\rho d^3p_\mu d^3p_\nu d^3p_{\delta'} d^3p_{\alpha'} d^3p_\alpha d^3p_\beta \sqrt{\frac{m_\mu m_\nu m_{\delta'} m_{\alpha'}}{E_{\vec{p}_\mu} E_{\vec{p}_\nu} E_{\vec{p}_{\delta'}} E_{\vec{p}_{\alpha'}}}} \\
& \delta^{(3)}(\vec{K}-\vec{K}_0)\delta(k-k_0)\delta^{(3)}(\vec{K}_B-\vec{P}_B)\delta^{(3)}(\vec{K}_C-\vec{P}_C)\delta^{(3)}(\vec{P}_A)\frac{Y_{lm}(\hat{k})}{k} \\
& \phi_B(\vec{p}_B)\phi_C(\vec{p}_C)\phi_A(\vec{p}_A)\, K(|\vec{p}_\mu+\vec{p}_\nu|)\delta^{(3)}(\vec{p}_\mu+\vec{p}_\nu+\vec{p}_{\delta'}-\vec{p}_{\alpha'}) \\
& \sum_{\alpha',\delta',\mu,\nu} \delta_{\alpha'\alpha}\delta^{(3)}(\vec{p}_{\alpha'}-\vec{p}_\alpha)\delta_{\delta\delta'}\delta^{(3)}(\vec{p}_\delta-\vec{p}_{\delta'})\delta_{\epsilon\nu}\delta^{(3)}(\vec{p}_\epsilon-\vec{p}_\nu)\delta_{\lambda\mu}\delta^{(3)}(\vec{p}_\lambda-\vec{p}_\mu) \\
& \delta_{\rho\beta}\delta^{(3)}(\vec{p}_\rho-\vec{p}_\beta)\,[\bar{u}_\mu(\vec{p}_\mu)\Gamma v_\nu(\vec{p}_\nu)]\,[\bar{u}_{\delta'}(\vec{p}_{\delta'})\Gamma u_{\alpha'}(\vec{p}_{\alpha'})]\,.
\end{aligned} \tag{4.37}$$

Now using some δ-functions in momentum and spin of quarks (antiquarks) we can simplify the above expression

$$\begin{aligned}
\mathcal{I}_{\rm spin-space} =& \frac{1}{\sqrt{1+\delta_{BC}}} \sum_{m,M_{BC},M_B,M_C} \langle J_{BC}M_{BC}lm|J_TM_T\rangle \langle J_BM_BJ_CM_C|J_{BC}M_{BC}\rangle \\
& \int d^3K_B d^3K_C d^3p_\delta d^3p_\rho d^3p_\mu d^3p_\nu d^3p_\alpha d^3p_\beta \sqrt{\frac{m_\mu m_\nu m_\delta m_\alpha}{E_{\vec{p}_\mu} E_{\vec{p}_\nu} E_{\vec{p}_\delta} E_{\vec{p}_\alpha}}} \\
& \delta^{(3)}(\vec{K}-\vec{K}_0)\delta(k-k_0)\delta^{(3)}(\vec{K}_B-\vec{P}_B)\delta^{(3)}(\vec{K}_C-\vec{P}_C)\delta^{(3)}(\vec{P}_A)\frac{Y_{lm}(\hat{k})}{k} \\
& \phi_B(\vec{p}_B)\phi_C(\vec{p}_C)\phi_A(\vec{p}_A)\, K(|\vec{p}_\mu+\vec{p}_\nu|)\delta^{(3)}(\vec{p}_\delta-(\vec{p}_\alpha-\vec{p}_\mu-\vec{p}_\nu)) \\
& \delta_{\rho\beta}\delta^{(3)}(\vec{p}_\rho-\vec{p}_\beta)\,[\bar{u}_\mu(\vec{p}_\mu)\Gamma v_\nu(\vec{p}_\nu)]\,[\bar{u}_\delta(\vec{p}_\delta)\Gamma u_\alpha(\vec{p}_\alpha)]\,.
\end{aligned} \tag{4.38}$$

The nonrelativistic reduction of Eq. (4.38) without specifying the JKJ decay model is

$$\begin{aligned}
\mathcal{I}_{\rm spin-space} =& \frac{1}{\sqrt{1+\delta_{BC}}} \sum_{m,M_{BC},M_B,M_C} \langle J_{BC}M_{BC}lm|J_TM_T\rangle \langle J_BM_BJ_CM_C|J_{BC}M_{BC}\rangle \\
& \int d^3K_B d^3K_C d^3p_\delta d^3p_\rho d^3p_\mu d^3p_\nu d^3p_\alpha d^3p_\beta\, \delta^{(3)}(\vec{K}-\vec{K}_0)\delta(k-k_0)\frac{Y_{lm}(\hat{k})}{k} \\
& \delta^{(3)}(\vec{K}_B-\vec{P}_B)\delta^{(3)}(\vec{K}_C-\vec{P}_C)\delta^{(3)}(\vec{P}_A)\phi_B(\vec{p}_B)\phi_C(\vec{p}_C)\phi_A(\vec{p}_A) \\
& K(|\vec{p}_\mu+\vec{p}_\nu|)\delta^{(3)}(\vec{p}_\delta-(\vec{p}_\alpha-\vec{p}_\mu-\vec{p}_\nu))\delta_{\rho\beta}\delta^{(3)}(\vec{p}_\rho-\vec{p}_\beta) \\
& \lim_{v/c\to 0}[\bar{u}_\mu(\vec{p}_\mu)\Gamma v_\nu(\vec{p}_\nu)] \lim_{v/c\to 0}[\bar{u}_\delta(\vec{p}_\delta)\Gamma u_\alpha(\vec{p}_\alpha)]\,.
\end{aligned} \tag{4.39}$$

Then, the expression for the different contributions are

- The sKs decay model

$$\begin{aligned}\mathcal{I}^{\rm sKs}_{\rm spin-space} =& \frac{-1}{\sqrt{1+\delta_{BC}}}\frac{1}{2m_\nu}\sqrt{2^5\pi}\int d^3K_B d^3K_C d^3p_\alpha d^3p_\beta d^3p_\mu d^3p_\nu d^3p_\delta \\ & \delta^{(3)}(\vec{K}-\vec{K}_0)\delta^{(3)}(\vec{K}_B-\vec{P}_B)\delta^{(3)}(\vec{K}_C-\vec{P}_C)\delta^{(3)}(\vec{P}_A)\frac{\delta(k-k_0)}{k} \\ & \delta^{(3)}\left(\vec{p}_\delta-(\vec{p}_\alpha-\vec{p}_\mu-\vec{p}_\nu)\right)K(|\vec{p}_\mu+\vec{p}_\nu|) \\ & \left\langle\left[[[\phi_B(\vec{p}_B)(s_\alpha s_\nu)S_B]\,J_B\,[\phi_C(\vec{p}_C)(s_\mu s_\beta)S_C]\,J_C]\,J_{BC}Y_l(\hat{k})\right]\,J_T\right| \\ & \left|\left[[\phi_A(\vec{p}_A)(s_\alpha s_\beta)S_A]\,J_A\left[\mathcal{Y}_1\left(\frac{\vec{p}_\mu-\vec{p}_\nu}{2}\right)(s_\mu s_\nu)1\right]0\right]\,J_A\right\rangle .\end{aligned} \tag{4.40}$$

- The j^0Kj^0 decay model

$$\begin{aligned}\mathcal{I}^{\rm j^0Kj^0}_{\rm spin-space} =& \frac{1}{\sqrt{1+\delta_{BC}}}\frac{1}{2m_\nu}\sqrt{2^3\pi}\int d^3K_B d^3K_C d^3p_\alpha d^3p_\beta d^3p_\mu d^3p_\nu d^3p_\delta \\ & \delta^{(3)}(\vec{K}-\vec{K}_0)\delta^{(3)}(\vec{K}_B-\vec{P}_B)\delta^{(3)}(\vec{K}_C-\vec{P}_C)\delta^{(3)}(\vec{P}_A)\frac{\delta(k-k_0)}{k} \\ & \delta^{(3)}\left(\vec{p}_\delta-(\vec{p}_\alpha-\vec{p}_\mu-\vec{p}_\nu)\right)K(|\vec{p}_\mu+\vec{p}_\nu|) \\ & \left\langle\left[[[\phi_B(\vec{p}_B)(s_\alpha s_\nu)S_B]\,J_B\,[\phi_C(\vec{p}_C)(s_\mu s_\beta)S_C]\,J_C]\,J_{BC}Y_l(\hat{k})\right]\,J_T\right| \\ & \left|\left[[\phi_A(\vec{p}_A)(s_\alpha s_\beta)S_A]\,J_A\,[\mathcal{Y}_1\left(\vec{p}_\mu+\vec{p}_\nu\right)(s_\mu s_\nu)1]\,0]\,J_A\right\rangle .\end{aligned} \tag{4.41}$$

- The j^TKj^T decay model

$$\begin{aligned}\mathcal{I}^{\rm j^TKj^T}_{\rm spin-space} =& \frac{1}{\sqrt{1+\delta_{BC}}}\sum_{m,M_{BC},M_B,M_C}\langle J_{BC}M_{BC}lm|J_TM_T\rangle\,\langle J_BM_BJ_CM_C|J_{BC}M_{BC}\rangle \\ & \int d^3K_B d^3K_C d^3p_\delta d^3p_\rho d^3p_\mu d^3p_\nu d^3p_\alpha d^3p_\beta\,\delta^{(3)}(\vec{K}-\vec{K}_0)\delta(k-k_0)\frac{Y_{lm}(\hat{k})}{k} \\ & \delta^{(3)}(\vec{K}_B-\vec{P}_B)\delta^{(3)}(\vec{K}_C-\vec{P}_C)\delta^{(3)}(\vec{P}_A)\phi_B(\vec{p}_B)\phi_C(\vec{p}_C)\phi_A(\vec{p}_A) \\ & K(|\vec{p}_\mu+\vec{p}_\nu|)\delta^{(3)}(\vec{p}_\delta-(\vec{p}_\alpha-\vec{p}_\mu-\vec{p}_\nu))\delta_{\rho\beta}\delta^{(3)}(\vec{p}_\rho-\vec{p}_\beta) \\ & \lim_{v/c\to 0}\left[\bar{u}_\mu(\vec{p}_\mu)\gamma^i v_\nu(\vec{p}_\nu)\right]\left(\delta_{ij}-\frac{Q_iQ_j}{\vec{Q}^2}\right)\lim_{v/c\to 0}\left[\bar{u}_\delta(\vec{p}_\delta)\gamma^j u_\alpha(\vec{p}_\alpha)\right] .\end{aligned} \tag{4.42}$$

The procedure followed, according to Ref. [194], to solve the above spin-space overlap integrals is given in Appendix E.

4.3 Decay width

The total width is the sum over the partial widths characterized by the quantum numbers J_{BC} and l

$$\Gamma_{A\to BC} = \sum_{J_{BC},l}\Gamma_{A\to BC}(J_{BC},l), \tag{4.43}$$

where

$$\Gamma_{A\to BC}(J_{BC},l) = 2\pi \int dk_0 \delta(E_A - E_{BC})|\mathcal{M}_{A\to BC}(k_0)|^2. \tag{4.44}$$

We use relativistic phase space, so

$$\Gamma_{A\to BC}(J_{BC},l) = 2\pi \frac{E_B(k_0)E_C(k_0)}{m_A k_0}|\mathcal{M}_{A\to BC}(k_0)|^2, \tag{4.45}$$

where

$$k_0 = \frac{\sqrt{[m_A^2 - (m_B - m_C)^2][m_A^2 - (m_B + m_C)^2]}}{2m_A}, \tag{4.46}$$

is the on-shell relative momentum of mesons B and C.

The above formula is only valid for mesons B and C with small widths. If we consider the process $A \to B + C$ with the subsequent decay of the meson B into two mesons B_1 and B_2 we must take into account the width of the daughter meson, B, by replacing the Dirac δ-function in Eq. (4.44).

Following the formalism of Ref. [195], one may regard the δ-function as arising from the narrow-width limit of the energy denominator

$$\frac{1}{E_A - E_{BC} - i\epsilon} = \mathcal{P}\frac{1}{E_A - E_{BC}} + i\pi\delta(E_A - E_{BC}), \tag{4.47}$$

where ϵ is related to the total width of the unstable final state. For daughter mesons that are broad, the energy denominator becomes

$$\frac{1}{E_A - E_{BC} - i\frac{\Gamma_B}{2}} = \frac{E_A - E_{BC} + i\frac{\Gamma_B}{2}}{(E_A - E_{BC})^2 + \frac{\Gamma_B^2}{4}}, \tag{4.48}$$

implying the replacement

$$\delta(E_A - E_{BC}) \to \frac{\Gamma_B}{2\pi\left[(E_A - E_{BC})^2 + \frac{\Gamma_B^2}{4}\right]}. \tag{4.49}$$

The decay rate for $A \to (B_1B_2)_B + C$ then generalizes to [184]

$$\Gamma_{A\to(B_1B_2)_BC}(J_{BC},l) = \int_0^{k_{\max}} dk\, \frac{|\mathcal{M}_{A\to BC}(k)|^2\, \Gamma_{B\to B_1B_2}(k)}{(E_A - E_{BC})^2 + \frac{\Gamma_B^2}{4}}, \tag{4.50}$$

where $\Gamma_{B\to B_1B_2}(k)$ is the energy-dependent partial width of the unstable daughter meson.

The variable of integration in the expression above is k, the modulus of the three-momentum of the daughter meson B. In the rest frame of A, this ranges from $k = 0$ (B_1 and B_2 back to back, with $\vec{k}_1 = -\vec{k}_2$) to $k_{\max}$ (B_1 and B_2 collinear). These limits correspond, respectively, to $m_B(k = 0) = m_A - m_C$ and $m_B(k = k_{\max}) = m_{B_1} + m_{B_2}$, where $m_B(k)$ is the momentum dependent effective mass of the daughter meson B, so

$$k_{\max} = \frac{\sqrt{[m_A^2 - (m_{B_1} + m_{B_2} + m_C)^2]\,[m_A^2 - (m_{B_1} + m_{B_2} - m_C)^2]}}{2m_A}. \tag{4.51}$$

4.4 Running of the $^3P_0$ γ strength

The $^3P_0$ model has been extensively applied to meson and baryon strong decays with considerable success (see Ref. [196] for recent summaries of the $^3P_0$ model). An important characteristic, apart from its simplicity, is that the model provides the gross features of various transitions with only one parameter, the strength γ of the decay interaction, which is regarded as a free constant and is fitted to the data.

It is generally believed that the pair-production strength parameter, γ, is roughly flavor-independent for decays involving production of $u\bar{u}$, $d\bar{d}$ and $s\bar{s}$ pairs. A total of 32 experimentally well-determined decay rates have been fitted in Ref. [197] using the $^3P_0$ model, the large experimental errors preclude definitive conclusions about the dependence of γ with respect the flavor sector. The authors follow the convention of using a unique value for the γ parameter. However, it is important to note that only 3 of the total 32 decay modes are referred to the heavy quark sector. They are $D^{*+} \to D^0\pi^+$, $\psi(3770) \to D\bar{D}$ and $D^*_{s2} \to DK + D^*K + D_s\eta$. There are no data about the bottomonium sector and the remaining 29 decay modes involve light and strange mesons.

We have seen in a previous section an equivalent formulation of the $^3P_0$ model given by an interaction Hamiltonian involving Dirac quark fields, Eq. (4.1). This presents a coupling constant, g_s, which is related with the pair-production strength parameter, γ, as $\gamma = g_s/2m$, being m the mass of the created quark (antiquark). If g_s is related to fundamental QCD parameters, among them the strong coupling constant, one expects that g_s, and hence γ, depends on the scale.

Our purpose here is to calculate through the $^3P_0$ model the total strong decay widths of the mesons which belong to charmed, charmed-strange, hidden charm and hidden bottom sectors. Certainly, the theoretical results suffer from uncertainties coming from the decay model itself in the description of the creation vertex and from the wave functions used. Therefore, we expect to reach a global description of the meson strong decays in every quark sector, but the details of each decay mode could fail. Our main goal is to perform a global fit of the experimental data that elucidates the γ dependence on the scale.

To perform the overall fit of the decay widths, not all of the experimental data are equally reliable. Table 4.1 shows the experimental data taken for the fit. In the case of the charmed and charmed-strange mesons we have considered the total decay widths of the mesons which belong to the $j^P_q = 3/2^+$ doublet, mainly that of the member of the doublet whose quantum numbers are $J^P = 2^+$. This is because any quark model predicts the doublet $j^P_q = \frac{3}{2}^+$ in reasonably agreement with the experiment. Focusing on the 2^+ meson there are no doubts about its nature and wave function composition. Moreover, in the infinite heavy quark mass limit these states are narrow, and so we expect that their resonance parameters are better determined than other states of the same sector. For the charmonium and bottomonium sectors, we have considered that the best experimental measurements of strong decay widths are those of the states immediately above the open-flavor threshold. This means the total decay width of the $\psi(3770)$ resonance in the charmonium sector and the $\Upsilon(4S)$ resonance in the bottomonium sector.

Once the experimental data have been established, we propose a scale-dependent

Meson	I	J	P	C	Mass (MeV)	$\Gamma_{\text{Exp.}}$ (MeV)	
$D_1(2420)^{\pm}$	1/2	1	+1	-	2423.4 ± 3.1	25 ± 6	[78]
$D_2^*(2460)^{\pm}$	1/2	2	+1	-	2460.1 ± 4.4	37 ± 6	[78]
$D_{s1}(2536)^{\pm}$	0	1	+1	-	2535.12 ± 0.25	1.03 ± 0.13	[198]
$D_{s2}^*(2575)^{\pm}$	0	2	+1	-	2572.6 ± 0.9	20 ± 5	[78]
$\psi(3770)$	0	1	-1	-1	3775.2 ± 1.7	27.6 ± 1.0	[78]
$\Upsilon(4S)$	0	1	-1	-1	10579.4 ± 1.2	20.5 ± 2.5	[78]

Table 4.1. Meson decay widths which have been taken into account in the fit of the scale-dependent strength, γ. Some properties of these mesons are also shown.

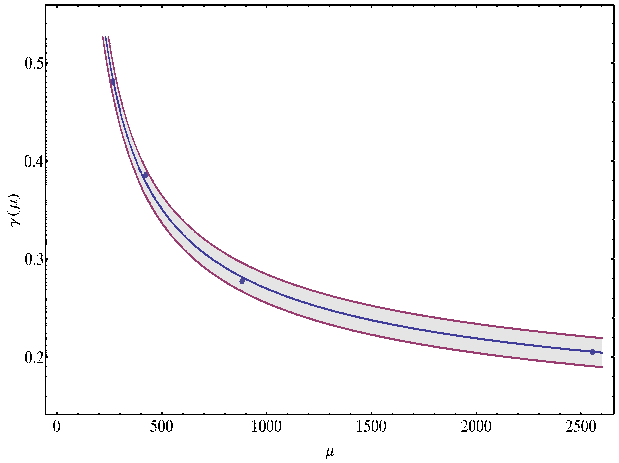

Figure 4.5. The scale-dependent strength, γ, in function of the reduced mass of the $q\bar{q}$ pair of the decaying meson, μ. The data points are the value of γ needed to reproduce the meson decay widths shown in Table 4.1. The solid line is the fit and the shaded area is the confidence interval with 90% confidence level.

strength, γ, given by

$$\gamma(\mu) = \frac{\gamma_0}{\log\left(\frac{\mu}{\mu_\gamma}\right)}, \tag{4.52}$$

where μ is the reduced mass of the $q\bar{q}$ pair of the decaying meson and $\gamma_0 = 0.81 \pm 0.02$ and $\mu_\gamma = 49.84 \pm 2.58\,\text{MeV}$ are the parameters determined through the total decay widths mentioned above.

Fig. 4.5 shows the scale-dependent strength, γ, in function of the reduced mass of the $q\bar{q}$ of the decaying meson, μ. The data points are the value of γ needed to reproduce the meson decay widths shown in Table 4.1. The solid line is the fit and the shaded area is the confidence interval with 90% confidence level. For completeness, we show in Table 4.2 the values of the scale-dependent strength, γ, in the different flavor sectors following Eq. (4.52).

Table 4.3 shows our results for the total strong decay widths of the mesons which belong to charmed, charmed-strange, hidden charm and hidden bottom sectors. We get a quite reasonable global description of the total decay widths. A detailed study to the decay modes of the different mesons will be done later, but now we can give

	Light mesons			Heavy-light mesons				Heavy mesons		
	$(n\bar{n})$	$(n\bar{s})$	$(s\bar{s})$	$(n\bar{c})$	$(s\bar{c})$	$(n\bar{b})$	$(s\bar{b})$	$(c\bar{c})$	$(c\bar{b})$	$(b\bar{b})$
μ	156.5	200.1	277.5	265.8	422.1	294.9	500.6	881.5	1310.8	2555.0
γ	0.707	0.582	0.471	0.483	0.379	0.455	0.351	0.282	0.247	0.205

Table 4.2. Values of the scale-dependent strength γ in the different quark sectors following Eq. (4.52). The reduced mass of the $q\bar{q}$ pair of the decaying meson, μ, is given in MeV.

Meson	I	J	P	C	n	Mass (MeV)	$\Gamma_{\text{Exp.}}$ (MeV) [78]	$\Gamma_{\text{The.}}$ (MeV)
$D^*(2010)^{\pm}$	0.5	1	-1	-	1	2010.25 ± 0.14	0.096 ± 0.022	0.036
$D_0^*(2400)^{\pm}$	0.5	0	$+1$	-	1	2403 ± 38	283 ± 42	212.01
$D_1(2420)^{\pm}$	0.5	1	$+1$	-	1	2423.4 ± 3.1	25 ± 6	25.27
$D_1(2430)^0$	0.5	1	$+1$	-	2	2427 ± 36	384 ± 150	229.12
$D_2^*(2460)^{\pm}$	0.5	2	$+1$	-	1	2460.1 ± 4.4	37 ± 6	64.07
$D(2550)^0$	0.5	0	-1	-	2	2539.4 ± 8.2	130 ± 18	132.07
$D^*(2600)^0$	0.5	1	-1	-	2	2608.7 ± 3.5	93 ± 14	96.91
$D_J(2750)^0$	0.5	2	-1	-	1	2752.4 ± 3.2	71 ± 13	229.86
$D_J^*(2760)^0$	0.5	3	-1	-	1	2763.3 ± 3.3	60.9 ± 6.2	116.41
$D_{s1}(2536)^{\pm}$	0	1	$+1$	-	1	2535.12 ± 0.25	1.03 ± 0.13 [198]	0.99
$D_{s2}^*(2575)^{\pm}$	0	2	$+1$	-	1	2572.6 ± 0.9	20 ± 5	18.67
$D_{s1}^*(2710)^{\pm}$	0	1	-1	-	2	2710 ± 14	149 ± 65	170.76
$D_{sJ}^*(2860)^{\pm}$	0	$\begin{bmatrix}1\\3\end{bmatrix}$	-1	-	$\begin{bmatrix}3\\1\end{bmatrix}$	2862 ± 6	48 ± 7	$\begin{bmatrix}153.19\\85.12\end{bmatrix}$
$D_{sJ}(3040)^{\pm}$	0	1	$+1$	-	$\begin{bmatrix}3\\4\end{bmatrix}$	3044 ± 31	239 ± 71	$\begin{bmatrix}301.52\\432.54\end{bmatrix}$
$\psi(3770)$	0	1	-1	-1	3	3775.2 ± 1.7	27.6 ± 1.0	26.47
$\psi(4040)$	0	1	-1	-1	4	4039 ± 1	80 ± 10	111.27
$\psi(4160)$	0	1	-1	-1	5	4153 ± 3	103 ± 8	115.95
$X(4360)$	0	1	-1	-1	6	4361 ± 9	74 ± 18	113.92
$\psi(4415)$	0	1	-1	-1	7	4421 ± 4	119 ± 16 [84]	159.02
$X(4640)$	0	1	-1	-1	8	4634 ± 8	92 ± 52	206.37
$X(4660)$	0	1	-1	-1	9	4664 ± 11	48 ± 15	135.06
$\Upsilon(4S)$	0	1	-1	-1	6	10579.4 ± 1.2	20.5 ± 2.5	20.59
$\Upsilon(10860)$	0	1	-1	-1	8	10865 ± 8	55 ± 28	27.89
$\Upsilon(11020)$	0	1	-1	-1	10	11019 ± 8	79 ± 16	79.16

Table 4.3. Calculated through the $^3P_0$ model, the strong total decay widths of the mesons which belong to charmed, charmed-strange, hidden charm and hidden bottom sectors. The value of the parameter γ in every quark sector is given by Eq. (4.52).

general comments.

The results predicted by the $^3P_0$ model for the well established charmed mesons are in good agreement with the experimental data except for one case, the total decay width of the D^* meson. The D^* decays only into $D\pi$ channel via strong interaction and it is assumed that the total decay width is given mainly by this decay mode. However, the disagreement may be due to, at least, two reasons. The first one is that the available phase space is very small and so final-state interactions can be important enhancing the

decay width. The second one is that the neutral-charged case, $D^*(2007)^0$, presents a branching fraction of $(38.1\pm2.9)\%$ for its electromagnetic decay $D^*(2007)^0 \to D^0\gamma$ [78], which means a large contribution to the total decay width.

Our theoretical results are in good agreement with the experimental data in the charmed-strange sector. Note that this agreement holds for the new $D^*_{s1}(2710)$, $D^*_{sJ}(2860)$ and $D_{sJ}(3040)$ resonances which have been recently observed by the BaBar Collaboration [135].

The $\psi(3770)$ meson decays into the DD channel, being this the only open-flavor final state. Its updated branching fraction reported by the PDG has been taken into account in the global fit because its non-DD decay modes sum together a branching fraction of about 10%. One can see in Table 4.3 that the general trend is well reproduced for the total decay widths of the 1^{--} charmonium states.

We obtain a good agreement between experimental and theoretical total decay widths in the bottomonium sector. The most significant disagreement is found for the $\Upsilon(5S)$ state, note however the large error in the experimental data.

4.5 Results

This section is devoted to investigate the strong decays of mesons through the two models explained above. It complements the information about the structure of mesons since the matrix elements present an overlap integral between the wave functions of the initial and final mesons.

We begin with the strong decays of $J^{PC} = 1^{--}$ $c\bar{c}$ states into open-charm mesons. We compare our predictions coming from the $^3P_0$ decay model and the microscopic one. Comments on the results of different microscopic models are also included. Then, we extend the calculation of the strong decays to the rest of charmonium spectrum. This will provide useful information in order to assign $c\bar{c}$ states to possible XYZ mesons. We continue with a thorough study of the open-flavor strong decays of the charmed and charmed-strange mesons. This gives us the assignment of quantum numbers. Finally, results on the $J^{PC} = 1^{--}$ bottomonium family are shown.

4.5.1 Results for ψ states

From an experimental point of view there are a few data in the open-charm decays of the 1^{--} $c\bar{c}$ resonances. The main experimental data are the resonance parameters, mass and total decay width, of the excited ψ states fitting the R value measured in the relevant energy region.

Tables 4.4 and 4.5 show the strong decay widths predicted by the $^3P_0$ and the microscopic models for the 1^{--} $c\bar{c}$ states established in Table 3.1. The notation D_1D_2 includes the $D_1\bar{D}_2$ and $\bar{D}_1D_2$ combination of well defined CP quantum numbers. For the kinematics we use experimental masses whenever they are available.

One can see that the general trend of the total decay widths is well reproduced in the case of the $^3P_0$ model. The total widths are lower in the microscopic model without improving the agreement with the experimental data. However, the microscopic model gives the correct order of magnitude of the strong decays with no free parameter, as the strength γ introduced by the $^3P_0$ model.

Meson	State	Channel	$\Gamma_{^3P_0}$	$\mathcal{B}_{^3P_0}$	$\Gamma_{\text{Mic.}}$	$\mathcal{B}_{\text{Mic.}}$
$\psi(3770)$	1^3D_1	D^+D^-	11.34	42.8	8.03	42.3
		$D^0\bar{D}^0$	15.13	57.2	10.94	57.7
		DD	26.47	100	18.97	100
27.6 ± 1.0		total	26.47		18.97	
$\psi(4040)$	3^3S_1	DD	4.61	4.1	10.17	26.0
		DD^*	22.23	20.0	18.75	47.9
		D^*D^*	82.35	74.0	9.06	23.2
		D_sD_s	2.08	1.9	1.14	2.9
80 ± 10		total	111.27		39.12	
$\psi(4160)$	2^3D_1	DD	22.82	19.7	17.03	52.1
		DD^*	2.22	1.9	7.38	22.6
		D^*D^*	83.73	72.2	5.28	16.2
		D_sD_s	0.24	0.2	2.61	7.9
		$D_sD_s^*$	6.94	6.0	0.40	1.2
103 ± 8		total	115.95		32.70	
$X(4360)$	4^3S_1	DD	8.02	7.0	5.73	5.6
		DD^*	8.19	7.2	29.81	29.2
		D^*D^*	8.87	7.8	46.46	45.5
		DD_1	54.51	47.8	2.18	2.1
		DD_1'	4.29	3.8	12.02	11.7
		DD_2^*	27.17	23.8	0.56	0.6
		D_sD_s	0.07	0.1	1.86	1.8
		$D_sD_s^*$	1.90	1.7	3.36	3.3
		$D_s^*D_s^*$	0.91	0.8	0.17	0.2
$74 \pm 15 \pm 10$		total	113.92		102.15	
$\psi(4415)$	3^3D_1	DD	15.11	9.5	7.93	18.5
		DD^*	5.82	3.7	6.66	15.6
		D^*D^*	32.56	20.5	7.23	16.9
		DD_1	64.77	40.7	6.06	14.2
		DD_1'	6.92	4.4	2.12	5.0
		DD_2^*	23.60	14.8	1.82	4.3
		$D^*D_0^*$	7.12	4.5	2.39	5.6
		D_sD_s	0.31	0.2	2.22	5.2
		$D_sD_s^*$	0.68	0.4	1.09	2.5
		$D_s^*D_s^*$	2.13	1.3	5.20	12.2
62 ± 20		total	159.01		42.72	

Table 4.4. Open-flavor strong decay widths, in MeV, and branchings, in %, of ψ states.

The total width of the $\psi(3770)$ predicted by the microscopic model is lower than the $^3P_0$ model. We find the same situation for the next two resonances, $\psi(4040)$ and $\psi(4160)$. Later we will see that taking into account only the j^0Kj^0 decay model as in Refs. [34, 95, 186] the widths grow.

Meson	State	Channel	$\Gamma_{^3P_0}$	$\mathcal{B}_{^3P_0}$	$\Gamma_{\text{Mic.}}$	$\mathcal{B}_{\text{Mic.}}$
$X(4630)$	5^3S_1	DD	6.62	3.2	1.44	0.8
		DD^*	26.23	12.7	15.82	8.4
		D^*D^*	15.57	7.5	30.40	16.2
		DD_1	2.88	1.4	18.70	9.9
		DD_1'	4.52	2.2	2.58	1.4
		DD_2^*	0.00	0.0	21.14	11.2
		$D^*D_0^*$	6.97	3.4	10.10	5.4
		D^*D_1	39.21	19.0	22.47	11.9
		D^*D_1'	14.35	7.0	26.24	13.9
		$D^*D_2^*$	80.47	39.0	18.28	9.7
		D_sD_s	0.92	0.4	1.28	0.7
		$D_sD_s^*$	0.30	0.1	6.70	3.6
		$D_s^*D_s^*$	1.14	0.6	6.34	3.4
		D_sD_{s1}	2.82	1.4	0.92	0.5
		D_sD_{s1}'	0.79	0.4	0.03	0.0
		$D_sD_{s2}^*$	0.19	0.1	0.22	0.1
		$D_s^*D_{s0}^*$	2.76	1.3	1.30	0.7
		$D_s^*D_{s1}$	0.14	0.1	3.74	2.0
		$D_s^*D_{s1}'$	0.26	0.1	0.29	0.1
		$D_{s0}^*D_{s0}^*$	0.22	0.1	0.23	0.1
92^{+40+10}_{-24-21}		total	206.37		188.22	
$X(4660)$	4^3D_1	DD	10.92	8.1	3.21	2.3
		DD^*	7.55	5.6	4.10	2.9
		D^*D^*	38.04	28.2	2.67	1.9
		DD_1	2.41	1.8	20.51	14.4
		DD_1'	0.51	0.4	2.62	1.8
		DD_2^*	0.00	0.0	6.75	4.8
		$D^*D_0^*$	3.44	2.5	0.71	0.5
		D^*D_1	34.83	25.8	10.89	7.7
		D^*D_1'	6.98	5.1	2.96	2.1
		$D^*D_2^*$	21.92	16.2	77.52	54.5
		D_sD_s	0.96	0.7	1.46	1.0
		$D_sD_s^*$	0.00	0.0	1.35	0.9
		$D_s^*D_s^*$	0.33	0.2	4.28	3.0
		D_sD_{s1}	3.63	2.7	0.0	0.0
		D_sD_{s1}'	1.09	0.8	0.62	0.4
		$D_sD_{s2}^*$	0.08	0.1	0.07	0.1
		$D_s^*D_{s0}^*$	1.18	0.9	0.43	0.3
		$D_s^*D_{s1}$	0.48	0.4	0.93	0.6
		$D_s^*D_{s1}'$	0.17	0.1	0.37	0.3
		$D_{s0}^*D_{s0}^*$	0.53	0.4	0.74	0.5
$48 \pm 15 \pm 3$		total	135.06		142.19	

Table 4.5. Open-flavor strong decay widths, in MeV, and branchings, in %, of ψ states (Continuation).

Decay	Ref. [186]	j^0Kj^0	Mic.	Exp. [78]
$\psi(3770) \to DD$	20.1	29.8	19.0	27.6 ± 1
$\psi(4040) \to DD$	0.1	1.4	10.2	
$\psi(4040) \to DD^*$	33.0	25.2	18.7	
$\psi(4040) \to D^*D^*$	33.0	35.0	9.1	
$\psi(4040) \to D_sD_s$	8.0	0.3	1.1	
total	74.0	61.9	39.1	80 ± 10
$\psi(4160) \to DD$	3.2	25.0	17.0	
$\psi(4160) \to DD^*$	6.9	0.5	7.4	
$\psi(4160) \to D^*D^*$	41.9	21.3	5.3	
$\psi(4160) \to D_sD_s$	5.6	0.03	2.6	
$\psi(4160) \to D_sD_s^*$	11.0	0.6	0.4	
total	69.2	47.4	32.7	103 ± 8

Table 4.6. Open-flavor strong decay widths, in MeV, of ψ states reported in Ref. [186] and our decay rates taking into account the static vector contribution or the full model.

If one compares the total widths of the next two resonances, $X(4360)$ and $\psi(4415)$, the microscopic decay model predicts a better result than the $^3P_0$ one for the total width of $\psi(4415)$. However, we should mention that the experimental data from Ref. [78] are clustered around two values ($\sim$100 MeV and $\sim$50 MeV) corresponding the lower one to very old measurements. The recent experimental result of Seth *et al.* [84] ($\Gamma = 119 \pm 16$ MeV) is in reasonable agreement with the prediction of the $^3P_0$ model and a factor 3 greater than that predicted by the microscopic model.

When we go up through the spectrum, the states are more and more wide and the total widths for S and D-waves are larger in both decay models, always D-wave widths are smaller. This is the case of the two states in the vicinity of 4660 MeV. The small total width of the $X(4660)$ favors the 4^3D_1 option for this state although interference between the two states can be the origin of the poor description of the total decay widths.

It is difficult to compare our results from the microscopic decay model with former similar calculations because either they are not fitted to the heavy quark sector [187] or do not include the same pieces of the current [34, 95, 186]. For the sake of the comparison we show in Table 4.6 the results of Ref. [186] together with our model prediction including only the static vector contribution and the full decay model. The basic difference between the two calculations is that in Ref. [186] the coupling with the meson-meson channels is treated nonperturbatively and this enhances the results when the threshold is close to the state. The predictions of the full decay model are below the experimental data and taking only the j^0Kj^0 contribution the decay rates grow.

The decay width of $\psi(3770)$ into DD has been widely studied in the literature. This is because the DD is the only open threshold for the $\psi(3770)$ resonance and therefore the total width should be given almost by its decay into DD. However, during the last years the non-DD contribution to the total decay width was measured to be large, 15%. Now, the PDG [78] provides a branching fraction of $\mathcal{B}(\psi(3770) \to DD) = (93^{+8}_{-9})\%$, in good agreement with the theoretical expectations. The predicted width of $\psi(3770) \to DD$ decay in Ref. [186] is similar to those predicted by j^0Kj^0 contribution

State	Ratio	Ref. [186]	j^0Kj^0	Mic.	$^3P_0$	Exp. [78]
$\psi(4040)$	$D\bar{D}/D\bar{D}^*$	0.003	0.06	0.54	0.21	$0.24 \pm 0.05 \pm 0.12$
	$D^*\bar{D}^*/D\bar{D}^*$	1.00	1.39	0.48	3.70	$0.18 \pm 0.14 \pm 0.03$
$\psi(4160)$	$D\bar{D}/D^*\bar{D}^*$	0.08	1.17	3.23	0.27	$0.02 \pm 0.03 \pm 0.02$
	$D\bar{D}^*/D^*\bar{D}^*$	0.16	0.02	1.40	0.03	$0.34 \pm 0.14 \pm 0.05$
$X(4360)$	$D\bar{D}/D^*\bar{D}^*$	-	0.40	0.12	0.90	$0.14 \pm 0.12 \pm 0.03$
	$D\bar{D}^*/D^*\bar{D}^*$	-	0.08	0.64	0.92	$0.17 \pm 0.25 \pm 0.03$
$\psi(4415)$	$D\bar{D}/D^*\bar{D}^*$	-	1.54	1.10	0.46	$0.14 \pm 0.12 \pm 0.03$
	$D\bar{D}^*/D^*\bar{D}^*$	-	0.28	0.92	0.18	$0.17 \pm 0.25 \pm 0.03$

Table 4.7. Open-flavor strong ratios of ψ states predicted by different decay models and their comparison with the experimental data.

and the full decay model. If we apply the microscopic decay model of Ref. [187] to the charmonium sector, the result for that decay is very large, 104.0 MeV.

Finally, in Table 4.7 we compare the experimental ratios of some charmonium decays with the prediction of different models. None of them can explain the experimental data. In Ref. [199] a coupled channel calculation in the 4.1 GeV energy region including the 3^3S_1, $\psi(4040)$, and 2^3D_1, $\psi(4160)$, $c\bar{c}$ states and the DD, DD^*, D^*D^*, D_sD_s, $D_sD_s^*$ and $D_s^*D_s^*$ meson-meson channels has been performed. The branching fractions of the resulting dressed 3^3S_1 and 2^3D_1 $c\bar{c}$ states improve the agreement with the experimental data.

Any decay model fails to explain all experimental data about the strong decays of charmonium, and so more theoretical and experimental effort is needed to solve this problem.

4.5.2 Results for the rest of charmonium states

We calculate in this section the strong decays into open-charm mesons for the rest of charmonium states reported in Table 3.1. It completes our study of strong decays in the charmonium sector and reports information about our assignments as $c\bar{c}$ states of some XYZ mesons.

The η_c states

The $\eta_c(3S)$ is the first state which can decay into open-charm mesons, being its mass 4054 MeV. Table 4.8 shows the different channels and their partial widths predicted by the $^3P_0$ and the microscopic decay models. This state should be observed in the DD^* and D^*D^* channels and its total width is large in the $^3P_0$ model and moderate in the microscopic decay model. The difference between the predictions of the two theoretical decay models is important. In fact the dominant decay channel is different among the two models.

The h_c states

Focusing our interest on the h_c meson, Table 4.9 shows the open-charm strong decays calculated by the two decay models. These numerical results could be useful for future

Meson	State	Channel	$\Gamma_{^3P_0}$	$\mathcal{B}_{^3P_0}$	$\Gamma_{\text{Mic.}}$	$\mathcal{B}_{\text{Mic.}}$
η_c	3^1S_0	DD^*	38.72	22.8	19.66	71.4
		D^*D^*	131.50	77.2	7.89	28.6
		total	170.23		27.55	

Table 4.8. Open-flavor strong decay widths, in MeV, and branchings, in %, of η_c states.

Meson	State	Channel	$\Gamma_{^3P_0}$	$\mathcal{B}_{^3P_0}$	$\Gamma_{\text{Mic.}}$	$\mathcal{B}_{\text{Mic.}}$
h_c	2^1P_1	DD^*	88.78	100	6.87	100
		total	88.78		6.87	
	3^1P_1	DD^*	35.03	56.8	20.49	20.8
		D^*D^*	8.46	13.7	27.68	28.2
		DD_0^*	10.88	17.6	41.42	42.1
		$D_sD_s^*$	4.77	7.7	5.80	5.9
		$D_s^*D_s^*$	2.59	4.2	2.90	3.0
		total	61.73		98.29	

Table 4.9. Open-flavor strong decay widths, in MeV, and branchings, in %, of h_c states.

experimental findings. For instance, the 2^1P_1 state has a mass of 3956 MeV and by conservation of quantum numbers it only decays to the DD^* channel. However, while this state appears wide in the $^3P_0$ model is not so much in the case of the microscopic decay model. For the 3^1P_1 state, both models predict a relatively wide resonance with dominant decay channel DD^* and DD_0^* for the $^3P_0$ and the microscopic decay model, respectively. In the case of the microscopic model its decays into DD^* and D^*D^* are of relevance.

The χ_{cJ} states

In Table 4.10 one can find the open-charm strong decay widths of χ_{cJ} states.

For the $2P$ $c\bar{c}$ multiplet some candidates have appeared in the last years, these are $X(3872)$, $X(3915)$, $Y(3940)$, $X(3940)$ and $Z(3930)$. In the previous Chapter, we have made assignments for the $X(3915)$ and $Z(3930)$ as $c\bar{c}$ states. Recently, the $X(3915)$ and $Y(3940)$ have been proposed as the same state due to the compatibility of their measured properties [13].

We have assigned the 2^3P_0 state to the $X(3915)$. The mass predicted is 3909, in very good agreement with the experimental measurement, and we have also calculated its electromagnetic decays. Now we are ready to give its full width. Table 4.10 shows our results with the $^3P_0$ and the microscopic models. The numbers in parentheses have been calculated using the experimental mass and some assumption for the assignment. We also give our prediction using the theoretical mass for completeness. The $^3P_0$ model predicts an extremely narrow state while the microscopic model increases the agreement but remains lower than the experimental data.

It is generally accepted that the $Z(3930)$ is the $\chi_{c2}(2P)$ state. Assuming this assignment due to the agreement between theoretical and experimental masses, we

Meson	State	Channel	$\Gamma_{^3P_0}$	$\mathcal{B}_{^3P_0}$	$\Gamma_{\text{Mic.}}$	$\mathcal{B}_{\text{Mic.}}$
χ_{c0}	2^3P_0	DD	0.81 (0.17)	100 (100)	6.15 (7.60)	100 (100)
$(17 \pm 10 \pm 3$ [85]		total	0.81 (0.17)		6.15 (7.60)	
	3^3P_0	DD	10.67	21.5	22.83	26.6
		D^*D^*	33.29	67.2	58.22	67.9
		D_sD_s	3.26	6.6	2.44	2.8
		$D_s^*D_s^*$	2.34	4.7	2.27	2.7
		total	49.56		85.76	
χ_{c1}	2^3P_1	DD^*	130.55	100	4.79	100
		total	130.55		4.79	
	3^3P_1	DD^*	17.57	58.7	26.05	40.8
		D^*D^*	0.39	1.3	34.46	53.9
		DD_0^*	0.24	0.8	0.08	0.1
		$D_sD_s^*$	8.56	28.6	2.35	3.7
		$D_s^*D_s^*$	3.17	10.6	0.95	1.5
		total	29.93		63.89	
χ_{c2}	2^3P_2	DD	35.44 (33.66)	38.4 (64.0)	2.68 (2.47)	30.9 (60.0)
		DD^*	56.54 (18.94)	61.2 (36.0)	5.98 (1.68)	69.0 (40.0)
		D_sD_s	0.36 (−)	0.4 (−)	0.01 (−)	0.1 (−)
$(29 \pm 10 \pm 2)$ [88]		total	92.34 (52.60)		8.67 (4.15)	
	1^3F_2	DD	44.71	44.5	19.39	61.2
		DD^*	50.10	49.8	11.85	37.4
		D^*D^*	0.84	0.8	0.06	0.2
		D_sD_s	4.94	4.9	0.39	1.2
		total	100.58		31.69	

Table 4.10. Open-flavor strong decay widths, in MeV, and branchings, in %, of χ_{cJ} states. The numbers in parentheses are calculated using the experimental mass and some assumption for the assignment. The symbol (−) indicates that the corresponding open-flavor channel is closed when we calculate with the experimental mass.

calculate its strong decays in Table 4.10. Again the numbers in parentheses have been calculated using the experimental mass and the others using our theoretical prediction. The total decay rate predicted by the $^3P_0$ model is reasonably good when using the experimental mass. It is interesting to observe that the dominant decay channel changes when we calculate with the experimental mass, being this the DD channel in which $Z(3930)$ is observed. Both decay models predict the same branchings and behaviour when we calculate with the theoretical or the experimental masses. We show in Table 4.11 our results and the experimental measurements performed by Belle [88] and BaBar [200] for some observables concerning the $Z(3930)$. One can see the good agreement obtained for the product $\Gamma_{\gamma\gamma}\mathcal{B}(Z(3930) \to D\bar{D})$ in both decay models.

The next states of χ_{cJ} mesons are 3^3P_0, 3^3P_1 and 1^3F_2. The $3P$ states have an

Observable	The.	Belle [88]	BaBar [200]
Mass (MeV)	3969	$3929 \pm 5 \pm 2$	$3926.7 \pm 2.7 \pm 1.1$
Width (MeV)	$\begin{bmatrix} 52.60 \\ 4.15 \end{bmatrix}$	$29 \pm 10 \pm 2$	$21.3 \pm 6.8 \pm 3.6$
$\Gamma_{\gamma\gamma}\mathcal{B}(D\bar{D})$ (keV)	$\begin{bmatrix} 0.17 \\ 0.16 \end{bmatrix}$	$0.18 \pm 0.05 \pm 0.03$	$0.24 \pm 0.05 \pm 0.04$

Table 4.11. Different observables of $Z(3930)$ as a 2^3P_2 state. Values within brackets are the theoretical results if one considers the $^3P_0$ model (upper value) and the microscopic model (lower value) for the involved strong decay.

expected mean multiplet mass of about 4.3 GeV and many open-charm channels are open at the $3P$ mass scale. When we calculate the total width through the decay models, we find narrower states in the $^3P_0$ model than in the microscopic decay model except for the 1^3F_2 state where the inverse situation holds. This is because the partial widths of the 1^3F_2 state into the DD and DD^* predicted by the $^3P_0$ model are larger than in the microscopic decay model. However, both decay models agree, predicting these two decay modes as the dominant.

The 3^3P_1 should be seen in DD^* and D^*D^* channels in the case of the microscopic model and only in DD^* according to the $^3P_0$ model. The prediction of both models for the 2^3P_1 is also very different, while the $^3P_0$ model predicts a broad state, the microscopic one predicts a relatively narrow meson.

We have ruled out the assignment of $Z(3930)$ as the 1^3F_2 state attending the mass. Following the $^3P_0$ decay model, one possibility to distinguish between the 2^3P_2 and 1^3F_2 assignments is measuring the ratio between DD and DD^* decay modes because the situation for both states is just the opposite.

D-wave states with $J = 2$

Tables 4.12 and 4.13 show the strong decays into open-charm mesons for the $^1D_2$ and $^3D_2$ states. The $^3P_0$ model predicts broad states with total widths about 150 MeV. However, the microscopic decay model anticipates relatively narrow states with total widths of 30 MeV.

The 2^1D_2 state decays into DD^* and D^*D^* final states with the same strength, both decay models predict similar branching fractions despite of the difference on the absolute values. The partial widths are moderate, even larger in the $^3P_0$ model, indicating that this state can be seen experimentally in both channels. There is a strong disagreement between the predictions of the $^3P_0$ and the microscopic model about the decays of the 2^3D_2 state. The $^3P_0$ model predicts a similar situation than in the case of the 2^1D_2 state for the decays into DD^* and D^*D^*, whereas the microscopic model predicts a suppressed D^*D^* channel with respect the DD^* one.

The $S + S$ channels appear important for the 3^1D_2 and 3^3D_2 states, but also the $S + P$ channels as DD_2^* and DD_1' are significant. In fact, DD_2^* and DD_1' are dominant following the prediction of the $^3P_0$ model and of the same order of magnitude as DD^* and D^*D^* in the case of the microscopic decay model.

Meson	State	Channel	$\Gamma_{^3P_0}$	$\mathcal{B}_{^3P_0}$	$\Gamma_{\rm Mic.}$	$\mathcal{B}_{\rm Mic.}$
η_{c2}	2^1D_2	DD^*	71.24	50.4	8.95	47.1
		D^*D^*	60.76	43.0	9.36	49.2
		$D_sD_s^*$	9.31	6.6	0.70	3.7
		total	141.32		19.01	
	3^1D_2	DD^*	39.46	22.1	5.82	17.5
		D^*D^*	21.53	12.1	7.35	22.1
		DD_0^*	1.12	0.6	1.25	3.7
		DD_1	0.02	0.0	0.23	0.7
		DD_1'	0.07	0.0	0.18	0.5
		DD_2^*	62.75	35.1	4.94	14.8
		$D^*D_0^*$	0.25	0.1	0.05	0.2
		D^*D_1	4.79	2.7	0.55	1.6
		D^*D_1'	43.67	24.4	7.82	23.5
		$D_sD_s^*$	1.43	0.8	2.30	6.9
		$D_s^*D_s^*$	2.24	1.3	2.26	6.8
		$D_sD_{s0}^*$	1.35	0.8	0.56	1.7
		D_sD_{s1}	0.00	0.0	0.0	0.0
		$D_s^*D_{s0}^*$	0.00	0.0	0.0	0.0
		total	178.69		33.31	

Table 4.12. Open-flavor strong decay widths, in MeV, and branchings, in %, of η_{c2} states.

4.5.3 Results for open-charm mesons

Using the $^3P_0$ and the microscopic models, we study two-body strong decays of the newly observed charmed mesons $D(2550)$, $D^*(2600)$, $D_J(2750)$ and $D_J^*(2760)$, and charmed-strange mesons $D_{s1}^*(2710)$, $D_{sJ}^*(2860)$ and $D_{sJ}(3040)$. This allows us to characterize these resonances and justify the quantum number assignments made in Table 3.18.

The running of the strength γ of the $^3P_0$ model is given by Eq. (4.52). It allows us to obtain a quite reasonable global description of the decay widths along the different flavor sectors. The value of γ, which will be used in the description of the strong decays of charmed and charmed-strange mesons, can be seen in Table 4.2. The microscopic decay model assumes that the strong decays are driven by the same interquark Hamiltonian which determines the spectrum, thus it has some flavor dependences. Among others, we must take into account the running of the strong coupling constant and the different contributions of the diagrams d_{1q} and $d_{1\bar{q}}$ due to the different mass of the quark and the antiquark of the original meson. We use always experimental masses for all mesons involved in the decays.

Tables 4.14 and 4.15 show the results predicted by the $^3P_0$ and the microscopic decay models for the well established charmed and charmed-strange mesons, respectively. We show the absolute values and the branching fractions, the comparison with the available experimental data is also included. One can see the good agreement between the theoretical results of the $^3P_0$ model and the experimental data in most cases. The microscopic model predicts always lower strong decay widths although it is interesting

Meson	State	Channel	$\Gamma_{^3P_0}$	$\mathcal{B}_{^3P_0}$	$\Gamma_{\rm Mic.}$	$\mathcal{B}_{\rm Mic.}$
ψ_2	2^3D_2	DD^*	53.63	40.5	14.92	72.8
		D^*D^*	66.18	49.9	4.41	21.5
		$D_sD_s^*$	12.68	9.6	1.16	5.7
		total	132.48		20.49	
	3^3D_2	DD^*	36.05	19.6	10.43	24.8
		D^*D^*	27.63	15.1	4.24	10.1
		DD_0^*	0.01	0.0	0.79	1.9
		DD_1	1.98	1.1	2.54	6.1
		DD_1'	13.41	7.3	3.76	8.9
		DD_2^*	49.16	26.8	2.37	5.6
		$D^*D_0^*$	8.93	4.9	1.78	4.2
		D^*D_1	6.65	3.6	3.74	8.9
		D^*D_1'	36.85	20.1	6.60	15.7
		$D_sD_s^*$	1.27	0.7	2.93	7.0
		$D_s^*D_s^*$	1.53	0.8	2.76	6.7
		$D_sD_{s0}^*$	0.00	0.0	0.06	0.1
		D_sD_{s1}	0.02	0.0	0.0	0.0
		$D_s^*D_{s0}^*$	0.02	0.0	0.0	0.0
		total	183.50		42.00	

Table 4.13. Open-flavor strong decay widths, in MeV, and branchings, in %, of ψ_2 states.

to note that the branching fractions predicted by both decay models are very similar in the charmed and charmed-strange sectors.

In Ref. [133] the BaBar Collaboration reported the new charmed states $D(2550)$, $D^*(2600)$, $D_J(2750)$ and $D_J^*(2760)$ in inclusive e^+e^- collisions. The $D(2550)$ and $D_J(2750)$ were observed in $D^{*+}\pi^-$ channel, the $D_J^*(2760)$ was observed in $D^+\pi^-$ channel, and the $D^*(2600)$ was observed in both $D^{*+}\pi^-$ and $D^+\pi^-$ channels. The resulting masses and widths of these four states with neutral-charge are

$$\begin{aligned}
M(D(2550)^0) &= 2539.4 \pm 4.5 \pm 6.8\,\text{MeV}, & \Gamma(D(2550)^0) &= 130 \pm 12 \pm 13\,\text{MeV},\\
M(D^*(2600)^0) &= 2608.7 \pm 2.4 \pm 2.5\,\text{MeV}, & \Gamma(D^*(2600)^0) &= 93 \pm 6 \pm 13\,\text{MeV},\\
M(D_J(2750)^0) &= 2752.4 \pm 1.7 \pm 2.7\,\text{MeV}, & \Gamma(D_J(2750)^0) &= 71 \pm 6 \pm 11\,\text{MeV},\\
M(D_J^*(2760)^0) &= 2763.3 \pm 2.3 \pm 2.3\,\text{MeV}, & \Gamma(D_J^*(2760)^0) &= 60.9 \pm 5.1 \pm 3.6\,\text{MeV},
\end{aligned} \tag{4.53}$$

and the following ratios of branching fractions were also obtained

$$\begin{aligned}
\frac{\mathcal{B}(D_2^*(2460)^0 \to D^+\pi^-)}{\mathcal{B}(D_2^*(2460)^0 \to D^{*+}\pi^-)} &= 1.47 \pm 0.03 \pm 0.16,\\
\frac{\mathcal{B}(D^*(2600)^0 \to D^+\pi^-)}{\mathcal{B}(D^*(2600)^0 \to D^{*+}\pi^-)} &= 0.32 \pm 0.02 \pm 0.09,\\
\frac{\mathcal{B}(D_J^*(2760)^0 \to D^+\pi^-)}{\mathcal{B}(D_J(2750)^0 \to D^{*+}\pi^-)} &= 0.42 \pm 0.05 \pm 0.11.
\end{aligned} \tag{4.54}$$

Meson	nJ^P	Channel	$\Gamma_{^3P_0}$	$\mathcal{B}_{^3P_0}$	$\Gamma_{\text{Mic.}}$	$\mathcal{B}_{\text{Mic.}}$	Exp.
$D^*(2007)^0$	$1\,1^-$	$D^0\pi^0$	15.70×10^{-3}		8.72×10^{-3}		$(61.9 \pm 2.9)\%$
		total	15.70×10^{-3}		8.72×10^{-3}		$< 2.1\,\text{MeV}$
$D^*(2010)^+$	$1\,1^-$	$D^+\pi^0$	11.44×10^{-3}	31.74	6.34×10^{-3}	31.72	$(30.7 \pm 0.5)\%$
		$D^0\pi^+$	24.61×10^{-3}	68.26	13.65×10^{-3}	68.28	$(67.7 \pm 0.5)\%$
		total	36.05×10^{-3}		19.99×10^{-3}		$(96 \pm 4 \pm 22)\,\text{keV}$
$D_0^*(2400)^0$	$1\,0^+$	$D^0\pi^0$	81.74	33.14	5.82	33.81	
		$D^+\pi^-$	164.92	66.86	11.40	66.19	
		total	246.65		17.22		$(267 \pm 40)\,\text{MeV}$
$D_0^*(2400)^+$	$1\,0^+$	$D^+\pi^0$	70.97	33.47	8.25	32.99	
		$D^0\pi^+$	141.05	66.53	16.76	67.01	
		total	212.01		25.01		$(283 \pm 24 \pm 34)\,\text{MeV}$
$D_1(2420)^0$	$1\,1^+$	$D^{*0}\pi^0$	8.38	34.49	5.78	33.90	
		$D^{*+}\pi^-$	15.91	65.51	11.27	66.10	
		total	24.29		17.05		$(27.1 \pm 2.7)\,\text{MeV}$
$D_1(2420)^+$	$1\,1^+$	$D^{*+}\pi^0$	8.31	32.87	5.75	33.05	
		$D^{*0}\pi^+$	16.97	67.13	11.65	66.95	
		total	25.27		17.40		$(25 \pm 6)\,\text{MeV}$
$D_1(2430)^0$	$2\,1^+$	$D^{*0}\pi^0$	75.93	33.14	13.54	33.46	
		$D^{*+}\pi^-$	153.19	66.86	26.93	66.54	
		total	229.12		40.47		$(384^{+107}_{-75} \pm 74)\,\text{MeV}$
$D_2^*(2460)^0$	$1\,2^+$	$D^0\pi^0$	13.80	21.87	1.29	23.08	
		$D^+\pi^-$	26.68	42.31	2.42	43.29	
		$D^{*0}\pi^0$	7.67	12.17	0.66	11.81	
		$D^{*+}\pi^-$	14.64	23.22	1.22	21.82	
		$D^0\eta$	0.28	0.43	0.0028	0.05	
		total	63.08		5.59		$(49.0 \pm 1.4)\,\text{MeV}$
$D_2^*(2460)^+$	$1\,2^+$	$D^+\pi^0$	13.48	21.04	1.24	21.56	
		$D^0\pi^+$	27.60	43.07	2.57	44.70	
		$D^{*+}\pi^0$	7.50	11.70	0.63	10.96	
		$D^{*0}\pi^+$	15.28	23.84	1.31	22.78	
		$D^+\eta$	0.23	0.35	0.0021	0.04	
		total	64.07		5.75		$(37 \pm 6)\,\text{MeV}$

Table 4.14. Open-flavor strong decay widths, in MeV, and branchings, in %, of the well established D mesons.

The $D(2550)$ meson has been seen only in the decay mode $D^*\pi$, thus its possible spin-parity quantum numbers up to $J = 3$ are $J^P = 0^-$, 1^+, 2^- and 3^+. It is the lower in mass of the newly discovered mesons and within the possible assignments, the 0^- is the most plausible because the remaining options are very far in mass, $\sim 3.0\,\text{GeV}$, according to our quark model prediction. Table 4.16 shows the decay widths of the $D(2550)$ meson. There are only two open channels, $D^*\pi$ and $D_0^*\pi$, with different predictions attending both decay models. The total width predicted by the $^3P_0$ model is in very good agreement with the experimental one, however, the microscopic model predicts a lower value. The helicity-angle distribution of $D(2550)$ turns out to be also consistent with the prediction of a 2^1S_0 state. Therefore, the 2^1S_0 assignment appears

Meson	nJ^P	Channel	$\Gamma_{^3P_0}$	$\mathcal{B}_{^3P_0}$	$\Gamma_{\text{Mic.}}$	$\mathcal{B}_{\text{Mic.}}$	Exp.
$D_{s1}(2536)^+$	$1\,1^+$	$D^{*+}K^0$	0.43	43.48	4.86	47.32	
		$D^{*0}K^+$	0.56	56.52	5.41	52.68	
		total	0.99		10.27		$< 2.3\,\text{MeV}$
$D^*_{s2}(2573)^+$	$1\,2^+$	D^+K^0	8.02	42.95	3.03	44.27	
		D^0K^+	8.69	46.54	3.36	49.09	
		$D^{*+}K^0$	0.82	4.40	0.19	2.78	
		$D^{*0}K^+$	1.06	5.67	0.25	3.65	
		$D_s^+\eta$	0.08	0.44	0.014	0.21	
		total	18.67		6.84		$20 \pm 5\,\text{MeV}$

Table 4.15. Open-flavor strong decay widths, in MeV, and branchings, in %, of the well established D_s mesons.

	$D(2550)$ as $nJ^P = 2\,0^-$			
Channel	$\Gamma_{^3P_0}$	$\mathcal{B}_{^3P_0}$	$\Gamma_{\text{Mic.}}$	$\mathcal{B}_{\text{Mic.}}$
$D^*\pi$	131.90	99.87	0.17	0.87
$D_0^*\pi$	0.18	0.13	19.48	99.13
total	132.07		19.65	

Table 4.16. Open-flavor strong decay widths, in MeV, and branchings, in %, of the $D(2550)$ meson with quantum numbers $nJ^P = 2\,0^-$.

the most plausible looking our results.

The $D^*(2600)$ meson decays into $D\pi$ and $D^*\pi$ final states, thus its possible quantum numbers are $J^P = 1^-$, 2^+ and 3^-. The helicity-angle distribution of $D^*(2600)$ is found to be consistent with $J^P = 1^-$. Moreover, its mass makes it the perfect candidate to be the spin partner of the $D(2550)$ meson. The predicted mass is about 100 MeV above the experimental value and this is typically found in quark models. Table 4.17 shows its strong decays as a 2^3S_1 state, we find $D^*\pi$ as the dominant decay mode being its decay into $D\pi$ final state smaller in the $^3P_0$ model and of the same order of magnitude in the case of the microscopic one. Therefore the ratio of branching fractions measured experimentally are predicted as

$$\frac{\mathcal{B}(D^*(2600)^0 \to D^+\pi^-)}{\mathcal{B}(D^*(2600)^0 \to D^{*+}\pi^-)} = \begin{cases} 0.32 \pm 0.02 \pm 0.09 & \text{Exp.} \\ 0.20 & ^3P_0 \\ 1.09 & \text{Mic.} \end{cases} \tag{4.55}$$

The $^3P_0$ model predicts a reasonable value if we compare with the experimental one, but the microscopic prediction is worse. The total width predicted by the $^3P_0$ model is again in good agreement with the experimental data. The prediction of the microscopic model is lower than the experimental one but with the correct order of magnitude. If this assignment was correct, there would be traces of $D\eta$, D_sK and $D^*\eta$.

There is a strong discussion in the literature about the possible quantum numbers that could have the mesons $D_J(2750)$ and $D^*_J(2760)$ providing a wide range of

	$D^*(2600)$ as $nJ^P = 2\,1^-$			
Channel	$\Gamma_{^3P_0}$	$\mathcal{B}_{^3P_0}$	$\Gamma_{\text{Mic.}}$	$\mathcal{B}_{\text{Mic.}}$
$D\pi$	10.84	11.19	23.17	44.14
$D^*\pi$	54.10	55.83	21.20	40.39
$D\eta$	11.86	12.24	2.23	4.25
D_sK	8.73	9.01	3.11	5.92
$D^*\eta$	9.65	9.95	1.10	2.10
$D_1\pi$	0.28	0.29	1.67	3.18
$D_1'\pi$	1.44	1.49	0.0071	0.01
$D_2^*\pi$	0.01	0.00	0.0066	0.01
total	96.91		52.49	

Table 4.17. Open-flavor strong decay widths, in MeV, and branchings, in %, of the $D^*(2600)$ meson with quantum numbers $nJ^P = 2\,1^-$.

assignments. It is important to take into account the experimental observations about these two mesons reported in Ref. [133] before assigning any quantum number. First, despite of the two mesons are close in mass and their total widths are similar, they are considered different particles. Second, the helicity-angle distribution of both mesons is compatible with an angular momentum between quark and antiquark equal to $L = 2$. Third, the $D_J(2750)$ and $D_J^*(2760)$ mesons have been seen only in the decay mode $D^*\pi$ and $D\pi$, respectively. And finally, the following branching ratio has been measured

$$\frac{\mathcal{B}(D_J^*(2760)^0 \to D^+\pi^-)}{\mathcal{B}(D_J(2750)^0 \to D^{*+}\pi^-)} = 0.42 \pm 0.05 \pm 0.11. \tag{4.56}$$

These data allow two scenarios. The first one in which the $D_J(2750)$ has quantum numbers $nJ^P = 1\,2^-$ or $3\,1^-$ and the $D_J^*(2760)$ meson is a $1\,3^-$ state. And the second one in which the $D_J(2750)$ meson has quantum numbers $nJ^P = 1\,2^-$ or $1\,3^-$ and the $D_J^*(2760)$ meson is a $3\,1^-$ state. Tables 4.18 and 4.19 show the open-flavor strong decays of both mesons taking into account the two allowed scenarios. We concentrate on the prediction of the $^3P_0$ decay model to distinguish between the different quantum numbers. The model prediction for the mass of the $nJ^P = 3\,1^-$ state is 2935 MeV, which is larger than those of the $D_J(2750)$ and $D_J^*(2760)$ mesons. Moreover, the theoretical decay width for the $nJ^P = 3\,1^-$ state considering that this is either the $D_J(2750)$ or $D_J^*(2760)$ meson is $\sim$300 MeV, in strong disagreement with the experimental data. This rules out the scenario 2, where the $D_J^*(2760)$ meson is considered as the $nJ^P = 3\,1^-$ state, and simplifies the scenario 1, where the $D_J(2750)$ meson as the $nJ^P = 1\,2^-$ state and the $D_J^*(2760)$ meson as the $nJ^P = 1\,3^-$ state seem the most plausible assignments. The $^3P_0$ model, assuming the possible assignment, gives a total width of 230 MeV and 116 MeV for the $D_J(2750)$ and $D_J^*(2760)$ meson, respectively. We obtain a value of 0.68 for the branching ratio written in Eq. (4.56).

Two new charmed-strange resonances, $D_{s1}^*(2710)$ and $D_{sJ}^*(2860)$, have been observed by the BaBar Collaboration in both DK and D^*K channels [135]. The

	$D_J(2750)$ as $nJ^P = 1\,2^-$				$D_J(2750)$ as $nJ^P = 3\,1^-$				$D_J^*(2760)$ as $nJ^P = 1\,3^-$			
Channel	$\Gamma_{^3P_0}$	$\mathcal{B}_{^3P_0}$	$\Gamma_{\rm Mic.}$	$\mathcal{B}_{\rm Mic.}$	$\Gamma_{^3P_0}$	$\mathcal{B}_{^3P_0}$	$\Gamma_{\rm Mic.}$	$\mathcal{B}_{\rm Mic.}$	$\Gamma_{^3P_0}$	$\mathcal{B}_{^3P_0}$	$\Gamma_{\rm Mic.}$	$\mathcal{B}_{\rm Mic.}$
$D\pi$	-	-	-	-	25.87	7.64	16.17	12.00	48.37	41.55	0.13	1.62
$D^*\pi$	71.11	30.93	6.14	10.01	24.89	7.35	0.01	0.01	43.44	37.31	0.16	1.99
$D\eta$	-	-	-	-	13.90	4.11	5.93	4.40	7.08	6.08	0.04	0.50
D_sK	-	-	-	-	34.81	10.29	11.43	8.48	2.68	2.29	0.0049	0.06
$D_0^*\pi$	0.92	0.40	0.49	0.80	-	-	-	-	-	-	-	-
$D^*\eta$	4.01	1.75	1.13	1.84	10.21	3.02	0.44	0.33	2.78	2.39	0.12	1.49
$D_1\pi$	3.91	1.70	2.96	4.82	154.29	45.59	77.47	57.49	0.88	0.76	2.22	27.59
$D_1'\pi$	0.14	0.06	0.08	0.13	1.30	0.38	5.50	4.08	1.06	0.91	1.64	20.38
$D_2^*\pi$	0.95	0.41	3.74	6.10	3.38	1.00	1.92	1.43	3.03	2.60	3.36	41.75
D_s^*K	0.81	0.35	0.91	1.48	13.41	3.96	0.45	0.33	0.56	0.48	0.0018	0.02
$D_sK_0^*$	0.35	0.15	0.04	0.07	-	-	-	-	-	-	-	-
$D\rho$	113.28	49.28	36.34	59.22	44.04	13.01	12.10	8.98	5.42	4.66	0.28	3.48
$D\omega$	34.43	14.97	9.53	15.53	12.36	3.65	3.33	2.47	1.13	0.97	0.09	1.12
total	229.86		61.37		338.46		134.75		116.41		8.05	

Table 4.18. (Scenario 1) Open-flavor strong decay widths, in MeV, and branchings, in %, of the $D_J(2750)$ and $D_J^*(2760)$ mesons with quantum numbers $nJ^P = 1\,2^-$ or $3\,1^-$ and $1\,3^-$, respectively.

	$D_J(2750)$ as $nJ^P = 1\,2^-$				$D_J(2750)$ as $nJ^P = 1\,3^-$				$D_J^*(2760)$ as $nJ^P = 3\,1^-$			
Channel	$\Gamma_{^3P_0}$	$\mathcal{B}_{^3P_0}$	$\Gamma_{\rm Mic.}$	$\mathcal{B}_{\rm Mic.}$	$\Gamma_{^3P_0}$	$\mathcal{B}_{^3P_0}$	$\Gamma_{\rm Mic.}$	$\mathcal{B}_{\rm Mic.}$	$\Gamma_{^3P_0}$	$\mathcal{B}_{^3P_0}$	$\Gamma_{\rm Mic.}$	$\mathcal{B}_{\rm Mic.}$
$D\pi$	-	-	-	-	46.32	43.03	0.07	1.05	24.22	7.15	16.46	12.14
$D^*\pi$	71.11	30.93	6.14	10.01	40.83	37.93	0.07	1.05	23.94	7.07	0.02	0.01
$D\eta$	-	-	-	-	6.48	6.01	0.05	0.75	13.34	3.94	5.99	4.42
D_sK	-	-	-	-	2.36	2.18	0.0052	0.08	35.52	10.49	11.99	8.84
$D_0^*\pi$	0.92	0.40	0.49	0.80	-	-	-	-	-	-	-	-
$D^*\eta$	4.01	1.75	1.13	1.84	2.36	2.18	0.12	1.80	10.28	3.04	0.41	0.30
$D_1\pi$	3.91	1.70	2.96	4.82	0.74	0.68	1.84	27.63	151.33	44.69	73.97	54.54
$D_1'\pi$	0.14	0.06	0.08	0.13	0.92	0.85	1.47	22.07	1.27	0.37	5.39	3.97
$D_2^*\pi$	0.95	0.41	3.74	6.10	2.43	2.25	2.73	41.05	4.22	1.25	4.49	3.31
D_s^*K	0.81	0.35	0.91	1.48	0.46	0.42	0.0016	0.02	14.54	4.29	0.49	0.36
$D_sK_0^*$	0.35	0.15	0.04	0.07	-	-	-	-	-	-	-	-
$D\rho$	113.28	49.28	36.34	59.22	4.01	3.72	0.23	3.45	46.68	13.78	12.85	9.48
$D\omega$	34.43	14.97	9.53	15.53	0.81	0.75	0.07	1.05	13.31	3.93	3.56	2.63
total	229.86		61.37		107.64		6.66		338.63		135.62	

Table 4.19. (Scenario 2) Open-flavor strong decay widths, in MeV, and branchings, in %, of the $D_J(2750)$ and $D_J^*(2760)$ mesons with quantum numbers $nJ^P = 1\,2^-$ or $1\,3^-$ and $3\,1^-$, respectively.

available experimental results on these two states are

$$\begin{aligned} M(D_{s1}^*(2710)^+) &= 2710 \pm 2^{+12}_{-7}\,\text{MeV}, \qquad \Gamma(D_{s1}^*(2710)^+) = 149 \pm 7^{+39}_{-52}\,\text{MeV}, \\ M(D_{sJ}^*(2860)^+) &= 2862 \pm 2^{+5}_{-2}\,\text{MeV}, \qquad \Gamma(D_{sJ}^*(2860)^+) = 48 \pm 3 \pm 6\,\text{MeV}, \end{aligned} \tag{4.57}$$

with respect masses and widths, and the next branching ratios

$$\frac{\mathcal{B}(D_{s1}^*(2710)^+ \to D^*K)}{\mathcal{B}(D_{s1}^*(2710)^+ \to DK)} = 0.91 \pm 0.13 \pm 0.12,$$

	$D_{s1}^*(2710)$ as $nJ^P = 2\,1^-$			
Channel	$\Gamma_{^3P_0}$	$\mathcal{B}_{^3P_0}$	$\Gamma_{\text{Mic.}}$	$\mathcal{B}_{\text{Mic.}}$
D^0K^+	18.30	10.72	0.55	0.62
D^+K^0	18.69	10.95	0.54	0.61
$D^{*0}K^+$	49.27	28.85	0.02	0.02
$D^{*+}K^0$	48.51	28.41	0.03	0.03
$D_s\eta$	3.67	2.15	0.30	0.34
$D_s^*\eta$	9.51	5.57	0.03	0.03
$D^*K_0^*$	22.80	13.35	87.21	98.35
total	170.76		88.68	

Table 4.20. Open-flavor strong decay widths, in MeV, and branchings, in %, of the $D_{s1}^*(2710)$ meson with quantum numbers $nJ^P = 2\,1^-$.

$$\frac{\mathcal{B}(D_{sJ}^*(2860)^+ \to D^*K)}{\mathcal{B}(D_{sJ}^*(2860)^+ \to DK)} = 1.10 \pm 0.15 \pm 0.19, \tag{4.58}$$

with $DK = D^+K^0 + D^0K^+$ and $D^*K = D^{*+}K^0 + D^{*0}K^+$. In the D^*K channel, the BaBar Collaboration have also found the evidence for the $D_{sJ}(3040)$ whose mass and width are $3044 \pm 8^{+30}_{-5}$ MeV and $239 \pm 35^{+46}_{-42}$ MeV, respectively. There is no signal of $D_{sJ}(3040)$ in the DK channel [135].

It is commonly believed that the $D_{s1}^*(2710)$ is the first excitation of the D_s^* meson. Our quark model predicts a mass in this energy range but also for the 2^1S_0 state. However, if the $D_{s1}^*(2710)$ had quantum numbers $J^P = 0^-$ it would not decay into DK final state, and this is incompatible with the branching ratio measured experimentally. Therefore, Table 4.20 shows the open-flavor strong decays of the $D_{s1}^*(2710)$ meson as the 2^3S_1 state. Both decay models give a large total width, being the prediction of the $^3P_0$ model in agreement with the experimental data. The result of the microscopic model is lower than the experimental one. The branching ratio of Eq. (4.58) predicted by both decay models is

$$\frac{\mathcal{B}(D_{s1}^*(2710)^+ \to D^*K)}{\mathcal{B}(D_{s1}^*(2710)^+ \to DK)} = \begin{cases} 0.91 \pm 0.13 \pm 0.12 & \text{Exp.} \\ 2.64 & ^3P_0 \\ 0.05 & \text{Mic.} \end{cases} \tag{4.59}$$

which are in strong disagreement with the experimental value. We observe a strong coupling of the 2^3S_1 state with the $D^*K_0^*$ final channel in the microscopic model but also a moderate coupling is noticed with the $^3P_0$ model.

Once the assignment of the $D_{s1}^*(2710)$ is done and according to the observed decay modes, the possible spin-parity quantum numbers of the $D_{sJ}^*(2860)$ are $J^P = 1^-$, 2^+ and 3^-. The 2^+ assignment is disfavored because it would be the excitation of the $D_{s2}^*(2573)$ meson and our model predicts a mass about 3.1 GeV. In Table 4.21 we show the open-flavor strong decays of the $D_{sJ}^*(2860)$ as the third excitation of the 1^- meson and as the ground state of 3^- meson. The comparison between experimental data and

	$D^*_{sJ}(2860)$ as $nJ^P = 3\,1^-$				$D^*_{sJ}(2860)$ as $nJ^P = 1\,3^-$			
Channel	$\Gamma_{^3P_0}$	$\mathcal{B}_{^3P_0}$	$\Gamma_{\rm Mic.}$	$\mathcal{B}_{\rm Mic.}$	$\Gamma_{^3P_0}$	$\mathcal{B}_{^3P_0}$	$\Gamma_{\rm Mic.}$	$\mathcal{B}_{\rm Mic.}$
D^0K^+	26.28	17.15	0.19	0.15	19.60	23.03	1.79	18.38
D^+K^0	27.06	17.66	0.20	0.16	18.97	22.29	1.65	16.94
$D^{*0}K^+$	19.28	12.58	3.67	2.92	13.38	15.71	0.19	1.92
$D^{*+}K^0$	19.15	12.50	3.58	2.84	12.79	15.03	0.16	1.64
$D_s\eta$	12.12	7.92	0.42	0.33	1.06	1.24	0.03	0.31
$D^*_s\eta$	5.06	3.30	0.06	0.05	0.35	0.41	0.0036	0.03
$D^*K^*_0$	7.15	4.67	117.55	93.36	16.16	18.99	5.92	60.78
DK^*	37.10	24.22	0.24	0.19	2.81	3.30	0.0007	0.00
total	153.19		125.91		85.12		9.74	

Table 4.21. Open-flavor strong decay widths, in MeV, and branchings, in %, of the $D^*_{sJ}(2860)$ meson with quantum numbers $nJ^P = 3\,1^-$ or $1\,3^-$.

	$D_{sJ}(3040)$ as $nJ^P = 3\,1^+$				$D_{sJ}(3040)$ as $nJ^P = 4\,1^+$			
Channel	$\Gamma_{^3P_0}$	$\mathcal{B}_{^3P_0}$	$\Gamma_{\rm Mic.}$	$\mathcal{B}_{\rm Mic.}$	$\Gamma_{^3P_0}$	$\mathcal{B}_{^3P_0}$	$\Gamma_{\rm Mic.}$	$\mathcal{B}_{\rm Mic.}$
$D^{*0}K^+$	12.56	4.16	12.23	10.05	26.49	6.13	10.83	3.14
$D^{*+}K^0$	12.66	4.20	12.16	9.99	26.99	6.24	10.86	3.15
DK^*_0	0.76	0.25	3.51	2.88	0.30	0.07	17.61	5.10
$D^*_s\eta$	3.26	1.08	1.95	1.60	4.97	1.15	2.92	0.85
$D^*K^*_0$	0.02	0.01	1.08	0.89	1.10	0.25	0.70	0.20
DK^*	44.28	14.69	0.30	0.25	100.38	23.21	8.00	2.32
$D^*_{s0}\eta$	0.97	0.32	0.43	0.35	1.66	0.38	0.03	0.01
D^*_0K	2.81	0.93	0.08	0.07	2.31	0.53	5.90	1.71
D^*K^*	156.78	52.00	13.43	11.03	130.91	30.27	20.78	6.02
D_1K	39.81	13.20	58.04	47.67	11.58	2.68	26.01	7.54
D'_1K	0.69	0.23	0.40	0.33	0.04	0.01	5.27	1.53
D^*_2K	11.19	3.71	12.63	10.37	123.74	28.61	235.67	68.30
$D_s\phi$	15.54	5.15	4.73	3.88	1.97	0.45	0.15	0.04
$D_{s1}\eta$	0.19	0.07	0.78	0.64	0.09	0.02	0.30	0.09
total	301.52		121.75		432.54		345.03	

Table 4.22. Open-flavor strong decay widths, in MeV, and branchings, in %, of the $D_{sJ}(3040)$ meson with quantum numbers $nJ^P = 3\,1^+$ or $4\,1^+$.

our predictions is as follow

$$\Gamma(D^*_{sJ}(2860)) = \begin{cases} 48 \pm 3 \pm 6\,\text{MeV} & \text{Exp.} \\ \begin{bmatrix} 153.19 & 3\,1^- \\ 85.12 & 1\,3^- \end{bmatrix} & {}^3P_0 \\ \begin{bmatrix} 125.91 & 3\,1^- \\ 9.74 & 1\,3^- \end{bmatrix} & \text{Mic.} \end{cases}$$

$$\frac{\mathcal{B}(D_{sJ}^*(2860)^+ \to D^*K)}{\mathcal{B}(D_{sJ}^*(2860)^+ \to DK)} = \begin{cases} 1.10 \pm 0.15 \pm 0.19 & \text{Exp.} \\ \begin{bmatrix} 0.72 & 3\,1^- \\ 0.68 & 1\,3^- \end{bmatrix} & {}^3P_0 \\ \begin{bmatrix} 18.58 & 3\,1^- \\ 0.10 & 1\,3^- \end{bmatrix} & \text{Mic.} \end{cases} \tag{4.60}$$

The microscopic model does not give satisfactory results. Following the $^3P_0$ model, the $nJ^P = 1\,3^-$ assignment appears to be the most plausible, with reasonable values for the total decay width and the branching ratio. The total width might not be sufficient to discard the other possibility, moreover, the ratio is in reasonable agreement with the experimental one. Therefore, to distinguish between the two possibilities further experimental studies in the remaining decay modes $D_s\eta$, $D_s^*\eta$, $D^*K_0^*$ and DK^* are needed. The $nJ^P = 3\,1^-$ state has traces in $D_s\eta$ and $D_s^*\eta$ while the $1\,3^-$ state has none of them. Moreover, the dominant decay mode between $D^*K_0^*$ and DK^* changes depending on the assignment.

The mean $2P$ multiplet mass is predicted to be near the mass of the $D_{sJ}(3040)$ resonance. Therefore, the possible assignments are the 0^+ which only decays into DK, the 1^+ which only decays into D^*K and the 2^+ which decays into DK and D^*K. The only decay mode in which $D_{sJ}(3040)$ has been seen until now is the D^*K, and so the most possible assignment is that the $D_{sJ}(3040)$ meson being the next excitation in the 1^+ channel. Table 4.22 shows the open-flavor strong decays of the $D_{sJ}(3040)$ meson as the $nJ^P = 3\,1^+$ or $4\,1^+$ state. The mass of $D_{sJ}(3040)$ is large enough to allow decays to $(D_0^*, D_1')K$, $(D_1, D_2^*)K$ and $D_{s0}^*\eta$, with different features in the two cases. Other allowed modes are DK^* and $D_s\phi$. Its total width, $239 \pm 35^{+46}_{-42}$ MeV, indicates that this state should be very broad. The $nJ^P = 3\,1^+$ and $4\,1^+$ states seem to have large total decay widths according to the prediction of the $^3P_0$ model, being that of the $nJ^P = 3\,1^+$ state in better agreement with the experimental data.

4.5.4 Results for Υ states

Table 4.23 shows the strong decay widths predicted by the $^3P_0$ and the microscopic models for the 1^{--} $b\bar{b}$ states which are well established in PDG [78]. Following Eq. (4.52), the value of γ of the $^3P_0$ model is 0.205. The notation B_1B_2 includes the $B_1\bar{B}_2$ and $\bar{B}_1B_2$ combination of well defined CP quantum numbers. For the kinematics we use experimental masses.

One can see that the general trend of the total decay widths is well reproduced in the case of the $^3P_0$ model. The total widths are lower in the microscopic model without improving the agreement with the experimental data.

The $\Upsilon(4S)$ is the first 1^{--} bottomonium state above the BB threshold, 10.56 GeV. This state only decays into the BB final channel. We have incorporated the isospin breaking via the experimental masses. In Table 4.23 we compare the theoretical branching fractions with the experimental ones for the two possible channels B^+B^- and $B^0\bar{B}^0$. One can see that despite the mass of the $\Upsilon(4S)$ is very close to the thresholds, the difference between branching fractions of both channels is negligible due to the small difference between masses of the $B^\pm$ and B^0. Our branching fractions are in agreement with the experimental data in both decay models although the width predicted by the

Meson	State	Channel	$\Gamma_{^3P_0}$	$\mathcal{B}_{^3P_0}$	$\Gamma_{\rm Mic.}$	$\mathcal{B}_{\rm Mic.}$	$\mathcal{B}_{\rm Exp.}$ [78]
$\Upsilon(4S)$	4^3S_1	B^+B^-	10.41	50.54	1.31	50.58	51.6 ± 0.6
		$B^0\bar{B}^0$	10.18	49.46	1.28	49.42	48.4 ± 0.6
		BB	20.59	100	2.59	100	> 96
20.5 ± 2.5		total	20.59		2.59		
$\Upsilon(10860)$	5^3S_1	BB	6.22	22.29	3.55	11.21	5.5 ± 1.0
		BB^*	11.83	42.41	13.78	43.54	13.7 ± 1.6
		B^*B^*	0.09	0.32	12.17	38.45	38.1 ± 3.4
		B_sB_s	0.96	3.45	0.014	0.04	0.5 ± 0.5
		$B_sB_s^*$	1.15	4.11	0.37	1.17	1.4 ± 0.6
		$B_s^*B_s^*$	7.65	27.42	1.77	5.59	17.4 ± 2.7
		$B_s^{(*)}B_s^{(*)}$	9.76	34.98	2.15	6.80	19.3 ± 2.9
55 ± 28		total	27.89		31.65		
$\Upsilon(11020)$	6^3S_1	BB	4.18	5.28	0.72	3.24	
		BB^*	15.49	19.57	6.30	28.34	
		BB_1	40.08	50.64	2.70	12.14	
		BB_1'	3.95	4.98	0.62	2.79	
		B^*B^*	11.87	14.99	11.43	51.42	
		B_sB_s	0.07	0.09	0.20	0.90	
		$B_sB_s^*$	1.50	1.89	0.23	1.03	
		$B_s^*B_s^*$	2.02	2.56	0.031	0.14	
79 ± 16		total	79.16		22.23		

Table 4.23. Open-flavor strong decay widths, in MeV, and branchings, in %, of Υ states. Experimental data are taken from Ref. [78].

microscopic model is quite small.

The possible two-body final states of the $\Upsilon(5S)$ are BB, BB^*, B^*B^*, B_sB_s $B_sB_s^*$ $B_s^*B_s^*$. Despite the $^3P_0$ model predicts a total width and branching fractions in reasonable agreement with the experimental data, there are two theoretical values that strongly disagree with the experimental ones. On one hand, the channel B^*B^*, being dominant according to the experimental data, appears suppressed in the $^3P_0$ model. This is due to the small value of the overlap integral between wave functions. On the other hand, the branching fraction $\mathcal{B}(\Upsilon(5S) \to B_s^{(*)}B_s^{(*)})$ is about a factor 2 higher than that measured experimentally. We have recovered a reasonable width with the the microscopic model although the branchings are not good.

There is no data about the open-flavor strong decays of the $\Upsilon(6S)$ resonance. Only its total width has been reported in the PDG. Whereas the $^3P_0$ model predicts a total width in good agreement with the experimental one, the microscopic model predicts one too small. The final channels BB^*, BB_1 and B^*B^* are dominant according with both decay models.

4.6 Charmonium resonances in the string breaking region

The breaking of the color electric string between two static sources is a phenomenon predicted by QCD and it is the basis of the meson decay and the hadronization process. Although there is no analytical proof, it is a general belief that confinement merges from the force between the gluon color charges. When two quarks are separated, due to the non-Abelian character of the theory, the gluon fields self interact forming color strings which brings the quarks together. In a pure gluon gauge theory the potential energy of the $q\bar{q}$ pair grows linearly with the quark-antiquark distance. However in full QCD the presence of sea quarks may soften the linear potential, due to the screening of the color charges, and eventually leads to the breaking of the string.

Lattice QCD calculations with dynamical fermions indicate that color screening effects on the linear potential do exist at large distances and can be parametrized in terms of a screening length μ^{-1} [201]. Recently string breaking effects have been shown for $n_f = 2$ lattice QCD [68].

From a phenomenological point of view the screening effects can be related to properties of the quarkonium system. In fact, the knowledge of the properties of the high excited quarkonium states may help to determine the form of the confinement in this region.

The Belle Collaboration have very recently reported a measurement of the exclusive $e^+e^- \to \Lambda_c\bar{\Lambda}_c$ cross section [87]. A clear peak at $M = 4634^{+8+5}_{-7-8}\,\mathrm{MeV}$ is observed. Besides this significant near threshold enhancement, the cross section shows several structures up to 5.4 GeV. Similar structures has been observed in the exclusive measurements of the $e^+e^- \to D^{*\pm}D^{*\mp}$ cross section using initial state radiation [202] and in the analysis of the $e^+e^- \to J/\psi\pi\pi$ data [89].

These data have been analyzed by different authors. Van Beveren *et al.* [203, 204] conclude that the near threshold enhancement can be explained as a combined effect of a normal threshold behavior and a sub-threshold zero in the amplitude at 4.5 GeV. Moreover, they found indications for four not very broad (30 − 60 MeV) new $c\bar{c}$ states at 4.79 GeV, 4.87 GeV, 5.13 GeV and 5.29 GeV. On the other hand Bugg [205] concludes from the analysis of the same data that the near threshold enhancement may be interpreted as the $X(4660)$ when a proper form factor is used in the phase space.

Although data are not yet conclusive, the region above the $\Lambda_c\bar{\Lambda}_c$ threshold is of indubitable interest to determine the behavior of the confinement interaction near the string breaking region.

In this section we undertake the study of the $J^{PC} = 1^{--}$ $c\bar{c}$ high excited states up to the string breaking threshold. These are the accessible quantum numbers from the e^+e^- entrance channel. Our aim is to characterize these states (energies, leptonic and strong widths) to look for these properties in future experiments.

In Table 4.24 we summarize our results. Our state with a mass of 4614 MeV is identified with the $X(4630)$ meson. The $X(4660)$ resonance is assigned to the following state in mass, $M = 4641\,\mathrm{MeV}$. In addition we found 14 bound states up to $12\,^3S_1$ and $11\,^3D_1$. Some of them coincide with the ones suggested by [204] although, given the experimental uncertainties, we do not want to stress too much this agreement. The main feature concerning the masses is that as far as we approach to the string breaking threshold the S and D-wave states become more and more degenerated making difficult to separate them experimentally. Moreover the leptonic and strong widths become

State	$M_{\text{The.}}$ (MeV)	$M_{\text{Exp.}}$ (MeV)	$\Gamma_{e^+e^-}$ (keV)	Dominant	$\mathcal{B}$	Γ_{total} (MeV)
$5\,^3S_1$	4614	4634^{+8+5}_{-7-8}	0.57	$D^*D_2^*$	0.41	206.37
$4\,^3D_1$	4641	4664 ± 11	0.31	D^*D^*	0.30	135.06
$6\,^3S_1$	4791	4790	0.42	$D^*D_2^*$	0.33	103.86
$5\,^3D_1$	4810		0.28	D^*D^*	0.40	68.12
		4870				
$7\,^3S_1$	4929		0.32	D^*D^*	0.20	66.45
$6\,^3D_1$	4944		0.24	D^*D^*	0.40	55.93
$8\,^3S_1$	5036		0.24	D^*D^*	0.24	52.95
$7\,^3D_1$	5048		0.20	D^*D^*	0.33	52.35
$9\,^3S_1$	5117		0.17	D^*D^*	0.26	41.23
$8\,^3D_1$	5126	5130	0.16	D^*D^*	0.30	42.19
$10\,^3S_1$	5175		0.12	D^*D^*	0.25	30.24
$9\,^3D_1$	5182		0.11	D^*D^*	0.27	32.39
$11\,^3S_1$	5214		0.07	D^*D^*	0.24	20.21
$10\,^3D_1$	5219		0.07	D^*D^*	0.25	21.29
$12\,^3S_1$	5236		0.03	D^*D^*	0.24	10.15
$11\,^3D_1$	5239		0.03	D^*D^*	0.24	9.98
		5290				

Table 4.24. High excited $J^{PC} = 1^{--}$ $c\bar{c}$ states. Some properties are shown.

smaller. This can be seen in panels (a) and (b) of Fig. 4.6 where, for completeness, we have included the results obtained for the lower 1^{--} $c\bar{c}$ states. The measured strong widths agree reasonably well with our calculation, reaching a maximum around a mass of $M = 4.6\,\text{GeV}$. After this maximum, the widths decrease due to the competition between phase space and meson wave function overlaps. In almost all the resonances the most important decay channel is the D^*D^*. The experimental data around 4.6 GeV is clearly out of the systematic, which maybe an indication of a more complex structure for the $X(4630)$ and $X(4660)$ states.

The situation is similar regarding the leptonic widths shown in panel (b) of Fig. 4.6. As in the former figure we show the results for the lower states together with our current results. Once again the model reproduces the measured widths showing a clear difference between S and D wave states. This behavior is an important tool to assign quantum numbers to the resonances. In particular the measurement of the $X(4360)$ leptonic width will confirm our assignment. As far as we are approaching to the string breaking threshold the widths are narrower and the difference between S and D-wave states become smaller.

In panel (c) of Fig. 4.6 we show the quadratic mean radius for these mesons. As expected these are extended objects with a radius that grows as one gets closer to the string breaking threshold.

Then the scenario drawn from this calculation consists in several narrow resonances near the string breaking threshold which include S and D-wave states. The only possible way to resolve these two angular momentum contributions is to look to some specific ratio, like $R = \frac{\Gamma(X \to DD^*)}{\Gamma(X \to D^*D^*)}$ shown in panel (d) of Fig. 4.6, which range from 1.5

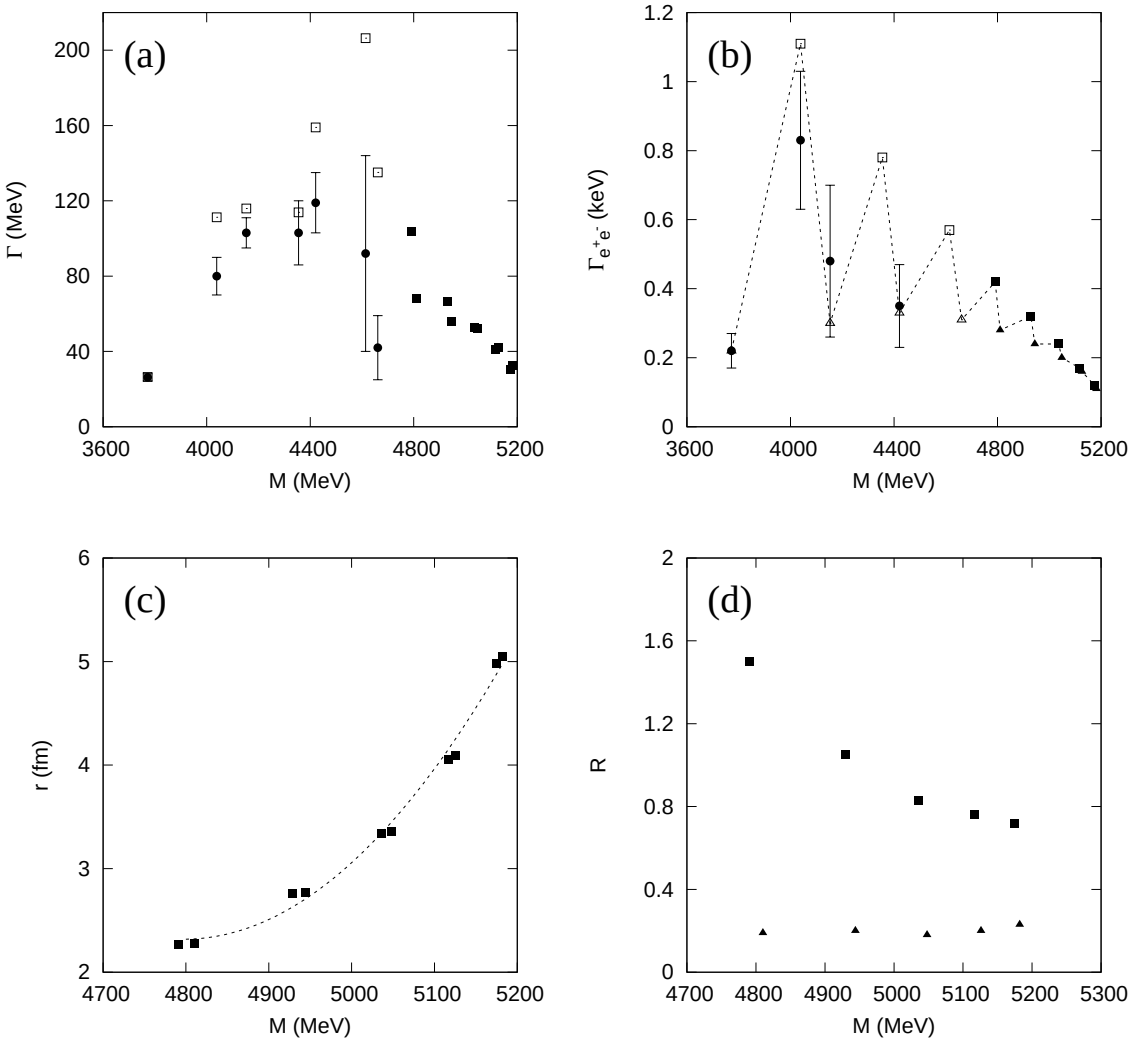

Figure 4.6. **(a):** Total widths, in MeV, of the 1^{--} $c\bar{c}$ states. Solid dots are the experimental data taken from Refs. [78, 87, 206]. Solid (open) squares are our results for the higher (lower) states. **(b):** Leptonic widths, in keV, of the 1^{--} $c\bar{c}$ states. Solid dots are the experimental data taken from Refs. [78, 97]. Solid (open) squares are our results for higher (lower) S-wave states. Solid (open) triangles are our results for higher (lower) D-wave states. **(c):** Solid squares are the theoretical mean square radius, in fm, of the resonances in Table 4.24. **(d):** The ratio $R = \frac{\Gamma(X\to DD^*)}{\Gamma(X\to D^*D^*)}$ predicted by the model is shown by solid squares (triangles) for S-wave (D-wave) states.

to 0.7 for S-wave states and is around 0.2 for D-wave states.

Finally, we compare our results with the $e^+e^- \to J/\psi\pi\pi$ and $e^+e^- \to \Lambda_c\bar{\Lambda}_c$ data. We will use those of van Beveren *et al.* [203, 204] where the subtraction of the non-resonant signal has been carried out assuming Breit Wigner forms for the $c\bar{c}$ resonances. Some of the experimental predicted structures are well reproduced. The most significant differences are the resonance below 4.9 GeV and the one around 5.3 GeV. The discrepancy at 4.9 GeV cannot be explained by interference effects or modifications in the Breit-Wigner shapes because the nearby resonances are too separated, as shown in Fig. 4.7. The discrepancy around 5.3 GeV has a different origin

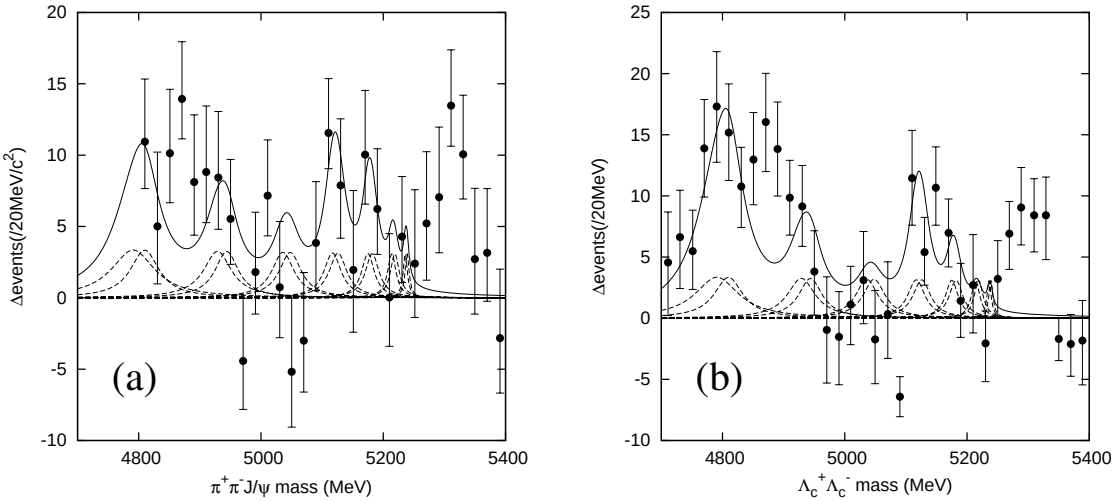

Figure 4.7. Fit to the $J/\psi\pi^+\pi^-$ [203] and the $e^+e^- \to \Lambda_c^+\Lambda_c^-$ [204] data, shown by solid dots, using the resonances from Table 4.24. The solid line shows the full result while the dashed lines show the position of each resonance.

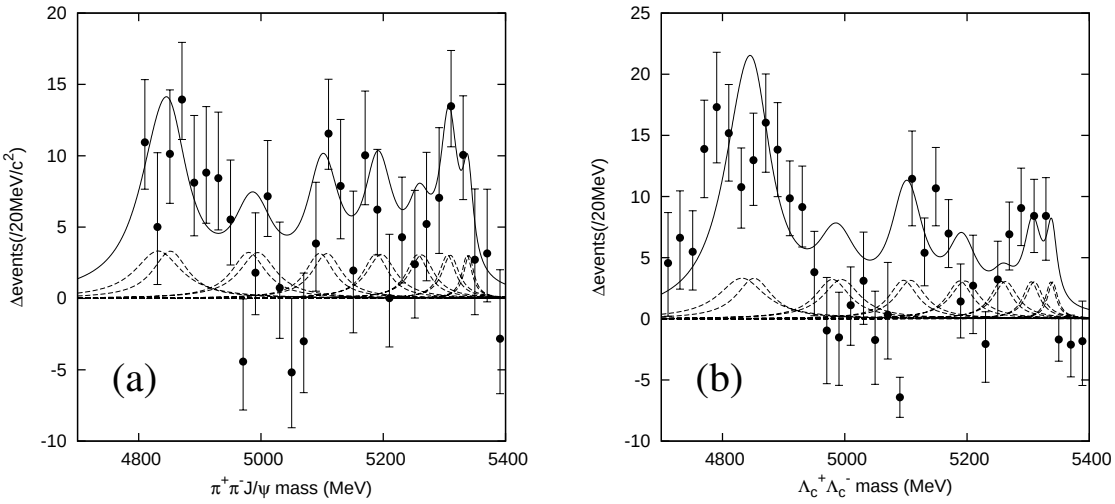

Figure 4.8. Same as in Fig. 4.7 varying the confinement parameters as explained in the text.

because our threshold is below this region.

In order to show the sensitivity of the spectra to the confinement potential parameters we have changed the a_c and μ_c model parameters of the confining interaction, leaving its product constant which guarantees that the slope of the confinement remains the same. The results are shown in Fig. 4.8. With this parametrization we clearly improve the agreement in the 5.3 GeV region, although the precision of the data is not enough to decide about the 4.9 GeV region. The price to pay is to loose part of the consistency with the whole meson spectra. These results show the interest of this region to constrain the confinement interaction.

4.7 Charmonium resonances in e^+e^- exclusive reactions

Exclusive open-charm production in e^+e^- annihilation provides important information on the charm quark dynamics in the $4-5\,\mathrm{GeV}$ puzzling region of the $J^{PC}=1^{--}$ charmonium spectrum. The heaviest well-established $J^{PC}=1^{--}$ charmonium state, $\psi(4415)$, was first observed 30 years ago by the MARK I and DASP Collaborations [207, 208]. Subsequently, e^+e^- annihilation cross section measurements in the region of the $\psi(4415)$ were reported by the Crystall Ball and BES groups [209, 210]. No update of resonance parameters was done until 2005 when an alternative fit to these last data was performed by Seth [84]. Recently the BES Collaboration reported new values for the $\psi(3770)$, $\psi(4040)$, $\psi(4160)$ and $\psi(4415)$ resonance parameters which are derived from a global fit to their cross section measurements [97].

The Belle Collaboration has recently performed measurements of the exclusive cross section for the processes $e^+e^-\to D^0D^-\pi^+$ [211] and $e^+e^-\to D^0D^{*-}\pi^+$ [212] over the center-of-mass energy range $4.0\,\mathrm{GeV}$ to $5.0\,\mathrm{GeV}$. In the first reaction they found a prominent peak in the cross section which is interpreted as the $\psi(4415)$. From the study of the resonant structure in the $\psi(4415)$ decay, they conclude that the final channel $D^0D^-\pi^+$ is reached through the $D\bar{D}_2^*(2460)$ intermediate state. Using a relativistic Breit-Wigner function parametrization they obtain the value of the $\mathcal{B}(\psi(4415)\to D\bar{D}_2^*(2460))\times\mathcal{B}(\bar{D}_2^*(2460)\to D\pi^+)$ product of branching fractions and the mass and width of the $\psi(4415)$. From the measurement of the $e^+e^-\to D^0D^{*-}\pi^+$ exclusive cross section reported in Ref. [212], they provide upper limits on the peak cross section for the process $e^+e^-\to X\to D^0D^{*-}\pi^+$ where X denotes $X(4260)$, $X(4360)$, $\psi(4415)$, $X(4630)$ and $X(4660)$. Although only the value concerning the $\psi(4415)$ is significant.

We have seen that our assignment of the $\psi(4415)$ as a D-wave state leaving the $4S$ state for the $X(4360)$ agrees with the last measurements of the leptonic width [97]. Now we want to perform a study of the two above reactions to test if our result is also compatible with the measurements of Belle.

We assume the reaction $e^+e^-\to X\to DD^{(*)}\pi$ and parametrize the cross section using a relativistic Breit-Wigner function including Blatt-Weisskopf corrections. The relativistic Breit-Wigner amplitude for the process $e^+e^-\to$ *resonance* $\to$ *hadronic final state* f at center-of-mass energy $\sqrt{S}$ can be written as

$$\mathcal{T}_r^f(\sqrt{S})=\frac{M_r\sqrt{\Gamma_r^{ee}\Gamma_r^f}}{S-M_r^2+iM_r\Gamma_r}e^{i\delta_r}, \tag{4.61}$$

where r indicates the resonance being studied, M_r is the nominal mass, Γ_r is the full width, Γ_r^{ee} is the leptonic width, Γ_r^f is the hadronic width for the decaying channel f and δ_r is a relative phase.

When there are more than one resonance in the same energy range and we measure the same decay channel, the spin-averaged cross section is a coherent sum of the Breit-Wigner amplitudes for each resonance

$$\sigma(\sqrt{S})=\frac{(2J+1)}{(2S_1+1)(2S_2+1)}\frac{16\pi}{S}\left|\sum_r\frac{M_r\sqrt{\Gamma_r^{ee}\Gamma_r^f}}{S-M_r^2+iM_r\Gamma_r}e^{i\delta_r}\right|^2. \tag{4.62}$$

Now, we introduce the energy dependence of the widths following Ref. [97]. The angular momentum dominant partial width of a resonance decaying into one channel is given by [213]

$$\Gamma_r^f(\sqrt{S}) = \hat{\Gamma}_r \frac{Z_f^{2L+1}}{B_L}, \tag{4.63}$$

with Z_f defined as $Z_f \equiv \rho P_f$, where P_f is the decay momentum and ρ is a free parameter whose value is around the range of the interaction (on the order of a few fermis), the physical results are insensitive to its precise value. The energy-dependent partial wave functions $B_L(Z_f)$ are given in Ref. [213] or [214]

$$\begin{aligned} B_0 &= 1, \\ B_1 &= 1 + Z_f^2, \\ B_2 &= 9 + 3Z_f^2 + Z_f^4, \\ B_3 &= 225 + 45Z_f^2 + 6Z_f^4 + Z_f^6, \end{aligned} \tag{4.64}$$

and $\hat{\Gamma}_r$ is related with the partial width at the mass of the resonance, Γ_0, as

$$\hat{\Gamma}_r = \Gamma_0 \frac{B_L(P_0)}{Z_f^{2L+1}(P_0)}. \tag{4.65}$$

Then our final expressions for the partial and total width are given by

$$\begin{aligned} \Gamma_r^f(\sqrt{S}) &= \Gamma_0 \frac{Z_f^{2L+1}(P_f)}{Z_f^{2L+1}(P_0)} \frac{B_L(P_0)}{B_L(P_f)}, \\ \Gamma_r(\sqrt{S}) &= \frac{2M_r}{M_r + \sqrt{S}} \sum_f \Gamma_r^f(\sqrt{S}), \end{aligned} \tag{4.66}$$

where the term $\frac{2M_r}{M_r+\sqrt{S}}$ is a relativistic correction factor [213].

4.7.1 The process $e^+e^- \to D^0D^-\pi^+$

This process has been studied by Pakhlova *et al.* in Ref. [211]. They perform a separate study of the $e^+e^- \to D\bar{D}_2^*(2460)$ and $e^+e^- \to D(D\pi)_{\text{non}-\bar{D}_2^*(2460)}$ concluding that the $e^+e^- \to D^0D^-\pi^+$ is dominated by $X \to D\bar{D}_2^*(2460)$.

Assuming $X \equiv \psi(4415)$ and a relativistic Breit-Wigner function to fit the data, the peak cross section for the process $e^+e^- \to X \to D\bar{D}_2^*(2460)$ is $\sigma(e^+e^- \to \psi(4415)) \times \mathcal{B}(\psi(4415) \to D\bar{D}_2^*(2460)) \times \mathcal{B}(\bar{D}_2^*(2460) \to D\pi^+) = (0.74 \pm 0.17 \pm 0.08)$ nb.

Using that

$$\sigma(e^+e^- \to X) = \frac{12\pi}{m_X^2} \frac{\Gamma_{ee}}{\Gamma_{\text{tot}}}, \tag{4.67}$$

the authors of Ref. [211] estimate $\mathcal{B}(\psi(4415) \to D\bar{D}_2^*(2460)) \times \mathcal{B}(\bar{D}_2^*(2460) \to D\pi^+) = (10.5 \pm 2.4 \pm 3.8)\%$ or $(19.5 \pm 4.5 \pm 9.2)\%$ depending on the different parametrization of the $\psi(4415)$ resonance (Refs. [78] and [97], respectively).

Furthermore, taken from Ref. [78] the branching fraction for $\bar{D}_2^*(2460) \to D\pi^+$, one can estimate $\mathcal{B}(\psi(4415) \to DD_2^*) = 0.47$ using the resonance parameters of Ref. [78]

	$X(4360)$		$\psi(4415)$	
	The.	Exp.	The.	Exp.
Mass (MeV)	4389	$4361 \pm 9 \pm 9$	4426	4415.1 ± 7.9
$\Gamma_{\rm tot}$ (MeV)	113.9	$74 \pm 15 \pm 10$	159.0	71.5 ± 19.0
Γ_{ee} (keV)	0.78	-	0.33	0.35 ± 0.12

Table 4.25. Resonance parameters predicted by our constituent quark model for the $X(4360)$ and $\psi(4415)$. The experimental data are taken from Ref. [78] for $X(4360)$ and Ref. [97] for $\psi(4415)$.

or 0.86 using those of Ref. [97]. Note that there are two final charged states in the calculation of $\mathcal{B}(\bar{D}_2^*(2460) \to D\pi^+)$ and we give the branching fraction of the process $\psi(4415) \to DD_2^*$ in function of the DD_2^* state and not in function of the $D\bar{D}_2^*$ one.

The theoretical calculation of the $e^+e^- \to D^0D^-\pi^+$ cross section can be divided in three steps. The first one is the resonance production $e^+e^- \to X$ which can be given in terms of the leptonic width. The second and third steps are the strong decays $\psi(4415) \to D\bar{D}_2^*(2460)$ and $\bar{D}_2^*(2460) \to D\pi^+$ which can be calculated using the $^3P_0$ model. These two partial widths are involved in the calculation of the Γ_r^f in Eq. (4.62) because in the case under study we have $\Gamma_r^f = \Gamma(X \equiv \psi(4415) \to D\bar{D}_2^*(2460) \to DD\pi^+)$ which is equal to $\Gamma(X \equiv \psi(4415) \to D\bar{D}_2^*(2460)) \times \mathcal{B}(\bar{D}_2^*(2460) \to D\pi^+)$.

We show the prediction of our model for the mass, the total width and the leptonic width of the resonance $\psi(4415)$ in Table 4.25. First, we calculate the branching fractions $\mathcal{B}(D_2^{*+} \to D^0\pi^+)$ and $\mathcal{B}(\bar{D}_2^{*0} \to D^-\pi^+)$

$$\begin{aligned} \mathcal{B}(D_2^{*+} \to D^0\pi^+) &= 0.4295 \ (\text{Exp.: } 0.4368 \pm 0.0901), \\ \mathcal{B}(\bar{D}_2^{*0} \to D^-\pi^+) &= 0.4296 \ (\text{Exp.: } 0.4706 \pm 0.0285), \end{aligned} \tag{4.68}$$

which agree with the experimental values of Ref. [78]. Furthermore the ratios

$$\begin{aligned} R_1 &= \frac{\Gamma(D_2^{*+} \to D^0\pi^+)}{\Gamma(D_2^{*+} \to D^{*0}\pi^+)} = 1.8106 \ (\text{Exp.: } 1.9 \pm 1.1 \pm 0.3), \\ R_2 &= \frac{\Gamma(\bar{D}_2^{*0} \to D^-\pi^+)}{\Gamma(\bar{D}_2^{*0} \to D^{*-}\pi^+)} = 1.8138 \ (\text{Exp.: } 1.56 \pm 0.16), \end{aligned} \tag{4.69}$$

also agree with the experimental data of Ref. [78].

However, when in a similar way we calculate the $\mathcal{B}(\psi(4415) \to DD_2^*)$ we obtain for the $\mathcal{B}(\psi(4415) \to DD_2^*) = 0.15$ which clearly disagrees with the estimation of Ref. [211].

Our model prediction for the cross section is shown in panel (a) of Fig. 4.9. One can see that our result is very far from the experimental data. In order to test if this disagreement is due to the $3D$ character of our resonance we repeat the calculation using the parametrization of Ref. [98] where the $\psi(4415)$ is described as a $4S$ state. Although the result approaches the experimental data, see Fig. 4.9(b), it still does not describe the full cross section. Certainly, the theoretical results have some uncertainties coming either from the wave functions used in the $^3P_0$ model or the leptonic width. To minimized these uncertainties we have used in Fig. 4.9(b) the experimental value for

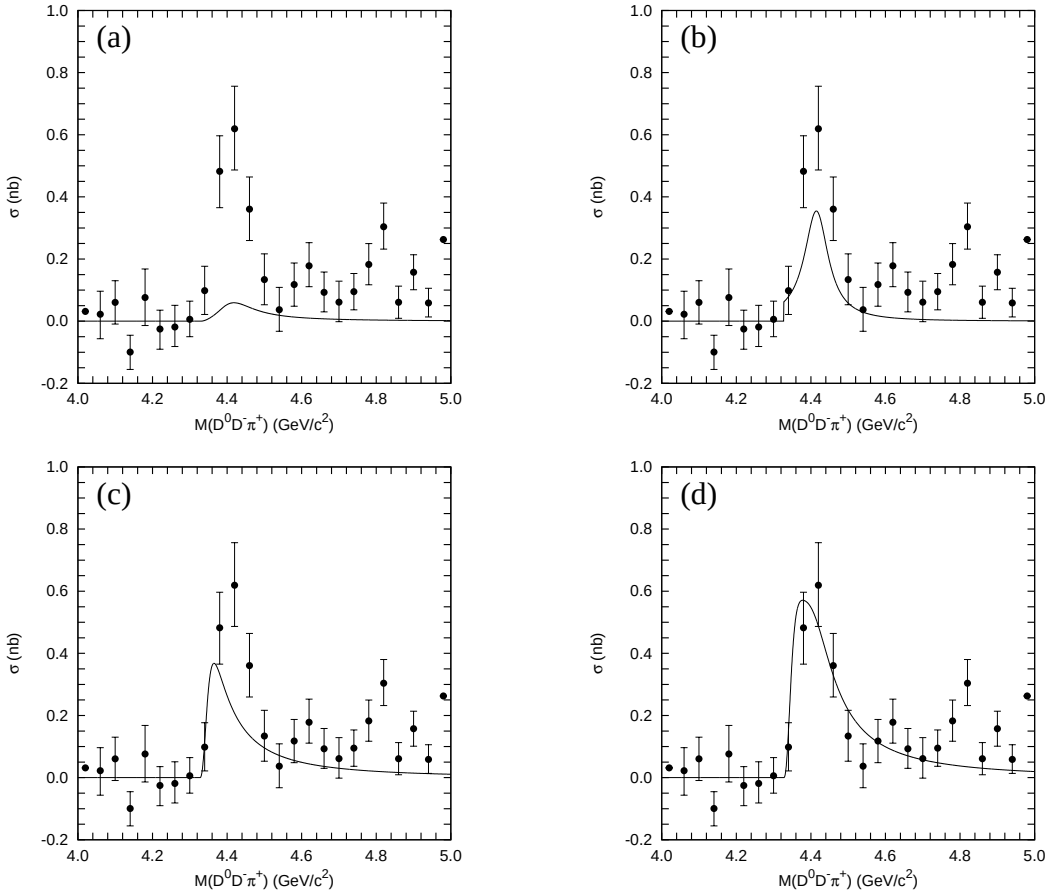

Figure 4.9. **(a)**: Our model prediction with only the resonance $\psi(4415)$. **(b)**: Model prediction of Ref. [98]. **(c)**: Our model prediction with only the resonance $X(4360)$. **(d)**: Our model prediction with the interference of the resonances $X(4360)$ and $\psi(4415)$.

the leptonic width [78]. Using the value $\Gamma_{e^+e^-}$ predicted by the model of Ref. [98], the result would be a factor $\sim$3 smaller.

Taken into account that the energy window around the nominal $\psi(4415)$ mass in the experiment of Ref. [211] is ± 100 MeV, we introduce in the calculation the resonance $X(4360)$ which appears as a $4S$ 1^{--} $c\bar{c}$ meson in our model. The predicted mass, total and leptonic widths are shown in Table 4.25. Panel (c) of Fig. 4.9 shows how this resonance alone cannot reproduce the data but the interference between the $X(4360)$ and $\psi(4415)$, panel (d) of Fig. 4.9, produces a remarkable agreement with the data.

Using the interference of the two resonances, the theoretical value for the exclusive cross section $\sigma(e^+e^- \to D\bar{D}_2^*(2460) \to D^0D^-\pi^+)$ at the $\psi(4415)$ mass is 0.48 nb. It is within the error bars of the experimental value $(0.62^{+0.14}_{-0.13})$ nb. Our result indicates that the two resonances are needed to explain the experimental data.

It is interesting to notice here that the $X(4360)$ has the DD_1 and DD_2^* as the dominant decay channels. Naively one would expect the D^*D^* channel to be dominant since its decay goes through a P-wave while the dominant channels goes through a D-wave. The suppression of the D^*D^* channel is due to the wave functions overlap in the decay process. In Fig. 4.10 we show the width dependence on the mass of the

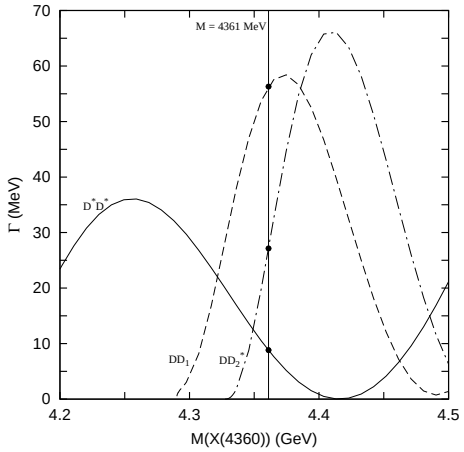

Figure 4.10. Open-flavor strong decay widths, in MeV, of the $X(4360)$ resonance in the D^*D^* (solid line), DD_1 (dashed line) and DD_2^* (dot-dashed line) channels as a function of the mass of the resonance, in GeV.

	$X(4360) \to D^*D^*$			$\psi(4415) \to D^*D^*$		
$^{2J_{BC}+1}l_{J_A}$	J_{BC}	l	$\Gamma_{A\to BC}(J_{BC},l)$ (MeV)	J_{BC}	l	$\Gamma_{A\to BC}(J_{BC},l)$ (MeV)
$^1P_1$	0	1	0.367	0	1	0.031
$^5P_1$	2	1	8.500	2	1	0.006
$^5F_1$	2	3	0.001	2	3	32.519
total			8.868			32.556

Table 4.26. Partial wave decomposition of the D^*D^* decay channel for the $X(4360)$ and the $\psi(4415)$ resonances.

resonance for the three dominant decay channels.

As the $X(4360)$ and $\psi(4415)$ resonances are separated by about 40 MeV and have a width of the order of 100 MeV it might be difficult to separate them from this experiment. Moreover in our model the decay width to the different channels for the $X(4360)$ and the $\psi(4415)$ are similar.

Following Ref. [98] a possible way to distinguish the S or D-wave character of the resonances would be to look at the angular distribution of the D^*D^* decay. In this decay channel there are contributions of three different amplitudes, $^{2J_{BC}+1}l_{J_A}$, as shown in Table 4.26. For an S-wave $c\bar{c}$ state the $^5P_1$ amplitude dominates and the $^5F_1$ amplitude is almost zero while it dominates the decay in the D-wave case. So at energies where the $X(4360)$ dominates the angular distribution should be consistent with a $^5P_1$ partial wave and where the $\psi(4415)$ dominates should be a $^5F_1$.

4.7.2 The process $e^+e^- \to D^0D^{*-}\pi^+$

Using the same philosophy we check the $e^+e^- \to D^0D^{*-}\pi^+$ exclusive cross section measured by the Belle Collaboration [212]. The exclusive cross section shows different structures which can be interpreted as resonances. The experimental analysis of [212] estimates from the amplitude of a relativistic Breit-Wigner function fitted to the data

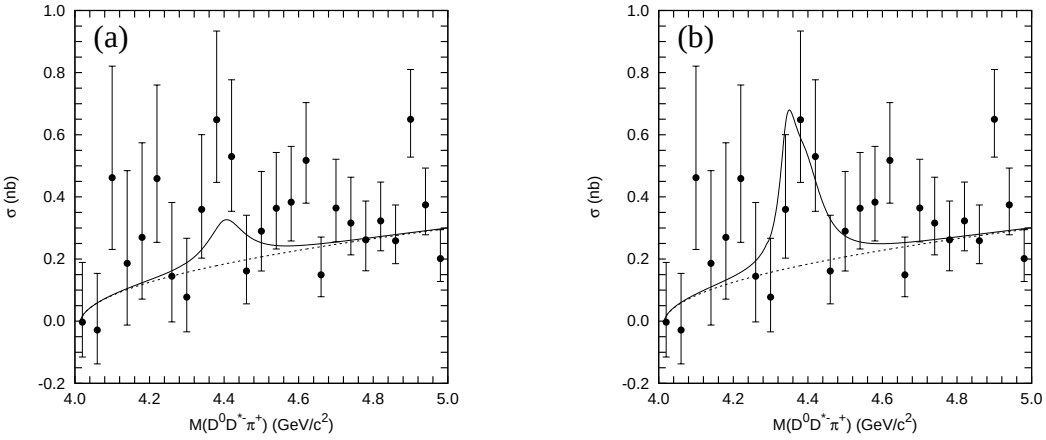

Figure 4.11. **(a)**: Our model prediction with only the resonance $\psi(4415)$. **(b)**: Our model prediction with the interference of the resonances $X(4360)$ and $\psi(4415)$.

	$\mathcal{B}_{ee} \times \mathcal{B}(X \to D^0 D^{*-}\pi^+)$	
X	The. $(\times 10^{-6})$	Exp. $(\times 10^{-6})$
$X(4360)$	0.25	< 0.72
$\psi(4415)$	0.35	< 0.99

Table 4.27. The product $\mathcal{B}_{ee} \times \mathcal{B}(X \to D^0 D^{*-}\pi^+)$ of branching fractions calculated theoretically for $X \equiv X(4360)$ or $X \equiv \psi(4415)$. Experimental data are taken from Ref. [212].

an upper limit of 0.76 nb for the peak cross section at $E_{\rm cm} = M_{\psi(4415)}$.

We calculate the cross section following the same procedure as before. Again the resonance production $e^+e^- \to X$ has been calculated and is given in Table 4.25. Now, the second and third steps are the strong decays $\psi(4415) \to D^{*-}D^{*+}$ and $D^{*+} \to D^0\pi^+$.

The theoretical result for the branching fraction $\mathcal{B}(D^{*+} \to D^0\pi^+)$ is 0.6870, in very good agreement with the experimental value 0.677 ± 0.006 of Ref. [78]. For the other branching fraction, $\mathcal{B}(\psi(4415) \to D^*D^*)$, there is no experimental data. Our theoretical result is 0.20.

The calculation of the cross section including the $\psi(3D)$ resonance with $M = 4426$ MeV alone does not reproduce the full strength of the resonance at $E_{\rm cm} = M_{\psi(4415)}$ and the result is improved when the $X(4360)$ is added. See Fig. 4.11.

From the cross section of Fig. 4.11(b) we calculate the peak cross section for the $e^+e^- \to D^0D^{*-}\pi^+$ process at $M(D^0D^{*-}\pi^+) = 4415$ MeV obtaining 0.45 nb which is compatible with the experimental upper limit 0.76 nb at 90% C.L.

This result is also compatible with the upper limits measured in Ref. [212] for the branchings $\mathcal{B}_{ee} \times \mathcal{B}(X \to D^0D^{*-}\pi^+)$ where X denotes the $X(4360)$ and $\psi(4415)$. In table 4.27 we compare our result with the experimental value.

The $X(4360)$ has been sometimes assigned as an unconventional charmonium state since it was discovered in the $e^+e^- \to \pi^+\pi^-\psi(2S)$ decay [86] and its open-charm decays were assumed to be suppressed. Ref. [212] gives the branching ratio $\mathcal{B}(X \to$

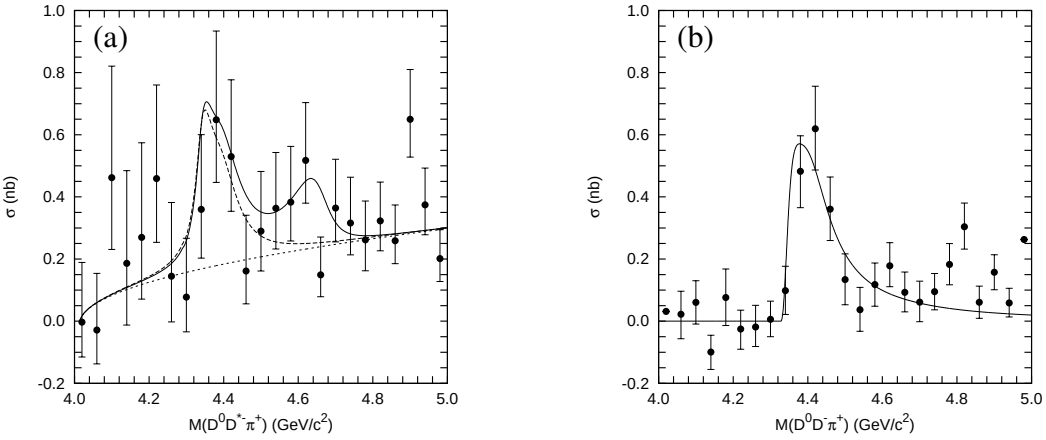

Figure 4.12. **(a)**: Model prediction of the reaction $e^+e^- \to D^0D^{*-}\pi^+$ with the resonances $X(4360)$ and $\psi(4415)$ (dashed line) and including $\psi(5S)$ and $\psi(4D)$ (solid line). **(b)**: Model prediction of the reaction $e^+e^- \to D^0D^-\pi^+$ with the resonances $X(4360)$ and $\psi(4415)$ (dashed line) and including $\psi(5S)$ and $\psi(4D)$ (solid line).

$D^0D^{*-}\pi^+)/\mathcal{B}(X \to \pi^+\pi^-\psi(2S)) < 8$. Since the $X \to \pi^+\pi^-\psi(2S)$ is an OZI suppressed decay the value of this upper limit means that the open-charm $D^{*+}D^{*+}$ where D^{*+} decay into $D^0\pi^+$ should be small, which is actually the case in our model. We get $\Gamma(D^0D^{*-}\pi^+) = \Gamma(X(4360) \to D^{*+}D^{*-})\mathcal{B}(D^{*+} \to D^0\pi^+) = 3.0\,\text{MeV}$ and combined with the experimental information we obtain $\Gamma(X(4360) \to \psi(2S)\pi^+\pi^-) \gtrsim 375\,\text{keV}$ which is in the same order of magnitude that other similar decays. From a theoretical point of view, the decay $(c\bar{c}) \to (c\bar{c})\pi\pi$ is described by QCD multipole expansion (QCDME). In this framework the $\psi(2S) \to \pi\pi J/\psi$ can be explained [215] and give the same order of magnitude. The following chapter is devoted to investigate if we can explain the value of $\Gamma(X(4360) \to \psi(2S)\pi^+\pi^-)$ using QCDME and assuming our assignment $4S\ 1^{--}\ c\bar{c}$ state for the meson $X(4360)$.

Finally, data of Ref. [212] show a bump around 4.6 GeV although data of Ref. [211] do not show this bump. Our model predicts two states $\psi(5S)$ and $\psi(4D)$ in this energy region. The inclusion of these two resonances improves the agreement with the cross section in the bump region, as we can see in panel (a) of Fig 4.12. This bump should not clearly appear in the $e^+e^- \to D^0D^-\pi^+$, as one can see in panel (b) of Fig. 4.12, due to the small width of the $\psi(5S)$ and $\psi(4D)$ states into $DD_2^*(2460)$ channel.

4.8 Description of the $D_{s1}(2536)^+$ decay properties

New data related with the $D_{s1}(2536)$ meson has appeared recently. The BaBar Collaboration has performed a high precision measurement of the $D_{s1}(2536)$ decay width obtaining a value of $(1.03 \pm 0.05 \pm 0.12)\,\text{MeV}$ [198]. Furthermore, the Belle Collaboration has reported the first observation of the $D_{s1}(2536)^+ \to D^+\pi^-K^+$ decay measuring the branching fraction [216]

$$\frac{D_{s1}(2536)^+ \to D^+\pi^-K^+}{D_{s1}(2536)^+ \to D^{*+}K^0} = (3.27 \pm 0.18 \pm 0.37)\%. \tag{4.70}$$

They also measured the ratio of the S-wave amplitude in the $D_{s1}(2536)^+ \to D^{*+}K^0$ decay finding a value of $0.72 \pm 0.05 \pm 0.01$.

In this Section we study, without heavy quark approximations, the reaction $D_{s1}(2536)^+ \to D^+\pi^-K^+$ as well as the angular decomposition of the $D_{s1}(2536)^+ \to D^{*+}K^0$ decay in order to gain insight into the structure of the P-wave charmed-strange mesons. As the $D^+\pi^-$ pair in the final state is the only $D\pi$ combination that cannot come from a D^* resonance, we will describe the reaction through a virtual D^{*0} meson since $M_{D^{*0}} < M_{D^+} + M_{\pi^-}$.

In the model described in this work, a tetraquark $c\bar{s}n\bar{n}$ state has been predicted by Vijande *et al.* in Ref. [217] with quantum numbers $IJ^P = 0\,1^+$ and mass $M = 2841\,\text{MeV}$. If this state is present it should be coupled to the $J^P = 1^+$ $c\bar{s}$ states.

Working in the HQS limit, the $c\bar{s}n\bar{n}$ tetraquark has three different spin states, $|0\,1/2\rangle$, $|1\,1/2\rangle$ and $|1\,3/2\rangle$ where the first index denotes the spin of the $n\bar{n}$ pair and the second the coupling with the $\bar{s}$ spin. Although we use the $^3P_0$ model to calculate the meson decay widths, a description of the coupling between the D_s meson and the tetraquark based on this model is beyond the scope of the present calculation. However, we will use it here to select the dominant couplings and parametrize the vertex as a constant C_S. The model assumes that the $n\bar{n}$ pair created is in a $J = 0$ state which means that the D_s states will only couple with the first tetraquark component which has spin $1/2$ for the three light quarks. In the HQS limit the heavy quark is an spectator and the angular momentum of the light quarks has to be conserved so that the tetraquark will only couple to the $c\bar{s}$ $j_q = 1/2$ state.

For that reason we couple the tetraquark structure with the $j_q = 1/2$ $c\bar{s}$ state. This choice differs from the one performed in Ref. [217] where the tetraquark is only coupled to the $^1P_1$ state and not to the $^3P_1$. However this choice has several advantages: it has the correct heavy quark limit, it may reproduce the narrow width of the $D_{s1}(2536)^+$ state and it is in agreement with the experimental situation which tells us that the prediction of the heavy quark limit is reasonable for the $j_q = 3/2$ state but not for the $j_q = 1/2$ one.

In this scenario we diagonalize the matrix

$$M = \begin{pmatrix} M_{^3P_1} & C_{SO} & \sqrt{\frac{2}{3}}\,C_S \\ C_{SO} & M_{^1P_1} & \sqrt{\frac{1}{3}}\,C_S \\ \sqrt{\frac{2}{3}}\,C_S & \sqrt{\frac{1}{3}}\,C_S & M_{c\bar{s}n\bar{n}} \end{pmatrix}, \tag{4.71}$$

where $M_{^3P_1} = 2571.5\,\text{MeV}$, $M_{^1P_1} = 2576.0\,\text{MeV}$ and $M_{c\bar{s}n\bar{n}} = 2841\,\text{MeV}$ are the masses of the states without couplings, the $C_{SO} = 19.6\,\text{MeV}$ is the coupling induced by the antisymmetric spin-orbit interaction calculated within the model and C_S is the parameter that gives the coupling between the $j_q = 1/2$ component of the $^3P_1$ and $^1P_1$ states and the tetraquark. The value of the parameter $C_S = 224\,\text{MeV}$ is fitted to the mass of the $D_{s1}(2460)$. We get the three eigenstates shown in Table 4.28. There we also show the probabilities of the three components for each state and the relative phases between different components. A 1^+ state with an important component of $c\bar{s}n\bar{n}$ tetraquark structure is found at 2973 MeV.

M (MeV)	$S(^3P_1)$	$P(^3P_1)$	$S(^1P_1)$	$P(^1P_1)$	$S(c\bar{s}n\bar{n})$	$P(c\bar{s}n\bar{n})$
2459	−	55.7	−	18.8	+	25.5
2557	+	27.7	−	72.1	+	0.2
2973	+	16.6	+	9.1	+	74.3

Table 4.28. Masses and probability distributions for the three eigenstates obtained from the coupling of the D_s and tetraquark states. The relative sign to the tetraquark component is also shown.

M (MeV)	Γ (MeV)	R_1	R_2	$R_3(\%)$
Exp.	$1.03 \pm 0.05 \pm 0.12$	1.27 ± 0.21	$0.72 \pm 0.05 \pm 0.01$	$3.27 \pm 0.18 \pm 0.37$
2557	0.99	1.31	0.66	14.07
2593	190.17	1.09	1.00	13.13
2554	11.24	1.11	0.97	13.19

Table 4.29. Width and the three branching ratios defined in the text. The first row shows the experimental data and the second shows our results for the $D_{s1}(2536)$ state given in Table 4.28. For completeness we give in the last two rows the results for the two 1^+ $c\bar{s}$ states predicted by the naive CQM.

We now calculate the different decay widths for the $D_{s1}(2536)^+$ state of Table 4.28. As expected the D^*K decay width is narrow $\Gamma = 0.99\,\text{MeV}$. As the DK decay is suppressed the total width would be mainly given by the D^*K channel and is in the order of the experimental value $\Gamma_{\text{exp}} = (1.03 \pm 0.05 \pm 0.12)\,\text{MeV}$ measured by BaBar [198]. Of course the value strongly depends on the $^3P_0$ γ strength parameter that has been determined by a global fit of the total decay widths of mesons which belong to charmed, charmed-strange, hidden charm and hidden bottom sectors. It also depends on the fact that we have only coupled the 1/2 state with the tetraquark making the remaining state a purest 3/2 which makes it narrower. If we would include an small coupling between the 3/2 state and the tetraquark our $D_{s1}(2536)$ will be broader.

There are two other experimental data that does not depend on the γ parameter, namely the branching ratio [78]

$$R_1 = \frac{\Gamma(D_{s1}(2536)^+ \to D^{*0}K^+)}{\Gamma(D_{s1}(2536)^+ \to D^{*+}K^0)} = 1.27 \pm 0.21, \tag{4.72}$$

and the ratio of S-wave over the full width for the $D^{*+}K^0$ decay [216]

$$R_2 = \frac{\Gamma_S(D_{s1}(2536)^+ \to D^{*+}K^0)}{\Gamma(D_{s1}(2536)^+ \to D^{*+}K^0)} = 0.72 \pm 0.05 \pm 0.01. \tag{4.73}$$

The first branching ratio should be 1 if the isospin symmetry was exact. However the charge symmetry breaking in the phase space makes it different from this value. The effect is sizable since the $D_{s1}(2536)^+$ is close to the D^*K threshold and for this reason it also depends on the details of the D_{s1} wave function. We get for this ratio the value $R_1 = 1.31$ in good agreement with the experimental one.

Notice that in order to get R_2 different from one, we need to have a state with high $j_q = 3/2$ component. In our case we get a value of $R_2 = 0.66$ close to the experimental

one. The fact that our result is smaller than the experimental value indicates that the probability of the $j_q = 3/2$ state is high which is in agreement with the fact that we get a narrow state.

Finally we calculate the branching

$$R_3 = \frac{\Gamma(D_{s1}(2536)^+ \to D^+\pi^- K^+)}{\Gamma(D_{s1}(2536)^+ \to D^{*+}K^0)} = (3.27 \pm 0.18 \pm 0.37)\%. \tag{4.74}$$

The reaction in the numerator goes through a virtual D^{*0} as explained previously and for that reason the branching is small. We get the value $R_3 = 14.1\%$, a factor $3-4$ greater than the experimental one. This value seems not to depend on the details of the D_{s1} wave function.

All these results for the width and the ratios R_1, R_2 and R_3 are summarized in Table 4.29. We also show, for the sake of completeness, the results for the two 1^+ states without coupling to the $c\bar{s}n\bar{n}$ tetraquark. None of these two states agree with the full set of experimental values.

Chapter 5

Hadronic transitions

We call hadronic transition to the reaction

$$\Phi_I \to \Phi_F + h, \tag{5.1}$$

where Φ_I, Φ_F and h stand for the initial state quarkonium, the final state quarkonium and the emitted light hadron(s), respectively. The kinematically allowed final hadron(s), h, are dominated by single particle (π^0, η, ω, ...) or two particle (2π or $2K$) states.

Hadronic transitions are one of the most important decay modes of heavy quarkonium when they are below open-flavor threshold. For instance, the first observed hadronic transition, $\psi(2S) \to J/\psi\pi\pi$, has a branching fraction of approximately 50% [78]. If these rates are large, they will significantly reduce the branching ratios of photon transitions.

However, hadronic transitions do not only concern the states below open-flavor threshold. Most of the XYZ mesons discovered recently have been found through them [13], but also they have been used to find expected charmonium and bottomonium states as the reported discovery of $h_b(1P)$ and $h_b(2P)$ produced via $e^+e^- \to h_b(nP)\pi\pi$ in the $\Upsilon(5S)$ region [140].

In the charmonium and bottomonium systems, the typical mass difference between initial and final mesons is around a few hundred MeV, so that the typical momentum of the light hadron(s), h, is low. Since they are converted from the gluons emitted by the heavy quark (antiquark) in the transition, the momentum of the emitted gluons is also low. Therefore perturbative QCD does not work in the description of these processes and certain nonperturbative approaches are needed for studying hadronic transitions. QCD multipole expansion (QCDME), proposed in Ref. [218] and recently reviewed in Ref. [215], appears as a feasible approach and has worked quite well in predicting hadronic transition rates in the $c\bar{c}$ and $b\bar{b}$ systems [219–222].

We want to apply the theoretical framework of QCDME to calculate the $\pi\pi$ transitions between the triplet states of $c\bar{c}$ and $b\bar{b}$ systems. QCDME approach requires a model for hybrid mesons, and so we propose one coming from our constituent quark model.

5.1 QCD multipole expansion

The multipole expansion has been widely used for studying radiation processes in which the electromagnetic field is radiated from local sources. If the radius, a, of a

local source is smaller than the wave length, λ, of the radiated electromagnetic field such that $a/\lambda \sim ka < 1$ (k stands for the momentum of the photon), ka can be a good expansion parameter and one can, for instance, expand the electromagnetic field in powers of ka.

The nonrelativistic nature of heavy quarkonium provides the possibility to solve the bound state problem through the Schrödinger equation with a given potential model. The typical root-mean-square radius, $a = \sqrt{r^2}$, of the $c\bar{c}$ and $b\bar{b}$ states obtained in this way is about 10^{-1} fm. The hadronic transitions are characterized by the emission of soft gluons with a momentum $k \sim$ a few hundred MeV, so that ka is of the order of 10^{-1} and the idea of multipole radiation can be applied.

The gauge-invariant formulation of multipole expansion within QCD was given by Tung-Mow Yan in Ref. [218]. Following Ref. [215], we introduce

$$\begin{aligned} \Psi(\vec{x},t) &= U^{-1}(\vec{x},t)\psi(x), \\ \frac{\lambda_a}{2}A^{a\prime}_\mu(\vec{x},t) &= U^{-1}(\vec{x},t)\frac{\lambda_a}{2}A^a_\mu(x)U(\vec{x},t) - \frac{i}{g_s}U^{-1}(\vec{x},t)\partial_\mu U(\vec{x},t), \end{aligned} \tag{5.2}$$

where $\psi(x)$ and $A^a_\mu(x)$ are the quark and gluon fields and $U(\vec{x},t)$ is defined by

$$U(\vec{x},t) \equiv P\exp\left[ig_s\int_{\vec{X}}^{\vec{x}}\frac{\lambda_a}{2}\vec{A}^a(\vec{x}',t)\cdot d\vec{x}'\right], \tag{5.3}$$

in which P is the path-ordering operation, the line integral is along the straight-line segment connecting the two ends, $\vec{X} \equiv (\vec{x}_1+\vec{x}_2)/2$ is the center of mass position of Q and $\bar{Q}$, and $\vec{x}$ denotes $\vec{x}_1$ or $\vec{x}_2$. With the transformed fields of Eq. (5.2), the part of the QCD Lagrangian related to the heavy quarks becomes

$$\begin{aligned} \mathcal{L}_Q = &\int\bar{\Psi}\left[\gamma^\mu\left(i\partial_\mu - g_s\frac{\lambda_a}{2}A^{a\prime}_\mu\right) - m\right]\Psi d^3x \\ &- \frac{1}{2}\frac{g_s^2}{4\pi}\int\sum_{a=0}^{8}\bar{\Psi}(\vec{x}_1,t)\gamma^0\frac{\lambda_a}{2}\Psi(\vec{x}_1,t)\frac{1}{|\vec{x}_1-\vec{x}_2|}\bar{\Psi}(\vec{x}_2,t)\gamma^0\frac{\lambda_a}{2}\Psi(\vec{x}_2,t)d^3x_1\,d^3x_2, \end{aligned} \tag{5.4}$$

where $\lambda_0/2 \equiv 1$. Note that the transformed quark field $\Psi(\vec{x},t)$ is dressed with gluons through $U^{-1}(\vec{x},t)$ defined in Eq. (5.3). From Eq. (5.4) the dressed quark field, $\Psi(\vec{x},t)$, is the field that interacts via the static Coulomb potential. In addition, it is the transformed gluon field $A^{a\prime}_\mu$, not the original A^a_μ, that appears in the covariant derivative in Eq. (5.4). $A^{a\prime}_\mu$ contains non-Abelian contributions through $U(\vec{x},t)$.

Based on Eq. (5.4) one can write an effective Lagrangian as

$$\begin{aligned} \mathcal{L}_Q^{\rm eff} = &\int\bar{\Psi}\left[\gamma^\mu\left(i\partial_\mu - g_s\frac{\lambda_a}{2}A^{a\prime}_\mu\right) - m\right]\Psi d^3x \\ &- \frac{1}{2}\int\sum_{a=0}^{8}\bar{\Psi}(\vec{x}_1,t)\gamma^0\frac{\lambda_a}{2}\Psi(\vec{x}_1,t)\,[\delta_{a0}V_1(|\vec{x}_1-\vec{x}_2|) \\ &+(1-\delta_{a0})V_2(|\vec{x}_1-\vec{x}_2|)]\,\bar{\Psi}(\vec{x}_2,t)\gamma^0\frac{\lambda_a}{2}\Psi(\vec{x}_2,t)d^3x_1\,d^3x_2, \end{aligned} \tag{5.5}$$

where $V_1(|\vec{x}_1 - \vec{x}_2|)$ is the static potential, including the confining potential, between Q and $\bar{Q}$ in the color-singlet state, and $V_2(|\vec{x}_1 - \vec{x}_2|)$ is the static potential between Q and $\bar{Q}$ in the color-octet state.

Inside the quarkonium one has that $|\vec{x} - \vec{X}| \leq a$, thus one can expand the gluon field $A^{a\prime}_{\mu}(\vec{x}, t)$ in Taylor series of $(\vec{x} - \vec{X})$ at the center of mass position $\vec{X}$. The Taylor series is an expansion in powers of the operators $(\vec{x} - \vec{X}) \cdot \vec{\nabla}$ and $(\vec{x} - \vec{X}) \times \vec{\nabla}$ applying to the gluon field. After operating on the gluon field with the gluon momentum k, these operators are of the order of ka. This series is QCD multipole expansion. The operation above leads to

$$\begin{aligned} A^{a\prime}_0(\vec{x}, t) &= A^{a\prime}_0(\vec{X}, t) - (\vec{x} - \vec{X}) \cdot \vec{E}^a(\vec{X}, t) + \ldots, \\ \vec{A}^{a\prime}(\vec{x}, t) &= -\frac{1}{2}(\vec{x} - \vec{X}) \times \vec{B}^a(\vec{X}, t) + \ldots, \end{aligned} \tag{5.6}$$

where $\vec{E}^a$ and $\vec{B}^a$ are color-electric and color-magnetic fields, respectively.

The Hamiltonian formulation is more convenient when one wants to apply nonrelativistic perturbation theory. The corresponding Hamiltonian derived from the above formulation is [215]

$$H^{\text{eff}}_{\text{QCD}} = H^{(0)}_{\text{QCD}} + H^{(1)}_{\text{QCD}}, \tag{5.7}$$

where

$$H^{(0)}_{\text{QCD}} = \int \Psi^{\dagger}(\vec{x}_1, t)\Psi(\vec{x}_1, t)\hat{H}\Psi^{\dagger}(\vec{x}_2, t)\Psi(\vec{x}_2, t)d^3x_1 d^3x_2 \tag{5.8}$$

with

$$\hat{H} \equiv -\frac{1}{2m_Q}(\partial_1^2 + \partial_2^2) + V_1(|\vec{x}_1 - \vec{x}_2|) + \sum_{a=1}^{8} \frac{\lambda_a}{2}\frac{\bar{\lambda}_a}{2} V_2(|\vec{x}_1 - \vec{x}_2|) + 2m_Q, \tag{5.9}$$

and

$$\begin{aligned} H^{(1)}_{\text{QCD}} &= H_1 + H_2, \\ H_1 &\equiv Q_a A^a_0(\vec{X}, t), \\ H_2 &\equiv -\vec{d}_a \cdot \vec{E}^a(\vec{X}, t) - \vec{m}_a \cdot \vec{B}^a(\vec{X}, t) + \ldots, \end{aligned} \tag{5.10}$$

in which

$$\begin{aligned} Q_a &\equiv g_E \int \Psi^{\dagger}(\vec{x}, t)\frac{\lambda_a}{2}\Psi(\vec{x}, t)d^3x, \\ \vec{d}_a &\equiv g_E \int (\vec{x} - \vec{X})\Psi^{\dagger}(\vec{x}, t)\frac{\lambda_a}{2}\Psi(\vec{x}, t)d^3x, \\ \vec{m}_a &\equiv \frac{g_M}{2}\int (\vec{x} - \vec{X}) \times \Psi^{\dagger}(\vec{x}, t)\,\vec{\gamma}\,\frac{\lambda_a}{2}\Psi(\vec{x}, t)d^3x, \end{aligned} \tag{5.11}$$

are the color charge, color-electric dipole moment, and color-magnetic dipole moment of the $Q\bar{Q}$ system, respectively. Considering that the heavy quark may have an anomalous magnetic moment, we have taken in Eqs. (5.11) the symbols g_E and g_M to denote the effective coupling constants for the electric and magnetic multipole gluon emissions, respectively.

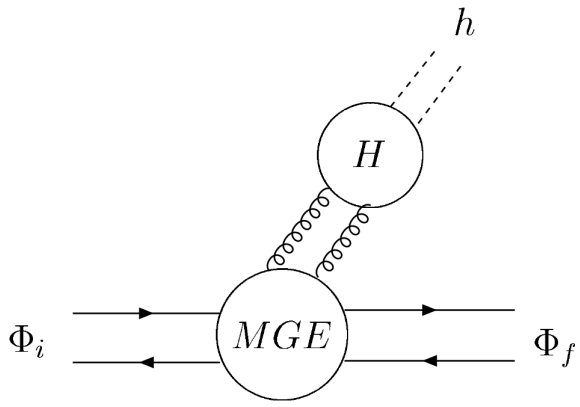

Figure 5.1. A hadronic transition as a two-step process, emission of gluons from heavy quarks (MGE) and the conversion of gluons into light hadrons (H).

We are going to take $H^{(0)}_{\rm QCD}$ as the zeroth order Hamiltonian, and take $H^{(1)}_{\rm QCD}$ as a perturbation. This is different from the ordinary perturbation theory since $H^{(0)}_{\rm QCD}$ is not a free field Hamiltonian. $H^{(0)}_{\rm QCD}$ contains strong interactions in the potentials in $\hat{H}$, so that the eigenstates of $H^{(0)}_{\rm QCD}$ are bound states rather than free field states. For a given potential model, the zeroth order solution can be obtained by solving the Schrödinger equation with the given potential. Moreover, we see from Eqs. (5.11) that only H_2 in $H^{(1)}_{\rm QCD}$ is of $\mathcal{O}((ka)^1)$. Note that H_1 is of $\mathcal{O}((ka)^0)$, we treat H_1 nonperturbatively and keep it in the propagator.

The general formula for the S matrix element between the initial state $|I\rangle$ and the final state $|F\rangle$ in this expansion has been given in Ref. [221], which is

$$\begin{aligned}\langle F|S|I\rangle =& -i2\pi\delta(E_F+\omega_F-E_I)\times \\ &\times\langle F|\,H_2\frac{1}{E_I-H^{(0)}_{QCD}+i\partial_0-H_1}H_2\cdots H_2\frac{1}{E_I-H^{(0)}_{QCD}+i\partial_0-H_1}H_2\,|I\rangle\,,\end{aligned} \tag{5.12}$$

where ω_F is the energy of the emitted gluons. This is the basic formula to study hadronic transitions in QCDME.

5.2 Spin-nonflip hadronic transitions with two pions

These processes are dominated by double electric-dipole transitions (E1E1). The transition amplitude can be obtained from the S matrix element presented in Eq. (5.12) which in this case is given by [215]

$$\mathcal{M}_{E1E1}=i\frac{g_E^2}{6}\,\langle\Phi_F h\,|\vec{x}\cdot\vec{E}\,\frac{1}{E_I-H^{(0)}_{QCD}-iD_0}\,\vec{x}\cdot\vec{E}|\,\Phi_I\rangle\,, \tag{5.13}$$

where $\vec{x}$ is the separation between Q and $\bar{Q}$, and $(D_0)_{bc}\equiv\delta_{bc}\partial_0-g_sf_{abc}A^a_0$. Let us insert a complete set of intermediate states with the principal quantum number K and

the orbital angular momentum L. Then Eq. (5.13) can be written as

$$\mathcal{M}_{E1E1} = i\frac{g_E^2}{6}\sum_{K,L,K',L'}\langle\Phi_F h|\vec{x}\cdot\vec{E}|KL\rangle\,\langle KL|\frac{1}{E_I - H_{QCD}^{(0)} - iD_0}|K'L'\rangle\,\langle K'L'|\vec{x}\cdot\vec{E}|\Phi_I\rangle\,. \tag{5.14}$$

The intermediate states in the hadronic transition are the states after the emission of the first gluon and before the emission of the second gluon, see Fig 5.1. They are states with a gluon and a color-octet $Q\bar{Q}$ and thus these states are the so-called hybrid states. It is difficult to calculate these hybrid states from first principles of QCD. So we take a reasonable model, which will be explained below, to describe them.

With this model, the transition amplitude, Eq. (5.14), becomes

$$\mathcal{M}_{E1E1} = i\frac{g_E^2}{6}\sum_{KL}\frac{\langle\Phi_F|x_k|KL\rangle\,\langle KL|x_l|\Phi_I\rangle}{E_I - E_{KL}}\,\langle\pi\pi|E_k^a E_l^a|0\rangle\,, \tag{5.15}$$

where E_{KL} is the energy eigenvalue of the intermediate vibrational state $|KL\rangle$. We see that, in this approach, the transition amplitude factorizes into the vertex of multipole gluon emissions (MGE) from the heavy quarks and the vertex of hadronization (H) describing the conversion of the emitted gluons into light hadron(s), see Fig 5.1. The first factor concerns the wave functions and energy eigenvalues of the initial and final state quarkonium and the intermediate states. These can be calculated for a given potential model. Let us now consider the treatment of the second factor. The scale of the H factor is the scale of light hadrons which is very low. Therefore the calculation of this matrix element is highly nonperturbative. Therefore we take a phenomenological approach based on an analysis of the structure of this matrix element using PCAC and soft pion technique in Ref. [223]. In the center-of-mass frame, the two pion momenta q_1 and q_2 are the only independent variables describing this matrix element. According with Refs. [223, 218], we can write this matrix element as [215]

$$\begin{aligned}\frac{g_E^2}{6}\,\langle\pi_\alpha(q_1)\pi_\beta(q_2)|E_k^a E_l^a|0\rangle = &\frac{\delta_{\alpha\beta}}{\sqrt{(2\omega_1)(2\omega_2)}}\times\\ &\times\left[C_1\delta_{kl}q_1^\mu q_{2\mu} + C_2\left(q_{1k}q_{2l} + q_{1l}q_{2k} - \frac{2}{3}\delta_{kl}\vec{q}_1\cdot\vec{q}_2\right)\right],\end{aligned} \tag{5.16}$$

where C_1 and C_2 are two unknown constants.

Finally, the transition rate is given by [219]

$$\begin{aligned}&\Gamma(\Phi_I(^{2s+1}l_{IJ_I}) \to \Phi_F(^{2s+1}l_{FJ_F})\pi\pi) =\\ &\delta_{l_I l_F}\delta_{J_I J_F}(G|C_1|^2 - \frac{2}{3}H|C_2|^2)\left|\sum_L(2L+1)\begin{pmatrix} l_I & 1 & L\\ 0 & 0 & 0\end{pmatrix}\begin{pmatrix} L & 1 & l_I\\ 0 & 0 & 0\end{pmatrix} f_{IF}^L\right|^2\\ &+(2l_I+1)(2l_F+1)(2J_F+1)\sum_k(2k+1)(1+(-1)^k)\begin{Bmatrix} s & l_F & J_F\\ k & J_I & l_I\end{Bmatrix}^2 H|C_2|^2\times\\ &\times\left|\sum_L(2L+1)\begin{pmatrix} l_F & 1 & L\\ 0 & 0 & 0\end{pmatrix}\begin{pmatrix} L & 1 & l_I\\ 0 & 0 & 0\end{pmatrix}\begin{Bmatrix} l_I & L & 1\\ 1 & k & l_F\end{Bmatrix} f_{IF}^L\right|^2,\end{aligned} \tag{5.17}$$

with

$$f_{IF}^{L} = \sum_{K} \frac{1}{M_I - M_{KL}} \left[\int dr r^3 R_F(r) R_{KL}(r) \right] \left[\int dr' r'^3 R_{KL}(r') R_I(r') \right], \qquad (5.18)$$

where $R_I(r)$, $R_F(r)$ and $R_{KL}(r)$ are the radial wave functions of the initial, final and intermediate vibrational states, respectively. The initial state and the vibrational state have masses M_I and M_{KL}.

The quantities G and H are the phase-space integrals

$$\begin{aligned} G =& \frac{3}{4}\frac{M_F}{M_I}\pi^3 \int dM_{\pi\pi}^2 \, K \left(1 - \frac{4m_\pi^2}{M_{\pi\pi}^2}\right)^{1/2} (M_{\pi\pi}^2 - 2m_\pi^2)^2, \\ H =& \frac{1}{20}\frac{M_F}{M_I}\pi^3 \int dM_{\pi\pi}^2 \, K \left(1 - \frac{4m_\pi^2}{M_{\pi\pi}^2}\right)^{1/2} \times \\ & \times \left[(M_{\pi\pi}^2 - 4m_\pi^2)^2 \left(1 + \frac{2}{3}\frac{K^2}{M_{\pi\pi}^2}\right) + \frac{8K^4}{15 M_{\pi\pi}^4} (M_{\pi\pi}^4 + 2m_\pi^2 M_{\pi\pi}^2 + 6m_\pi^4) \right], \end{aligned} \qquad (5.19)$$

with K given by

$$K = \frac{1}{2M_I} \left[(M_I + M_F)^2 - M_{\pi\pi}^2 \right]^{1/2} \left[(M_I - M_F)^2 - M_{\pi\pi}^2 \right]^{1/2}. \qquad (5.20)$$

The constant C_1 can be determined by the measured rate of $\psi' \to J/\psi\pi\pi$. However, the constant C_2 enters the decay rates for transitions such as $2^3P_{J'} \to 1^3P_J + \pi\pi$, $1^3D_1 \to 1^3S_1 + \pi\pi$, etc. We use the width measured experimentally for the $1^3D_1 \to 1^3S_1 + \pi\pi$ transition to determine C_2. Now we need a model which describes the vibrational states to perform the calculation.

5.3 A model for hybrid states

Although the gross features of the meson spectrum strongly suggests a $q\bar{q}$ structure assignment for most of the states, such simplicity looks peculiar when viewed from the perspective of QCD, in which quarks couple strongly with a self-interacting gluonic field. From the generic properties of QCD, we might expect to have states in which the gluonic field itself is excited and carries J^{PC} quantum numbers. A state is called glueball when any valence quark content is absent, the addition of a constituent quark-antiquark to an excited gluonic field gives us what we call a hybrid meson.

The gluonic quantum numbers couple to those of the $q\bar{q}$ pair. This coupling can give rise to so-called exotic J^{PC} mesons, but also can produce hybrid mesons with natural quantum numbers. We do not seek exotic states, we are more interested in those involved in the calculation of hadronic transitions within the QCDME.

Estimates of hybrid meson properties have traditionally followed from models. Two models that address this issue are the quark confining string (QCS) model [224–226] and the flux-tube model [227]. Both have been applied to the heavy quark sector. Within the nonrelativistic framework, the models assume that the heavy quark and antiquark are situated at the ends of the string and allow that the string vibrates. They calculate the vibrational energy of the string as a function of the distance between the

quark and the antiquark. This is then treated as an effective potential, $V_n(r)$, inserted into the bound state equation.

We adopt the QCS model because it was used in the early works of QCDME and it incorporates finite quark mass corrections. The QCS model is defined by a relativistic-, gauge- and reparametrization-invariant action describing quarks interacting with color $SU(3)$ gauge fields in a two dimensional world sheet. The model has no gluonic degrees of freedom, but has instead string degrees of freedom.

The string can carry energy-momentum only in the region between the quark and the antiquark, thus the quarks appear to be at the ends of the string. In the nonrelativistic limit, the quark mass is larger than the gluon-quark coupling constant (with mass dimension), and in the absence of light quarks, the longitudinal modes of the quark-antiquark pair plus the rotational modes of the string reduce to the naive $Q\bar{Q}$ model with a linear potential. It is important to realize that the linear potential is obtained when light degrees of freedom are factored out.

The string can also vibrate and these vibrational modes provide new states beyond the naive meson picture. The coupled equations that describe the dynamics of the string and the quark are very nonlinear so that there is no hope of solving them completely. We content ourselves with the following approximation scheme. First, we solve the string equation to obtain the vibrational mode energies as functions of r, the interquark distance. These are then inserted into the meson equation as an effective potential, $V_n(r)$, between the quark and the antiquark

$$\left[-\frac{1}{m_Q}\frac{\partial^2}{\partial r^2} + V_n(r) + \frac{L(L+1)}{m_Q r^2} + 2m_Q\right] u_{KL}(r) = E_{KL}u_{KL}(r), \tag{5.21}$$

where $u_{KL}(r)$ is the reduced wave function of the hybrid meson and n is the vibrational mode quantum number, for $n = 0$ we have the naive meson states. This approximation is valid if the vibrational energies are bigger than the quark longitudinal-mode energies. In the presence of both vibrational and rotational modes we will have a vibration-rotation coupling but we ignore that.

First let us make a very crude estimate of the vibrational-mode energy as a function of the distance r between the quark and the antiquark. We assume that the quark mass is heavy enough so that the ends of the string are essentially fixed and separated by a distance r. We also consider that the amplitude of the vibration is small compared with the distance between quark-antiquark, r. Therefore, the wave equation for a string is given by

$$\frac{\partial^2 y(x,t)}{\partial t^2} = v^2\frac{\partial^2 y(x,t)}{\partial x^2}, \tag{5.22}$$

with $v = \sqrt{\sigma/\rho}$. The string tension is σ and the mass density is ρ. Once boundary conditions are imposed, the solution to the wave equation can be written as

$$y(x,t) = \sum_{n=1}^{\infty} a_n \sin\left(\frac{n\pi x}{r}\right)\cos\left(\frac{n\pi v t}{r}\right), \tag{5.23}$$

where $k_n = \frac{n\pi}{r}$ and $\omega_n = \frac{n\pi v}{r}$. Now, it is important to note that we are referring to a flux of energy and thus we have $dm = dE$ with $dm = \rho dx$ and $dE = \sigma dx$. This means

that $\sigma = \rho$ and so $v = 1$. Then, the vibrational energy is given by

$$V_n^{(1)}(r) - \sigma r = \omega_n(r) = \frac{n\pi}{r}, \tag{5.24}$$

and can be written as

$$V_n^{(1)}(r) = \sigma r + \frac{n\pi}{r}. \tag{5.25}$$

This result for hybrid states is also obtained within the flux-tube model [227]. But physically, one expects that $V_n(r)$ remain finite and smooth when $r \to 0$. The solution proposed in Ref. [227] is to incorporate an *ad hoc* cutoff, but in the case of the QCS is to improve the approximation.

The next stage is to introduce a simple estimation of the shape of the vibrating string. We continue considering that the quark mass is heavy and the ends of the string are essentially fixed. Following Ref. [226] we obtain a vibrational energy given by

$$V_n^{(2)}(r) = \sigma r \left(1 + \frac{2n\pi}{\sigma r^2}\right)^{1/2}, \tag{5.26}$$

with

$$V_n^{(2)}(r) = \begin{cases} \sigma r + \frac{n\pi}{r} & r \to \infty, \\ (2n\pi\sigma)^{1/2}\left(1 + \frac{\sigma r^2}{4n\pi}\right) & r \to 0, \end{cases} \tag{5.27}$$

where now the potential is finite when $r \to 0$.

The last stage is to incorporate corrections to the finite quark mass. The expression of the vibrational energy is [226]

$$V_n^{(3)}(r) = \sigma r \left\{1 + \frac{2n\pi}{\sigma\left[(r-2d)^2 + 4d^2\right]}\right\}^{1/2} = \sigma r (2 - \alpha_n^2)^{-1/2}, \tag{5.28}$$

with

$$\alpha_n^2 = 1 + \frac{2n\pi}{2n\pi + \sigma\left[(r-2d)^2 + 4d^2\right]}, \tag{5.29}$$

a parameter related with the estimation of the shape of the vibrating string [226], it can take values $(1 \leq \alpha_n^2 \leq 2)$. The correction due to the finite quark mass is

$$d(m_Q, r, \sigma, n) = \frac{\sigma r^2 \alpha_n}{4(2m_Q + \sigma r \alpha_n)}. \tag{5.30}$$

For $n = 0$, $\alpha_n^2 = 1$ and $V_n^{(3)}(r)$ reduces to the naive $Q\bar{Q}$ one. We note that

$$V_n^{(3)}(r) = \begin{cases} \sigma r + \frac{2n\pi}{r} & r \to \infty, \\ (2n\pi\sigma)^{1/2}\left(1 + \frac{\sigma r}{2\sqrt{2}m_Q}\right) & r \to 0. \end{cases} \tag{5.31}$$

In our quark model, the central part of the confining potential has the following form

$$V_{\rm CON}^{\rm C}(r) = \frac{16}{3}[a_c(1 - e^{-\mu_c r}) - \Delta], \tag{5.32}$$

and can be written as

$$V_{\rm CON}^{\rm C}(r) = \sigma(r) r + {\rm cte}, \tag{5.33}$$

where

$$\begin{aligned} \sigma(r) &= \frac{16}{3}\, a_c \left(\frac{1 - e^{-\mu_c r}}{r} \right), \\ {\rm cte} &= -\frac{16}{3}\, \Delta. \end{aligned} \tag{5.34}$$

This means that our effective string tension, $\sigma(r)$, is not a constant but depends on the interquark distance, r. In fact, it decreases with respect r until it reaches the string breaking region.

Following the ideas of Ref. [228], the potential for hybrid mesons derived from our constituent quark model has the following expression

$$V_{\rm hyb}(r) = V_{\rm OGE}^{\rm C}(r) + V_{\rm CON}^{\rm C}(r) + [V_n(r) - \sigma(r) r] + \widetilde{C}, \tag{5.35}$$

where we have not taken into account the spin-dependent terms. $V_{\rm OGE}^{\rm C}(r) + V_{\rm CON}^{\rm C}(r)$ is the naive quark-antiquark potential and $V_n(r)$ is the vibrational one. We must subtract the term $\sigma(r) r$ because it appears twice, one in $V_{\rm CON}^{\rm C}(r)$ and the other one in $V_n(r)$. The constant term $\widetilde{C}$ is a free parameter of the hybrid model and in principle can be different depending on the flavor sector. Its particular value will depend on our theoretical results obtained from a global fit of the spin-nonflip hadronic transitions between triplet states of charmonium and bottomonium.

More explicitly, our different contributions are

$$\begin{aligned} V_{\rm OGE}^{\rm C}(r) &= -\frac{4\alpha_s}{3r}, \\ V_{\rm CON}^{\rm C}(r) &= \frac{16}{3}[a_c(1 - e^{-\mu_c r}) - \Delta], \\ V_n(r) = V_n^{(3)}(r) &= \sigma(r) r \left\{ 1 + \frac{2n\pi}{\sigma(r)\left[(r - 2d)^2 + 4d^2\right]} \right\}^{1/2}, \end{aligned} \tag{5.36}$$

where

$$d(m_Q, r, \sigma, n) = \frac{\sigma(r) r^2 \alpha_n}{4(2m_Q + \sigma(r) r \alpha_n)}. \tag{5.37}$$

One can realize that, just like the naive quark model, the hybrid potential has a threshold defined by

$$V_{\rm hyb}(r) \xrightarrow{r \to \infty} \frac{16}{3}\,(a_c - \Delta) + \widetilde{C}, \tag{5.38}$$

The naive meson potential $(Q\bar{Q})$ and the hybrid meson potential $(Q\bar{Q}g)$ with respect the interquark distance are drawn in Fig. 5.2.

5.4 Results

We are ready to calculate spin-nonflip $\pi\pi$ transitions between triplet states of charmonium and bottomonium.

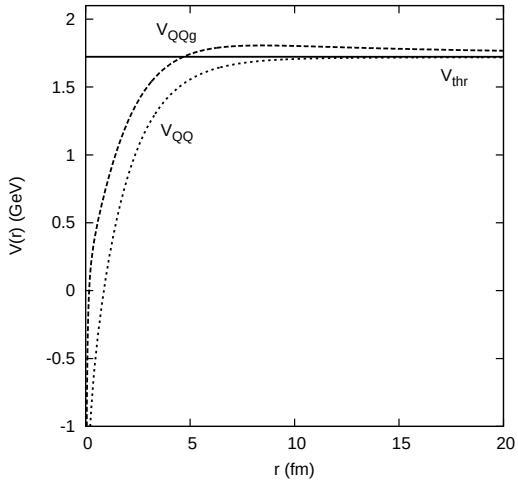

Figure 5.2. Naive meson potential ($Q\bar{Q}$) and hybrid meson potential ($Q\bar{Q}g$), in GeV, with respect the interquark distance, in fm.

Initial Meson	Final Meson	$\Gamma_{\text{The.}}$ (keV)	$\Gamma_{\text{Exp.}}$ (keV)	
$\psi(2S)$	J/ψ	93.3 ± 5.4	96.1 ± 5.5	[78]
$\psi(3770)$	J/ψ	53.8 ± 8.4	53.27 ± 7.96	[78]
$X(4360)$	$\psi(2S)$	1770 ± 185	$\frac{821.4 \pm 240.1}{\Gamma_{ee}(\text{keV})}$	[78]
$X(4660)$	$\psi(2S)$	73 ± 12	$\frac{105.6 \pm 54.4}{\Gamma_{ee}(\text{keV})}$	[78]
$\Upsilon(2S)$	$\Upsilon(1S)$	7.77 ± 0.78	5.79 ± 0.49	[78]
$\Upsilon(3S)$	$\Upsilon(1S)$	0.91 ± 0.34	0.89 ± 0.08	[78]
	$\Upsilon(2S)$	0.37 ± 0.14	0.50 ± 0.06	[78]
$\Upsilon(4S)$	$\Upsilon(1S)$	4.53 ± 0.63	$3.65 \pm 0.67 \pm 0.65$	[229]
	$\Upsilon(2S)$	0.10 ± 0.12	2.7 ± 0.8	[230]

Table 5.1. Spin-nonflip $\pi^+\pi^-$ transitions between triplet states of charmonium and bottomonium which have been fitted to the experimental data to determine the free parameters. See the text for details.

Following Eq. (5.17), we need the radial wave function and the mass for the initial and final 1^{--} states, but also for the intermediate vibrational states. In this case it is more convenient to integrate the Schrödinger equation using the Numerov method instead of the GEM one.

The calculation of hybrid charmonium and bottomonium spectrum requires fixing the value of $\widetilde{C}$ in Eq. (5.35). We have fitted it from the available experimental data referred to the $\pi\pi$ transitions in which we are interested. Table 5.1 shows the spin-nonflip $\pi^+\pi^-$ transitions between ψ and Υ states. These transitions have been fitted to the experimental data to determine the free parameters, which are

$$\begin{aligned} |C_1|^2 &= (8.61 \pm 0.45) \times 10^{-5}, & |C_2|^2 &= (2.97 \pm 0.44) \times 10^{-4}, \\ \widetilde{C}_{c\bar{c}} &= (3.86 \pm 0.31)\,\text{MeV}, & \widetilde{C}_{b\bar{b}} &= (25.5 \pm 3.8)\,\text{MeV}, \end{aligned} \tag{5.39}$$

where the first two parameters come from the QCDME approach and, as we have seen,

are related to our ignorance about the mechanism of the conversion of the emitted gluons into light hadron(s). The last two are the free constant, $\widetilde{C}$, of Eq. (5.35) which has been considered as dependent on the flavor sector.

From Table 5.1 one can realize that we predict large widths for the processes $X(4360) \to \pi^+\pi^-\psi(2S)$ and $X(4660) \to \pi^+\pi^-\psi(2S)$. The $X(4360)$ and $X(4660)$ have been assigned in our model as conventional 1^{--} $c\bar{c}$ states. Furthermore, we obtain a reasonable global description of the hadronic widths for which there are experimental data. We have taken into account the errors on the parameters to present the theoretical values.

The PDG [78] collects two experimental values which involve the width of $X(4360) \to \pi^+\pi^-\psi(2S)$. These are

$$\begin{aligned} R_1 &= \frac{\Gamma(\pi^+\pi^-\psi(2S)) \times \Gamma_{ee}}{\Gamma_{\rm tot}} = 11.1^{+1.3}_{-1.2}\,{\rm eV}, \\ R_2 &= \frac{\Gamma(D^0 D^{*-}\pi^+)}{\Gamma(\pi^+\pi^-\psi(2S))} < 8. \end{aligned} \tag{5.40}$$

From the first one, we obtain the experimental value shown in Table 5.1 when the total width reported in Ref. [78] is included. Moreover, if we use our prediction of the $X(4360)$ leptonic width, 0.78 keV, the estimated width for the process $X(4360) \to \pi^+\pi^-\psi(2S)$ is $\sim$1.1 MeV, which is in the order of magnitude of the theoretical result. From the second one, we have seen before that our value of $\Gamma(X(4360) \to D^0 D^{*-}\pi^+)$ is 3 MeV, and so we estimate $\Gamma(X(4360) \to \pi^+\pi^-\psi(2S)) > 0.4$ MeV that is also compatible with our value shown in Table 5.1.

The same kind of experimental information is available for the $X(4660)$ particle in the PDG. In this case we have

$$\begin{aligned} R'_1 &= \frac{\Gamma(\pi^+\pi^-\psi(2S)) \times \Gamma_{ee}}{\Gamma_{\rm tot}} = 2.2^{+0.7}_{-0.6}\,{\rm eV}, \\ R'_2 &= \frac{\Gamma(D^0 D^{*-}\pi^+)}{\Gamma(\pi^+\pi^-\psi(2S))} < 10. \end{aligned} \tag{5.41}$$

Again, from the first one, we obtain the experimental value shown in Table 5.1 when the total width reported in Ref. [78] is included. The predicted value of the leptonic width for $X(4660)$ is 0.31 keV such that $\Gamma(X(4660) \to \pi^+\pi^-\psi(2S)) \sim 0.3$ MeV is an estimation. The theoretical prediction seems to be below the estimation. From the second one, we estimate $\Gamma(X(4660) \to \pi^+\pi^-\psi(2S)) > 1.3$ MeV, which is also larger than the theoretical result.

The Refs. [229] and [230] mentioned in Table 5.1 are those which have reported the last experimental data related to the hadronic transitions shown. We obtain good agreement for the first one, but for the second one our theoretical result is low.

Once we have fixed the value of the flavor-dependent constant, $\widetilde{C}$, the Tables 5.2 and 5.3 show, respectively, the hybrid charmonium and bottomonium spectrum. The mean square radius for each state is also included.

The ground state of hybrid mesons in other approaches, such as the flux-tube model, models with a constituent gluon and Lattice QCD, is one that has a unit of angular momentum. We predict in the $L = 1$ $(c\bar{c}g)$ sector a ground state with a mass of 4.3 GeV. It is located around the upper limit predicted by other approaches, $4.1 - 4.3$ GeV.

K	$L=0$		$L=1$		$L=2$	
	Mass (MeV)	$\langle r^2\rangle^{1/2}$ (fm)	Mass (MeV)	$\langle r^2\rangle^{1/2}$ (fm)	Mass (MeV)	$\langle r^2\rangle^{1/2}$ (fm)
1	4079	0.49	4347	0.76	4533	1.00
2	4461	0.97	4635	1.22	4772	1.46
3	4724	1.43	4851	1.69	4955	1.95
4	4920	1.90	5016	2.20	5096	2.50
5	5070	2.44	5141	2.79	5201	3.16
6	5182	3.08	5234	3.53	-	-
Threshold $\equiv 5245$ MeV						

Table 5.2. Hybrid mesons calculated in the $c\bar{c}$ sector. The parameter α_n whose range is $1 < \alpha_n < \sqrt{2}$ modifies the energy in 30 MeV, we have taken $\alpha_n = \sqrt{1.5}$.

K	$L=0$		$L=1$		$L=2$	
	Mass (MeV)	$\langle r^2\rangle^{1/2}$ (fm)	Mass (MeV)	$\langle r^2\rangle^{1/2}$ (fm)	Mass (MeV)	$\langle r^2\rangle^{1/2}$ (fm)
1	10545	0.32	10760	0.52	10896	0.68
2	10831	0.65	10973	0.81	11083	0.95
3	11037	0.92	11150	1.08	11241	1.21
4	11206	1.18	11299	1.34	11376	1.48
5	11349	1.45	11427	1.60	11493	1.75
6	11470	1.71	11537	1.88	11594	2.03
7	11575	2.00	11632	2.17	11680	2.34
8	11664	2.30	11713	2.49	11754	2.68
9	11741	2.63	11782	2.84	11817	3.05
10	11806	3.00	11840	3.24	11869	3.47
11	11860	3.41	11888	3.67	-	-
12	11902	3.84	-	-	-	-
Threshold $\equiv 11917$ MeV						

Table 5.3. Hybrid mesons calculated in the $b\bar{b}$ sector. The parameter α_n whose range is $1 < \alpha_n < \sqrt{2}$ modifies the energy in 30 MeV, we have taken $\alpha_n = \sqrt{1.5}$.

The hybrid mesons which participate to the two-pion transitions of the $J^{PC} = 1^{--}$ charmonium and bottomonium mesons are just those with $L = 1$. One can see in Table 5.2 that the ground state and the first excitation of $L = 1$ hybrid charmonium mesons are close to $X(4360)$ and $X(4660)$, respectively. The width calculated using Eq. (5.17) is sensible to the position in the spectrum of the hybrid meson with respect that of the initial meson through Eq. (5.18). This explains why we are able to describe well established hadronic transitions and, at the same time, to have large widths for the processes $X(4360) \to \pi^+\pi^-\psi(2S)$ and $X(4660) \to \pi^+\pi^-\psi(2S)$.

Finally, Tables 5.4, 5.5 and 5.6 show the spin-nonflip $\pi^+\pi^-$ transitions between 1^{--} charmonium and bottomonium states.

Within the charmonium sector, besides the results already discussed, there are two more experimental data referred to the processes $\psi(4040) \to \pi^+\pi^- J/\psi$ and

Initial Meson	Final Meson	$\Gamma_{\text{The.}}$ (keV)	$\Gamma_{\text{Exp.}}$ (keV)	
$\psi(2S)$	$\psi(1S)$	93.3 ± 5.4	96.1 ± 5.5	[78]
$\psi(1D)$	$\psi(1S)$	53.8 ± 8.4	53.27 ± 7.96	[78]
$\psi(3S)$	$\psi(1S)$	78.3 ± 4.6	< 320	[78]
	$\psi(2S)$	7.71 ± 0.76	-	
$\psi(2D)$	$\psi(1S)$	129 ± 20	< 309	[78]
	$\psi(2S)$	21.0 ± 3.5	-	
	$\psi(1D)$	34.2 ± 2.2	-	
$\psi(4S)$	$\psi(1S)$	27265 ± 3573	-	
	$\psi(2S)$	1770 ± 185	$\frac{821.4 \pm 240.1}{\Gamma_{ee}(\text{keV})}$	[78]
	$\psi(1D)$	59.1 ± 10.4	-	
	$\psi(3S)$	13.5 ± 1.1	-	
$\psi(3D)$	$\psi(1S)$	2.9 ± 1.0	-	
	$\psi(2S)$	53.6 ± 8.3	-	
	$\psi(1D)$	285 ± 15	-	
	$\psi(3S)$	6.8 ± 1.4	-	
$\psi(5S)$	$\psi(1S)$	4025 ± 609	-	
	$\psi(2S)$	334 ± 86	-	
	$\psi(1D)$	3.2 ± 1.7	-	
	$\psi(3S)$	909 ± 87	-	
	$\psi(2D)$	11.7 ± 2.4	-	
$\psi(4D)$	$\psi(1S)$	10.2 ± 3.8	-	
	$\psi(2S)$	73 ± 12	$\frac{105.6 \pm 54.4}{\Gamma_{ee}(\text{keV})}$	[78]
	$\psi(1D)$	267 ± 18	-	
	$\psi(3S)$	32.4 ± 5.3	-	
	$\psi(2D)$	125.3 ± 7.6	-	
	$\psi(4S)$	0.065 ± 0.098	-	

Table 5.4. Spin-nonflip $\pi^+\pi^-$ transitions between ψ states.

$\psi(4160) \to \pi^+\pi^- J/\psi$. They are upper limits to the width and therefore they are not taken into account in the fit. Our predictions, $(78.3 \pm 4.6)\,\text{keV} < 320\,\text{keV}$ and $(129 \pm 20)\,\text{keV} < 309\,\text{keV}$, are compatible with the data.

We obtain a width of about 27 MeV for the process $X(4360) \to \pi^+\pi^- J/\psi$. Although our theoretical value is not very realistic, we can assert that if the $X(4360)$ has been seen in $\pi^+\pi^-\psi(2S)$ channel, it should be also seen in $\pi^+\pi^- J/\psi$ one. This is not the case for the $X(4660)$ if one follows our assignment of this state.

The $\pi\pi$ transitions of the $\psi(5S)$, which is assigned in our model to the $X(4630)$, also deserves our attention. It is difficult to disentangle the structure of this particle and to differentiate it with the $X(4660)$, the hadronic transitions presented here can be used to gain insight about these two particles. If the denoted $X(4660)$ was seen in

Initial Meson	Final Meson	$\Gamma_{\text{The.}}$ (keV)	$\Gamma_{\text{Exp.}}$ (keV)	
$\Upsilon(2S)$	$\Upsilon(1S)$	7.77 ± 0.78	5.79 ± 0.49	[78]
$\Upsilon(1D)$	$\Upsilon(1S)$	5.3 ± 1.2	-	
$\Upsilon(3S)$	$\Upsilon(1S)$	0.91 ± 0.34	0.89 ± 0.08	[78]
	$\Upsilon(2S)$	0.37 ± 0.14	0.50 ± 0.06	[78]
$\Upsilon(2D)$	$\Upsilon(1S)$	0.50 ± 0.30	-	
	$\Upsilon(2S)$	0.15 ± 0.15	-	
	$\Upsilon(1D)$	0.03 ± 0.04	-	
$\Upsilon(4S)$	$\Upsilon(1S)$	4.53 ± 0.63	$\begin{bmatrix} 1.7 \pm 0.2 \\ 1.8 \pm 0.4 \\ 3.65 \pm 0.67 \pm 0.65 \end{bmatrix}$	$\begin{bmatrix} [78] \\ [230] \\ [229] \end{bmatrix}$
	$\Upsilon(2S)$	0.10 ± 0.12	$\begin{bmatrix} 1.8 \pm 0.3 \\ 2.7 \pm 0.8 \end{bmatrix}$	$\begin{bmatrix} [78] \\ [230] \end{bmatrix}$
	$\Upsilon(1D)$	0.015 ± 0.049	-	
$\Upsilon(3D)$	$\Upsilon(1S)$	0.33 ± 0.25	-	
	$\Upsilon(2S)$	0.06 ± 0.10	-	
	$\Upsilon(1D)$	0.32 ± 0.19	-	
	$\Upsilon(3S)$	0.0003 ± 0.0072	-	
$\Upsilon(5S)$	$\Upsilon(1S)$	16.2 ± 2.9	$590 \pm 40 \pm 90$	[231]
	$\Upsilon(2S)$	21.9 ± 2.0	$850 \pm 70 \pm 160$	[231]
	$\Upsilon(1D)$	1.14 ± 0.46	-	
	$\Upsilon(3S)$	2.29 ± 0.68	$520^{+200}_{-170} \pm 100$	[231]
	$\Upsilon(2D)$	0.17 ± 0.17	-	
	$\Upsilon(4S)$	0.070 ± 0.064	-	
$\Upsilon(4D)$	$\Upsilon(1S)$	6.0 ± 2.2	-	
	$\Upsilon(2S)$	1.91 ± 0.68	-	
	$\Upsilon(1D)$	13.89 ± 1.90	-	
	$\Upsilon(3S)$	0.026 ± 0.079	-	
	$\Upsilon(2D)$	0.16 ± 0.18	-	

Table 5.5. Spin-nonflip $\pi^+\pi^-$ transitions between Υ states.

$\pi^+\pi^- J/\psi$ and $\pi^+\pi^-\psi(2S)$ channels, the best candidate would be the $X(4630)$, but if it was seen only in $\pi^+\pi^-\psi(2S)$ channel our assignment would be correct.

Within the bottomonium sector, the predicted $\pi\pi$ hadronic transitions of the $\Upsilon(2S)$ and $\Upsilon(3S)$ states agree with the experimental data.

We use for the global fit the last experimental data related with the $\pi\pi$ transitions of the $\Upsilon(4S)$ state. Table 5.5 shows the different experimental values. Despite being different, measurements of the widths for the transitions $\Upsilon(4S) \to \pi^+\pi^-\Upsilon(1S)$ and $\Upsilon(4S) \to \pi^+\pi^-\Upsilon(2S)$ are in the order of keV. Our result for $\Upsilon(4S) \to \pi^+\pi^-\Upsilon(1S)$ is in very good agreement with the experimental one. However, we find a strong

Initial Meson	Final Meson	$\Gamma_{\text{The.}}$ (keV)	$\Gamma_{\text{Exp.}}$ (keV)
$\Upsilon(6S)$	$\Upsilon(1S)$	1781 ± 79	-
	$\Upsilon(2S)$	277 ± 13	-
	$\Upsilon(1D)$	9.7 ± 1.8	-
	$\Upsilon(3S)$	121.1 ± 5.8	-
	$\Upsilon(2D)$	4.9 ± 1.1	-
	$\Upsilon(4S)$	4.97 ± 0.52	-
	$\Upsilon(3D)$	0.040 ± 0.075	-
$\Upsilon(5D)$	$\Upsilon(1S)$	4376 ± 642	-
	$\Upsilon(2S)$	483 ± 71	-
	$\Upsilon(1D)$	1274 ± 55	-
	$\Upsilon(3S)$	292 ± 43	-
	$\Upsilon(2D)$	1637 ± 71	-
	$\Upsilon(4S)$	1.45 ± 051	-
	$\Upsilon(3D)$	4.99 ± 0.52	-

Table 5.6. Spin-nonflip $\pi^+\pi^-$ transitions between Υ states (Continuation).

disagreement between our prediction and the experimental data for the transition $\Upsilon(4S) \to \pi^+\pi^-\Upsilon(2S)$. Our theoretical value lies an order of magnitude below the data.

Anomalous large rates of $e^+e^- \to \Upsilon(1S)\pi^+\pi^-$, $\Upsilon(2S)\pi^+\pi^-$, $\Upsilon(3S)\pi^+\pi^-$ near the peak of the $\Upsilon(5S)$ resonance were observed by the Belle Collaboration [231]. They are larger than the dipion-transition rates between the lower members of the Υ family by 2 orders of magnitude. The Belle data are those shown in Table 5.5, as one can see, our results are in strong disagreement with the experimental ones. There are two possibilities that may offer reasonable interpretations of the anomalous large rates. First, these anomalous production rates announced by Belle are from an exotic resonance structure different from $\Upsilon(10860)$ [232–234] . The second is that there may exist extra contributions that differ from the direct dipion emission, e.g. the study of the $\Upsilon(10860) \to \Upsilon(1S, 2S)\pi^+\pi^-$ decays in Ref. [235].

Finally, we separate in Table 5.6 the resonances $\Upsilon(6S)$ and $\Upsilon(5D)$. The hadronic transitions of these states suffer from large uncertainties regarding the variation of the constant $\widetilde{C}_{b\bar{b}}$ within its error range. Therefore, our theoretical results in Table 5.6 are those without taking into account this variation, we only move the parameters $|C_1|^2$ and $|C_2|^2$ within their error ranges. These two resonances of bottomonium are where get the larger values of the widths, in the order of MeV.

Chapter 6

Weak decays of heavy mesons

Through e^+e^- collisions with an energy tuned to the different bottomonium resonances, the B-factories have become an important source of data on heavy hadrons in the last years. The bottomonium states decay into a pair of B mesons, e.g. the $\Upsilon(4S)$ resonance decays in almost 100% of cases to a $B\bar{B}$ pair, and these B mesons decay subsequently into charmed and charmless hadrons via weak interaction.

The kinematically clean environment, reached by the B-factories, of B meson decays has given rise to a number of exciting discoveries in the c-quark sector, most of the hadronic B decays involve $b \to c$ transition at the quark level. To describe theoretically the properties of these new conventional or unexpected hadrons, one must deal with weak interaction observables which are generally concerned to the semileptonic and nonleptonic decays of b-hadrons.

In this chapter we have performed a calculation of the semileptonic and nonleptonic decays of B and B_s mesons into charmed and charmed-strange mesons. The final goal is to determine the matrix elements needed to calculate explicitly processes like "$B \to XYZ$ + anything" which are generally attached to properties of the XYZ mesons. One of the main objectives pursued in this dissertation is the analysis of the heavy meson decays and for that reason we also want to incorporate the study of weak decays.

6.1 Semileptonic B (B_s) decays into D^{**} (D_s^{**}) mesons

Different Collaborations have recently reported semileptonic B decays into orbitally excited charmed mesons providing detailed results of branching fractions. The theoretical analysis of these data, which include both weak and strong decays, offers the possibility for a stringent test of meson models.

Moreover, an accurate determination of the $|V_{cb}|$ and $|V_{ub}|$ Cabbibo-Kobayashi-Maskawa (CKM) matrix elements demands a detailed knowledge of semileptonic decays of b-hadrons. Decays including orbitally excited charmed meson in the final state provide a substantial contribution to the total semileptonic decay width. Furthermore, a better understanding of these processes is also necessary in the analysis of signals and backgrounds of inclusive and exclusive measurements of b-hadron decays.

The Belle Collaboration [236], using a full reconstruction tagging method to suppress the large combinatorial background, reported data on the product of branching fractions $\mathcal{B}(B^+ \to D^{**}l^+\nu_l) \times \mathcal{B}(D^{**} \to D^{(*)}\pi)$, where, in the usual notation, l stands for a light e or μ lepton, the $D_0^*(2400)$, $D_1(2430)$, $D_1(2420)$ and $D_2^*(2460)$

	Belle [236] ($\times 10^{-3}$)	BaBar [237, 238] ($\times 10^{-3}$)
$D_0^*(2400)$		
$\mathcal{B}(B^+ \to \bar{D}_0^*(2400)^0 l^+ \nu_l)\mathcal{B}(\bar{D}_0^*(2400)^0 \to D^- \pi^+)$	$2.4 \pm 0.4 \pm 0.6$	$2.6 \pm 0.5 \pm 0.4$
$\mathcal{B}(B^0 \to D_0^*(2400)^- l^+ \nu_l)\mathcal{B}(D_0^*(2400)^- \to \bar{D}^0 \pi^-)$	$2.0 \pm 0.7 \pm 0.5$	$4.4 \pm 0.8 \pm 0.6$
$D_1(2430)$		
$\mathcal{B}(B^+ \to \bar{D}_1(2430)^0 l^+ \nu_l)\mathcal{B}(\bar{D}_1(2430)^0 \to D^{*-} \pi^+)$	< 0.7	$2.7 \pm 0.4 \pm 0.5$
$\mathcal{B}(B^0 \to D_1(2430)^- l^+ \nu_l)\mathcal{B}(D_1(2430)^- \to \bar{D}^{*0} \pi^-)$	< 5	$3.1 \pm 0.7 \pm 0.5$
$D_1(2420)$		
$\mathcal{B}(B^+ \to \bar{D}_1(2420)^0 l^+ \nu_l)\mathcal{B}(\bar{D}_1(2420)^0 \to D^{*-} \pi^+)$	$4.2 \pm 0.7 \pm 0.7$	$2.97 \pm 0.17 \pm 0.17$
$\mathcal{B}(B^0 \to D_1(2420)^- l^+ \nu_l)\mathcal{B}(D_1(2420)^- \to \bar{D}^{*0} \pi^-)$	$5.4 \pm 1.9 \pm 0.9$	$2.78 \pm 0.24 \pm 0.25$
$D_2^*(2460)$		
$\mathcal{B}(B^+ \to \bar{D}_2^*(2460)^0 l^+ \nu_l)\mathcal{B}(\bar{D}_2^*(2460)^0 \to D^- \pi^+)$	$2.2 \pm 0.3 \pm 0.4$	$1.4 \pm 0.2 \pm 0.2^{(*)}$
$\mathcal{B}(B^+ \to \bar{D}_2^*(2460)^0 l^+ \nu_l)\mathcal{B}(\bar{D}_2^*(2460)^0 \to D^{*-} \pi^+)$	$1.8 \pm 0.6 \pm 0.3$	$0.9 \pm 0.2 \pm 0.2^{(*)}$
$\mathcal{B}(B^+ \to \bar{D}_2^*(2460)^0 l^+ \nu_l)\mathcal{B}(\bar{D}_2^*(2460)^0 \to D^{(*)-} \pi^+)$	$4.0 \pm 0.7 \pm 0.5$	$2.3 \pm 0.2 \pm 0.2$
$\mathcal{B}(B^0 \to D_2^*(2460)^- l^+ \nu_l)\mathcal{B}(D_2^*(2460)^- \to \bar{D}^0 \pi^-)$	$2.2 \pm 0.4 \pm 0.4$	$1.1 \pm 0.2 \pm 0.1^{(*)}$
$\mathcal{B}(B^0 \to D_2^*(2460)^- l^+ \nu_l)\mathcal{B}(D_2^*(2460)^- \to \bar{D}^{*0} \pi^-)$	< 3	$0.7 \pm 0.2 \pm 0.1^{(*)}$
$\mathcal{B}(B^0 \to D_2^*(2460)^- l^+ \nu_l)\mathcal{B}(D_2^*(2460)^- \to \bar{D}^{(*)0} \pi^-)$	< 5.2	$1.8 \pm 0.3 \pm 0.1$
$\mathcal{B}_{D/D^{(*)}}$	0.55 ± 0.03	$0.62 \pm 0.03 \pm 0.02$

Table 6.1. Most recent experimental measurements reported by the Belle and BaBar Collaborations. l stands for a light e or μ lepton. The symbol $(*)$ indicates results estimated from the original data by using $B_{D/D^{(*)}}$.

mesons are denoted generically as D^{**}, and the D^* and D mesons as $D^{(*)}$.

D^{**} decays are reconstructed in the decay chains $D^{**} \to D^* \pi^\pm$ and $D^{**} \to D\pi^\pm$. In particular, the $D_0^*(2400)$ meson decays only through the $D\pi$ channel, while the $D_1(2430)$ and $D_1(2420)$ mesons decay only via $D^*\pi$. Both $D\pi$ and $D^*\pi$ channels are opened in the case of $D_2^*(2460)$.

In the case of BaBar data [237, 238] the branching fractions $\mathcal{B}(D_2^*(2460) \to D^{(*)}\pi)$ include both the D^* and D contributions. As they also provide the ratio $\mathcal{B}_{D/D^{(*)}}$ we estimate the D^* and D contributions separately. The experimental results of both Collaborations are given in Table 6.1.

A similar analysis can be done in the strange sector for the B_s meson semileptonic decays. Here the intermediate states are the orbitally charmed-strange mesons, D_s^{**}, and the available final channels are DK and D^*K. The PDG reports a value $\mathcal{B}(B_s^0 \to D_{s1}(2536)^- \mu^+ \nu_\mu) \times \mathcal{B}(D_{s1}(2536)^- \to D^{*-} \bar{K}^0) = 2.4 \pm 0.7$ [78] based on their best value for $\mathcal{B}(\bar{b} \to B_s^0)$ and the experimental data for $\mathcal{B}(\bar{b} \to B_s^0)\mathcal{B}(B_s^0 \to D_{s1}(2536)^- \mu^+ \nu_\mu)\mathcal{B}(D_{s1}(2536)^- \to D^{*-} \bar{K}^0)$ measured by the D0 Collaboration [239].

All these magnitudes can be consistently calculated in the framework of constituent quark models because they can simultaneously account for the hadronic part of the weak process and the strong meson decays. In this context, meson strong decay will be

	$D_0^*(2400)$	$D_1(2420)$	$D_1(2430)$	$D_2^*(2460)$
$^3P_0$	+, 1.0000	-	-	-
$^1P_1$	-	−, 0.5903	−, 0.4097	-
$^3P_1$	-	+, 0.4097	−, 0.5903	-
$^3P_2$	-	-	-	+, 0.99993
$1/2, 0^+$	+, 1.0000	-	-	-
$1/2, 1^+$	-	+, 0.0063	−, 0.9937	-
$3/2, 1^+$	-	+, 0.9937	+, 0.0063	-
$3/2, 2^+$	-	-	-	+, 0.99993
	$D_{s0}^*(2317)$	$D_{s1}(2536)$	$D_{s1}(2460)$	$D_{s2}^*(2573)$
$^3P_0$	+, 1.0000	-	-	-
$^1P_1$	-	−, 0.7210	−, 0.1880	-
$^3P_1$	-	+, 0.2770	−, 0.5570	-
$^3P_2$	-	-	-	+, 0.99991
$1/2, 0^+$	+, 1.0000	-	-	-
$1/2, 1^+$	-	−, 0.0038	−, 0.7390	-
$3/2, 1^+$	-	+, 0.9942	−, 0.0060	-
$3/2, 2^+$	-	-	-	+, 0.99991

Table 6.2. Probability distributions and their relative phases for the four states predicted by CQM. In the 1^+ strange sector the effects of non-$q\bar{q}$ components are included; see text for details.

described through the $^3P_0$ and the microscopic decay models presented before. As for the weak process the matrix elements factorize into a leptonic and a hadronic part. It is the hadronic part that contains the nonperturbative strong interaction effects and we will evaluate it within our constituent quark model. Further details on the semileptonic decay calculation based on Refs. [240, 241] can be seen in Appendix F.

The semileptonic decays of the B meson into orbitally excited charmed mesons have been studied before within Heavy Quark Effective Theory (HQET) in Refs. [242, 243]. There, only relative branching ratios could be predicted and their results depended on the approximation used and on two unknown functions, τ_1 and τ_2, that describe corrections of order $\Lambda_{\rm QCD}/m_Q$. Only the ratio $\Gamma_{D^{**}}^{\lambda=0}/\Gamma_{D^{**}}$, semileptonic decay rate with a helicity 0 D^{**} final meson over total semileptonic decay rate to that meson, seemed to be stable in the different approximations. We will comment on this below.

The description of the mesons involved in the reactions is given by our quark model. Focusing on the D^{**} (D_s^{**}) low-lying positive parity excitations, our CQM model predicts the mixed states shown in Table 6.2. We have studied in a previous section the $J^P = 1^+$ charmed-strange mesons finding that the $J^P = 1^+$ $D_{s1}(2460)$ has an important non-$q\bar{q}$ contribution whereas the $J^P = 1^+$ $D_{s1}(2536)$ is almost a pure $q\bar{q}$ state. The presence of non-$q\bar{q}$ degrees of freedom in the $J^P = 1^+$ charmed-strange meson sector enhances the $j_q = 3/2$ component of the $D_{s1}(2536)$. This wave function explains most of the experimental data and it is the one we will use here. For this sector only the $q\bar{q}$ probabilities are given in Table 6.2.

	$B^+ \to \bar{D}_0^*(2400)^0 l^+ \nu_l$	$B^0 \to D_0^*(2400)^- l^+ \nu_l$
Γ_U	0.00	0.00
$\tilde{\Gamma}_U$	0.00	0.00
Γ_L	1.30	1.16
$\tilde{\Gamma}_L$	6.83×10^{-7}	6.45×10^{-7}
$\tilde{\Gamma}_S$	2.05×10^{-6}	1.93×10^{-6}
Γ	1.30	1.16

Table 6.3. Helicity contributions and total decay width, in units of 10^{-15} GeV, for the $D_0^*(2400)$ meson.

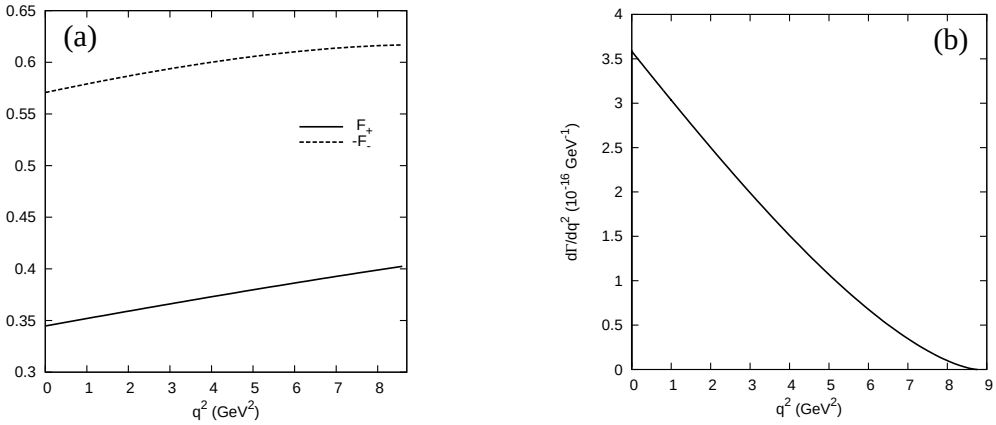

Figure 6.1. Form factors and differential decay width for the $B^+ \to \bar{D}_0^*(2400)^0 l^+ \nu_l$ decay as a function of q^2. Very similar results are obtained for the $B^0 \to D_0^*(2400)^- l^+ \nu_l$ decay. **(a)**: Form factors predicted by CQM. **(b)**: Differential decay width predicted by CQM.

6.1.1 Semileptonic B decays into D^{**} mesons

Semileptonic $B \to D_0^*(2400) l \nu_l$ decay

The measured branching fractions are $\mathcal{B}(B^+ \to \bar{D}_0^*(2400)^0 l^+ \nu_l)\, \mathcal{B}(\bar{D}_0^*(2400)^0 \to D^- \pi^+)$ and $\mathcal{B}(B^0 \to D_0^*(2400)^- l^+ \nu_l) \mathcal{B}(D_0^*(2400)^- \to \bar{D}^0 \pi^-)$. The meson $D_0^*(2400)$ has $J^P = 0^+$ quantum numbers and, therefore, due to parity conservation, it decays only into $D\pi$, so that we have $\mathcal{B}(\bar{D}_0^*(2400)^0 \to D^- \pi^+) = \mathcal{B}(D_0^*(2400)^- \to \bar{D}^0 \pi^-) = 2/3$ coming from isospin symmetry.

Table 6.3 shows the different helicity contributions to the semileptonic width. In both cases the dominant contribution is given by Γ_L while the rest are negligible. The difference between the semileptonic width of the charged and neutral B meson is due to the large mass difference between the $D_0^*(2400)^0$ and $D_0^*(2400)^{\pm}$ mesons for which we take the masses reported in Ref. [78].

Figure 6.1 shows the q^2 dependence in the form factors and in the differential decay width for $\mathcal{B}(B^+ \to \bar{D}_0^*(2400)^0 l^+ \nu_l)$, panels (a) and (b), respectively. Similar results (not shown) are obtained for the $\mathcal{B}(B^0 \to D_0^*(2400)^- l^+ \nu_l)$ case.

	$B^+ \to \bar{D}_1(2430)^0 l^+ \nu_l$	$B^0 \to D_1(2430)^- l^+ \nu_l$
Γ_U	0.23	0.23
$\tilde{\Gamma}_U$	1.35×10^{-8}	1.35×10^{-8}
Γ_L	0.56	0.56
$\tilde{\Gamma}_L$	4.12×10^{-7}	4.12×10^{-7}
$\tilde{\Gamma}_S$	1.27×10^{-6}	1.27×10^{-6}
Γ	0.79	0.80

Table 6.4. Helicity contributions and total decay width, in units of 10^{-15} GeV, for the $D_1(2430)$ meson.

The final results for the product of branching fractions are

$$\begin{aligned} &\mathcal{B}(B^+ \to \bar{D}_0^*(2400)^0 l^+ \nu_l)\mathcal{B}(\bar{D}_0^*(2400)^0 \to D^- \pi^+) = 2.15 \times 10^{-3}, \\ &\mathcal{B}(B^0 \to D_0^*(2400)^- l^+ \nu_l)\mathcal{B}(D_0^*(2400)^- \to \bar{D}^0 \pi^-) = 1.80 \times 10^{-3}, \end{aligned} \tag{6.1}$$

which compare very well with Belle data [236], $(2.4 \pm 0.4 \pm 0.6) \times 10^{-3}$ and $(2.0 \pm 0.7 \pm 0.5) \times 10^{-3}$, respectively.

Semileptonic $B \to D_1(2430) l \nu_l$ decay

The only Okubo-Zweig-Iizuka (OZI)-allowed decay channel for the $D_1(2430)$ meson is the $D_1(2430) \to D^* \pi$ so that isospin symmetry predicts a branching fraction $\mathcal{B}(D_1(2430) \to D^* \pi^\pm) = 2/3$.

Table 6.4 shows the different helicity contributions to the semileptonic width of $B^+ \to \bar{D}_1(2430)^0 l^+ \nu_l$ and $B^0 \to D_1(2430)^- l^+ \nu_l$ calculated in the framework of the CQM. In this case, Γ_U and Γ_L are of the same order of magnitude and give the total semileptonic decay rate.

Panels (a) and (b) of Fig. 6.2 show the q^2 dependence of the form factors and the differential decay width for the neutral $D_1(2430)$ channel. A very similar result is obtained for the $D_1(2430)^-$ case.

We have in this case the product of branching fractions

$$\begin{aligned} &\mathcal{B}(B^+ \to \bar{D}_1(2430)^0 l^+ \nu_l)\mathcal{B}(\bar{D}_1(2430)^0 \to D^{*-} \pi^+) = 1.32 \times 10^{-3}, \\ &\mathcal{B}(B^0 \to D_1(2430)^- l^+ \nu_l)\mathcal{B}(D_1(2430)^- \to \bar{D}^{*0} \pi^-) = 1.23 \times 10^{-3}, \end{aligned} \tag{6.2}$$

which are a rough factor of 2 smaller than the results from the BaBar Collaboration [237], $(2.7 \pm 0.4 \pm 0.5) \times 10^{-3}$ and $(3.1 \pm 0.7 \pm 0.5) \times 10^{-3}$, respectively.

Semileptonic $B \to D_1(2420) l \nu_l$ decay

As in the previous case, the branching fraction $\mathcal{B}(D_1(2420) \to D^* \pi^\pm)$ is again 2/3 in our model because $D_1(2420) \to D^* \pi$ is the only OZI-allowed decay channel.

Table 6.5 shows the different helicity contributions to the semileptonic width of the reactions $B^+ \to \bar{D}_1(2420)^0 l^+ \nu_l$ and $B^0 \to D_1(2420)^- l^+ \nu_l$. The most important contribution is given by Γ_L. The ratio $\Gamma_L/\Gamma = 0.75$ gives the probability for the

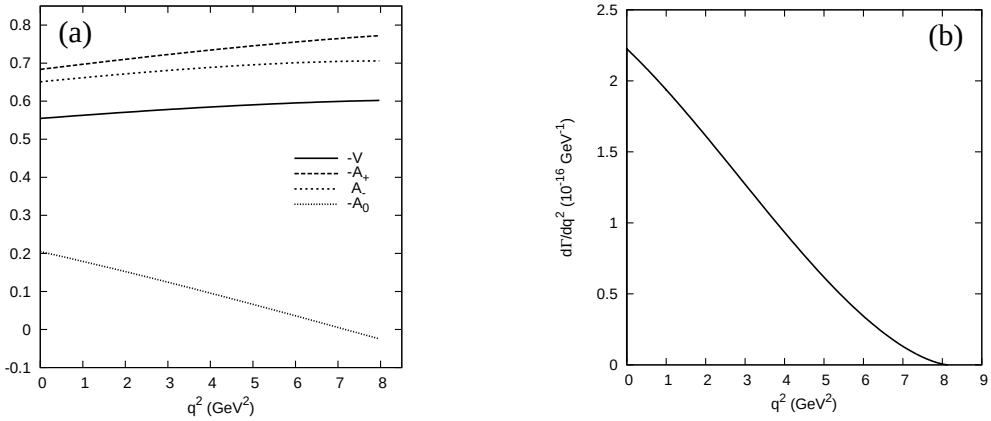

Figure 6.2. Form factors and differential decay width for the $B^+ \to \bar{D}_1(2430)^0 l^+ \nu_l$ decay as a function of q^2. Very similar results are obtained for the $B^0 \to D_1(2430)^- l^+ \nu_l$ decay. **(a)**: Form factors predicted by CQM. **(b)**: Differential decay width predicted by CQM.

	$B^+ \to \bar{D}_1(2420)^0 l^+ \nu_l$	$B^0 \to D_1(2420)^- l^+ \nu_l$
Γ_U	0.38	0.38
$\tilde{\Gamma}_U$	1.94×10^{-8}	1.93×10^{-8}
Γ_L	1.17	1.16
$\tilde{\Gamma}_L$	7.16×10^{-7}	7.15×10^{-7}
$\tilde{\Gamma}_S$	2.17×10^{-6}	2.17×10^{-6}
Γ	1.55	1.54

Table 6.5. Helicity contributions and total decay width, in units of 10^{-15} GeV, for the $D_1(2420)$ meson.

final $D_1(2420)$ meson to have helicity 0. This result is in agreement with the values $0.72 - 0.81$ obtained in the HQET calculation of Ref. [243].

Fig. 6.3 shows the q^2 dependence of the form factors and the differential decay width for neutral $D_1(2420)$ channel, in panels (a) and (b), respectively. Again, a very similar result is obtained for the charged case.

The product of branching fractions are

$$\begin{aligned} \mathcal{B}(B^+ \to \bar{D}_1(2420)^0 l^+ \nu_l)\mathcal{B}(\bar{D}_1(2420)^0 \to D^{*-}\pi^+) &= 2.57 \times 10^{-3}, \\ \mathcal{B}(B^0 \to D_1(2420)^- l^+ \nu_l)\mathcal{B}(D_1(2420)^- \to \bar{D}^{*0}\pi^-) &= 2.39 \times 10^{-3}, \end{aligned} \tag{6.3}$$

which in this case compare very well with the latest BaBar data [238], $(2.97 \pm 0.17 \pm 0.17) \times 10^{-3}$ and $(2.78 \pm 0.24 \pm 0.25) \times 10^{-3}$, respectively.

Semileptonic $B \to D_2^*(2460) l \nu_l$ decay

The semileptonic decay is studied by reconstructing the decay channel $D_2^*(2460) \to D^{(*)}\pi^-$, using the decay chain $D^* \to D^0\pi$ for D^* meson and $D^0 \to K^-\pi^+$ or $D^+ \to K^-\pi^+\pi^+$ for D meson. What is actually measured is the product of

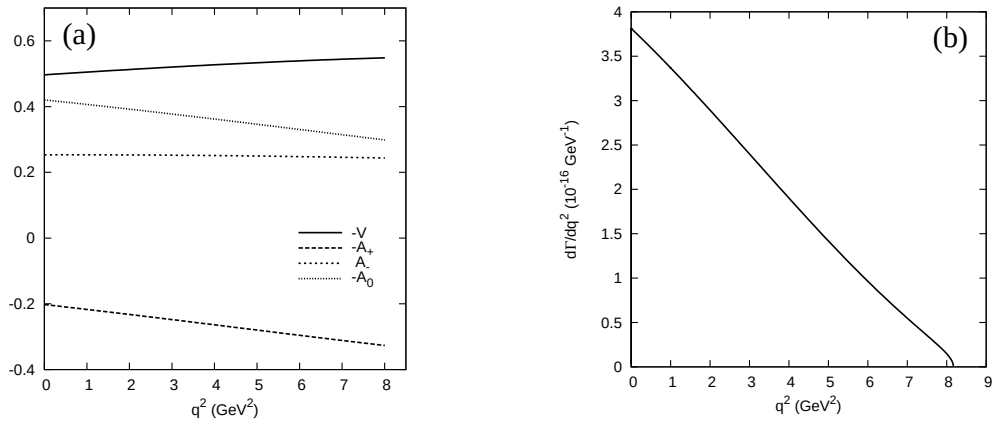

Figure 6.3. Form factors and differential decay width for the $B^+ \to \bar{D}_1(2420)^0 l^+ \nu_l$ decay as a function of q^2. The differences with respect $B^0 \to D_1(2420)^- l^+ \nu_l$ are negligible. **(a)**: Form factors predicted by CQM. **(b)**: Differential decay width predicted by CQM.

	$B^+ \to \bar{D}_2^*(2460)^0 l^+ \nu_l$	$B^0 \to D_2^*(2460)^- l^+ \nu_l$
Γ_U	0.44	0.44
$\tilde{\Gamma}_U$	2.56×10^{-8}	2.57×10^{-8}
Γ_L	0.90	0.91
$\tilde{\Gamma}_L$	5.27×10^{-7}	5.29×10^{-7}
$\tilde{\Gamma}_S$	1.54×10^{-6}	1.55×10^{-6}
Γ	1.34	1.35

Table 6.6. Helicity contributions and total decay width, in units of 10^{-15} GeV, for the $D_2^*(2460)$ meson.

branching fractions $\mathcal{B}(B^+ \to \bar{D}_2^*(2460)^0 l^+ \nu_l)\mathcal{B}(\bar{D}_2^*(2460)^0 \to D^- \pi^+)$ and $\mathcal{B}(B^+ \to \bar{D}_2^*(2460)^0 l^+ \nu_l)\mathcal{B}(\bar{D}_2^*(2460)^0 \to D^{*-} \pi^+)$.

In Table 6.6 we show the different helicity contributions to the total width. The main contribution is Γ_L in both neutral and charged $D_2^*(2460)$ channels, providing almost 2/3 of the total width. The following one is Γ_U, the rest of the contributions being negligible. Again our ratio $\Gamma_L/\Gamma = 0.67$ is in agreement with the values $0.63-0.64$ obtained in Ref. [243] using HQET.

Figure 6.4 shows the q^2 dependence in the form factors and in the differential decay width, panels (a) and (b), respectively, for the $B^+ \to \bar{D}_2^*(2460)^0 l^+ \nu_l$ decay. Very similar results (not shown) are obtained for the $B^0 \to D_2^*(2460)^- l^+ \nu_l$ case.

The subsequent strong decays which appear are $D_2^*(2460) \to D^* \pi^-$ and $D_2^*(2460) \to D\pi^-$. In Table 6.7 we show the strong decay branching ratios obtained with the $^3P_0$ and the microscopic models. They are in good agreement with experimental data [78].

Finally, we obtain the products of branching fractions for both decay chains considering that the total width of the $D_2^*(2460)$ meson is the sum of the partial widths

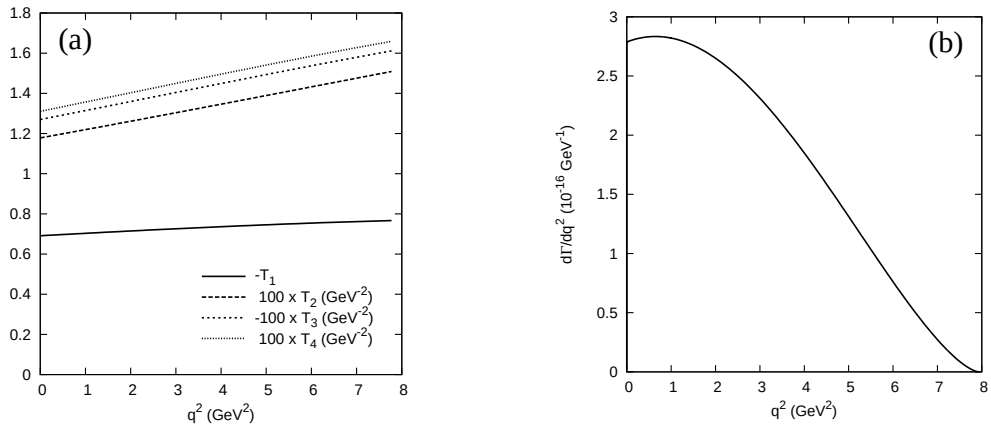

Figure 6.4. Form factors and differential decay width for the $B^+ \to \bar{D}_2^*(2460)^0 l^+ \nu_l$ decay as a function of q^2. Very similar results are obtained for the $B^0 \to D_2^*(2460)^- l^+ \nu_l$ decay. **(a)**: Form factors predicted by CQM. **(b)**: Differential decay width predicted by CQM.

Branching ratio	Exp.	$^3P_0$	Mic.
$\Gamma(D_2^{*+} \to D^0\pi^+)/\Gamma(D_2^{*+} \to D^{*0}\pi^+)$	$1.9 \pm 1.1 \pm 0.3$	1.80	1.97
$\Gamma(D_2^{*0} \to D^+\pi^-)/\Gamma(D_2^{*0} \to D^{*+}\pi^-)$	1.56 ± 0.16	1.82	1.97
$\Gamma(D_2^* \to D\pi)/\Gamma(D_2^* \to D^{(*)}\pi)$	$0.62 \pm 0.03 \pm 0.02$	0.65	0.66

Table 6.7. Open-flavor strong branching ratios for $D_2^*(2460)$ collected by the PDG [78] and our theoretical results calculated through the $^3P_0$ and the microscopic models.

of $D^*\pi$ and $D\pi$ channels since these are the only OZI-allowed processes

$$\begin{aligned}
\mathcal{B}(B^+ \to \bar{D}_2^*(2460)^0 l^+ \nu_l)\mathcal{B}(\bar{D}_2^*(2460)^0 \to D^-\pi^+) &= \begin{cases} 1.44 \times 10^{-3} \\ 1.48 \times 10^{-3} \end{cases} \\
\mathcal{B}(B^+ \to \bar{D}_2^*(2460)^0 l^+ \nu_l)\mathcal{B}(\bar{D}_2^*(2460)^0 \to D^{*-}\pi^+) &= \begin{cases} 0.79 \times 10^{-3} \\ 0.75 \times 10^{-3} \end{cases} \\
\mathcal{B}(B^0 \to D_2^*(2460)^- l^+ \nu_l)\mathcal{B}(D_2^*(2460)^- \to \bar{D}^0\pi^-) &= \begin{cases} 1.34 \times 10^{-3} \\ 1.38 \times 10^{-3} \end{cases} \\
\mathcal{B}(B^0 \to D_2^*(2460)^- l^+ \nu_l)\mathcal{B}(D_2^*(2460)^- \to \bar{D}^{*0}\pi^-) &= \begin{cases} 0.74 \times 10^{-3} \\ 0.70 \times 10^{-3} \end{cases}
\end{aligned} \tag{6.4}$$

where the first one refers to the calculation using the $^3P_0$ model and the second one comes from the microscopic model. These results are in very good agreement with BaBar data [238], $(1.4 \pm 0.2 \pm 0.2) \times 10^{-3}$ and $(0.9 \pm 0.2 \pm 0.2) \times 10^{-3}$ for the $\bar{D}_2^*(2460)^0$ meson, and $(1.1 \pm 0.2 \pm 0.1) \times 10^{-3}$ and $(0.7 \pm 0.2 \pm 0.1) \times 10^{-3}$ for the $D_2^*(2460)^-$ meson.

Summary of the results

Final results and their comparison with the experimental data are given in Table 6.8. Except for the $D_1(2430)$, the predictions are in very good agreement with the latest

	Belle [236] ($\times 10^{-3}$)	BaBar [237, 238] ($\times 10^{-3}$)	$^3P_0$ ($\times 10^{-3}$)	Mic. ($\times 10^{-3}$)
$D_0^*(2400)$				
$\mathcal{B}(B^+ \to \bar{D}_0^*(2400)^0 l^+ \nu_l)\mathcal{B}(\bar{D}_0^*(2400)^0 \to D^- \pi^+)$	$2.4 \pm 0.4 \pm 0.6$	$2.6 \pm 0.5 \pm 0.4$	2.15	2.15
$\mathcal{B}(B^0 \to D_0^*(2400)^- l^+ \nu_l)\mathcal{B}(D_0^*(2400)^- \to \bar{D}^0 \pi^-)$	$2.0 \pm 0.7 \pm 0.5$	$4.4 \pm 0.8 \pm 0.6$	1.80	1.80
$D_1(2430)$				
$\mathcal{B}(B^+ \to \bar{D}_1(2430)^0 l^+ \nu_l)\mathcal{B}(\bar{D}_1(2430)^0 \to D^{*-} \pi^+)$	< 0.7	$2.7 \pm 0.4 \pm 0.5$	1.32	1.32
$\mathcal{B}(B^0 \to D_1(2430)^- l^+ \nu_l)\mathcal{B}(D_1(2430)^- \to \bar{D}^{*0} \pi^-)$	< 5	$3.1 \pm 0.7 \pm 0.5$	1.23	1.23
$D_1(2420)$				
$\mathcal{B}(B^+ \to \bar{D}_1(2420)^0 l^+ \nu_l)\mathcal{B}(\bar{D}_1(2420)^0 \to D^{*-} \pi^+)$	$4.2 \pm 0.7 \pm 0.7$	$2.97 \pm 0.17 \pm 0.17$	2.57	2.57
$\mathcal{B}(B^0 \to D_1(2420)^- l^+ \nu_l)\mathcal{B}(D_1(2420)^- \to \bar{D}^{*0} \pi^-)$	$5.4 \pm 1.9 \pm 0.9$	$2.78 \pm 0.24 \pm 0.25$	2.39	2.39
$D_2^*(2460)$				
$\mathcal{B}(B^+ \to \bar{D}_2^*(2460)^0 l^+ \nu_l)\mathcal{B}(\bar{D}_2^*(2460)^0 \to D^- \pi^+)$	$2.2 \pm 0.3 \pm 0.4$	$1.4 \pm 0.2 \pm 0.2^{(*)}$	1.43	1.47
$\mathcal{B}(B^+ \to \bar{D}_2^*(2460)^0 l^+ \nu_l)\mathcal{B}(\bar{D}_2^*(2460)^0 \to D^{*-} \pi^+)$	$1.8 \pm 0.6 \pm 0.3$	$0.9 \pm 0.2 \pm 0.2^{(*)}$	0.79	0.75
$\mathcal{B}(B^+ \to \bar{D}_2^*(2460)^0 l^+ \nu_l)\mathcal{B}(\bar{D}_2^*(2460)^0 \to D^{(*)-} \pi^+)$	$4.0 \pm 0.7 \pm 0.5$	$2.3 \pm 0.2 \pm 0.2$	2.22	2.22
$\mathcal{B}(B^0 \to D_2^*(2460)^- l^+ \nu_l)\mathcal{B}(D_2^*(2460)^- \to \bar{D}^0 \pi^-)$	$2.2 \pm 0.4 \pm 0.4$	$1.1 \pm 0.2 \pm 0.1^{(*)}$	1.34	1.38
$\mathcal{B}(B^0 \to D_2^*(2460)^- l^+ \nu_l)\mathcal{B}(D_2^*(2460)^- \to \bar{D}^{*0} \pi^-)$	< 3	$0.7 \pm 0.2 \pm 0.1^{(*)}$	0.74	0.70
$\mathcal{B}(B^0 \to D_2^*(2460)^- l^+ \nu_l)\mathcal{B}(D_2^*(2460)^- \to \bar{D}^{(*)0} \pi^-)$	< 5.2	$1.8 \pm 0.3 \pm 0.1$	2.08	2.08
$\mathcal{B}_{D/D^{(*)}}$	0.55 ± 0.03	$0.62 \pm 0.03 \pm 0.02$	0.65	0.66

Table 6.8. Most recent experimental measurements reported by the Belle and BaBar Collaborations and their comparison with our results. l stands for a light e or μ lepton. The symbol $(*)$ indicates the estimated results from the original data using $B_{D/D^{(*)}}$.

experimental measurements, Belle for $D_0^*(2400)$ and BaBar for $D_1(2420)$ and $D_2^*(2460)$. For the $D_1(2430)$ there is also a strong disagreement between experimental data in the neutral case.

6.1.2 Semileptonic B_s decays into D_s^{**} mesons

The semileptonic decays of B_s meson into orbitally excited charmed-strange mesons (D_s^{**}) provides an extra opportunity to get more insight into this system.

We have mentioned that the $j_q = 1/2$ doublet, $D_{s0}^*(2317)$ and $D_{s1}(2460)$, shows surprisingly light masses which are below the DK and D^*K thresholds, respectively. These unexpected properties have triggered many theoretical interpretations, including four quark states, molecules, and the coupling of the $q\bar{q}$ components with different structures. In this work, we have seen that while the $D_{s0}^*(2317)$ meson can be explained as a $q\bar{q}$ structure, the $D_{s1}(2460)$ meson has an important non-$q\bar{q}$ contribution.

We have calculated the semileptonic B_s decays assuming that the D_s^{**} mesons are pure $q\bar{q}$ systems. For the $D_{s0}^*(2317)$ and $D_{s1}(2460)$, which are below the corresponding $D^{(*)}K$ thresholds, we only quote the weak decay branching fractions. Concerning the $D_{s1}(2460)$, the $^1P_1$ and $^3P_1$ probabilities change with the coupling to non-$q\bar{q}$ degrees of freedom. What we do here is to vary these probabilities (including the phase) in order to obtain the limits of the decay width in the case of the $D_{s1}(2460)$ being a pure $q\bar{q}$ state, see Fig. 6.5. Assuming that non-$q\bar{q}$ components will give a small contribution to the weak decay, experimental results lower than these limits will be an indication of a

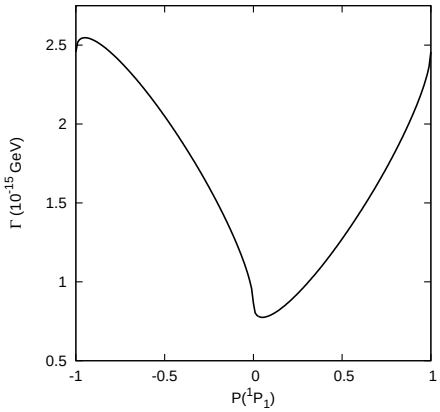

Figure 6.5. Decay width for the $B_s^0 \to D_{s1}(2460)^- \mu^+ \nu_\mu$ decay as a function of the ${}^1P_1$ component probability. The sign reflects the relative phase between ${}^1P_1$ and ${}^3P_1$ components: -1 opposite phase and $+1$ same phase.

	Experiment ($\times 10^{-3}$)	Theory ($\times 10^{-3}$)	
$D_{s0}^*(2317)$			
$\mathcal{B}(B_s^0 \to D_{s0}^*(2318)^- \mu^+ \nu_\mu)$	-	4.43	
$D_{s1}(2460)$			
$\mathcal{B}(B_s^0 \to D_{s1}(2460)^- \mu^+ \nu_\mu)$	-	$1.74 - 5.70$	
$D_{s1}(2536)$		${}^3P_0$	Mic.
$\mathcal{B}(B_s^0 \to D_{s1}(2536)^- \mu^+ \nu_\mu)\mathcal{B}(D_{s1}(2536)^- \to D^{*-} \bar{K}^0)$	2.4 ± 0.7 [78, 239]	2.05	2.24
$D_{s2}^*(2573)$		${}^3P_0$	Mic.
$\mathcal{B}(B_s^0 \to D_{s2}^*(2573)^- \mu^+ \nu_\mu)\mathcal{B}(D_{s2}^*(2573)^- \to D^- \bar{K}^0)$	-	1.70	1.77
$\mathcal{B}(B_s^0 \to D_{s2}^*(2573)^- \mu^+ \nu_\mu)\mathcal{B}(D_{s2}^*(2573)^- \to D^{*-} \bar{K}^0)$	-	0.18	0.11
$\mathcal{B}(B_s^0 \to D_{s2}^*(2573)^- \mu^+ \nu_\mu)\mathcal{B}(D_{s2}^*(2573)^- \to D^{(*)-} \bar{K}^0)$	-	1.88	1.88

Table 6.9. Our predictions and their comparison with the available experimental data for semileptonic B_s decays into orbitally excited charmed-strange mesons.

more complex structure for this meson.

For the decay into $D_{s1}(2536)$, our model predicts the weak decay branching fraction $\mathcal{B}(B_s^0 \to D_{s1}(2536)\mu^+\nu_\mu) = 4.77 \times 10^{-3}$ and the strong branching fraction $\mathcal{B}(D_{s1}(2536)^- \to D^{*-}\bar{K}^0) = 0.43$ (0.47) for the ${}^3P_0$ (microscopic) model. The final result appears in Table 6.9. It is compatible with the existing experimental data [78], which to us is a confirmation of our result about the $q\bar{q}$ nature of this state.

In the case of the $D_{s2}^*(2573)$ meson the open strong decays are DK and D^*K, so the experimental measurements must be referred to $\mathcal{B}(B_s^0 \to D_{s2}^*(2573)^- \mu^+ \nu_\mu)$ $\mathcal{B}(D_{s2}^*(2573)^- \to D^- \bar{K}^0)$ and $\mathcal{B}(B_s^0 \to D_{s2}^*(2573)^- \mu^+ \nu_\mu)\mathcal{B}(D_{s2}^*(2573)^- \to D^{*-} \bar{K}^0)$.

For the weak branching fraction we get in this case $\mathcal{B}(B_s^0 \to D_{s2}^*(2573)^- \mu^+ \nu_\mu) =$

3.76×10^{-3}. For the strong decay part of the reaction, we obtain in our model

$$\begin{aligned} \mathcal{B}(D_{s2}^{*-} \to D^- \bar{K}^0) &= \begin{cases} 0.45 \\ 0.47 \end{cases} \\ \mathcal{B}(D_{s2}^{*-} \to D^{*-} \bar{K}^0) &= \begin{cases} 0.047 \\ 0.030 \end{cases} \end{aligned} \tag{6.5}$$

where the first one refers to the calculation using the $^3P_0$ model and the second one comes from the microscopic model. Besides we predict the ratio

$$\frac{\Gamma(D_{s2}^* \to DK)}{\Gamma(D_{s2}^* \to DK) + \Gamma(D_{s2}^* \to D^*K)} = \begin{cases} 0.91 & ^3P_0 \\ 0.94 & \text{Mic.} \end{cases} \tag{6.6}$$

Our final results can be seen in Table. 6.9.

6.2 Nonleptonic B decays into $D^{(*)}D_{sJ}$ final states

The nonleptonic decays of B mesons, described at the quark level by an effective four-quark interaction $\bar{b} \to \bar{c}c\bar{s}$, have been used to search for new charmonium and charmed-strange mesons and to study their properties in detail. Within the charmed-strange sector, the BaBar Collaboration found, in the inclusive $D_s^+\pi^0$ invariant mass distribution from e^+e^- annihilation data, the narrow state $D_{s0}^*(2317)$ [37]. The CLEO Collaboration, aiming to confirm the previous state, observed its doublet partner $D_{s1}(2460)$ in the $D_s^{*+}\pi^0$ final state [38]. However, the properties of these states were not well known until the Belle Collaboration observed the $B \to \bar{D}D_{s0}^*(2317)$ and $B \to \bar{D}D_{s1}(2460)$ decays [244].

First observations of the $B \to \bar{D}^{(*)}D_{s1}(2536)$ decay modes have been reported by BaBar [245, 246] and an upper limit on the decay $B^0 \to D^{*-}D_{s1}(2536)^+$ was also obtained by Belle [247]. The most recent analysis of the production of $D_{s1}(2536)^+$ in double charmed B meson decays has been reported by the Belle Collaboration in Ref. [248]. Using the latest measurements of the $B \to D^{(*)}D_{sJ}$ branching fractions [78] they calculate the ratios

$$\begin{aligned} R_{D0} &= \frac{\mathcal{B}(B \to DD_{s0}^*(2317))}{\mathcal{B}(B \to DD_s)} = 0.10 \pm 0.03, \\ R_{D^*0} &= \frac{\mathcal{B}(B \to D^*D_{s0}^*(2317))}{\mathcal{B}(B \to D^*D_s)} = 0.15 \pm 0.06, \\ R_{D1} &= \frac{\mathcal{B}(B \to DD_{s1}(2460))}{\mathcal{B}(B \to DD_s^*)} = 0.44 \pm 0.11, \\ R_{D^*1} &= \frac{\mathcal{B}(B \to D^*D_{s1}(2460))}{\mathcal{B}(B \to D^*D_s^*)} = 0.58 \pm 0.12. \end{aligned} \tag{6.7}$$

In addition, the same ratios are calculated for $B \to D^{(*)}D_{s1}(2536)^+$ decays using

combined results by the BaBar [246] and Belle [248] Collaborations

$$\begin{aligned} R_{D1'} &= \frac{\mathcal{B}(B \to DD_{s1}(2536))}{\mathcal{B}(B \to DD_s^*)} = 0.049 \pm 0.010, \\ R_{D^*1'} &= \frac{\mathcal{B}(B \to D^*D_{s1}(2536))}{\mathcal{B}(B \to D^*D_s^*)} = 0.044 \pm 0.010. \end{aligned} \tag{6.8}$$

The branching fraction measurements of the decays $B \to D^{(*)}D_{sJ}$ provide valuable information that makes possible to check the structure of the $D_{s0}^*(2317)$, $D_{s1}(2460)$ and $D_{s1}(2536)$ mesons [249, 250].

From a theoretical point of view, this kind of decays can be described using the factorization approximation [241]. This amounts to evaluate the matrix element which describes the $B \to D^{(*)}D_{sJ}$ weak decay process as a product of two matrix elements, the first one to describe the B weak transition into the $D^{(*)}$ meson and the second one for the weak creation of the $c\bar{s}$ pair which makes the D_{sJ} meson. The latter matrix element is proportional to the corresponding D_{sJ} meson decay constant.

The D_{sJ} meson decay constants are not known experimentally except for the ground state, D_s, which has been measured by different Collaborations. Another way to study D_{sJ} mesons that does not rely on the knowledge of their decay constants is through the decays $B_s \to D_{sJ}M$ where M is a meson with a well known decay constant. However, the experimental study of these processes is currently difficult for several reasons. First, B-factories would need to collect data at the $\Upsilon(5S)$ resonance. Second, the kinematically clean environment of B meson decays does not hold in B_s decays. And finally, the fraction of events with a pair of B_s mesons over the total number of events with a pair of b-flavored hadrons has been measured to be relatively small, $f_s[\Upsilon(5S)] = 0.193 \pm 0.029$. These difficulties leave, for the time being, the $B \to D^{(*)}D_{sJ}$ decay processes as our best option to study D_{sJ} meson properties.

According to Refs. [249, 250], within the factorization approximation and in the heavy quark limit, the ratios in Eqs. (6.7) and (6.8) can be written as

$$\begin{aligned} R_{D0} = R_{D^*0} &= \left| \frac{f_{D_{s0}^*(2317)}}{f_{D_s}} \right|^2, \\ R_{D1} = R_{D^*1} &= \left| \frac{f_{D_{s1}(2460)}}{f_{D_s^*}} \right|^2, \\ R_{D1'} = R_{D^*1'} &= \left| \frac{f_{D_{s1}(2536)}}{f_{D_s^*}} \right|^2, \end{aligned} \tag{6.9}$$

where the phase space effects are neglected because they are subleading in the heavy quark expansion. Now, in the heavy quark limit one has $f_{D_{s0}^*(2317)} = f_{D_{s1}(2460)}$, $f_{D_s} = f_{D_s^*}$ and $f_{D_{s1}(2536)} = 0$. Moreover, there are several estimates of the decay constants, always in the heavy quark limit [251–253], that predict for P-wave, $j_q = 1/2$ states similar decay constants as for the ground state mesons (i.e. $f_{D_{s0}^*(2317)} = f_{D_s}$ and $f_{D_{s1}(2460)} = f_{D_s^*}$), and very small decay constants for P-wave, $j_q = 3/2$ states. These approximations lead to ratios of order one for the $D_{s0}^*(2317)$ and $D_{s1}(2460)$ mesons, and very small for $D_{s1}(2536)$. While the decay into $D_{s1}(2536)$ follows the expectations, this is not the case for the $D_{s0}^*(2317)$ and $D_{s1}(2460)$ mesons. This fact has motivated

the authors of Ref. [250] to argue that either those two states are not canonical $c\bar{s}$ mesons or that the factorization approximation does not hold for decays involving those particles.

Leaving aside that the factorization approximation has been recently analyzed in Refs. [254–256] finding that it works well in these kind of processes, we will concentrate in the influence of the the effect of the finite c-quark mass in the theoretical predictions. As found in Ref. [257], $1/m_Q$ contributions give large corrections to various quantities describing $B \to D^{**}$ transitions and we expect they also play an important role in this case. It is possible that taking into account the finite mass of the charmed quark one can distinguish better between $q\bar{q}$ and non-$q\bar{q}$ structures for the D_{sJ} mesons.

The mesons involved in the reactions, particularly the charmed-strange ones, have been discussed extensively in previous sections of this work. The most relevant features to take into account here are: we have reached a good description of the ground state B and the singlet and triplet S-wave charmed mesons, D and D^*. We have seen that the interpretation of the $D^*_{s0}(2317)$ as a canonical $c\bar{s}$ state is plausible since its mass goes down to the experimental value when the one-loop QCD corrections to the OGE potential are taken into account. The presence of non-$q\bar{q}$ degrees of freedom in the $J^P = 1^+$ $c\bar{s}$ sector makes that the $J^P = 1^+$ $D_{s1}(2460)$ has an important non-$q\bar{q}$ contribution whereas the $J^P = 1^+$ $D_{s1}(2536)$ is almost a pure $q\bar{q}$ state.

The nonleptonic decay width for $B \to D^{(*)} D_{sJ}$ processes in the factorization approximation and using helicity formalism [240, 241] is given in Appendix F. The final expression of the decay rate reads

$$\Gamma = \frac{G_F^2}{16\pi m_B^2} |V_{cb}|^2 |V_{cs}|^2 a_1^2 \, \frac{\lambda^{1/2}(m_B^2, m_{D^{(*)}}^2, m_{D_{sJ}}^2)}{2m_B} \, m_{D_{sJ}}^2 f_{D_{sJ}}^2 \mathcal{H}_{tt}^{B\to D^{(*)}}(m_{D_{sJ}}^2), \tag{6.10}$$

for D_{sJ} a pseudoscalar or scalar meson, and

$$\begin{aligned} \Gamma =& \frac{G_F^2}{16\pi m_B^2} |V_{cb}|^2 |V_{cs}|^2 a_1^2 \, \frac{\lambda^{1/2}(m_B^2, m_{D^{(*)}}^2, m_{D_{sJ}}^2)}{2m_B} \, m_{D_{sJ}}^2 f_{D_{sJ}}^2 \times \\ & \times \left[\mathcal{H}_{+1+1}^{B\to D^{(*)}}(m_{D_{sJ}}^2) + \mathcal{H}_{-1-1}^{B\to D^{(*)}}(m_{D_{sJ}}^2) + \mathcal{H}_{00}^{B\to D^{(*)}}(m_{D_{sJ}}^2) \right], \end{aligned} \tag{6.11}$$

for D_{sJ} a vector or axial-vector meson. $G_F = 1.16637(1) \times 10^{-5}\,\mathrm{GeV}^{-2}$ is the Fermi constant [78], $\lambda(a,b,c) = (a+b-c)^2 - 4ab$. V_{cb} and V_{cs} are the cb and cs elements of the CKM matrix for which we use $V_{cb} = 0.0413$ and $V_{cs} = 0.974$. $\mathcal{H}_{rs}$ are the helicity components of the hadron tensor evaluated at $q^2 = m_{D_{sJ}}^2$ and we use $a_1 = 1.14$. The expressions of the decay constants needed are given in the Appendix F.

From Eqs. (6.10) and (6.11) we arrive at

$$
\begin{aligned}
R_{D0} =& \frac{\lambda^{1/2}\left(m_B^2, m_D^2, m_{D_{s0}^*(2317)}^2\right) m_{D_{s0}^*(2317)}^2 f_{D_{s0}^*(2317)}^2 \mathcal{H}_{tt}^{B\to D}\left(m_{D_{s0}^*(2317)}^2\right)}{\lambda^{1/2}(m_B^2, m_D^2, m_{D_s}^2) m_{D_s}^2 f_{D_s}^2 \mathcal{H}_{tt}^{B\to D}(m_{D_s}^2)}, \\
R_{D1} =& \frac{\lambda^{1/2}\left(m_B^2, m_D^2, m_{D_{s1}(2460)}^2\right) m_{D_{s1}(2460)}^2 f_{D_{s1}(2460)}^2}{\lambda^{1/2}(m_B^2, m_D^2, m_{D_s^*}^2) m_{D_s^*}^2 f_{D_s^*}^2} \times \\
& \times \frac{\left[\mathcal{H}_{+1+1}^{B\to D}\left(m_{D_{s1}(2460)}^2\right) + \mathcal{H}_{-1-1}^{B\to D}\left(m_{D_{s1}(2460)}^2\right) + \mathcal{H}_{00}^{B\to D}\left(m_{D_{s1}(2460)}^2\right)\right]}{\left[\mathcal{H}_{+1+1}^{B\to D}(m_{D_s^*}^2) + \mathcal{H}_{-1-1}^{B\to D}(m_{D_s^*}^2) + \mathcal{H}_{00}^{B\to D}(m_{D_s^*}^2)\right]}, \\
R_{D1'} =& \frac{\lambda^{1/2}\left(m_B^2, m_D^2, m_{D_{s1}(2536)}^2\right) m_{D_{s1}(2536)}^2 f_{D_{s1}(2536)}^2}{\lambda^{1/2}(m_B^2, m_D^2, m_{D_s^*}^2) m_{D_s^*}^2 f_{D_s^*}^2} \times \\
& \times \frac{\left[\mathcal{H}_{+1+1}^{B\to D}\left(m_{D_{s1}(2536)}^2\right) + \mathcal{H}_{-1-1}^{B\to D}\left(m_{D_{s1}(2536)}^2\right) + \mathcal{H}_{00}^{B\to D}\left(m_{D_{s1}(2536)}^2\right)\right]}{\left[\mathcal{H}_{+1+1}^{B\to D}(m_{D_s^*}^2) + \mathcal{H}_{-1-1}^{B\to D}(m_{D_s^*}^2) + \mathcal{H}_{00}^{B\to D}(m_{D_s^*}^2)\right]},
\end{aligned}
\tag{6.12}
$$

and the same for R_{D^*0}, R_{D^*1} and $R_{D^*1'}$ but replacing the meson D by the meson D^*.

Using experimental masses we obtain the ratios

$$
\begin{aligned}
R_{D0} &= 0.9008 \times \left|\frac{f_{D_{s0}^*(2317)}}{f_{D_s}}\right|^2, \\
R_{D^*0} &= 0.7166 \times \left|\frac{f_{D_{s0}^*(2317)}}{f_{D_s}}\right|^2.
\end{aligned}
\tag{6.13}
$$

The double ratio R_{D^*0}/R_{D0} does not depend on decay constants, and in our model we obtain $R_{D^*0}/R_{D0} = 0.7955$. The experimental value is given by $R_{D^*0}/R_{D0} = 1.50 \pm 0.75$. Our result is small compared to the central experimental value but we are compatible within 1σ. In the case of the meson $D_{s1}(2460)$ we obtain

$$
\begin{aligned}
R_{D1} &= 0.7040 \times \left|\frac{f_{D_{s1}(2460)}}{f_{D_s^*}}\right|^2, \\
R_{D^*1} &= 1.0039 \times \left|\frac{f_{D_{s1}(2460)}}{f_{D_s^*}}\right|^2,
\end{aligned}
\tag{6.14}
$$

and for the double ratio R_{D^*1}/R_{D1} we get 1.4260, which agrees well with the experimental result $R_{D^*1}/R_{D1} = 1.32 \pm 0.43$. Finally, for the meson $D_{s1}(2536)$ we obtain

$$
\begin{aligned}
R_{D1'} &= 0.6370 \times \left|\frac{f_{D_{s1}(2536)}}{f_{D_s^*}}\right|^2, \\
R_{D^*1'} &= 0.9923 \times \left|\frac{f_{D_{s1}(2536)}}{f_{D_s^*}}\right|^2,
\end{aligned}
\tag{6.15}
$$

and for the double ratio $R_{D^*1'}/R_{D1'}$, our value is 1.5578 which in this case is 2σ above the experimental one, 0.90 ± 0.27.

Approach	f_D (MeV)	f_{D_s} (MeV)	f_{D_s}/f_D
Ours	$297.019^{(\dagger)}$	$416.827^{(\dagger)}$	$1.40^{(\dagger)}$
	$214.613^{(\ddagger)}$	$286.382^{(\ddagger)}$	$1.33^{(\ddagger)}$
Experiment	206.7 ± 8.9	257.5 ± 6.1	1.25 ± 0.06
Lattice (HPQCD+UKQCD)	208 ± 4	241 ± 3	1.162 ± 0.009
Lattice (FNAL+MILC+HPQCD)	217 ± 10	260 ± 10	1.20 ± 0.02
PQL	197 ± 9	244 ± 8	1.24 ± 0.03
QL (QCDSF)	$206 \pm 6 \pm 3 \pm 22$	$220 \pm 6 \pm 5 \pm 11$	$1.07 \pm 0.02 \pm 0.02$
QL (Taiwan)	$235 \pm 8 \pm 14$	$266 \pm 10 \pm 18$	$1.13 \pm 0.03 \pm 0.05$
QL (UKQCD)	$210 \pm 10^{+17}_{-16}$	$236 \pm 8^{+17}_{-14}$	$1.13 \pm 0.02^{+0.04}_{-0.02}$
QL	$211 \pm 14^{+2}_{-12}$	$231 \pm 12^{+6}_{-1}$	1.10 ± 0.02
QCD Sum Rules	177 ± 21	205 ± 22	$1.16 \pm 0.01 \pm 0.03$
QCD Sum Rules	203 ± 20	235 ± 24	1.15 ± 0.04
Field Correlators	210 ± 10	260 ± 10	1.24 ± 0.03
Light Front	206	268.3 ± 19.1	1.30 ± 0.04
Approach	f_{D^*} (MeV)	$f_{D_s^*}$ (MeV)	$f_{D_s^*}/f_{D^*}$
Ours	$247.865^{(\dagger)}$	$329.441^{(\dagger)}$	$1.33^{(\dagger)}$
RBS	340 ± 22	375 ± 24	1.10 ± 0.06
RQM	315	335	1.06
QL (Italy)	234	254	$1.04 \pm 0.01^{+2}_{-4}$
QL (UKQCD)	$245 \pm 20^{+0}_{-2}$	$272 \pm 16^{+0}_{-20}$	1.11 ± 0.03
BS	237	242	1.02
RM	262 ± 10	298 ± 11	1.14 ± 0.09

Table 6.10. Theoretical predictions of decay constants for pseudoscalar and vector charmed mesons. The data have been taken from Ref. [78] for pseudoscalar mesons and from Ref. [258] for vector mesons. PQL ≡ Partially-Quenched Lattice calculation, QL ≡ Quenched Lattice calculations, RBS ≡ Relativistic Bethe-Salpeter, RQM ≡ Relativistic Quark Model, BS ≡ Bethe-Salpeter Method and RM ≡ Relativistic Mock meson model.

The quality of the experimental numbers does not allow to be very conclusive as to the goodness of the factorization approximation. But one thing that can be concluded from Eqs. (6.13), (6.14) and (6.15) is that one cannot ignore, as done when using the infinite heavy quark mass limit, phase space and weak matrix element corrections even if they are subleading in the heavy quark mass expansion.

The decay constants of pseudoscalar and vector mesons in charmed and charmed-strange sectors are given in Table 6.10. We compare our results with the experimental data and those predicted by different approaches and collected in Refs. [78, 258]. Our original values are those with the symbol (†). The decay constants of vector mesons agree with other approaches. In the case of the pseudoscalar mesons, the decay constants are simply too large. The reason for that is the following: Our CQM presents an OGE potential which has a spin-spin contact hyperfine interaction that is proportional to a Dirac delta function, conveniently regularized, at the origin. The corresponding regularization parameter was fitted to determine the hyperfine splittings between the n^1S_0 and n^3S_1 states in the different flavor sectors, achieving a good agreement in all of them. While most of the physical observables are insensitive to the

Meson	f_D (MeV)	$\sqrt{M_D} f_D$ (GeV$^{3/2}$)
$D^*_{s0}(2317)$	118.706	0.181
$D_{s1}(2460)$	165.097	0.259
$D_{s1}(2536)$	59.176	0.094

Table 6.11. Decay constants calculated within the CQM including one-loop QCD corrections to the OGE potential and a non-$q\bar{q}$ structure in channel 1^+.

regularization of this delta term, those related with annihilation processes are affected as shown in Section 3.7.1. The effect is very small in the $^3S_1$ channel as the delta term is repulsive in this case. It is negligible for higher partial waves due to the shielding by the centrifugal barrier. However, it is sizable in the $^1S_0$ channel for which the delta term is attractive.

One expects that the wave functions of the 1^1S_0 and 1^3S_1 states are very similar [259]. In fact, they are equal if the Dirac delta term is ignored. The values with the symbol (‡) in Table 6.10 are referred to the pseudoscalar decay constants which have been calculated using the wave function of the corresponding $^3S_1$ state. We recover the agreement with experiment and also with the predictions of different theoretical approaches. The f_{D_s}/f_D and $f_{D_s^*}/f_{D^*}$ ratios are also shown in the last column of Table 6.10. They are not very sensitive to the delta term and our values agree nicely with experiment and the values obtained in other approaches.

Table 6.11 summarizes the remaining decay constants needed for the calculation we are interested in. There, we show the results from the constituent quark model in which the 1-loop QCD corrections to the OGE potential and the presence of non-$q\bar{q}$ degrees of freedom in $J^P = 1^+$ charmed-strange meson sector are included. If one compares f_{D_s} ($f_{D_s^*}$) to $f_{D^*_{s0}(2317)}$ ($f_{D_{s1}(2460)}$), one finds that the latter is suppressed.

Refs. [260] and [261] calculate the lower bounds of the decay constants of $D^*_{s0}(2317)$ and $D_{s1}(2460)$ analyzing experimental data related to $B \to DD_{sJ}$. Ref. [260] provides the following lower limits

$$
\begin{aligned}
|a_1|\, f_{D^*_{s0}(2317)} &= \begin{cases} 58 - 83\,\text{MeV} & \text{from } B^- \text{ decays}, \\ 63 - 86\,\text{MeV} & \text{from } \bar{B}^0 \text{ decays}, \end{cases} \\
|a_1|\, f_{D_{s1}(2460)} &= \begin{cases} 188^{+40}_{-54}\,\text{MeV} & \text{from } B^- \text{ decays}, \\ 152^{+43}_{-62}\,\text{MeV} & \text{from } \bar{B}^0 \text{ decays}, \end{cases}
\end{aligned}
\tag{6.16}
$$

and the authors of Ref. [261] get

$$
\begin{aligned}
|a_1|\, f_{D^*_{s0}(2317)} &= 74 \pm 11, \\
|a_1|\, f_{D_{s1}(2460)} &= 166 \pm 20,
\end{aligned}
\tag{6.17}
$$

where the parameter $|a_1| \sim 1$. Our results are compatible with these lower limits.

Our results for the decay constants clearly deviate from the ones obtained in the infinite heavy quark mass limit. In that limit one gets $f_{D^*_{s0}(2317)} = f_{D_s}$, $f_{D_{s1}(2460)} = f_{D_s^*}$ and $f_{D_{s1}(2536)} = 0$, results that lead to a strong disagreement with experiment for the decay width ratios in Eqs. (6.7) and (6.8). That was already noticed in Ref. [250],

	$X \equiv D^*_{s0}(2317)$		$X \equiv D_{s1}(2460)$		$X \equiv D_{s1}(2536)$	
	The.	Exp.	The.	Exp.	The.	Exp.
$\mathcal{B}(B \to DX)/\mathcal{B}(B \to DD_s)$	$0.19^{(*)}$	0.10 ± 0.03	-	-	-	-
$\mathcal{B}(B \to D^*X)/\mathcal{B}(B \to D^*D_s)$	$0.15^{(*)}$	0.15 ± 0.06	-	-	-	-
$\mathcal{B}(B \to DX)/\mathcal{B}(B \to DD^*_s)$	-	-	$\begin{bmatrix}0.176^{(1)}\\0.177^{(2)}\end{bmatrix}$	0.44 ± 0.11	$\begin{bmatrix}0.071^{(1)}\\0.021^{(2)}\end{bmatrix}$	0.049 ± 0.010
$\mathcal{B}(B \to D^*X)/\mathcal{B}(B \to D^*D^*_s)$	-	-	$\begin{bmatrix}0.251^{(1)}\\0.252^{(2)}\end{bmatrix}$	0.58 ± 0.12	$\begin{bmatrix}0.110^{(1)}\\0.032^{(2)}\end{bmatrix}$	0.044 ± 0.010

Table 6.12. Ratios of branching fractions for nonleptonic decays $B \to D^{(*)}D_{sJ}$. The symbol $(*)$ indicates that the ratios have been calculated using the experimental pseudoscalar decay constant in Table 6.10. For the $D_{s1}(2460)$ and $D_{s1}(2536)$ mesons, the ratios have been calculated without (1) and with (2) taking into account the non-$q\bar{q}$ degrees of freedom in the $J^P = 1^+$ channel.

where the authors, using the experimental ratios, estimated that $f_{D^*_{s0}(2317)} \sim \frac{1}{3} f_{D_s}$ and $f_{D^*_{s0}(2317)} \sim f_{D_{s1}(2460)}$ instead. We obtain $f_{D^*_{s0}(2317)}/f_{D_s} = 0.36$, $f_{D^*_{s0}(2317)} \sim 0.72 f_{D_{s1}(2460)}$ and $f_{D_{s1}(2536)} = 59.176\,\text{MeV}$, the latter being small compared to the others but certainly not zero.

Finally, we show in Table 6.12 our results for the ratios written in Eqs. (6.7) and (6.8). The symbol $(*)$ indicates that the ratios have been calculated using the experimental pseudoscalar decay constant in Table 6.10. We get results close to or within the experimental error bars for the $D^*_{s0}(2317)$ meson, which to us is an indication that this meson could be a canonical $c\bar{s}$ state. The incorporation of the non-$q\bar{q}$ degrees of freedom in the $J^P = 1^+$ channel, enhances the $j_q = 3/2$ component of the $D_{s1}(2536)$ meson and it gives rise to ratios in better agreement with experiment. Note that this state is still an almost pure $q\bar{q}$ state in our description.

The situation is more complicated for the $D_{s1}(2460)$ meson. The probability distributions of its ${}^1P_1$ and ${}^3P_1$ components are corrected by the inclusion of non-$q\bar{q}$ degrees of freedom, the latter making a $\sim 25\%$ of the wave function. In our calculation, only the pure $q\bar{q}$ component of the $D_{s1}(2460)$ meson has been used to evaluate the $\Gamma(B \to D^{(*)}D_{s1}(2460))$ decay width. The values we get for the corresponding ratios in Eqs. (6.7) are lower than the experimental data.

Chapter 7
Conclusions

An exhaustive study of heavy meson properties within a nonrelativistic constituent quark model, which successfully describes hadron phenomenology and hadronic reactions, has been presented in this dissertation. Within the heavy quark sector, we have focused on the spectroscopy and on the electromagnetic, strong and weak decays. One of the main objectives pursued in this work is the analysis of the heavy meson decays. The description of the approaches used and the discussion of our results, comparing them with the experimental data and also with the results coming from different theoretical approaches, can be followed along the work. As it is demonstrated, it is possible to perform fine studies in the heavy quark sector using the simple and, at the same time, powerful quark model picture.

A review of the main properties of QCD and how these are incorporated in the quark model has been presented. The constituent quark model incorporates perturbative effects through the one-gluon exchange and nonperturbative effects as the spontaneous chiral symmetry breaking and confinement.

To find new physics it is very important to test the theoretical model with as many as possible known states. It allows us to clearly understand the strengths and weaknesses of the model and to extract later reliable predictions. Moreover, it is widely believed that confinement is flavor independent, and so the interactions which largely determine the high energy quarkonium spectrum should be constraint by the light quark sector. Based on the above two cornerstones, we have performed a fine tune of the model parameters to describe the spectrum of light mesons up to the recent higher excited states reported by Crystal Barrel Collaboration. We have shown that the large degeneracy observed in the excited part of the meson spectra can be explained as an effect of the flattening of the confinement potential due to the color screening. This confinement behavior produces similar effects to chiral symmetry restoration although predicts different results for observables like the leptonic decay widths. The measurement of these observables may be very interesting to understand the confinement properties and the chiral symmetry restoration.

The chiral symmetry is explicitly broken in the heavy quark sector and so its consequences, the dynamically generated light quark mass and the interaction through Goldstone bosons, are not present. An exhaustive study of heavy meson spectra in terms of $q\bar{q}$ components has been performed. The model can be used as a template against which to compare the new XYZ mesons, whose nature is still unknown and some of them are in conflict with standard quarkonium interpretations. The electromagnetic decays has been included in this part of the work. The study of these processes could provide us with valuable information on the meson structure since the

operator of electromagnetic transitions is very well known.

A quite reasonable global description of the heavy meson spectra has been reached. Some tentative assignments of the XYZ mesons has been done. Throughout the work we have tried to explain other properties of the XYZ mesons to give a reliable confirmation of our interpretations. For those mesons which we suspect more complex structures than $q\bar{q}$, we have given some explanation when possible.

Besides the well established ψ states, we have assigned as $q\bar{q}$ structures the $X(4360)$, $X(4630)$ and $X(4660)$ mesons. However, the $G(3900)$, $X(4008)$ and $X(4260)$ states can not be accommodated in the spectrum and probably its structure is more complex than a simple $c\bar{c}$ pair.

The experimental measurement of the hyperfine mass splitting in the charmonium and bottomonium sectors gives valuable information about the spin-spin interaction. In both sectors, different Collaborations have observed that the hyperfine mass splitting is compatible with zero. Our theoretical results are in perfect agreement.

In general, the experimental data and our theoretical results are in good agreement in the bottomonium sector. In the last years, the Belle, BaBar and even ATLAS Collaborations have reported discoveries like the $\eta_b(1S)$, the $h_b(1P)$ and $h_b(2P)$, and the $\chi_b(3P)$ multiplet. All of them agrees well with our theoretical predictions. The description of the open-bottom mesons has been given since they participate in the weak decays studied here, in general our results are in good agreement with the experimental data.

Certain modifications to the model have been suggested. We have studied the influence of the Lorentz structure of the confinement in the spectra, to do that we have focused on some physical observables which are more sensible to this effect. We conclude that the confinement interaction is dominantly scalar and the inclusion of the tensor and spin-spin terms coming from the vector nature of the confinement does not affect the global description of the spectrum in the different sectors.

The spectra of charmed and charmed-strange mesons contain a number of long known and well established states, all of them are low-lying states. We have succeeded describing them except the doublet $j_q^P = \frac{1}{2}^+$. In the last years several new resonances have been observed, we have discussed their quantum numbers attending mainly their strong decays. The spin-dependence of the model is based on the Fermi-Breit reduction of the one-gluon exchange interaction supplemented with the spin-orbit term of the scalar-vector Lorentz confinement. The inclusion of one-loop QCD corrections to the spin-dependent terms of the OGE has served to explain the lower mass of the $D_{s0}^*(2317)$ meson as a canonical $c\bar{s}$ structure. This effect does not solve the puzzle of the 1^+ mesons. We have studied the $J^P = 1^+$ charmed-strange mesons, finding that the $J^P = 1^+$ $D_{s1}(2460)$ has an important non-$q\bar{q}$ contribution whereas the $J^P = 1^+$ $D_{s1}(2536)$ is almost a pure $q\bar{q}$ state. The presence of non-$q\bar{q}$ degrees of freedom in the $J^P = 1^+$ charmed-strange meson sector enhances the $j_q = 3/2$ component of the $D_{s1}(2536)$. This wave function explains most of the experimental data.

The renormalization with boundary conditions applied to the constituent quark model allows us to disentangle the physics of the ground state to that of the excited states. Moreover, this has led to remove the *ad hoc* cutoffs of the model and, subsequently, to develop a clear study of some properties of mesons as functions of parameters with physical meaning.

We have performed a calculation of the strong decay widths of the mesons which belong to charmed, charmed-strange, hidden charm and hidden bottom sectors. We have used two different decay models, the $^3P_0$ model and a microscopic one, to deal with this issue.

The $^3P_0$ model has a free parameter, the strength γ of the decay interaction, which is fitted to the data. We propose a scale-dependent strength, γ, as a function of the reduced mass of the $q\bar{q}$ pair of the decaying meson to achieve a global description of the meson strong decays. The dependence of γ is logarithmically in the reduced mass. The results predicted by the $^3P_0$ model with the suggested running of the γ parameter are in a global agreement with the experimental data, being remarkable in most of the studied cases.

The development of a microscopic model that describes the meson strong decays through the same interquark Hamiltonian which determines the spectrum has been one of the main objectives in the study of strong decays. In general, the total widths are lower in the microscopic model than in the $^3P_0$ model without improving the agreement with the experimental data. The comparison with other microscopic decay models has been done. Despite of the difficulty of comparing our results with those of other similar calculations, we discuss about the Lorentz structure of the confinement, mainly responsible of the meson decays. We can conclude that a pure scalar linear confining interaction, which is generally accepted, predicts large widths. A static vector linear confining interaction predicts reasonable widths. Using a mixture of scalar-vector linear screened confining interaction, we also obtain the correct order of magnitude.

The QCD multipole expansion appears as a feasible approach to determine hadronic transition rates in the $c\bar{c}$ and $b\bar{b}$ systems. This has been used to calculate spin-nonflip transitions between vector charmonium and bottomonium states with two pions in the final state. QCD multipole expansion requires a model for hybrid mesons and so we have proposed one coming from our constituent quark model. The model assumes that the heavy quark and antiquark are connected by a string and they are situated at the ends of the string. We allow that the string vibrates and calculate the vibrational energy of the string as a function of the distance between the quark and the antiquark. This is then treated as an effective potential inserted into the bound state equation. The width calculated through QCD multipole expansion is sensible to the position in the spectrum of the hybrid meson with respect to the decaying meson. We have predicted hybrid mesons, which participate in the decay amplitude, close to the $X(4360)$ and $X(4660)$ mesons. This explains why we are able to describe well established hadronic transitions and, at the same time, to have large widths for the processes $X(4360) \to \pi^+\pi^-\psi(2S)$ and $X(4660) \to \pi^+\pi^-\psi(2S)$.

The B-factories have become a fundamental tool to investigate experimentally heavy hadrons in the last years. They have led to the discovery of many new states in the open-charm and charmonium sectors. The experimental data concerning these new states are usually accompanied by information about weak decays of b-hadrons. The theoretical study of semileptonic and nonleptonic decays of B mesons has allowed us to implement the usually approaches used in this field.

We have performed a calculation of the branching fractions for the semileptonic decays of B and B_s mesons into final states containing orbitally excited charmed and charmed-strange mesons, respectively. Our results for B semileptonic decays into

$D_0^*(2400)$, $D_1(2420)$ and $D_2^*(2460)$ are in good agreement with the latest experimental measurements. In the case of the $D_1(2430)$ meson, the prediction lies a factor of 2 below BaBar data although the disagreement between BaBar and Belle data for the neutral case is evident. In the case of B_s semileptonic decays, our prediction for the $\mathcal{B}(B_s^0 \to D_{s1}(2536)^- \mu^+ \nu_\mu)\mathcal{B}(D_{s1}(2536)^- \to D^{*-}\bar{K}^0)$ product of branching fractions is in agreement with the experimental data. This, together with the strong decay properties studied for the $D_{s1}(2536)$ meson, is to us evidence of a dominant $q\bar{q}$ structure for the $D_{s1}(2536)$ meson. We have given also predictions for decays into other D_s^{**} mesons which can be useful to test the $q\bar{q}$ nature of these states.

Since the nonleptonic B meson decays into $D^{(*)}D_{sJ}$ provide valuable information about the structure of the $D_{s0}^*(2317)$, $D_{s1}(2460)$ and $D_{s1}(2536)$ mesons, an analysis of these decays is also included. The strong disagreement found between the heavy quark limit predictions and the experimental data has motivated the introduction of the finite c-quark mass effects, which has been done easily in the context of the constituent quark model. We have got results close to or within the experimental error bars for the $D_{s0}^*(2317)$ meson, which is again an indication that this meson could be a canonical $c\bar{s}$ state. The description of the $D_{s1}(2536)$ meson as an almost 1^+, $j_q = 3/2$ $c\bar{s}$ state provides theoretical ratios in better agreement with experiment. The $D_{s1}(2460)$ has a sizable non-$q\bar{q}$ component which contributes to the decays under study. This contribution has not been calculated. We have computed the ratios considering only the contribution coming from the $q\bar{q}$ structure of the $D_{s1}(2460)$ meson. The ratios are a factor 2 below the experimental ones.

One striking feature of our model is the new assignment of the $\psi(4415)$ as a D-wave state leaving the $4S$ state for the $X(4360)$. This agrees with the last measurements of its leptonic and total decay widths. We test if our result is also compatible with the measurement of the exclusive cross section for the processes $e^+e^- \to D^0D^-\pi^+$ and $e^+e^- \to D^0D^{*-}\pi^+$. Including both resonances our model is able to explain, despite the theoretical uncertainties, the data within the experimental accuracy. We have also explained the large value of $\Gamma(X(4360) \to \psi(2S)\pi^+\pi^-)$ using QCDME and assuming our assignment $4S$ 1^{--} $c\bar{c}$ state for the meson $X(4360)$.

We have calculated the total strong decay widths of the heavy mesons using the $^3P_0$ model. The global fit to the experimental data has elucidated the dependence on the scale of the $^3P_0$ free parameter γ. It depends logarithmically on the reduced mass of the $q\bar{q}$ pair of the decaying meson. Our results are in a global agreement with the experimental data, being remarkable in most of the cases studied.

Finally, we have assumed the presence of non-$q\bar{q}$ degrees of freedom in the $J^P = 1^+$ charmed-strange meson sector to enhance the $j_q = 3/2$ component of the $D_{s1}(2536)$ meson. Independently of the mechanism that produces this effect, it has become clear that the description of the $D_{s1}(2536)$ meson as a $j_q = 3/2$ $c\bar{s}$ state is necessary to get a simultaneously explanation of its decay properties. We test this fact in both strong and weak decay observables and in all of them an almost pure $j_q = 3/2$ $c\bar{s}$ wave function has led to the description of the experimental data.

Appendix A

Useful formulas within GEM

The complex-range Gaussian basis functions have been written as

$$\begin{aligned}\phi_{nl}^{\mathrm{GC}}(r) &= N_{nl}^{\mathrm{GC}} r^l \frac{e^{-\eta_n r^2} + e^{-\eta_n^* r^2}}{2}, \\ \phi_{nl}^{\mathrm{GS}}(r) &= N_{nl}^{\mathrm{GS}} r^l \frac{e^{-\eta_n r^2} - e^{-\eta_n^* r^2}}{2i},\end{aligned} \tag{A.1}$$

where $n = 1, \ldots, n_{\max}$, N_{nl}^{GC} and N_{nl}^{GS} are normalization constants, $\eta_n = (1+i\alpha)\nu_n$ and $\eta_n^* = (1-i\alpha)\nu_n$ are the complex size parameters, and ν_n are in geometric progression. These functions can be expressed as a linear combination of more simple functions

$$\begin{aligned}\phi_{nl}^{\mathrm{GC}}(r) &= \frac{N_{nl}^{\mathrm{GC}}}{2N_{nl}} \left[\phi_{nl}(r, \eta_n) + \phi_{nl}(r, \eta_n^*)\right], \\ \phi_{nl}^{\mathrm{GS}}(r) &= \frac{N_{nl}^{\mathrm{GS}}}{2iN_{nl}} \left[\phi_{nl}(r, \eta_n) - \phi_{nl}(r, \eta_n^*)\right],\end{aligned} \tag{A.2}$$

where

$$\begin{aligned}\phi_{nl}(r, \eta_n) &= N_{nl} r^l e^{-\eta_n r^2}, \\ \phi_{nl}(r, \eta_n^*) &= N_{nl}^* r^l e^{-\eta_n^* r^2} = N_{nl} r^l e^{-\eta_n^* r^2},\end{aligned} \tag{A.3}$$

and with N_{nl} a normalization constant given by

$$N_{nl} = \left(\frac{2^{l+2} (2\nu_n)^{l+\frac{3}{2}}}{\sqrt{\pi}\,(2l+1)!!} \right)^{\frac{1}{2}}. \tag{A.4}$$

Therefore, N_{nl}^{GC} and N_{nl}^{GS} can be written as

$$\begin{aligned}N_{nl}^{\mathrm{GC}} &= \frac{2N_{nl}}{\sqrt{2 + N_{nl}^2 I(2l, 2\eta_n) + N_{nl}^2 I(2l, 2\eta_n^*)}}, \\ N_{nl}^{\mathrm{GS}} &= \frac{2N_{nl}}{\sqrt{2 - N_{nl}^2 I(2l, 2\eta_n) - N_{nl}^2 I(2l, 2\eta_n^*)}},\end{aligned} \tag{A.5}$$

with

$$I(\alpha, \beta) = \int_0^\infty r^{2+\alpha} e^{-\beta r^2} dr = \frac{1}{2} \beta^{-\left(\frac{\alpha}{2}+\frac{3}{2}\right)} \Gamma\left(\frac{\alpha}{2} + \frac{3}{2}\right). \tag{A.6}$$

Then, for any linear operator, $\mathcal{O}$, the matrix elements in the complex-range Gaussian basis functions can be written as a linear combination of matrix elements in function of the more simple basis

$$\begin{aligned}
\left\langle \phi^{\mathrm{GC}}_{n'l}(r)|\mathcal{O}|\phi^{\mathrm{GC}}_{nl}(r)\right\rangle &= \frac{N^{\mathrm{GC}}_{n'l}N^{\mathrm{GC}}_{nl}}{4N_{n'l}N_{nl}}\left[+ \left\langle \phi_{n'l}\left(r,\eta_{n'}\right)|\mathcal{O}|\phi_{nl}\left(r,\eta_{n}\right)\right\rangle + \left\langle \phi_{n'l}\left(r,\eta_{n'}\right)|\mathcal{O}|\phi_{nl}\left(r,\eta^{*}_{n}\right)\right\rangle \right.\\
&\left. + \left\langle \phi_{n'l}\left(r,\eta^{*}_{n'}\right)|\mathcal{O}|\phi_{nl}\left(r,\eta_{n}\right)\right\rangle + \left\langle \phi_{n'l}\left(r,\eta^{*}_{n'}\right)|\mathcal{O}|\phi_{nl}\left(r,\eta^{*}_{n}\right)\right\rangle\right],\\
\left\langle \phi^{\mathrm{GC}}_{n'l}(r)|\mathcal{O}|\phi^{\mathrm{GS}}_{nl}(r)\right\rangle &= \frac{N^{\mathrm{GC}}_{n'l}N^{\mathrm{GS}}_{nl}}{4iN_{n'l}N_{nl}}\left[+ \left\langle \phi_{n'l}\left(r,\eta_{n'}\right)|\mathcal{O}|\phi_{nl}\left(r,\eta_{n}\right)\right\rangle - \left\langle \phi_{n'l}\left(r,\eta_{n'}\right)|\mathcal{O}|\phi_{nl}\left(r,\eta^{*}_{n}\right)\right\rangle \right.\\
&\left. + \left\langle \phi_{n'l}\left(r,\eta^{*}_{n'}\right)|\mathcal{O}|\phi_{nl}\left(r,\eta_{n}\right)\right\rangle - \left\langle \phi_{n'l}\left(r,\eta^{*}_{n'}\right)|\mathcal{O}|\phi_{nl}\left(r,\eta^{*}_{n}\right)\right\rangle\right],\\
\left\langle \phi^{\mathrm{GS}}_{n'l}(r)|\mathcal{O}|\phi^{\mathrm{GC}}_{nl}(r)\right\rangle &= \frac{N^{\mathrm{GS}}_{n'l}N^{\mathrm{GC}}_{nl}}{-4iN_{n'l}N_{nl}}\left[+ \left\langle \phi_{n'l}\left(r,\eta_{n'}\right)|\mathcal{O}|\phi_{nl}\left(r,\eta_{n}\right)\right\rangle + \left\langle \phi_{n'l}\left(r,\eta_{n'}\right)|\mathcal{O}|\phi_{nl}\left(r,\eta^{*}_{n}\right)\right\rangle \right.\\
&\left. - \left\langle \phi_{n'l}\left(r,\eta^{*}_{n'}\right)|\mathcal{O}|\phi_{nl}\left(r,\eta_{n}\right)\right\rangle - \left\langle \phi_{n'l}\left(r,\eta^{*}_{n'}\right)|\mathcal{O}|\phi_{nl}\left(r,\eta^{*}_{n}\right)\right\rangle\right],\\
\left\langle \phi^{\mathrm{GS}}_{n'l}(r)|\mathcal{O}|\phi^{\mathrm{GS}}_{nl}(r)\right\rangle &= \frac{N^{\mathrm{GS}}_{n'l}N^{\mathrm{GS}}_{nl}}{4N_{n'l}N_{nl}}\left[+ \left\langle \phi_{n'l}\left(r,\eta_{n'}\right)|\mathcal{O}|\phi_{nl}\left(r,\eta_{n}\right)\right\rangle - \left\langle \phi_{n'l}\left(r,\eta_{n'}\right)|\mathcal{O}|\phi_{nl}\left(r,\eta^{*}_{n}\right)\right\rangle \right.\\
&\left. - \left\langle \phi_{n'l}\left(r,\eta^{*}_{n'}\right)|\mathcal{O}|\phi_{nl}\left(r,\eta_{n}\right)\right\rangle + \left\langle \phi_{n'l}\left(r,\eta^{*}_{n'}\right)|\mathcal{O}|\phi_{nl}\left(r,\eta^{*}_{n}\right)\right\rangle\right].
\end{aligned} \tag{A.7}$$

Some examples of the matrix elements in the simple basis are

- Overlap

$$\begin{aligned}
\left\langle \phi_{n'l}\left(r,\eta_{n'}\right)|\phi_{nl}\left(r,\eta_{n}\right)\right\rangle &= N_{n'l}N_{nl}I\left(2l,\eta^{*}_{n'}+\eta_{n}\right),\\
\left\langle \phi_{n'l}\left(r,\eta_{n'}\right)|\phi_{nl}\left(r,\eta^{*}_{n}\right)\right\rangle &= N_{n'l}N_{nl}I\left(2l,\eta^{*}_{n'}+\eta^{*}_{n}\right),\\
\left\langle \phi_{n'l}\left(r,\eta^{*}_{n'}\right)|\phi_{nl}\left(r,\eta_{n}\right)\right\rangle &= N_{n'l}N_{nl}I\left(2l,\eta_{n'}+\eta_{n}\right),\\
\left\langle \phi_{n'l}\left(r,\eta^{*}_{n'}\right)|\phi_{nl}\left(r,\eta^{*}_{n}\right)\right\rangle &= N_{n'l}N_{nl}I\left(2l,\eta_{n'}+\eta^{*}_{n}\right).
\end{aligned} \tag{A.8}$$

- Powers of radial coordinate, r^{γ}

$$\begin{aligned}
\left\langle \phi_{n'l}\left(r,\eta_{n'}\right)|r^{\gamma}|\phi_{nl}\left(r,\eta_{n}\right)\right\rangle &= N_{n'l}N_{nl}I\left(2l+\gamma,\eta^{*}_{n'}+\eta_{n}\right),\\
\left\langle \phi_{n'l}\left(r,\eta_{n'}\right)|r^{\gamma}|\phi_{nl}\left(r,\eta^{*}_{n}\right)\right\rangle &= N_{n'l}N_{nl}I\left(2l+\gamma,\eta^{*}_{n'}+\eta^{*}_{n}\right),\\
\left\langle \phi_{n'l}\left(r,\eta^{*}_{n'}\right)|r^{\gamma}|\phi_{nl}\left(r,\eta_{n}\right)\right\rangle &= N_{n'l}N_{nl}I\left(2l+\gamma,\eta_{n'}+\eta_{n}\right),\\
\left\langle \phi_{n'l}\left(r,\eta^{*}_{n'}\right)|r^{\gamma}|\phi_{nl}\left(r,\eta^{*}_{n}\right)\right\rangle &= N_{n'l}N_{nl}I\left(2l+\gamma,\eta_{n'}+\eta^{*}_{n}\right).
\end{aligned} \tag{A.9}$$

- Nonrelativistic kinetic energy, $\frac{p^2}{2\mu} = \frac{-1}{2\mu}\left[\frac{\partial^2}{\partial r^2}+\frac{2}{r}\frac{\partial}{\partial r}-\frac{l(l+1)}{r^2}\right]$

  - The term $\frac{-1}{2\mu}\left[\frac{\partial^2}{\partial r^2}+\frac{2}{r}\frac{\partial}{\partial r}\right]$

$$\begin{aligned}
&\left\langle \phi_{n'l}\left(r,\eta_{n'}\right)|\frac{-1}{2\mu}\left[\frac{\partial^2}{\partial r^2}+\frac{2}{r}\frac{\partial}{\partial r}\right]|\,\phi_{nl}\left(r,\eta_{n}\right)\right\rangle = -\frac{1}{2\mu}N_{n'l}N_{nl}\times\\
&\times\left[l(l+1)I(2l-2,\eta^{*}_{n'}+\eta_{n}) + 4\eta_{n}^{2}I(2l+2,\eta^{*}_{n'}+\eta_{n}) - 2\eta_{n}(2l+3)I(2l,\eta^{*}_{n'}+\eta_{n})\right],\\
&\left\langle \phi_{n'l}\left(r,\eta_{n'}\right)|\frac{-1}{2\mu}\left[\frac{\partial^2}{\partial r^2}+\frac{2}{r}\frac{\partial}{\partial r}\right]|\,\phi_{nl}\left(r,\eta^{*}_{n}\right)\right\rangle = -\frac{1}{2\mu}N_{n'l}N_{nl}\times\\
&\times\left[l(l+1)I(2l-2,\eta^{*}_{n'}+\eta^{*}_{n}) + 4{\eta^{*}_{n}}^{2}I(2l+2,\eta^{*}_{n'}+\eta^{*}_{n}) - 2\eta^{*}_{n}(2l+3)I(2l,\eta^{*}_{n'}+\eta^{*}_{n})\right],
\end{aligned} \tag{A.10}$$

$$\langle\phi_{n'l}\left(r,\eta^*_{n'}\right)|\frac{-1}{2\mu}\left[\frac{\partial^2}{\partial r^2}+\frac{2}{r}\frac{\partial}{\partial r}\right]|\,\phi_{nl}\left(r,\eta_n\right)\rangle=-\frac{1}{2\mu}N_{n'l}N_{nl}\times$$
$$\times\left[l(l+1)I(2l-2,\eta_{n'}+\eta_n)+4\eta_n^2I(2l+2,\eta_{n'}+\eta_n)-2\eta_n(2l+3)I(2l,\eta_{n'}+\eta_n)\right],$$

$$\langle\phi_{n'l}\left(r,\eta^*_{n'}\right)|\frac{-1}{2\mu}\left[\frac{\partial^2}{\partial r^2}+\frac{2}{r}\frac{\partial}{\partial r}\right]|\,\phi_{nl}\left(r,\eta^*_n\right)\rangle=-\frac{1}{2\mu}N_{n'l}N_{nl}\times$$
$$\times\left[l(l+1)I(2l-2,\eta_{n'}+\eta^*_n)+4{\eta^*_n}^2I(2l+2,\eta_{n'}+\eta^*_n)-2\eta^*_n(2l+3)I(2l,\eta_{n'}+\eta^*_n)\right]. \tag{A.11}$$

– The term $\frac{1}{2\mu}\frac{l(l+1)}{r^2}$

$$\langle\phi_{n'l}\left(r,\eta_{n'}\right)|\frac{1}{2\mu}\frac{l(l+1)}{r^2}|\,\phi_{nl}\left(r,\eta_n\right)\rangle=\frac{1}{2\mu}N_{n'l}N_{nl}l(l+1)I(2l-2,\eta^*_{n'}+\eta_n),$$
$$\langle\phi_{n'l}\left(r,\eta_{n'}\right)|\frac{1}{2\mu}\frac{l(l+1)}{r^2}|\,\phi_{nl}\left(r,\eta^*_n\right)\rangle=\frac{1}{2\mu}N_{n'l}N_{nl}l(l+1)I(2l-2,\eta^*_{n'}+\eta^*_n),$$
$$\langle\phi_{n'l}\left(r,\eta^*_{n'}\right)|\frac{1}{2\mu}\frac{l(l+1)}{r^2}|\,\phi_{nl}\left(r,\eta_n\right)\rangle=\frac{1}{2\mu}N_{n'l}N_{nl}l(l+1)I(2l-2,\eta_{n'}+\eta_n),$$
$$\langle\phi_{n'l}\left(r,\eta^*_{n'}\right)|\frac{1}{2\mu}\frac{l(l+1)}{r^2}|\,\phi_{nl}\left(r,\eta^*_n\right)\rangle=\frac{1}{2\mu}N_{n'l}N_{nl}l(l+1)I(2l-2,\eta_{n'}+\eta^*_n). \tag{A.12}$$

- Yukawa potential, $V(r)=-C\,\frac{e^{-\mu r}}{\mu r}$

$$\langle\phi_{n'l}\left(r,\eta_{n'}\right)|V(r)|\phi_{nl}\left(r,\eta_n\right)\rangle=-\frac{C}{\mu}N_{n'l}N_{nl}I_{2l+1}\left(\eta^*_{n'}+\eta_n,\mu\right),$$
$$\langle\phi_{n'l}\left(r,\eta_{n'}\right)|V(r)|\phi_{nl}\left(r,\eta^*_n\right)\rangle=-\frac{C}{\mu}N_{n'l}N_{nl}I_{2l+1}\left(\eta^*_{n'}+\eta^*_n,\mu\right),$$
$$\langle\phi_{n'l}\left(r,\eta^*_{n'}\right)|V(r)|\phi_{nl}\left(r,\eta_n\right)\rangle=-\frac{C}{\mu}N_{n'l}N_{nl}I_{2l+1}\left(\eta_{n'}+\eta_n,\mu\right),$$
$$\langle\phi_{n'l}\left(r,\eta^*_{n'}\right)|V(r)|\phi_{nl}\left(r,\eta^*_n\right)\rangle=-\frac{C}{\mu}N_{n'l}N_{nl}I_{2l+1}\left(\eta_{n'}+\eta^*_n,\mu\right), \tag{A.13}$$

where $I_n(A,b)$ is

$$I_n(A,b)=\int_0^\infty x^n e^{-Ax^2-bx}dx, \tag{A.14}$$

with the following recurrence rule [262]

$$I_{n+1}(A,b)=-\frac{1}{\sqrt{A}}uI_n(A,b)+\frac{n}{2A}I_{n-1}(A,b), \tag{A.15}$$

where $u=\frac{b}{2\sqrt{A}}$. Now, if $\rho(u)=\sqrt{\pi}e^{u^2}\left[1-\phi(u)\right]$ with $\phi(u)$ the error function, we have

$$I_0=\frac{\rho(u)}{2\sqrt{A}}\qquad\text{with }\ \mathbb{R}\left[A\right]>0,$$
$$I_1=\frac{1-u\rho(u)}{2A}\qquad\text{with }\ \mathbb{R}\left[A\right]>0\ \text{ and }\ \left|\arg\left(\frac{b}{2}\right)\right|<\frac{\pi}{2}. \tag{A.16}$$

Appendix B

Tables of light meson masses

We discuss the experimental situation and remark the most important aspects of our theoretical results as we go along the light meson spectrum. The tables are organized in the following form: we separate the $I = 0$ and $I = 1$ sectors. In both sectors there is a first table that shows the well established states in the Particle Data Group (PDG) [78] up to the lower limit (1.9 GeV) of the experiment performed by the Crystal Barrel Collaboration. The successive tables show the states that appear in Ref. [77] which is a summary of the data analysis.

In Ref. [77] resonances have a "star rating" up to 4*. The highest class requires observation of 3 or more strong, unmistakable peaks and a good mass determination (with error $\delta M \leq 40$ MeV). Such states are equivalent to those in the summary table of the Particle Data Group. The 3* resonances are reasonable well established, usually in two strong channels with error for masses ≤ 40 MeV; some are established in 3 channels but with δM in the range $40 - 70$ MeV. The 2* resonances need confirmation elsewhere, they are observed either in one strong channel with $\delta M < 40$ MeV or in 2 channels with sizable error in the mass. Finally, 1* states are tentative, weak channels and poor mass determination.

Most resonances from the Crystal Barrel in-flight analysis are listed by the Particle Data Group in a section called "Other Light Unflavored Mesons". The reason is that the Particle Data Group requires confirmation from a separate experiment, rather than from different channels of data in one experiment. There is very little other coverage of this mass range from other experiments and Ref. [77] is the only one that gives an idea about the status of the different resonances. That is why we follow the procedure described above.

B.1 Lower energy region of the $I = 0$ meson spectrum

Table B.1 shows the well established resonances in the PDG [78] up to the lower limit (1.9 GeV) of the experiment performed by the Crystal Barrel Collaboration.

Our constituent quark model gives a theoretical mass of 547 MeV for η that is in good agreement with the experimental data. The η' is 100 MeV below the experimental mass. However, η' could have a structure more complex than a naive $q\bar{q}$. It may have a gluonic component or be a hybrid meson that explains our lower result. We only obtain one 0^{-+} state in the 1.5 GeV energy region although PDG gives three states $\eta(1290)$, $\eta(1405)$ and $\eta(1475)$. The first one decays exclusively into $a_0\pi^0$, the second one into $a_0\pi^0$ and $K^*\bar{K}$ and the last one exclusively into $K^*\bar{K}$. The theoretical mass

J^{PC}	State	The. (MeV)	Exp. (MeV) [78]
0^{-+}	η	547	547.853 ± 0.024
0^{-+}	η'	862	957.78 ± 0.06
0^{-+}	$\eta(1295)$	-	1294 ± 4
0^{-+}	$\begin{bmatrix}\eta(1405)\\ \eta(1475)\end{bmatrix}$	1493	$\begin{bmatrix}1409.8 \pm 2.5\\ 1476 \pm 4\end{bmatrix}$
0^{-+}	$\eta(1760)$	1668	1756 ± 9
0^{++}	$f_0(600)$	720	$400 - 1200$
0^{++}	$f_0(980)$	-	980 ± 10
0^{++}	$f_0(1370)$	1325	$1200 - 1500$
0^{++}	$f_0(1500)$	1616	1505 ± 6
0^{++}	$f_0(1710)$	-	1720 ± 6
1^{+-}	$h_1(1170)$	1292	1170 ± 20
1^{+-}	$h_1(1380)$	1517	1386 ± 19
1^{+-}	$h_1(1595)$	1826	$1594 \pm 15^{+10}_{-60}$
1^{--}	$\omega(782)$	569	782.65 ± 0.12
1^{--}	$\phi(1020)$	985	1019.455 ± 0.020
1^{--}	$\omega(1420)$	1484	$1400 - 1450$
1^{--}	$\omega(1650)$	1619	1670 ± 30
1^{--}	$\phi(1680)$	1750	1680 ± 20
1^{++}	$f_1(1285)$	1338	1281.8 ± 0.6
1^{++}	$\begin{bmatrix}f_1(1420)\\ f_1(1510)\end{bmatrix}$	1525	$\begin{bmatrix}1426.4 \pm 0.9\\ 1518 \pm 5\end{bmatrix}$
2^{-+}	$\eta_2(1645)$	1685	1617 ± 5
2^{++}	$f_2(1270)$	1306	1275.1 ± 1.2
2^{++}	$f_2(1430)$	-	~ 1430
2^{++}	$f_2'(1525)$	1552	1525 ± 5
2^{++}	$f_2(1565)$	-	1562 ± 13
2^{++}	$f_2(1640)$	-	1639 ± 6
2^{++}	$f_2(1810)$	1832	1815 ± 12
3^{--}	ω_3	1696	1667 ± 4

Table B.1. $I = 0$ light meson spectrum, in MeV. We show the states below the lower limit of the experiment performed by the Crystal Barrel Collaboration (1.9 GeV).

is 1493 MeV and so its assignment would be for $\eta(1475)$. However, the predominant channel $n\bar{n}$ makes difficult to explain its decay into $K^*\bar{K}$.

The isoscalar scalar mesons deserve a special mention because the quark model does not implement structures more complex than a $q\bar{q}$ one. It is known that tetraquarks may have a great influence in this sector [52], hence it is reasonable that the theoretical results differ from the experimental data.

There is a discrepancy between the experimental and predicted mass for the $\omega(782)$. The model was originally developed for the description of the NN sector being the pseudoscalar interaction a basic piece. When transformed to the quark-antiquark sector, the additional sign given by G-parity is the responsible for the decreasing in energy of the ω mass with respect to its isospin spin partner, the ρ meson. The

$\omega - \rho$ splitting was solved in Ref. [263] where the authors realized that the model do not implement the full octet of the scalar mesons, only the σ-exchange, loosing an isospin-dependent scalar interaction which is important in the study of baryon-baryon interaction. Looking at the excitations of the ω meson, we get a good agreement with the experimental data indicating also that maybe the pseudoscalar interaction is not described correctly at short distances but it is adequate at large distances.

The two lowest states with quantum numbers $J^{PC} = 3^{--}$ are the $\omega_3(1670)$ and $\phi_3(1850)$ resonances with dominant flavor content $n\bar{n}$ and $s\bar{s}$, respectively. The model prediction is 1696 MeV for the first particle and 1908 MeV for the last one, in very good agreement with the experimental data.

There are three states with quantum numbers $J^{PC} = 1^{++}$ around 1.3 GeV, the $f_1(1285)$, $f_1(1420)$ and $f_1(1510)$ states. However, there are many experiments, as those of the Refs. [264] and [265], that have been developed to measure the axial vector particle and they distinguish only two states, $f_1(1285)$ and $f_1(1420)$, although the mass splitting between $f_1(1420)$ and $f_1(1510)$ is sufficiently large respect the resolution of the experiments. All these observations express skepticism regarding the existence of the $f_1(1510)$ [266]. Our model gives two states with masses 1338 MeV and 1525 MeV and dominant flavor component $n\bar{n}$ and $s\bar{s}$, respectively.

The first two states predicted by our model with quantum numbers $J^{PC} = 1^{+-}$ are $h_1(1170) = 1292$ MeV and $h_1(1380) = 1517$ MeV. The first state is predominantly $n\bar{n}$ but the second one is $s\bar{s}$. Although the prediction of our model for the second state is higher than the experimental data, the more recent measurement for this state is 1440 ± 60 MeV [267], rather close to the theoretical result.

Experimentally there is a proliferation of isoscalar 2^{++} states in an energy region that has been suggested as coexisting with 2^{++} glueballs. Our model prediction confirms $f_2(1270)$, $f_2'(1525)$ and $f_2(1810)$ as naive $q\bar{q}$ states but have not results for $f_2(1430)$, $f_2(1565)$ and $f_2(1640)$ of which structure seems more complex than $q\bar{q}$.

Finally, our model gives a good global description of the lowest part of the spectrum with $I = 0$ in spite of the discrepancies or comments that we have done above.

B.2 Higher energy region of the $I = 0$ meson spectrum

Higher excited light states with $I = 0$, $C = +1$ and $I = 0$, $C = -1$ are shown in Tables B.2 and B.3, respectively.

The OGE potential has a Coulomb-like term at short distances which is the result of the computation of QCD at its perturbative regime, ultraviolet momenta. However, in QCD, self-interactions generate a momentum-dependent mass for the gluon, which is large at infrared momenta but vanishes in the ultraviolet [270]. This means that the Coulomb contribution at large distances is not reliable and should be modified. Our constituent quark model has a Coulomb-like contribution with infinite range and thus there is an infinite number of bound states before the continuum. These states have not physical meaning and are not considered. The typical bounding energy of these states in the light sector is $\frac{1}{2}\mu\alpha^2 \sim 20$ MeV and their typical radius is $a = \hbar c/\alpha\mu = 2.5$ fm.

We give the results of the $I = 0$, $C = +1$ states above 1.9 GeV in Table B.2. The resonances with $J^{PC} = 0^{++}$, 2^{++} and 4^{++} are observed in two-body channels, where the polarization data are available, and therefore the significance of these resonances is

J^{PC}	State	The. (MeV)	Exp. (MeV)	[268]
0^{-+}	η	1953	2010^{+35}_{-60}	2^*
0^{-+}	η	2131	-	-
0^{-+}	η	2206	2285 ± 20	3^*
0^{++}	f_0	1919	2020 ± 38	3^*
0^{++}	f_0	2035	2102 ± 13	4^*
0^{++}	$f_0(2200)$	2229	2189 ± 13	[78]
0^{++}	f_0	-	2337 ± 14	3^*
1^{++}	f_1	1851	1971 ± 15	3^*
1^{++}	f_1	-	2310 ± 60	2^*
2^{-+}	η_2	1895	1870 ± 16	4^*
2^{-+}	η_2	2050	2030 ± 16	3^*
2^{-+}	η_2	2253	2267 ± 14	4^*
2^{++}	f_2	1975	1934 ± 20	4^*
2^{++}	f_2	2063	$\begin{bmatrix} 2001 \pm 10 \\ 2010 \pm 25 \end{bmatrix}$	$\begin{bmatrix} 4^* \\ 3^* \end{bmatrix}$
2^{++}	$f_2(2150)$	2133	2157 ± 12	[78]
2^{++}	$f_J(2220)$	2189	2231.1 ± 3.5	[78]
2^{++}	f_2	2210	2240 ± 15	4^*
2^{++}	f_2	2288	2293 ± 13	4^*
3^{++}	f_3	2002	2048 ± 8	4^*
3^{++}	f_3	-	2303 ± 15	4^*
4^{-+}	η_4	-	2328 ± 38	2^*
4^{++}	f_4	2024	2018 ± 6	4^*
4^{++}	f_4	2228	2283 ± 17	4^*

Table B.2. $I = 0$, $C = +1$ light meson spectrum, in MeV, above 1.9 GeV. The data are taken from Ref. [268] which has a summary in this sector of the data analysis performed by the Crystal Barrel Collaboration.

higher. Resonances with $J^{PC} = 0^{-+}$, 1^{++}, 2^{-+}, 3^{++} and 4^{-+} appear only in three-body channels but the statistics for $\eta\pi^0\pi^0$ is very high.

There is a good agreement between the theoretical prediction and the experimental data. This is of a great importance because the resonances measured with quantum numbers $I = 0$ and $C = +1$ are the best established experimentally due to the available polarization data.

The resonances $f_4(2050)$ and $f_4(2300)$ are two of them within the highest mass range. Our prediction agrees reasonably well.

It is necessary to discuss separately 2^{-+} states at 1645, 1870 and 2030 MeV (the $\eta_2(2267)$ is clearly seen in the analysis of the data). They appear in $\eta\pi^0\pi^0\pi^0$ data in the production reaction $\bar{p}p \to \pi^0(\eta\pi\pi)$. The lower one was initially observed decaying purely to $a_2(1320)\pi$ at 1645 MeV. This fits nicely as the expected partner of the well known $I = 1$ $\pi_2(1670)$. However, the same data contained a second strong signal in the $f_2(1270)\eta$ final state at 1870 MeV. The second signal could not be explained as the high mass tail of $\eta_2(1645)$ decaying to $f_2\eta$. Both resonances were subsequently confirmed by the WA102 Collaboration. They observed the $\eta_2(1645)$ in decays to $\eta\pi\pi$ and $\eta_2(1870)$ in decays to both $\eta\pi\pi$ and $K\bar{K}\pi$. The $\eta_2(1645)$ and $\eta_2(2030)$ can be

J^{PC}	State	The. (MeV)	Exp. (MeV)	[269]
1^{--}	ω/ϕ	1860	1854 ± 7	[78]
1^{--}	ω/ϕ	1943	1960 ± 25	3^*
1^{--}	ω/ϕ	2012	-	-
1^{--}	ω/ϕ	$\begin{bmatrix}2182\\2205\end{bmatrix}$	2205 ± 30	1^*
1^{+-}	h_1	2041	1965 ± 45	2^*
1^{+-}	h_1	$\begin{bmatrix}2130\\2287\end{bmatrix}$	2215 ± 40	2^*
2^{--}	ω_2	1711	-	-
2^{--}	ω_2	$\begin{bmatrix}1901\\2065\end{bmatrix}$	1975 ± 20	3^*
2^{--}	ω_2	2259	2195 ± 30	2^*
3^{--}	ω_3	1908	1945 ± 20	3^*
3^{--}	ω_3	2057	-	-
3^{--}	ω_3	$\begin{bmatrix}2250\\2257\end{bmatrix}$	2255 ± 15	$2/3^*$
3^{--}	ω_3	2290	2285 ± 60	$2/3^*$
3^{+-}	h_3	1985	2025 ± 20	2^*
3^{+-}	h_3	$\begin{bmatrix}2195\\2217\end{bmatrix}$	2275 ± 25	3^*
4^{--}	ω_4	-	2250 ± 30	1^*

Table B.3. $I = 0$, $C = -1$ light meson spectrum, in MeV, above 1.9 GeV. The data are taken from Ref. [269] which has a summary in this sector of the data analysis performed by the Crystal Barrel Collaboration.

explained as $q\bar{q}$ states in other quark models, whilst the absent of the $\eta_2(1870)$ state is generally related to the possibility that this meson could be a hybrid. There are in the literature references as [271] that predict light hybrid mesons around $1.8-1.9$ GeV. We predict all the states of the η_2 meson, even the $\eta_2(2267)$ state. In particular, our result for the $\eta_2(1870)$ state indicates that it is almost a $s\bar{s}$ state with quantum numbers 2^{-+}, which explains its observation in the final decay channel $K\bar{K}\pi$.

The highest states in Table B.2 are not predicted theoretically due to these states are above the string breaking threshold for us. With respect the remaining resonances, there are predictions given by the model for all of them. We conclude that a good description has been reached of the higher states for $I = 0$, $C = +1$ sector.

The analysis of the $I = 0$, $C = -1$ high excited states of light meson spectrum is more involved and thus the resonances of this sector are the worse established. The reasons, among others, are that the statistics for the $\omega\eta$ channel is low and there are uncertainties in parameterizing the broad $\pi\pi$ S-wave amplitude above 1 GeV that introduce possible systematic errors into the physics background.

One can see in Table B.3 that the disagreement is more notable for these resonances. However, the experimental status of them is less promising. We obtain predictions in good agreement for all resonances whose status is at least 3^*. We have a reasonable agreement for the states whose status is $2/3^*$. The 3^* refers to their existence, but the 2^* refers to the imprecise identification of masses.

J^{PC}	State	The. (MeV)	Exp. (MeV) [78]
0^{-+}	π	138	138.03899 ± 0.00045
0^{-+}	$\pi(1300)$	1341	1300 ± 100
0^{-+}	$\pi(1800)$	1865	1816 ± 14
0^{++}	$a_0(980)$	1145	980 ± 20
0^{++}	$a_0(1450)$	1755	1474 ± 19
1^{+-}	$b_1(1235)$	1264	1229.5 ± 3.2
1^{--}	$\rho(770)$	772	775.49 ± 0.34
1^{--}	$\rho(1450)$	-	1465 ± 25
1^{--}	$\rho(1570)$	1555	$1570 \pm 36 \pm 62$
1^{--}	$\rho(1700)$	1647	1720 ± 20
1^{--}	$\rho(1900)$	1977	$1909 \pm 17 \pm 25$
1^{++}	$a_1(1260)$	1270	1230 ± 40
1^{++}	$a_1(1640)$	1816	1647 ± 22
2^{-+}	$\pi_2(1670)$	1685	1672.4 ± 3.2
2^{++}	$a_2(1320)$	1341	1318.3 ± 0.6
2^{++}	$a_2(1700)$	1853	1732 ± 16
3^{--}	$\rho_3(1690)$	1705	1686 ± 4

Table B.4. $I = 1$ light meson spectrum, in MeV. We show the states below the lower limit of the experiment performed by the Crystal Barrel Collaboration (1.9 GeV).

The assignment of the two lowest states of the ω_3 resonance is in good agreement with the experimental data. The subsequent theoretical states agree again with those measured experimentally, except for the 2057 MeV state predicted by the model. Therefore, it is possible that there is a new resonance about 2.1 GeV.

B.3 Lower energy region of the $I = 1$ meson spectrum

Table B.4 shows a good agreement between theoretical results and the experimental data for the lower states of $I = 1$ mesons. The r_g and a_s model parameters were fitted in Ref. [52] to reproduce the splitting between the $a_1(1260)$ and $a_2(1320)$ mesons. With the fine tune of the model parameters, the theoretical result for these states is 1270 MeV and 1341 MeV, respectively.

We cannot predict simultaneously the $\rho(1450)$ and $\rho(1570)$ states. While the $\rho(1450)$ was discovered earlier, the $\rho(1570)$ has been reported in 2008 by Aubert *et al.* in Ref. [272]. The scene seems to be complicated due to the uncertainty in the measured mass and because the widths are enough large to disentangle experimentally both resonances. We can only say that our first excitation of the $\rho(770)$ meson has a mass of 1555 MeV.

The greatest discrepancy between theory and experiment is the prediction for a_0 states. These states are isovector scalar mesons and, of course, they suffer from the same speculations about the f_0 meson. Our model does not implement exotic structures and the discrepancy for this particle is reasonable.

J^{PC}	State	The. (MeV)	Exp. (MeV)	[273]
0^{++}	a_0	2092	2025 ± 30	2^*
0^{-+}	π	2152	2070 ± 35	2^*
0^{-+}	π	2295	2360 ± 25	2^*
1^{++}	a_1	2124	1930	?
1^{++}	a_1	2284	2270^{+55}_{-40}	2^*
2^{-+}	π_2	-	1880	4^*
2^{-+}	π_2	2049	2005 ± 15	3^*
2^{-+}	π_2	2252	2245 ± 60	2^*
2^{++}	a_2	1982	$\begin{bmatrix} 1950 \\ 2030 \pm 30 \end{bmatrix}$	$\begin{bmatrix} ? \\ 2^* \end{bmatrix}$
2^{++}	a_2	2145	2175 ± 40	2^*
2^{++}	a_2	2213	2255 ± 20	2^*
3^{++}	a_3	1988	2031 ± 12	3^*
3^{++}	a_3	2219	2275 ± 35	2^*
4^{-+}	π_4	-	2250 ± 15	3^*
4^{++}	a_4	1988	2005^{+25}_{-45}	2^*
4^{++}	a_4	2220	2255 ± 40	3^*

Table B.5. $I = 1$, $C = +1$ light meson spectrum, in MeV, above 1.9 GeV. The data are taken from Ref. [273] which has a summary in this sector of the data analysis performed by the Crystal Barrel Collaboration.

J^{PC}	State	The. (MeV)	Exp. (MeV)	[274]
1^{--}	ρ	2027	2000 ± 30	3^*
1^{--}	ρ	2210	2110 ± 35	3^*
1^{--}	ρ	2240	2265 ± 40	2^*
1^{+-}	b_1	1807	1960 ± 35	3^*
1^{+-}	b_1	$\begin{bmatrix} 2118 \\ 2281 \end{bmatrix}$	2240 ± 35	2^*
2^{--}	ρ_2	2049	1940 ± 40	2^*
2^{--}	ρ_2	2252	2225 ± 35	3^*
3^{--}	ρ_3	2062	1982 ± 14	4^*
3^{--}	ρ_3	2252	2260 ± 20	4^*
3^{+-}	b_3	1987	2032 ± 12	4^*
3^{+-}	b_3	2218	2245 ± 50	3^*
4^{--}	ρ_4	-	2230 ± 25	4^*

Table B.6. $I = 1$, $C = -1$ light meson spectrum, in MeV, above 1.9 GeV. The data are taken from Ref. [274] which has a summary in this sector of the data analysis performed by the Crystal Barrel Collaboration.

B.4 Higher energy region of the $I = 1$ meson spectrum

Higher excited states of light mesons with $I = 1$, $C = +1$ and $I = 1$, $C = -1$ are shown in Tables B.5 and B.6, respectively.

In the case of $I = 1$, $C = +1$ the channels available are $\pi^0\eta$, $\pi^0\eta'$, $3\pi^0$ and $\eta\eta\pi^0$.

Statistics is very high for $3\pi^0$ data but do not define the partial waves cleanly. One expects the spectrum of $I = 1$, $C = +1$ mesons to be close to that for $I = 0$, $C = +1$. Although results are indeed similar, they are much less accurate.

Table B.5 shows our predictions and the comparison with the experimental data. In general, there is a good agreement for all resonances. The most striking feature is that our model predicts all states of π_2 resonance except the most experimental determined $\pi_2(1880)$.

Data for the family $I = 1$, $C = -1$ are available from $\pi^-\pi^+$, $\omega\pi^0$ and $\omega\eta\pi^0$ final states. The measured masses of the different resonances together with their status and our prediction is shown in Table B.6.

A particular feature at low momenta is the very strong $\rho_3(1980)$ signal, our model predicts a state around this energy range but slightly higher. The $\rho_3(2260)$ also appears as a well established resonance and our prediction is 2252 MeV.

Concerning the 1^{--} state at 2000 MeV, the best mass of this state comes from $\pi^-\pi^+$ final channel and our prediction is within the error bars.

The upper 2^{--} state at 2225 MeV has not a 4^* status due to the correlations with 3^{--} and 1^{--} partial waves. Our prediction is 2252 MeV. The lower 2^{--} state at 1940 MeV is one of the two most weakly established states. Our model predicts a state which is 100 MeV higher in mass.

In conclusion, we have done a fine tune of the model of Ref. [52] to describe the degeneracy pattern observed at high energies in the light meson spectrum. Without degrading the description of the low energy spectrum, we obtain a reasonable results for all higher excited states of light mesons which have been established recently. One can find that the theoretical results are better in the $I = 1$ than in the $I = 0$ sector. This is because the $I = 0$ sector is more involved due to the mixing between the $n\bar{n}$ and $s\bar{s}$ components and the presence of exotic structures as glueballs and multiquark states.

Appendix C

Electromagnetic transitions

For quarkonium states below open-flavor threshold, electromagnetic (EM) transitions are often significant decay modes, giving a large contribution to their total decay width. In fact, the first charmonium states not directly produced in e^+e^- collisions, the χ_{cJ} states, were discovered in photon transitions of the ψ' resonance [275]. Even today, such transitions continue to be used to observe new quarkonium states and to test internal structure.

The theory of EM transitions between these quarkonium states is familiar for physicists because much of the terminology and techniques come from the study of EM transitions in atomic and nuclear systems.

Within a $Q_1\bar{Q}_2$ quarkonium system, the electromagnetic transition amplitude is determined by the matrix element of the EM current, $\langle f|j^\mu_{em}|i\rangle$, between an initial quarkonium state, i, and a final state, f. Including the emission of a photon of momentum k and polarization ϵ_γ, the general form of the transition amplitude is the sum of two terms

$$\mathcal{M}(i \to f) = \left[M^{(1)}(i \to f) + M^{(2)}(i \to f)\right] \cdot \epsilon_\gamma(k), \tag{C.1}$$

where in the term $M^{(1)}$ the photon is emitted off the quark Q_1 with mass m_1 and charge e_1, and in the corresponding term $M^{(2)}$ the photon is emitted off the antiquark $\bar{Q}_2$ with mass m_2 and charge $-e_2$.

Within nonrelativistic potential models, a quarkonium state is characterized by $n^{2S+1}L_J$ in spectroscopic notation. In the nonrelativistic limit the spin dependence of the quarkonium wave function decouples from the spatial dependence. The spatial part of the wave function can be expressed in terms of a radial wave function and the spherical harmonics. The spatial dependence of the EM transition amplitudes reduces to expectation values of various functions of quark position and momentum between the initial and final state wave functions.

C.1 Electric transitions

Electric transition does not change the quark spin and at its lowest nonrelativistic order is given by the electric dipole (E1) transition. The E1 transition has selection rules $\Delta L = \pm 1$ and $\Delta S = 0$. The spin-averaged electric transition rate between an initial state $i \equiv n^{2S+1}L_J$ and a final state $f \equiv n'^{\,2S'+1}L'_{J'}$ $(L = L' \pm 1)$ is [13]

$$\Gamma(i \equiv n^{2S+1}L_J \xrightarrow{\text{E1}} f \equiv n'^{\,2S'+1}L'_{J'}) = \frac{4\alpha e_Q^2}{3}(2J'+1)S^E_{if}k^3|\mathcal{E}_{if}|^2\frac{E_f}{M_i}, \tag{C.2}$$

where $e_Q = (e_1 m_2 - e_2 m_1)/(m_1 + m_2)$, E_f/M_i is a relativistic correction among others as using the eigenfunctions and eigenvalues of the Breit-Fermi Hamiltonian (Siegert's theorem). The momentum of the final photon is

$$k = \frac{(M_i^2 - M_f^2)}{2M_i}, \tag{C.3}$$

and the overlap integral $\mathcal{E}_{if}$ for $m_1 = m_2$ and $e_1 = -e_2 = e_Q$ is given by

$$\mathcal{E}_{if} = \frac{3}{k}\int_0^\infty R_{n'L'}(r)\left[\frac{kr}{2} j_0\left(\frac{kr}{2}\right) - j_1\left(\frac{kr}{2}\right)\right] R_{nL}(r)\, r^2 dr, \tag{C.4}$$

where $j_n(x)$ are spherical Bessel functions. Finally, the statistical factor $S_{if}^{\mathrm{E}} = S_{fi}^{\mathrm{E}}$ is

$$S_{if}^{\mathrm{E}} = \max(L, L') \begin{Bmatrix} J & 1 & J' \\ L' & S & L \end{Bmatrix}^2. \tag{C.5}$$

Note that at leading order in the multipole expansion the electric overlap integral $\mathcal{E}_{if}$ reduces to

$$\mathcal{E}_{if} = \int_0^\infty R_{n'L'}(r) r R_{nL}(r)\, r^2 dr. \tag{C.6}$$

C.2 Magnetic transitions

Magnetic transitions flip the quark spin. Transitions that do not change the orbital angular momentum are called magnetic dipole (M1) transitions. The spin-flip transition decay rate between an initial state $i \equiv n^{2S+1}L_J$ and a final state $f \equiv n'^{\,2S'+1}L_{J'}$ can be written as [13]

$$\Gamma(i \equiv n^{2S+1}L_J \xrightarrow{\mathrm{M1}} f \equiv n'^{\,2S'+1}L_{J'}) = \frac{4\alpha e_Q^2}{3m_Q^2}(2J'+1)k^3 S_{if}^M |\mathcal{M}_{if}|^2 \frac{E_f}{M_i}, \tag{C.7}$$

where e_Q is the electrical charge of the quark, $m_Q = m_1 = m_2$ is the mass of the quark or antiquark. The overlap integral is given by

$$\mathcal{M}_{fi} = (1 + \kappa_Q)\int_0^\infty R_{n'L}(r)\, j_0\left(\frac{kr}{2}\right) R_{nL}(r)\, r^2 dr. \tag{C.8}$$

The anomalous magnetic moment of a quarkonium is κ_Q and the statistical factor $S_{if}^{\mathrm{M}} = S_{fi}^{\mathrm{M}}$ is

$$S_{if}^{\mathrm{M}} = 6(2S+1)(2S'+1) \begin{Bmatrix} J & 1 & J' \\ S' & L & S \end{Bmatrix}^2 \begin{Bmatrix} 1 & 1/2 & 1/2 \\ 1/2 & S' & S \end{Bmatrix}^2. \tag{C.9}$$

At leading order in the multipole expansion, the overlap integral reduces to $\mathcal{M}_{fi} = \delta_{nn'}$. Transitions for which $n = n'$ are called allowed M1 transitions, transitions for which $n \neq n'$ are called hindered transitions.

C.3 Annihilation into electron-positron

The dominant contribution to the decay of quarkonium states into lepton pairs proceed via a single virtual photon, as long as the mass of the initial meson state is sufficiently small so that the contribution of a virtual Z can be ignored.

The leptonic width of n^3S_1 quarkonium including radiative QCD corrections is given by [276]

$$\Gamma(n^3S_1 \to e^+e^-) = \frac{4\alpha^2 e_Q^2 |R_{nS}(0)|^2}{M_{nS}^2}\left(1 - \frac{16\alpha_s}{3\pi}\right), \tag{C.10}$$

where e_Q is the quark charge in units of the charge of the electron, α and α_s are the fine structure and the strong coupling constants, respectively. The mass of the meson is M_{nS} and $R_{nS}(0)$ is the radial wave function of the meson evaluated at the origin. Similarly for 1^{--} D-wave quarkonium states, the leading order decay width into e^+e^- is given by [44]

$$\Gamma(n^3D_1 \to e^+e^-) = \frac{25\alpha^2 e_Q^2}{2m_Q^4 M_{nD}^2}|R''_{nD}(0)|^2. \tag{C.11}$$

Momentum-dependent effects could reveal significant corrections to the theoretical leptonic width. The expression for e^+e^- decay width of S-wave states in the center-of-mass frame of the meson and taking into account those effects can be written as [277]

$$\begin{aligned}\tilde{\Gamma}(n^3S_1 \to e^+e^-) =& 16\alpha^2 e_Q^2 \frac{m_Q^2}{M_{nS}^4}\frac{|\vec{k}|}{E_e}(3E_e^2 - |\vec{k}|^2)\times \\ &\times\left[\int_0^\infty \frac{E_Q + m_Q}{m_Q}\frac{|\vec{p}|^2}{E_Q}\left(1 + \frac{|\vec{p}|^2}{3(E_Q+m_Q)^2}\right)\psi(|\vec{p}|)d|\vec{p}|\right]^2,\end{aligned} \tag{C.12}$$

where the quark and lepton energies are respectively

$$\begin{aligned}E_Q &= \left(|\vec{p}|^2 + m_Q^2\right)^{1/2}, \\ E_e &= \left(|\vec{k}|^2 + m_e^2\right)^{1/2}.\end{aligned} \tag{C.13}$$

The static limit of Eq. (C.12) may be obtained by considering the nonrelativistic limit

$$\frac{|\vec{p}|^2}{m_Q^2} \ll 1, \tag{C.14}$$

and in this case the integral in Eq. (C.12) reduces to

$$\frac{2}{m_Q}\int_0^\infty \psi(|\vec{p}|)|\vec{p}|^2 d|\vec{p}|. \tag{C.15}$$

Recalling the Fourier transform

$$\phi(\vec{r}) = \frac{1}{(2\pi)^{3/2}}\int e^{i\vec{p}\cdot\vec{r}}\psi(\vec{p})d\vec{p}, \tag{C.16}$$

and evaluating at the origin, we have

$$\phi(\vec{r}=0) = \frac{1}{(2\pi)^{3/2}}\int \psi(\vec{p})d\vec{p} = \sqrt{\frac{2}{\pi}}\int_0^\infty |\vec{p}|^2\psi(|\vec{p}|)d|\vec{p}|, \tag{C.17}$$

so the integral above, Eq. (C.15), becomes

$$\frac{2}{m_Q}\int_0^\infty \psi(|\vec{p}|)|\vec{p}|^2 d|\vec{p}| = \frac{(2\pi)^{1/2}}{m_Q}\,\phi(\vec{r}=0). \tag{C.18}$$

With the kinematic relationships, the static limit of Eq. (C.12) is

$$\tilde{\Gamma}(n^3S_1 \to e^+e^-)\Big|_{\rm static} = \frac{16\pi\alpha^2 e_Q^2}{M_{nS}^2}|\phi(\vec{r}=0)|^2 = \frac{4\alpha^2 e_Q^2}{M_{nS}^2}|R(r=0)|^2, \tag{C.19}$$

which is the well-known van Royen-Weisskopf formula, Eq. (C.10).

C.4 Annihilation into 2γ and 3γ

States with even C-parity can annihilate into two photons [44, 278]. The amplitude of the two-photon annihilation of the P-wave states, $J^{PC} = 0^{++}$ and 2^{++}, is proportional to the first derivative of the radial wave function at the origin. The decay of $J^{PC} = 1^{++}$ into two photons is forbidden. The specific expressions [278] with the first short-distance QCD correction [279] are given by

$$\begin{aligned}
\Gamma(n^3P_0 \to \gamma\gamma) &= \frac{27e_Q^4\alpha^2}{m_Q^4}|R'_{nP}(0)|^2\left[1+\frac{\alpha_s}{3\pi}\left(\pi^2-\frac{28}{3}\right)\right],\\
\Gamma(n^3P_2 \to \gamma\gamma) &= \frac{36e_Q^4\alpha^2}{5m_Q^4}|R'_{nP}(0)|^2\left(1-\frac{16\alpha_s}{3\pi}\right).
\end{aligned} \tag{C.20}$$

For the n^1S_0 states the amplitude is proportional to the wave function at the origin. Including also the first short distance QCD correction [280] for the 2γ decay, one can write

$$\Gamma(n^1S_0 \to \gamma\gamma) = \frac{3e_Q^4\alpha^2}{m_Q^2}|R_{nS}(0)|^2\left[1-\frac{\alpha_s}{\pi}\left(\frac{20-\pi^2}{3}\right)\right]. \tag{C.21}$$

The rate of the decay n^1D_2 is given as [44]

$$\Gamma(n^1D_2 \to \gamma\gamma) = \frac{3e_Q^4\alpha^2}{m_Q^6}|R''_{nD}(0)|^2. \tag{C.22}$$

Finally, the annihilation of n^3S_1 into photons is given by the process $n^3S_1 \to 3\gamma$ due to the C-parity conservation. These decays have very small rates proportional to α^3

$$\Gamma(n^3S_1 \to 3\gamma) = \frac{4(\pi^2-9)\alpha^3 e_Q^6}{3\pi m_Q^2}|R_{nS}(0)|^2\left(1-\frac{12.6\alpha_s}{\pi}\right), \tag{C.23}$$

where the lowest-order result is similar to the corresponding orthopositronium decay formula [107] and the first QCD correction has been obtained [281] from the result for the one-loop QED correction to the orthopositronium decay rate [282].

Appendix D

General aspects of the renormalization approach

D.1 Renormalization conditions and error estimates

The boundary condition allows to connect the bound state to the excited states by the matching condition. We provide here an a priori and qualitative determination on the short-distance cutoff error of a excited state, $E_n(r_c)$, when the ground state is fixed to a given value E_0 for any value of the cutoff r_c.

We start with the ground state energy, E_0, which is fixed throughout and compute the logarithmic derivative of the ground state wave function at r_c which is matched to the corresponding quantity of the excited state. Then, we perform a calculation of the bound state energy, $E_n(r_c)$, which obviously depends on the cutoff radius. It is this r_c dependence the one we want to determine. Let us denote by $u_n(r, r_c)$ the excited wave function where the dependence on r_c is explicitly displayed. Under an infinitesimal change, $r_c \to r_c + \Delta r_c$ we get

$$-\Delta u_n'' + U\Delta u_n = \Delta E_n u_n + E_n \Delta u_n, \tag{D.1}$$

Note that the variation is defined for a fixed value of r,

$$\Delta u_n(r, r_c) = u_n(r, r_c + \Delta r_c) - u_n(r, r_c), \tag{D.2}$$

and hence

$$\Delta u_n'(r, r_c) = u_n'(r, r_c + \Delta r_c) - u_n'(r, r_c), \tag{D.3}$$

where here, the prime denotes derivative with respect to the r variable. Therefore, if we use the boundary condition

$$u_n'(r_c, r_c) = L_n(r_c) u_n(r_c, r_c), \tag{D.4}$$

we get

$$\Delta u_n'(r, r_c)\Big|_{r=r_c} = \Delta(L_n(r_c)u_n(r_c, r_c)) - \frac{\partial u_n'(r, r_c)}{\partial r_c}\Big|_{r=r_c} \Delta r_c. \tag{D.5}$$

From here we obtain

$$(L_n' + L_n^2 - U + E_n)u_n = -\frac{\partial u_n'}{\partial r_c} + L_n \frac{\partial u_n}{\partial r_c}, \tag{D.6}$$

and multiplying this equation by u_n and subtracting the original equation multiplied by Δu_n we get

$$-\Delta u_n'' u_n + u_n'' \Delta u_n = \Delta E_n u_n^2, \tag{D.7}$$

which integrating from r_c and infinity and using that for a bound state $u_n(r, r_c) \to 0$ at large distances we get

$$-\Delta u_n' u_n + u_n' \Delta u_n = \Delta E_n \int_{r_c}^{\infty} u_n^2. \tag{D.8}$$

On the other hand, since the ground state energy is fixed, $\Delta E_0 = 0$, we get

$$-\Delta u_0' u_0 + u_0' \Delta u_0 = 0, \tag{D.9}$$

and taking into account

$$\Delta E_n = (L_n' + L_n^2 - U + E_n) \frac{u_n(r_c)^2}{\int_{r_c}^{\infty} u_n(r)^2 dr}, \tag{D.10}$$

so that using $L_n = L_0$ we arrive at

$$\Delta(E_n - E_0) = (E_n - E_0) \frac{u_n(r_c)^2}{\int_{r_c}^{\infty} u_n(r)^2 dr} \Delta r_c. \tag{D.11}$$

Actually, integrating we get

$$[E_n(r_c) - E_0] \int_{r_c}^{\infty} dr\, u_n(r)^2 = \text{const.} \tag{D.12}$$

For a normalized state we have for small r_c

$$E_n(r_c) - E_0 = (E_n - E_0) \left[1 + r_c u_n(r_c)^2 + \dots\right]. \tag{D.13}$$

Therefore for a regular potential with a non-trivial boundary condition $u_n(0) \neq 0$ the error is at least linear. For a singular and attractive potential, $1/r^n$, the error is $\mathcal{O}(r_c^{1+n/2})$ up to some oscillations. As we see, the convergence is from above and proportional to the energy difference as well. This means that the effect of putting a finite cutoff fixing the ground state energy is repulsive and increases with the excitation energy.

D.2 Short-distance analysis of wave functions

In the renormalization scheme, the singular structure of the problem at short distances requires a specific analysis of the uncoupled and coupled equations. We summarize in this section a few interesting facts concerning the short distance behaviour of the wave functions.

D.2.1 Single channel case

In the case of nS states, an attractive OGE Coulomb-like behaviour holds, so that at short distances the reduced potential reads

$$U(r) \equiv 2\mu V(r) \to -\frac{1}{Rr}, \tag{D.14}$$

where R represents the relevant length scale in the reduced potential. Thus we have short-distance behaviour

$$u_n(r) \to A_n \left[1 - \frac{3r}{2R} - \frac{r}{R}\log\left(\frac{r}{R}\right)\right] + B_n r, \tag{D.15}$$

which is a linear combination of the regular wave function and the irregular one. On the other hand, the orthogonality condition, Eq. (3.23), implies $A_n/B_n = A_0/B_0$ so that

$$\frac{u_n(r_c)}{u_0(r_c)} \to \frac{A_n}{A_0}, \tag{D.16}$$

which shows that the ratio between wave functions becomes finite as the cutoff is removed, as can be seen at the left panel in Fig. 3.9.

For a power-like short-distance singular potential we may keep the strongest singularity

$$V(r) \to -\frac{C_n}{r^n}. \tag{D.17}$$

The solution of the Schrödinger equation requires the reduced potential

$$U(r) \equiv 2\mu V(r) \to -\frac{1}{R^2}\left(\frac{R}{r}\right)^n, \tag{D.18}$$

where for convenience the variable $R = (2\mu C_n)^{1/4}$ with length scale dimensions has been introduced. At short distances the reduced de Broglie wavelength is given by

$$\lambda(r) \equiv \frac{1}{\sqrt{-U(r)}} = R\left(\frac{r}{R}\right)^{\frac{n}{2}}, \tag{D.19}$$

which fulfills

$$\frac{d\lambda(r)}{dr} = \frac{n}{2}\left(\frac{r}{R}\right)^{\frac{n}{2}-1} \ll 1, \tag{D.20}$$

for $r \ll R$. In such a case the WKB method can be applied [283] yielding

$$u(r) \to u_{\rm WKB}(r) = \frac{A}{[-U(r)]^{1/4}} \sin\left[\int dr\sqrt{-U(r)} + \varphi\right], \tag{D.21}$$

where A and φ are undetermined amplitude and phase which may be obtained by matching to the exact solution in the region $r \sim R$. In the case of the singular potential given by Eq. (D.17) we have for the m-state

$$u_m(r) \to A_m\left(\frac{r}{R}\right)^{\frac{n}{4}} \sin\left[\frac{2}{2-n}\left(\frac{R}{r}\right)^{\frac{n}{2}-1} + \varphi_m\right]. \tag{D.22}$$

However, the orthogonality condition, Eq. (3.23), imply $\varphi_m = \varphi_0$. Thus we obtain

$$\frac{u_m(r_c)}{u_0(r_c)} \to \frac{A_m}{A_0}. \tag{D.23}$$

For $n = 3$ this is seen in the left panel in Fig. 3.9.

D.2.2 Coupled channel case

Now we undertake the short-distance analysis of the spin-orbit and tensor interactions. At short distances one may neglect all terms and just keep the $1/r^3$ singular contribution yielding

$$\begin{pmatrix} -u''(r) \\ -w''(r) \end{pmatrix} + \frac{R}{r^3} \begin{pmatrix} 0 & \frac{2\sqrt{2}}{3} \\ \frac{2\sqrt{2}}{3} & -\frac{20}{3} \end{pmatrix} \begin{pmatrix} u(r) \\ w(r) \end{pmatrix} = 0. \tag{D.24}$$

This system can be diagonalized by going to the rotated basis

$$\begin{pmatrix} v_1(r) \\ v_2(r) \end{pmatrix} = \begin{pmatrix} \cos\alpha & \sin\alpha \\ -\sin\alpha & \cos\alpha \end{pmatrix} \begin{pmatrix} u(r) \\ w(r) \end{pmatrix}, \tag{D.25}$$

where the new functions satisfy

$$\begin{aligned} -v_1''(r) + \frac{R_1}{r^3} v_1(r) = 0, \\ -v_2''(r) - \frac{R_2}{r^3} v_2(r) = 0, \end{aligned} \tag{D.26}$$

and the R_1 and $-R_2$ are the corresponding eigenvalues

$$\begin{aligned} R_1 &= R\left(-\frac{10}{3} + 2\sqrt{3}\right) > 0, \\ -R_2 &= R\left(-\frac{10}{3} - 2\sqrt{3}\right) < 0, \end{aligned} \tag{D.27}$$

and the mixing angle is $\alpha = 1.1^0$, a rather small value. At short distances the solutions of Eq. (D.26) could be analyzed via the WKB method as we have done in the previous section, but for this case we can undertake the analysis in terms of Bessel functions, whose short distance is analytically known. Actually, the solutions of $-y''(x) - y(x)/x^3 = 0$ are

$$\begin{aligned} \sqrt{x}\, J_1\left(\frac{2}{\sqrt{x}}\right) &= -\frac{x^{\frac{3}{4}}}{\sqrt{\pi}} \cos\left(\frac{\pi}{4} + \frac{2}{\sqrt{x}}\right) + \ldots, \\ \sqrt{x}\, Y_1\left(\frac{2}{\sqrt{x}}\right) &= -\frac{x^{\frac{3}{4}}}{\sqrt{\pi}} \cos\left(\frac{\pi}{4} - \frac{2}{\sqrt{x}}\right) + \ldots, \end{aligned}$$

whereas the solutions of $-y''(x) + y(x)/x^3 = 0$ are

$$\begin{aligned} \sqrt{x}\, K_1\left(\frac{2}{\sqrt{x}}\right) &= \frac{1}{2}\sqrt{\pi}\, x^{\frac{3}{4}}\, e^{-2/\sqrt{x}} + \ldots, \\ \sqrt{x}\, I_1\left(\frac{2}{\sqrt{x}}\right) &= \frac{1}{2\sqrt{\pi}}\, x^{\frac{3}{4}}\, e^{2/\sqrt{x}} + \ldots, \end{aligned} \tag{D.28}$$

All this amounts to write the solutions in the suitable form

$$\begin{aligned} v_1(r) &\to \left(\frac{r}{R_1}\right)^{\frac{3}{4}} \left[C_{1R}\, e^{+2\sqrt{\frac{R_1}{r}}} + C_{2R}\, e^{-2\sqrt{\frac{R_1}{r}}}\right], \\ v_2(r) &\to C_A \left(\frac{r}{R_2}\right)^{\frac{3}{4}} \sin\left(2\sqrt{\frac{R_2}{r}} + \varphi\right). \end{aligned} \tag{D.29}$$

The four constants appearing here, C_{1R}, C_{2R}, C_A and φ reflect that the total order of the system is four. The last equation also shows that generally solutions will diverge as $e^2\sqrt{R_1/r}$ at the origin, hence preventing the bound state normalization condition, unless $C_{1R} = 0$. In such a case the normalizable solution may be written as

$$\begin{aligned} u(r) \to &- \sin\alpha\, C_A \left(\frac{r}{R_2}\right)^{\frac{3}{4}} \sin\left(2\sqrt{\frac{R_2}{r}} + \varphi\right) + \cos\alpha\, C_{2R} \left(\frac{r}{R_1}\right)^{\frac{3}{4}} e^{-2\sqrt{\frac{R_1}{r}}}, \\ w(r) \to &+ \cos\alpha\, C_A \left(\frac{r}{R_2}\right)^{\frac{3}{4}} \sin\left(2\sqrt{\frac{R_2}{r}} + \varphi\right) + \sin\alpha\, C_{2R} \left(\frac{r}{R_1}\right)^{\frac{3}{4}} e^{-2\sqrt{\frac{R_1}{r}}}. \end{aligned} \tag{D.30}$$

The three independent constants appearing here for the regular solution C_A, C_{2R} and φ correspond to fix the energy $M_{J/\psi}$, the asymptotic D/S ratio η, and the normalization condition. Note that when integrating from large distances to short distances with a given bound state energy and an arbitrary η we would always have a contribution from the exponentially diverging solution since $C_{1R} \neq 0$. Thus, the condition $C_{1R} = 0$ predicts η from the bound state energy. The foregoing analysis shows that for the $1/r^3$ singularity appearing here the solution is ambiguous and the bound state energy for a given state has to be treated as an input. Of course, the orthogonality requirement between different states implies that if one state, (u_n, w_n), has a short-distance phase φ_n and another state, (u_m, w_m), has a short-distance phase φ_m, one has

$$\begin{aligned} 0 &= 2\mu(M_n - M_m) \int_0^\infty dr\, (u_n u_m + w_n w_m) \\ &= \left[u_n' u_m - u_n u_m' + w_n' w_m - w_n w_m'\right]\Big|_0^\infty \\ &= \frac{1}{R_2} C_{A,n} C_{A,m} \sin(\varphi_n - \varphi_m) \end{aligned} \tag{D.31}$$

whence $\varphi_n = \varphi_m$ is obtained. This shows that all states are linked through the spin-dependent splitting provided the ground state energy is given.

Appendix E

Matrix elements of strong decays

E.1 Nonrelativistic reduction of Dirac bilinears

The Dirac-Pauli and Majorana representations are the most famous ways of writing the γ^μ Dirac matrices. We use the Dirac-Pauli representation of the γ^μ Dirac matrices. The reason is that this representation has a simple nonrelativistic limit, and thus it is more suitable for us because we calculate the nonrelativistic reduction of the matrix elements. In terms of the Pauli 2×2 spin matrices

$$\sigma_1 = \begin{pmatrix} 0 & 1 \\ 1 & 0 \end{pmatrix}, \quad \sigma_2 = \begin{pmatrix} 0 & -i \\ i & 0 \end{pmatrix}, \quad \sigma_3 = \begin{pmatrix} 1 & 0 \\ 0 & -1 \end{pmatrix}, \tag{E.1}$$

the Dirac matrices can be written in this representation as

$$\gamma^0 = \begin{pmatrix} I & 0 \\ 0 & -I \end{pmatrix}, \quad \gamma^k = \begin{pmatrix} 0 & \sigma_k \\ -\sigma_k & 0 \end{pmatrix}, \quad \gamma^5 = \begin{pmatrix} 0 & I \\ I & 0 \end{pmatrix}. \tag{E.2}$$

A complete set of plane wave states is now easily constructed. The solutions of the Dirac equation with energy-momentum vectors $\pm p = (\pm E_{\vec{p}}, \vec{p})$ are given by

$$\begin{aligned} u_r(\vec{p}) &= \sqrt{\frac{E_{\vec{p}}+m}{2m}} \begin{pmatrix} \chi_r \\ \frac{\vec{p}\cdot\vec{\sigma}}{E_{\vec{p}}+m}\chi_r \end{pmatrix}, \\ \bar{u}_r(\vec{p}) &= \sqrt{\frac{E_{\vec{p}}+m}{2m}} \left(\chi_r^\dagger \quad , -\chi_r^\dagger \frac{\vec{p}\cdot\vec{\sigma}}{E_{\vec{p}}+m} \right), \\ v_r(\vec{p}) &= \sqrt{\frac{E_{\vec{p}}+m}{2m}} \begin{pmatrix} \frac{\vec{p}\cdot\vec{\sigma}}{E_{\vec{p}}+m}\chi'_r \\ \chi'_r \end{pmatrix}, \\ \bar{v}_r(\vec{p}) &= \sqrt{\frac{E_{\vec{p}}+m}{2m}} \left(\chi_r'^\dagger \frac{\vec{p}\cdot\vec{\sigma}}{E_{\vec{p}}+m} \quad , -\chi_r'^\dagger \right), \end{aligned} \tag{E.3}$$

where $\bar{u}_r(\vec{p}) = u_r^\dagger(\vec{p})\gamma^0$ and $v_r(\vec{p}) = v_r^\dagger(\vec{p})\gamma^0$. The two-component nonrelativistic spinors are defined as

$$\chi_1 \equiv \chi'_2 \equiv \begin{pmatrix} 1 \\ 0 \end{pmatrix}, \qquad \chi_2 \equiv \chi'_1 \equiv \begin{pmatrix} 0 \\ 1 \end{pmatrix}. \tag{E.4}$$

In our evaluation of decay matrix elements in JKJ models, we also require spin matrix elements, which involve the nonrelativistic $\mathcal{O}(p/m)$ matrix elements of Dirac

bilinears with $\Gamma = I$, γ^0, $\vec{\gamma}$ and Pauli spin matrix elements. These are

$$\begin{aligned}
\lim_{v/c\to 0}[\bar{u}_\mu(\vec{p}_\mu)\, I\, v_\nu(\vec{p}_\nu)] &= \frac{1}{2m_\mu}(\vec{p}_\nu - \vec{p}_\mu)\cdot\langle\mu|\vec{\sigma}|\nu\rangle = -\frac{1}{2m_\mu}\sqrt{2^5\pi}\left[\mathcal{Y}_1\left(\frac{\vec{p}_\mu - \vec{p}_\nu}{2}\right)\otimes\left(\frac{1}{2}\frac{1}{2}\right)1\right]_0,\\
\lim_{v/c\to 0}[\bar{u}_\mu(\vec{p}_\mu)\,\gamma^0\, v_\nu(\vec{p}_\nu)] &= \frac{1}{2m_\mu}(\vec{p}_\nu + \vec{p}_\mu)\cdot\langle\mu|\vec{\sigma}|\nu\rangle = +\frac{1}{2m_\mu}\sqrt{2^3\pi}\left[\mathcal{Y}_1(\vec{p}_\nu + \vec{p}_\mu)\otimes\left(\frac{1}{2}\frac{1}{2}\right)1\right]_0,\\
\lim_{v/c\to 0}[\bar{u}_\mu(\vec{p}_\mu)\,\vec{\gamma}\, v_\nu(\vec{p}_\nu)] &= \langle\mu|\vec{\sigma}|\nu\rangle\,,
\end{aligned} \tag{E.5}$$

and

$$\begin{aligned}
\lim_{v/c\to 0}[\bar{u}_\mu(\vec{p}_\mu)\, I\, u_\nu(\vec{p}_\nu)] &= \delta_{\mu\nu},\\
\lim_{v/c\to 0}[\bar{u}_\mu(\vec{p}_\mu)\,\gamma^0\, u_\nu(\vec{p}_\nu)] &= \delta_{\mu\nu},\\
\lim_{v/c\to 0}[\bar{u}_\mu(\vec{p}_\mu)\,\vec{\gamma}\, u_\nu(\vec{p}_\nu)] &= \frac{1}{2m_\nu}\left[(\vec{p}_\nu + \vec{p}_\mu)\delta_{\mu\nu} - i\,\langle\mu|\vec{\sigma}|\nu\rangle\times(\vec{p}_\mu - \vec{p}_\nu)\right],
\end{aligned} \tag{E.6}$$

where we have used the relation

$$\vec{Y}_1\cdot\langle\vec{\sigma}\rangle = -\sqrt{3}\,[Y_1\otimes\langle\vec{\sigma}\rangle]_0 = \sqrt{6}\left[Y_1\otimes\left(\frac{1}{2}\frac{1}{2}\right)1\right]_0. \tag{E.7}$$

E.2 Spin-space overlap integral of sKs decay model

We begin from the Eq. (4.40) and using the expressions below one can decouple the spin and angular momentum terms

$$\begin{aligned}
|[(L_A S_A)J_A][(11)0]J_A\rangle &= \sum_{L,S}\sqrt{(2L+1)(2S+1)(2J_A+1)}\begin{Bmatrix} L_A & S_A & J_A\\ 1 & 1 & 0\\ L & S & J_A\end{Bmatrix}|\,[(L_A 1)L]\,[(S_A 1)S]\,J_A\rangle\\
&= \sum_{L,S}\sqrt{(2L+1)(2S+1)(2J_A+1)}\,\frac{(-1)^{L_A+S+J_A+1}}{\sqrt{3(2J_A+1)}}\\
&\quad\begin{Bmatrix} S_A & L_A & J_A\\ L & S & 1\end{Bmatrix}|\,[(L_A 1)L]\,[(S_A 1)S]\,J_A\rangle\,,
\end{aligned}$$

$$\begin{aligned}
\langle[(L_B S_B)J_B]\,[(L_C S_C)J_C]\,J_{BC}| &= \sum_{L_{BC},S}\sqrt{(2L_{BC}+1)(2S+1)(2J_B+1)(2J_C+1)}\\
&\quad\begin{Bmatrix} L_B & S_B & J_B\\ L_C & S_C & J_C\\ L_{BC} & S & J_{BC}\end{Bmatrix}\langle[(L_B L_C)L_{BC}]\,[(S_B S_C)S]\,J_{BC}|,
\end{aligned}$$

$$\begin{aligned}
\langle[(L_{BC}S)J_{BC}]\,[l]\,J_T| &= \sum_{L}\sqrt{(2J_{BC}+1)(2L+1)}\,(-1)^{S+l+J_{BC}+L}\\
&\quad\begin{Bmatrix} S & L_{BC} & J_{BC}\\ l & J_T & L\end{Bmatrix}\langle[(L_{BC}l)L]\,[S]\,J_T|,
\end{aligned}$$

$$\begin{aligned}&\langle[(s_\alpha s_\nu)S_B]\,[(s_\mu s_\beta)S_C]\,S|\,[(s_\alpha s_\beta)S_A]\,[(s_\mu s_\nu)1]\,S\rangle = \\ &= (-1)^{-1+S_C}\sqrt{(2S_B+1)(2S_C+1)(2S_A+1)3}\begin{Bmatrix}1/2 & 1/2 & S_B\\ 1/2 & 1/2 & S_C\\ S_A & 1 & S\end{Bmatrix},\end{aligned} \tag{E.8}$$

to write

$$\mathcal{I}^{sKs}_{\text{spin}-\text{space}} = \frac{-1}{\sqrt{1+\delta_{BC}}}\frac{1}{2m_\nu}\sqrt{2^5\pi}\sum_{L_{BC},L,S}\mathcal{J}(A\to BC)\mathcal{E}(A\to BC), \tag{E.9}$$

with $\mathcal{J}(A\to BC)$ equal to Eq. (4.19) and

$$\begin{aligned}\mathcal{E}(A\to BC) = &\int d^3K_B d^3K_C d^3p_\alpha d^3p_\beta d^3p_\mu d^3p_\nu d^3p_\delta \\ &\delta^{(3)}(\vec{K}-\vec{K}_0)\delta^{(3)}(\vec{K}_B-\vec{P}_B)\delta^{(3)}(\vec{K}_C-\vec{P}_C)\delta^{(3)}(\vec{P}_A)\frac{\delta(k-k_0)}{k} \\ &\delta^{(3)}(\vec{p}_\delta-(\vec{p}_\alpha-\vec{p}_\mu-\vec{p}_\nu))K(|\vec{p}_\mu+\vec{p}_\nu|) \\ &\langle[[\phi_B(\vec{p}_B)\phi_C(\vec{p}_C)]\,L_{BC}Y_l(\hat{k})]\,L|\,[\phi_A(\vec{p}_A)\mathcal{Y}_1\left(\frac{\vec{p}_\mu-\vec{p}_\nu}{2}\right)]\,L\rangle\,.\end{aligned} \tag{E.10}$$

If we integrate in d^3p_δ using the δ-function, we obtain

$$\begin{aligned}\mathcal{E}(A\to BC) = &\int d^3K_B d^3K_C d^3p_\alpha d^3p_\beta d^3p_\mu d^3p_\nu\, K(|\vec{p}_\mu+\vec{p}_\nu|) \\ &\delta^{(3)}(\vec{K}-\vec{K}_0)\delta^{(3)}(\vec{K}_B-\vec{P}_B)\delta^{(3)}(\vec{K}_C-\vec{P}_C)\delta^{(3)}(\vec{P}_A)\frac{\delta(k-k_0)}{k} \\ &\langle[[\phi_B(\vec{p}_B)\phi_C(\vec{p}_C)]\,L_{BC}Y_l(\hat{k})]\,L|\,[\phi_A(\vec{p}_A)\mathcal{Y}_1\left(\frac{\vec{p}_\mu-\vec{p}_\nu}{2}\right)]\,L\rangle\,.\end{aligned} \tag{E.11}$$

It is easier to consider the involved masses in function of a reference one

$$\begin{aligned}\omega_\alpha &= \frac{m_\alpha}{m},\\ \omega_{\alpha\beta} &= \omega_\alpha+\omega_\beta,\end{aligned} \tag{E.12}$$

such that the masses of quarks, antiquarks and mesons are dimensionless. We try to write $\mathcal{E}(A\to BC)$ in function of the total and relative momenta of meson A, created pair $(\mu\nu)$ and system BC

$$\begin{aligned}\vec{P}_A &= \vec{p}_\alpha+\vec{p}_\beta, \qquad \vec{p}_A = \frac{\omega_\beta\vec{p}_\alpha-\omega_\alpha\vec{p}_\beta}{\omega_{\alpha\beta}},\\ \vec{P} &= \vec{p}_\mu+\vec{p}_\nu, \qquad \vec{p} = \frac{\vec{p}_\mu-\vec{p}_\nu}{2},\\ \vec{K} &= \vec{K}_B+\vec{K}_C, \qquad \vec{k} = \frac{\omega_C\vec{K}_B-\omega_B\vec{K}_C}{\omega_{BC}},\end{aligned} \tag{E.13}$$

such that the different momenta in function of those above can be expressed as follow

$$\begin{aligned}
\vec{p}_\alpha &= \vec{p}_A + \frac{\omega_\alpha}{\omega_{\alpha\beta}}\vec{P}_A,\\
\vec{p}_\beta &= -\vec{p}_A + \frac{\omega_\beta}{\omega_{\alpha\beta}}\vec{P}_A,\\
\vec{p}_\mu &= \vec{p} + \frac{1}{2}\vec{P},\\
\vec{p}_\nu &= -\vec{p} + \frac{1}{2}\vec{P},\\
\vec{K}_B &= \vec{k} + \frac{\omega_B}{\omega_{BC}}\vec{K},\\
\vec{K}_C &= -\vec{k} + \frac{\omega_C}{\omega_{BC}}\vec{K},\\
\vec{P}_B &= \vec{p}_A + \frac{\omega_\alpha}{\omega_{\alpha\beta}}\vec{P}_A - \vec{p} - \frac{1}{2}\vec{P},\\
\vec{p}_B &= \frac{\omega_\nu}{\omega_{\alpha\nu}}\vec{p}_A + \frac{\omega_\alpha\omega_\nu}{\omega_{\alpha\nu}\omega_{\alpha\beta}}\vec{P}_A + \frac{\omega_\alpha}{\omega_{\alpha\nu}}\vec{p} - \frac{(2\omega_\nu+\omega_\alpha)}{2\omega_{\alpha\nu}}\vec{P},\\
\vec{P}_C &= -\vec{p}_A + \frac{\omega_\beta}{\omega_{\alpha\beta}}\vec{P}_A + \vec{p} + \frac{1}{2}\vec{P},\\
\vec{p}_C &= \frac{\omega_\mu}{\omega_{\mu\beta}}\vec{p}_A - \frac{\omega_\mu\omega_\beta}{\omega_{\mu\beta}\omega_{\alpha\beta}}\vec{P}_A + \frac{\omega_\beta}{\omega_{\mu\beta}}\vec{p} + \frac{\omega_\beta}{2\omega_{\mu\beta}}\vec{P}.
\end{aligned} \tag{E.14}$$

Once we have integrated in some variables with the help of the δ-functions, the expression of $\mathcal{E}(A \to BC)$ is

$$\begin{aligned}
\mathcal{E}(A \to BC) = \int d^3k d^3p d^3P\, K(|\vec{P}|)\, \frac{\delta(k-k_0)}{k}\\
\langle [[\phi_B(\vec{p}_B)\phi_C(\vec{p}_C)]\, L_{BC} Y_l(\hat{k})]\, L|\, [\phi_A(\vec{p}_A)\mathcal{Y}_1(\vec{p})]\, L\rangle\,,
\end{aligned} \tag{E.15}$$

where

$$\begin{aligned}
\vec{p}_A &= \vec{k} + \vec{p} + \frac{1}{2}\vec{P},\\
\vec{p}_B &= \frac{\omega_\nu}{\omega_{\alpha\nu}}\vec{k} + \vec{p} - \frac{1}{2}\vec{P},\\
\vec{p}_C &= \frac{\omega_\mu}{\omega_{\mu\beta}}\vec{k} + \vec{p} + \frac{1}{2}\vec{P}.
\end{aligned} \tag{E.16}$$

Now the wave functions can be decomposed in the following way

$$\begin{aligned}
\phi_A(\vec{p}_A) &= f_A(p_A)\mathcal{Y}_{L_A}(\vec{p}_A),\\
\phi_B(\vec{p}_B) &= f_B(p_B)\mathcal{Y}_{L_B}(\vec{p}_B),\\
\phi_C(\vec{p}_C) &= f_C(p_C)\mathcal{Y}_{L_C}(\vec{p}_C),
\end{aligned} \tag{E.17}$$

where $f_A(p_A)$, $f_B(p_B)$ and $f_C(p_C)$ are expanded in terms of Gaussian basis functions

$$\begin{aligned} f_A(p_A) &= \sum_i d_i^A \exp\left(-\frac{A_i}{2}p_A^2\right), \\ f_B(p_B) &= \sum_j d_j^B \exp\left(-\frac{B_j}{2}p_B^2\right), \\ f_C(p_C) &= \sum_k d_k^C \exp\left(-\frac{C_k}{2}p_C^2\right), \end{aligned} \tag{E.18}$$

arriving to

$$\mathcal{E}(A \to BC) = \sum_{i,j,k} d_i^A d_j^B d_k^C \hat{\mathcal{E}}_{ijk}(A_i \to B_j C_k). \tag{E.19}$$

We make an abuse of notation for simplicity and consider $\hat{\mathcal{E}}_{ijk}(A_i \to B_j C_k)$ as $\hat{\mathcal{E}}(A \to BC)$ with

$$\begin{aligned} \hat{\mathcal{E}}(A \to BC) = \int d^3k d^3p d^3P\, K(P)\, \frac{\delta(k-k_0)}{k^{l+1}}\, \exp\left[-\frac{1}{2}(Ap_A^2 + Bp_B^2 + Cp_C^2)\right] \\ \left[\left[\mathcal{Y}_{L_B}(\vec{p}_B)\mathcal{Y}_{L_C}(\vec{p}_C)\right]_{L_{BC}} \mathcal{Y}_l(\vec{k})\right]_L \left[\mathcal{Y}_{L_A}(\vec{p}_A)\mathcal{Y}_1(\vec{p})\right]_L. \end{aligned} \tag{E.20}$$

To continue in the calculation of $\hat{\mathcal{E}}(A \to BC)$, it is necessary another change of variable

$$\vec{q} = \vec{p} - x\vec{P}, \tag{E.21}$$

which will help us to simplify the calculation of the exponential in the equation above. We arrive at

$$\begin{aligned} \hat{\mathcal{E}}(A \to BC) = \int d^3k d^3q d^3P\, K(P)\, \frac{\delta(k-k_0)}{k^{l+1}} \exp\left[-\frac{1}{2}(Ap_A^2 + Bp_B^2 + Cp_C^2)\right] \\ \left[\left[\mathcal{Y}_{L_B}(\vec{p}_B)\mathcal{Y}_{L_C}(\vec{p}_C)\right]_{L_{BC}} \mathcal{Y}_l(\vec{k})\right]_L \left[\mathcal{Y}_{L_A}(\vec{p}_A)\mathcal{Y}_1(\vec{p})\right]_L, \end{aligned} \tag{E.22}$$

with

$$\begin{aligned} \vec{p}_A &= \vec{k} + \vec{q} + \frac{2x+1}{2}\vec{P}, \\ \vec{p}_B &= \frac{\omega_\nu}{\omega_{\alpha\nu}}\vec{k} + \vec{q} + \frac{2x-1}{2}\vec{P}, \\ \vec{p}_C &= \frac{\omega_\mu}{\omega_{\mu\beta}}\vec{k} + \vec{q} + \frac{2x+1}{2}\vec{P}, \\ \vec{p} &= \vec{q} + x\vec{P}. \end{aligned} \tag{E.23}$$

Now we need the following expressions

- $\exp\left[-\frac{1}{2}\left(Ap_A^2+Bp_B^2+Cp_C^2\right)\right]=(4\pi)^2\exp\left[-Fk^2-Dq^2-\left(\frac{D^2-R^2}{4D}\right)P^2\right]$
  $\sum_{l_1,l_2,l_3}(-i)^{l_1+l_2}j_{l_1}(iGkq)j_{l_2}\left[i\left(S-\frac{GR}{2D}\right)kP\right]\Pi_{l_3}B^{l_3}_{l_1,l_2}P^{-l_2}k^{-l_3}q^{-l_1}\left[\mathcal{Y}_{l_2}(\vec{P})\left[\mathcal{Y}_{l_3}(\vec{k})\mathcal{Y}_{l_1}(\vec{q})\right]_{l_2}\right]_0,$

- $[\mathcal{Y}_{L_A}(\vec{p}_A)\mathcal{Y}_1(\vec{p})]_L=\sum_{l_1,l_2,l_3,l_4,l_5,l_6}(-1)^{1+L_A+l_5-l_1-l_3}\Pi_{L_A,L_A-l_1,1,l_4,l_5,l_6}C^{L_A}_{l_1}C^{L_A-l_1}_{l_2}C^1_{l_3}B^{l_4}_{l_1,l_3}$
  $B^{l_6}_{L_A-l_1-l_2,1-l_3}\left(\frac{2x+1}{2}\right)^{l_1}x^{l_3}P^{l_1+l_3-l_4}q^{1+L_A-l_1-l_2-l_3-l_6}\begin{Bmatrix}L_A-l_1-l_2 & l_2 & L_A-l_1\\ l_5 & 1-l_3 & l_6\end{Bmatrix}$
  $\begin{Bmatrix}l_1 & L_A-l_1 & L_A\\ l_3 & 1-l_3 & 1\\ l_4 & l_5 & L\end{Bmatrix}\left[\mathcal{Y}_{l_4}(\vec{P})\left[\mathcal{Y}_{l_2}(\vec{k})\mathcal{Y}_{l_6}(\vec{q})\right]_{l_5}\right]_L,$

- $\left[[\mathcal{Y}_{L_B}(\vec{p}_B)\mathcal{Y}_{L_C}(\vec{p}_C)]_{L_{BC}}\mathcal{Y}_l(\vec{k})\right]_L=\sum_{l_1,l_2,\ldots,l_9,l_{10}}(-1)^{L+l_8+l_{10}-l_5}\Pi_{L_B,L_B-l_1,L_C,L_C-l_3,L_{BC}}$
  $\Pi_{l_5,l_6,l_6,l_7,l_8,l_9,l_{10}}C^{L_B}_{l_1}C^{L_B-l_1}_{l_2}C^{L_C}_{l_3}C^{L_C-l_3}_{l_4}B^{l_5}_{l_1,l_3}B^{l_7}_{l_2,l_4}B^{l_8}_{L_B-l_1-l_2,L_C-l_3-l_4}B^{l_{10}}_{l_7,l}$
  $\left(\frac{2x-1}{2}\right)^{l_1}\left(\frac{\omega_\nu}{\omega_{\alpha\nu}}\right)^{l_2}\left(\frac{2x+1}{2}\right)^{l_3}\left(\frac{\omega_\mu}{\omega_{\mu\beta}}\right)^{l_4}P^{l_1+l_3-l_5}k^{l+l_2+l_4-l_{10}}q^{L_B+L_C-l_1-l_2-l_3-l_4-l_8}$
  $\begin{Bmatrix}l_6 & l_5 & L_{BC}\\ L & l & l_9\end{Bmatrix}\begin{Bmatrix}l_7 & l_8 & l_6\\ l_9 & l & l_{10}\end{Bmatrix}\begin{Bmatrix}l_1 & L_B-l_1 & L_B\\ l_3 & L_C-l_3 & L_C\\ l_5 & l_6 & L_{BC}\end{Bmatrix}\begin{Bmatrix}l_2 & L_B-l_1-l_2 & L_B-l_1\\ l_4 & L_C-l_3-l_4 & L_C-l_3\\ l_7 & l_8 & l_6\end{Bmatrix}$
  $\left[\mathcal{Y}_{l_5}(\vec{P})\left[\mathcal{Y}_{l_{10}}(\vec{k})\mathcal{Y}_{l_8}(\vec{q})\right]_{l_9}\right]_L,$ (E.24)

where we have chosen x to make zero the coefficient of the term $\vec{q}\cdot\vec{P}$, thus we get

$$\begin{aligned}
D&=\frac{1}{2}(A+B+C),\\
G&=A+\frac{\omega_\nu}{\omega_{\alpha\nu}}B+\frac{\omega_\mu}{\omega_{\mu\beta}}C,\\
x&=-\frac{R}{2D},\\
F&=\frac{1}{2}\left[A+\left(\frac{\omega_\nu}{\omega_{\alpha\nu}}\right)^2B+\left(\frac{\omega_\mu}{\omega_{\mu\beta}}\right)^2C\right],\\
R&=\frac{1}{2}(A-B+C),\\
S&=\frac{1}{2}\left(A-\frac{\omega_\nu}{\omega_{\alpha\nu}}B+\frac{\omega_\mu}{\omega_{\mu\beta}}C\right),
\end{aligned}\tag{E.25}$$

and we have used the next useful formulas

$$\begin{aligned} e^{-G\vec{k}\cdot\vec{\pi}} &= 4\pi\sum_{l=0}^{\infty}(-i)^l j_l(iGk\pi)\Pi_l\pi^{-l}k^{-l}[\mathcal{Y}_l(\vec{k})\mathcal{Y}_l(\vec{\pi})]_0, \\ \mathcal{Y}_{lm}(a\vec{x}_1+b\vec{x}_2) &= \sum_{l_1=0}^{l} C_{l_1}^l a^{l_1}b^{l-l_1}[\mathcal{Y}_{l_1}(\vec{x}_1)\mathcal{Y}_{l-l_1}(\vec{x}_2)]_{lm}, \\ [\mathcal{Y}_{l_1}(\vec{x})\mathcal{Y}_{l_2}(\vec{x})]_{lm} &= B_{l_1,l_2}^l x^{l_1+l_2-l}\mathcal{Y}_{lm}(\vec{x}), \end{aligned} \tag{E.26}$$

with

$$\begin{aligned} \Pi_l =& \sqrt{2l+1}\,, \\ C_{l_1}^l =& \sqrt{\frac{4\pi(2l+1)!}{(2l_1+1)!(2(l-l_1)+1)!}}\,, \\ B_{l_1,l_2}^l =& (-1)^l\sqrt{\frac{(2l_1+1)(2l_2+1)}{4\pi}}\begin{pmatrix} l_1 & l_2 & l \\ 0 & 0 & 0\end{pmatrix}. \end{aligned} \tag{E.27}$$

After some algebra manipulation our final expression is

$$\begin{aligned} &\hat{\mathcal{E}}(A\to BC) = (4\pi)^2\int dkdqdP\,\delta(k-k_0)K(P)e^{-Fk^2-Dq^2-\left(\frac{D^2-R^2}{4D}\right)P^2} \\ &\sum_{l_1,l_2\ldots l_{18},l_{19}}(-1)^{1+L_A+l_4+l_5+l_{14}+l_{15}+l_{16}+l_{18}-l_1-l_3-l_{11}}(-i)^{l_{17}+l_{18}}j_{l_{17}}(iGkq)j_{l_{18}}\left[i\left(S-\frac{GR}{2D}\right)kP\right] \\ &\left(\frac{2x+1}{2}\right)^{l_1}x^{l_3}\left(\frac{2x-1}{2}\right)^{l_7}\left(\frac{2x+1}{2}\right)^{l_9}\left(\frac{\omega_\nu}{\omega_{\alpha\nu}}\right)^{l_8}\left(\frac{\omega_\mu}{\omega_{\mu\beta}}\right)^{l_{10}}C_{l_1}^{L_A}C_{l_2}^{L_A-l_1}C_{l_3}^1C_{l_7}^{L_B}C_{l_8}^{L_B-l_7}C_{l_9}^{L_C} \\ &C_{l_{10}}^{L_C-l_9}B_{l_1,l_3}^{l_4}B_{L_A-l_1-l_2,1-l_3}^{l_6}B_{l_7,l_9}^{l_{11}}B_{l_8,l_{10}}^{l_{13}}B_{L_B-l_7-l_8,L_C-l_9-l_{10}}^{l_{14}}B_{l_{13},l}^{l_{16}}B_{l_{17}l_{18}}^{l_{19}}B_{l_{18},l_{11}}^{l_4}B_{l_{19},l_{16}}^{l_2}B_{l_{17},l_{14}}^{l_6} \\ &\Pi_{1,L_A,L_A-l_1,L_B,L_B-l_7,L_C,L_C-l_9,L_{BC},l_2,l_4,l_4,l_5,l_5,l_6,l_6,l_{11},l_{12},l_{12},l_{13},l_{14},l_{15},l_{15},l_{16},l_{19}} \\ &P^{2+l_1+l_3+l_7+l_9}k^{1+l_2+l_8+l_{10}}q^{3+L_A+L_B+L_C-l_1-l_2-l_3-l_7-l_8-l_9-l_{10}} \\ &\begin{Bmatrix} L_A-l_1-l_2 & l_2 & L_A-l_1 \\ l_5 & 1-l_3 & l_6\end{Bmatrix}\begin{Bmatrix} l_{12} & l_{11} & L_{BC} \\ L & l & l_{15}\end{Bmatrix}\begin{Bmatrix} l_{13} & l_{14} & l_{12} \\ l_{15} & l & l_{16}\end{Bmatrix}\begin{Bmatrix} l_5 & l_4 & L \\ l_{11} & l_{15} & l_{18}\end{Bmatrix} \\ &\begin{Bmatrix} l_1 & L_A-l_1 & L_A \\ l_3 & 1-l_3 & 1 \\ l_4 & l_5 & L\end{Bmatrix}\begin{Bmatrix} l_7 & L_B-l_7 & L_B \\ l_9 & L_C-l_9 & L_C \\ l_{11} & l_{12} & L_{BC}\end{Bmatrix}\begin{Bmatrix} l_8 & L_B-l_7-l_8 & L_B-l_7 \\ l_{10} & L_C-l_9-l_{10} & L_C-l_9 \\ l_{13} & l_{14} & l_{12}\end{Bmatrix}\begin{Bmatrix} l_{19} & l_{17} & l_{18} \\ l_{16} & l_{14} & l_{15} \\ l_2 & l_6 & l_5\end{Bmatrix}, \end{aligned} \tag{E.28}$$

and for the radial integrals one has

$$\begin{aligned} &\int dkdqdP\delta(k-k_0)K(P)e^{-Fk^2-Dq^2-\left(\frac{D^2-R^2}{4D}\right)P^2}(-i)^{l_{17}+l_{18}}j_{l_{17}}(iGkq)j_{l_{18}}\left[i\left(S-\frac{GR}{2D}\right)kP\right]\times \\ &\times P^{2+l_1+l_3+l_7+l_9}k^{1+l_2+l_8+l_{10}}q^{3+L_A+L_B+L_C-l_1-l_2-l_3-l_7-l_8-l_9-l_{10}} = \\ &= k_0^{1+l_2+l_8+l_{10}}e^{-Fk_0^2}\int_0^\infty dq\; q^{3+L_A+L_B+L_C-l_1-l_2-l_3-l_7-l_8-l_9-l_{10}}i_{l_{17}}(Gk_0q)e^{-Dq^2}\times \\ &\quad\times\int_0^\infty dPK(P)P^{2+l_1+l_3+l_7+l_9}i_{l_{18}}\left[\left(S-\frac{GR}{2D}\right)k_0P\right]e^{-\left(\frac{D^2-R^2}{4D}\right)P^2}. \end{aligned} \tag{E.29}$$

E.3 Spin-space overlap integral of j^0Kj^0 decay model

We begin from Eq. (4.41) and decouple the spin and angular momentum terms following Eq. (E.8) to write

$$\mathcal{I}^{j^0Kj^0}_{\text{spin-space}} = \frac{1}{\sqrt{1+\delta_{BC}}}\frac{1}{2m_\nu}\sqrt{2^3\pi}\sum_{L_{BC},L,S}\mathcal{J}(A\to BC)\mathcal{E}(A\to BC), \tag{E.30}$$

with $J(A\to BC)$ equal to Eq. (4.19) and

$$\begin{aligned}\mathcal{E}(A\to BC) = \int & d^3K_B d^3K_C d^3p_\alpha d^3p_\beta d^3p_\mu d^3p_\nu d^3p_\delta \\ & \delta^{(3)}(\vec{K}-\vec{K}_0)\delta^{(3)}(\vec{K}_B-\vec{P}_B)\delta^{(3)}(\vec{K}_C-\vec{P}_C)\delta^{(3)}(\vec{P}_A)\frac{\delta(k-k_0)}{k} \\ & \delta^{(3)}(\vec{p}_\delta-(\vec{p}_\alpha-\vec{p}_\mu-\vec{p}_\nu))K(|\vec{p}_\mu+\vec{p}_\nu|) \\ & \langle[[\phi_B(\vec{p}_B)\phi_C(\vec{p}_C)]\,L_{BC}Y_l(\hat{k})]\,L|\,[\phi_A(\vec{p}_A)\mathcal{Y}_1\,(\vec{p}_\mu+\vec{p}_\nu)]\,L\rangle\,.\end{aligned} \tag{E.31}$$

We proceed in the same way as in the case of the sKs decay model, the only difference is that the term $\mathcal{Y}_1\left(\frac{\vec{p}_\mu-\vec{p}_\nu}{2}\right)$ is changed by $\mathcal{Y}_1\,(\vec{p}_\mu+\vec{p}_\nu)$. Therefore we have

$$\begin{aligned}\hat{\mathcal{E}}(A\to BC) = \int & d^3k d^3q d^3P\,K(P)\,\frac{\delta(k-k_0)}{k^{l+1}}\exp\left[-\frac{1}{2}(Ap_A^2+Bp_B^2+Cp_C^2)\right] \\ & [[\mathcal{Y}_{L_B}(\vec{p}_B)\mathcal{Y}_{L_C}(\vec{p}_C)]]_{L_{BC}}\,\mathcal{Y}_l(\vec{k})]_L\,[\mathcal{Y}_{L_A}(\vec{p}_A)\mathcal{Y}_1(\vec{P})]_L\,,\end{aligned} \tag{E.32}$$

where the only new term is

$$\begin{aligned}\left[\mathcal{Y}_{L_A}(\vec{p}_A)\mathcal{Y}_1(\vec{P})\right]_L = & \sum_{l_1,l_2,l_3}(-1)^{1+l_1-l_3}\Pi_{L_A,l_3}C^{L_A}_{l_1}C^{L_A-l_1}_{l_2}B^{l_3}_{l_1,1}\left(\frac{2x+1}{2}\right)^{l_1}P^{1+l_1-l_3} \\ & \begin{Bmatrix}l_1 & L_A-l_1 & L_A\\ L & 1 & l_3\end{Bmatrix}\left[\mathcal{Y}_{l_3}(\vec{P})\left[\mathcal{Y}_{l_2}(\vec{k})\mathcal{Y}_{L_A-l_1-l_2}(\vec{q})\right]_{L_A-l_1}\right]_L,\end{aligned} \tag{E.33}$$

reaching the final expression

$$\begin{aligned}&\hat{\mathcal{E}}(A\to BC) = (4\pi)^2\int dkdqdP\delta(k-k_0)K(P)e^{-Fk^2-Dq^2-\left(\frac{D^2-R^2}{4D}\right)P^2}\sum_{l_1,\ldots,l_{16}}(-1)^{1+l_1+l_{11}+l_{12}+l_{13}+l_{15}-l_8} \\ &(-i)^{l_{14}+l_{15}}j_{l_{14}}(iGkq)j_{l_{15}}\left[i\left(S-\frac{GR}{2D}\right)kP\right]\left(\frac{2x+1}{2}\right)^{l_1}\left(\frac{2x-1}{2}\right)^{l_4}\left(\frac{2x+1}{2}\right)^{l_6}\left(\frac{\omega_\nu}{\omega_{\alpha\nu}}\right)^{l_5}\left(\frac{\omega_\mu}{\omega_{\mu\beta}}\right)^{l_7} \\ &C^{L_A}_{l_1}C^{L_A-l_1}_{l_2}C^{L_B}_{l_4}C^{L_B-l_4}_{l_5}C^{L_C}_{l_6}C^{L_C-l_6}_{l_7}B^{l_3}_{l_1,1}B^{l_8}_{l_4,l_6}B^{l_{10}}_{l_5,l_7}B^{l_{11}}_{L_B-l_4-l_5,L_C-l_6-l_7}B^{l_{13}}_{l_{10},l}B^{l_{16}}_{l_{14},l_{15}}B^{L_A-l_1-l_2}_{l_{14},l_{11}}B^{l_2}_{l_{16},l_{13}}B^{l_3}_{l_{15},l_8} \\ &\Pi_{L_A,L_A-l_1,L_A-l_1-l_2,L_B,L_B-l_4,L_C,L_C-l_6,L_{BC},l_2,l_3,l_3,l_8,l_9,l_9,l_{10},l_{11},l_{12},l_{12},l_{13},l_{16}} \\ &P^{3+l_1+l_4+l_6}k^{1+l_2+l_5+l_7}q^{2+L_A+L_B+L_C-l_1-l_2-l_4-l_5-l_6-l_7} \\ &\begin{Bmatrix}l_1 & L_A-l_1 & L_A\\ L & 1 & l_3\end{Bmatrix}\begin{Bmatrix}l_9 & l_8 & L_{BC}\\ L & l & l_{12}\end{Bmatrix}\begin{Bmatrix}l_{10} & l_{11} & l_9\\ l_{12} & l & l_{13}\end{Bmatrix}\begin{Bmatrix}L_A-l_1 & l_3 & L\\ l_8 & l_{12} & l_{15}\end{Bmatrix} \\ &\begin{Bmatrix}l_4 & L_B-l_4 & L_B\\ l_6 & L_C-l_6 & L_C\\ l_8 & l_9 & L_{BC}\end{Bmatrix}\begin{Bmatrix}l_5 & L_B-l_4-l_5 & L_B-l_4\\ l_7 & L_C-l_6-l_7 & L_C-l_6\\ l_{10} & l_{11} & l_9\end{Bmatrix}\begin{Bmatrix}l_{16} & l_{14} & l_{15}\\ l_{13} & l_{11} & l_{12}\\ l_2 & L_A-l_1-l_2 & L_A-l_1\end{Bmatrix},\end{aligned} \tag{E.34}$$

and for the radial integrals one has

$$\int dkdqdP\delta(k-k_0)K(P)e^{-Fk^2-Dq^2-\left(\frac{D^2-R^2}{4D}\right)P^2}(-i)^{l_{14}+l_{15}}j_{l_{14}}(iGkq)j_{l_{15}}\left[i\left(S-\frac{GR}{2D}\right)kP\right]\times$$
$$\times P^{3+l_1+l_4+l_6}k^{1+l_2+l_5+l_7}q^{2+L_A+L_B+L_C-l_1-l_2-l_4-l_5-l_6-l_7}$$
$$=k_0^{1+l_2+l_5+l_7}e^{-Fk_0^2}\times$$
$$\times\int dq\; q^{2+L_A+L_B+L_C-l_1-l_2-l_4-l_5-l_6-l_7}i_{l_{14}}(Gk_0q)e^{-Dq^2}$$
$$\times\int dP\,K(P)\,P^{3+l_1+l_4+l_6}i_{l_{15}}\left[\left(S-\frac{GR}{2D}\right)k_0P\right]e^{-\left(\frac{D^2-R^2}{4D}\right)P^2}. \tag{E.35}$$

E.4 Spin-space overlap integral of j^TKj^T decay model

We begin from Eq. (4.42) which has two terms if one considers the transversal components of the virtual massless particle.

E.4.1 Term in δ_{ij}

We have

$$\begin{aligned}\mathcal{I}^{j^TKj^T,\delta}_{\text{spin}-\text{space}}=&\frac{1}{\sqrt{1+\delta_{BC}}}\sum_{m,M_{BC},M_B,M_C}\langle J_{BC}M_{BC}lm|J_TM_T\rangle\,\langle J_BM_BJ_CM_C|J_{BC}M_{BC}\rangle\\&\int d^3K_Bd^3K_Cd^3p_\delta d^3p_\rho d^3p_\mu d^3p_\nu d^3p_\alpha d^3p_\beta\,\delta^{(3)}(\vec{K}-\vec{K}_0)\delta(k-k_0)\frac{Y_{lm}(\hat{k})}{k}\\&\delta^{(3)}(\vec{K}_B-\vec{P}_B)\delta^{(3)}(\vec{K}_C-\vec{P}_C)\delta^{(3)}(\vec{P}_A)\phi_B(\vec{p}_B)\phi_C(\vec{p}_C)\phi_A(\vec{p}_A)\\&K(|\vec{p}_\mu+\vec{p}_\nu|)\delta^{(3)}(\vec{p}_\delta-(\vec{p}_\alpha-\vec{p}_\mu-\vec{p}_\nu))\delta_{\rho\beta}\delta^{(3)}(\vec{p}_\rho-\vec{p}_\beta)\\&\frac{1}{2m_\alpha}\left[(\vec{p}_\alpha+\vec{p}_\delta)\,\delta_{\delta\alpha}-i\,\langle\delta|\vec{\sigma}|\alpha\rangle\times(\vec{p}_\delta-\vec{p}_\alpha)\right]\cdot\langle\mu\nu|\vec{\sigma}|0\rangle\,.\end{aligned} \tag{E.36}$$

such that this in turn has two terms.

First term

$$\begin{aligned}\mathcal{I}^{j^TKj^T,\delta1}_{\text{spin}-\text{space}}=&\frac{1}{\sqrt{1+\delta_{BC}}}\sum_{m,M_{BC},M_B,M_C}\langle J_{BC}M_{BC}lm|J_TM_T\rangle\,\langle J_BM_BJ_CM_C|J_{BC}M_{BC}\rangle\\&\int d^3K_Bd^3K_Cd^3p_\delta d^3p_\rho d^3p_\mu d^3p_\nu d^3p_\alpha d^3p_\beta\,\delta^{(3)}(\vec{K}-\vec{K}_0)\delta(k-k_0)\frac{Y_{lm}(\hat{k})}{k}\\&\delta^{(3)}(\vec{K}_B-\vec{P}_B)\delta^{(3)}(\vec{K}_C-\vec{P}_C)\delta^{(3)}(\vec{P}_A)\phi_B(\vec{p}_B)\phi_C(\vec{p}_C)\phi_A(\vec{p}_A)\\&K(|\vec{p}_\mu+\vec{p}_\nu|)\delta^{(3)}(\vec{p}_\delta-(\vec{p}_\alpha-\vec{p}_\mu-\vec{p}_\nu))\delta_{\rho\beta}\delta^{(3)}(\vec{p}_\rho-\vec{p}_\beta)\\&\frac{1}{2m_\alpha}\,\delta_{\delta\alpha}\;(\vec{p}_\alpha+\vec{p}_\delta)\cdot\langle\mu\nu|\vec{\sigma}|0\rangle\,,\end{aligned} \tag{E.37}$$

that rewriting

$$\begin{aligned}\mathcal{I}^{j^TKj^T,\delta 1}_{\text{spin}-\text{space}} =& \frac{1}{\sqrt{1+\delta_{BC}}}\frac{1}{2m_\alpha}\sqrt{2^3\pi}\int d^3K_B d^3K_C d^3p_\alpha d^3p_\beta d^3p_\mu d^3p_\nu d^3p_\delta \\ & \delta^{(3)}(\vec{K}-\vec{K}_0)\delta^{(3)}(\vec{K}_B-\vec{P}_B)\delta^{(3)}(\vec{K}_C-\vec{P}_C)\delta^{(3)}(\vec{P}_A)\frac{\delta(k-k_0)}{k} \\ & \delta^{(3)}(\vec{p}_\delta-(\vec{p}_\alpha-\vec{p}_\mu-\vec{p}_\nu))K(|\vec{p}_\mu+\vec{p}_\nu|) \\ & \langle\left[[[\phi_B(\vec{p}_B)(s_\alpha s_\nu)S_B]\,J_B\,[\phi_C(\vec{p}_C)(s_\mu s_\beta)S_C]\,J_C]\,J_{BC}Y_l(\hat{k})\right]J_T| \\ & |\,[[\phi_A(\vec{p}_A)(s_\alpha s_\beta)S_A]\,J_A\,[\mathcal{Y}_1\,(\vec{p}_\alpha+\vec{p}_\delta)\,(s_\mu s_\nu)1]\,0]\,J_A\rangle\,,\end{aligned} \tag{E.38}$$

and decoupling the spin and angular momentum terms following Eq. (E.8) we arrive to

$$\mathcal{I}^{j^TKj^T,\delta 1}_{\text{spin}-\text{space}} = \frac{1}{\sqrt{1+\delta_{BC}}}\frac{1}{2m_\alpha}\sqrt{2^3\pi}\sum_{L_{BC},L,S}\mathcal{J}(A\to BC)\mathcal{E}(A\to BC), \tag{E.39}$$

with $J(A\to BC)$ equal to Eq. (4.19) and

$$\begin{aligned}\mathcal{E}(A\to BC) =& \int d^3K_B d^3K_C d^3p_\alpha d^3p_\beta d^3p_\mu d^3p_\nu d^3p_\delta \\ & \delta^{(3)}(\vec{K}-\vec{K}_0)\delta^{(3)}(\vec{K}_B-\vec{P}_B)\delta^{(3)}(\vec{K}_C-\vec{P}_C)\delta^{(3)}(\vec{P}_A)\frac{\delta(k-k_0)}{k} \\ & \delta^{(3)}(\vec{p}_\delta-(\vec{p}_\alpha-\vec{p}_\mu-\vec{p}_\nu))K(|\vec{p}_\mu+\vec{p}_\nu|) \\ & \langle[[\phi_B(\vec{p}_B)\phi_C(\vec{p}_C)]\,L_{BC}Y_l(\hat{k})]\,L|\,[\phi_A(\vec{p}_A)\mathcal{Y}_1\,(\vec{p}_\alpha+\vec{p}_\delta)]\,L\rangle\,.\end{aligned} \tag{E.40}$$

We proceed in the same way as in the case of the sKs decay model, the only difference is that the term $\mathcal{Y}_1\left(\frac{\vec{p}_\mu-\vec{p}_\nu}{2}\right)$ is changed by $\mathcal{Y}_1\,(\vec{p}_\alpha+\vec{p}_\delta)$. Therefore we have

$$\begin{aligned}\hat{\mathcal{E}}(A\to BC) =& \int d^3k d^3q d^3P\,K(P)\,\frac{\delta(k-k_0)}{k^{l+1}}\exp\left[-\frac{1}{2}(Ap_A^2+Bp_B^2+Cp_C^2)\right] \\ & [[\mathcal{Y}_{L_B}(\vec{p}_B)\mathcal{Y}_{L_C}(\vec{p}_C)]_{L_{BC}}\,\mathcal{Y}_l(\vec{k})]_L\,[\mathcal{Y}_{L_A}(\vec{p}_A)\mathcal{Y}_1(2\vec{p}_A-\vec{P})]_L\,,\end{aligned} \tag{E.41}$$

where the only new term is

$$\begin{aligned}\left[\mathcal{Y}_{L_A}(\vec{p}_A)\mathcal{Y}_1(2\vec{p}_A-\vec{P})\right]_L =& 2\sum_{l_1,\ldots,l_8}\Pi_{1,L_A,L_A-l_1,1-l_3,l_5,l_6,l_7,l_8}C^{L_A}_{l_1}C^{L_A-l_1}_{l_2}C^{1}_{l_3}C^{1-l_3}_{l_4} \\ & B^{l_5}_{l_1,l_3}B^{l_7}_{l_2,l_4}B^{l_8}_{L_A-l_1-l_2,1-l_3-l_4}\left(\frac{2x+1}{2}\right)^{l_1}x^{l_3} \\ & P^{l_1+l_3-l_5}k^{l_2+l_4-l_7}q^{1+L_A-l_1-l_2-l_3-l_4-l_8}\begin{Bmatrix}l_1 & L_A-l_1 & L_A\\ l_3 & 1-l_3 & 1\\ l_5 & l_6 & L\end{Bmatrix} \\ & \begin{Bmatrix}l_2 & L_A-l_1-l_2 & L_A-l_1\\ l_4 & 1-l_3-l_4 & 1-l_3\\ l_7 & l_8 & l_6\end{Bmatrix}\left[\mathcal{Y}_{l_5}(\vec{P})\left[\mathcal{Y}_{l_7}(\vec{k})\mathcal{Y}_{l_8}(\vec{q})\right]_{l_6}\right]_L,\end{aligned} \tag{E.42}$$

reaching the final expression

$$\hat{\mathcal{E}}(A\to BC)=2(4\pi)^2\int dkdqdP\delta(k-k_0)K(P)e^{-Fk^2-Dq^2-\left(\frac{D^2-R^2}{4D}\right)P^2}$$
$$\sum_{l_1,\ldots,l_{21}}(-1)^{l_5+l_{16}+l_{17}+l_{18}+l_{20}-l_{13}}(-i)^{l_{19}+l_{20}}j_{l_{19}}(iGkq)j_{l_{20}}\left[i\left(S-\frac{GR}{2D}\right)kP\right]$$
$$\left(\frac{2x+1}{2}\right)^{l_1}x^{l_3}\left(\frac{2x-1}{2}\right)^{l_9}\left(\frac{\omega_\nu}{\omega_{\alpha\nu}}\right)^{l_{10}}\left(\frac{2x+1}{2}\right)^{l_{11}}\left(\frac{\omega_\mu}{\omega_{\mu\beta}}\right)^{l_{12}}C_{l_1}^{L_A}C_{l_2}^{L_A-l_1}C_{l_3}^{1}$$
$$C_{l_4}^{1-l_3}C_{l_9}^{L_B}C_{l_{10}}^{L_B-l_9}C_{l_{11}}^{L_C}C_{l_{12}}^{L_C-l_{11}}B_{l_1,l_3}^{l_5}B_{l_2,l_4}^{l_7}B_{L_A-l_1-l_2,1-l_3-l_4}^{l_8}B_{l_9,l_{11}}^{l_{13}}B_{l_{10},l_{12}}^{l_{15}}B_{L_B-l_9-l_{10},L_C-l_{11}-l_{12}}^{l_{16}}$$
$$B_{l_{15},l}^{l_{18}}B_{l_{19},l_{20}}^{l_{21}}B_{l_{20},l_{13}}^{l_5}B_{l_{21},l_{18}}^{l_7}B_{l_{19},l_{16}}^{l_8}\Pi_{1,L_A,L_A-l_1,L_B,L_B-l_9,L_C,L_C-l_{11},L_{BC},1-l_3,l_5,l_5,l_6,l_6,l_7,l_7,l_8,l_8}$$
$$\Pi_{l_{13},l_{14},l_{14},l_{15},l_{16},l_{17},l_{17},l_{18},l_{21}}P^{2+l_1+l_3+l_9+l_{11}}k^{1+l_2+l_4+l_{10}+l_{12}}q^{3+L_A+L_B+L_C-l_1-l_2-l_3-l_4-l_9-l_{10}-l_{11}-l_{12}}$$
$$\begin{Bmatrix}l_{14}&l_{13}&L_{BC}\\L&l&l_{17}\end{Bmatrix}\begin{Bmatrix}l_{15}&l_{16}&l_{14}\\l_{17}&l&l_{18}\end{Bmatrix}\begin{Bmatrix}l_6&l_5&L\\l_{13}&l_{17}&l_{20}\end{Bmatrix}\begin{Bmatrix}l_1&L_A-l_1&L_A\\l_3&1-l_3&1\\l_5&l_6&L\end{Bmatrix}\begin{Bmatrix}l_2&L_A-l_1-l_2&L_A-l_1\\l_4&1-l_3-l_4&1-l_3\\l_7&l_8&l_6\end{Bmatrix}$$
$$\begin{Bmatrix}l_9&L_B-l_9&L_B\\l_{11}&L_C-l_{11}&L_C\\l_{13}&l_{14}&L_{BC}\end{Bmatrix}\begin{Bmatrix}l_{10}&L_B-l_9-l_{10}&L_B-l_9\\l_{12}&L_C-l_{11}-l_{12}&L_C-l_{11}\\l_{15}&l_{16}&l_{14}\end{Bmatrix}\begin{Bmatrix}l_{21}&l_{19}&l_{20}\\l_{18}&l_{16}&l_{17}\\l_7&l_8&l_6\end{Bmatrix},\tag{E.43}$$

and for the radial integrals one has

$$\int dkdqdP\delta(k-k_0)K(P)e^{-Fk^2-Dq^2-\left(\frac{D^2-R^2}{4D}\right)P^2}(-i)^{l_{19}+l_{20}}j_{l_{19}}(iGkq)j_{l_{20}}\left[i\left(S-\frac{GR}{2D}\right)kP\right]\times$$
$$\times P^{2+l_1+l_3+l_9+l_{11}}k^{1+l_2+l_4+l_{10}+l_{12}}q^{3+L_A+L_B+L_C-l_1-l_2-l_3-l_4-l_9-l_{10}-l_{11}-l_{12}}$$
$$=k_0^{1+l_2+l_4+l_{10}+l_{12}}e^{-Fk_0^2}\times$$
$$\times\int dq\ q^{3+L_A+L_B+L_C-l_1-l_2-l_3-l_4-l_9-l_{10}-l_{11}-l_{12}}i_{l_{19}}(Gk_0q)e^{-Dq^2}$$
$$\times\int dPK(P)P^{2+l_1+l_3+l_9+l_{11}}i_{l_{20}}\left[\left(S-\frac{GR}{2D}\right)k_0P\right]e^{-\left(\frac{D^2-R^2}{4D}\right)P^2}.\tag{E.44}$$

Second term

$$\mathcal{I}^{j^TKj^T,\delta2}_{\text{spin}-\text{space}}=\frac{1}{\sqrt{1+\delta_{BC}}}\sum_{m,M_{BC},M_B,M_C}\langle J_{BC}M_{BC}lm|J_TM_T\rangle\langle J_BM_BJ_CM_C|J_{BC}M_{BC}\rangle$$
$$\int d^3K_Bd^3K_Cd^3p_\delta d^3p_\rho d^3p_\mu d^3p_\nu d^3p_\alpha d^3p_\beta\,\delta^{(3)}(\vec{K}-\vec{K}_0)\delta(k-k_0)\frac{Y_{lm}(\hat{k})}{k}$$
$$\delta^{(3)}(\vec{K}_B-\vec{P}_B)\delta^{(3)}(\vec{K}_C-\vec{P}_C)\delta^{(3)}(\vec{P}_A)\phi_B(\vec{p}_B)\phi_C(\vec{p}_C)\phi_A(\vec{p}_A)$$
$$K(|\vec{p}_\mu+\vec{p}_\nu|)\delta^{(3)}(\vec{p}_\delta-(\vec{p}_\alpha-\vec{p}_\mu-\vec{p}_\nu))\delta_{\rho\beta}\delta^{(3)}(\vec{p}_\rho-\vec{p}_\beta)$$
$$\frac{1}{2m_\alpha}\left[-i\langle\delta|\vec{\sigma}|\alpha\rangle\times(\vec{p}_\delta-\vec{p}_\alpha)\right]\cdot\langle\mu\nu|\vec{\sigma}|0\rangle,\tag{E.45}$$

which is the same that

$$\begin{aligned}\mathcal{I}^{j^TKj^T,\delta 2}_{\text{spin}-\text{space}} =& \frac{-1}{\sqrt{1+\delta_{BC}}}\frac{1}{2m_\alpha}\sqrt{\frac{2^7\pi}{3}}\sum_{m,M_{BC},M_B,M_C}\langle J_{BC}M_{BC}lm|J_TM_T\rangle\,\langle J_BM_BJ_CM_C|J_{BC}M_{BC}\rangle \\ &\int d^3K_Bd^3K_Cd^3p_\delta d^3p_\rho d^3p_\mu d^3p_\nu d^3p_\alpha d^3p_\beta\,\delta^{(3)}(\vec{K}-\vec{K}_0)\delta(k-k_0)\frac{Y_{lm}(\hat{k})}{k} \\ &\delta^{(3)}(\vec{K}_B-\vec{P}_B)\delta^{(3)}(\vec{K}_C-\vec{P}_C)\delta^{(3)}(\vec{P}_A)\phi_B(\vec{p}_B)\phi_C(\vec{p}_C)\phi_A(\vec{p}_A) \\ &K(|\vec{p}_\mu+\vec{p}_\nu|)\delta^{(3)}(\vec{p}_\delta-(\vec{p}_\alpha-\vec{p}_\mu-\vec{p}_\nu))\delta_{\rho\beta}\delta^{(3)}(\vec{p}_\rho-\vec{p}_\beta) \\ &[\hat{S}_1(\delta\alpha)\otimes\hat{S}_1(\mu\nu)]_1\cdot\mathcal{Y}_1(\vec{p}_\alpha-\vec{p}_\delta),\end{aligned} \tag{E.46}$$

and decoupling the spin and angular momentum terms following Eq. (E.8) and

$$\begin{aligned}&\langle(LS)J_T|\left[\hat{S}_1(\delta\alpha)\otimes\hat{S}_1(\mu\nu)\right]_1\cdot\mathcal{Y}_1(\vec{p}_\alpha-\vec{p}_\delta)|(L_AS_A)J_A\rangle \\ &=\delta_{J_TJ_A}(-1)^{J_A+L_A+S}\begin{Bmatrix}L & L_A & 1\\ S_A & S & J_A\end{Bmatrix}\langle L||\mathcal{Y}_1(\vec{p}_\alpha-\vec{p}_\delta)||L_A\rangle\,\frac{3\sqrt{3}}{2}\Pi_{S_A,S_B,S_C,S}(-1)^{1+S_C} \\ &\sum_x(-1)^x\Pi_{x,x}\begin{Bmatrix}1 & S_A & S\\ S_C & S_B & x\end{Bmatrix}\begin{Bmatrix}\frac{1}{2} & S_A & \frac{1}{2}\\ S_C & \frac{1}{2} & x\end{Bmatrix}\begin{Bmatrix}\frac{1}{2} & \frac{1}{2} & x\\ \frac{1}{2} & \frac{1}{2} & S_B\\ 1 & 1 & 1\end{Bmatrix},\end{aligned} \tag{E.47}$$

with

$$\begin{aligned}&\langle Sm_S|\left[\hat{S}_1(\delta\alpha)\otimes\hat{S}_1(\mu\nu)\right]_1|S_Am_{S_A}\rangle=\frac{3\sqrt{3}}{2}\Pi_{S_A,S_B,S_C,S}(-1)^{1+S_C}(-1)^{S+m_S} \\ &\begin{pmatrix}S & 1 & S_A\\ -m_S & c & m_{S_A}\end{pmatrix}\sum_x(-1)^x\Pi_{x,x}\begin{Bmatrix}1 & S_A & S\\ S_C & S_B & x\end{Bmatrix}\begin{Bmatrix}\frac{1}{2} & S_A & \frac{1}{2}\\ S_C & \frac{1}{2} & x\end{Bmatrix}\begin{Bmatrix}\frac{1}{2} & \frac{1}{2} & x\\ \frac{1}{2} & \frac{1}{2} & S_B\\ 1 & 1 & 1\end{Bmatrix},\end{aligned} \tag{E.48}$$

we arrive to

$$\mathcal{I}^{j^TKj^T,\delta 2}_{\text{spin}-\text{space}}=\frac{-1}{\sqrt{1+\delta_{BC}}}\frac{1}{2m_\alpha}\sqrt{\frac{2^7\pi}{3}}\sum_{L_{BC},L,S}\mathcal{J}(A\to BC)\mathcal{E}(A\to BC), \tag{E.49}$$

where

$$\begin{aligned}\mathcal{J}(A\to BC)=&\delta_{J_TJ_A}\frac{3\sqrt{3}}{2}(-1)^{1+J_A+L_A+S_C+J_{BC}+L+l}\Pi_{J_B,J_C,J_{BC},L_{BC},L,L,S_A,S_B,S_C,S,S} \\ &\begin{Bmatrix}L & L_A & 1\\ S_A & S & J_A\end{Bmatrix}\begin{Bmatrix}S & L_{BC} & J_{BC}\\ l & J_T & L\end{Bmatrix}\begin{Bmatrix}L_B & S_B & J_B\\ L_C & S_C & J_C\\ L_{BC} & S & J_{BC}\end{Bmatrix} \\ &\sum_x(-1)^x\Pi_{x,x}\begin{Bmatrix}1 & S_A & S\\ S_C & S_B & x\end{Bmatrix}\begin{Bmatrix}\frac{1}{2} & S_A & \frac{1}{2}\\ S_C & \frac{1}{2} & x\end{Bmatrix}\begin{Bmatrix}\frac{1}{2} & \frac{1}{2} & x\\ \frac{1}{2} & \frac{1}{2} & S_B\\ 1 & 1 & 1\end{Bmatrix},\end{aligned} \tag{E.50}$$

and

$$\begin{aligned}\mathcal{E}(A\to BC) = \int & d^3K_B d^3K_C d^3p_\alpha d^3p_\beta d^3p_\mu d^3p_\nu d^3p_\delta \\ & \delta^{(3)}(\vec{K}-\vec{K}_0)\delta^{(3)}(\vec{K}_B-\vec{P}_B)\delta^{(3)}(\vec{K}_C-\vec{P}_C)\delta^{(3)}(\vec{P}_A)\frac{\delta(k-k_0)}{k} \\ & \delta^{(3)}(\vec{p}_\delta-(\vec{p}_\alpha-\vec{p}_\mu-\vec{p}_\nu))K(|\vec{p}_\mu+\vec{p}_\nu|) \\ & \langle[[\phi_B(\vec{p}_B)\phi_C(\vec{p}_C)]\,L_{BC}Y_l(\hat{k})]\,L|\,[\phi_A(\vec{p}_A)\mathcal{Y}_1\,(\vec{p}_\alpha-\vec{p}_\delta)]\,L\rangle\,.\end{aligned} \tag{E.51}$$

If one integrates in d^3p_δ the expression of $\mathcal{E}(A\to BC)$ is the same as in the case of j^0Kj^0 decay model.

E.4.2 Term in $\frac{Q_iQ_j}{\vec{Q}^2}$

We have

$$\begin{aligned}\mathcal{I}^{j^TKj^T,Q^2}_{\text{spin}-\text{space}} =& \frac{-1}{\sqrt{1+\delta_{BC}}}\sum_{m,M_{BC},M_B,M_C}\langle J_{BC}M_{BC}lm|J_TM_T\rangle\,\langle J_BM_BJ_CM_C|J_{BC}M_{BC}\rangle \\ & \int d^3K_Bd^3K_Cd^3p_\delta d^3p_\rho d^3p_\mu d^3p_\nu d^3p_\alpha d^3p_\beta\,\delta^{(3)}(\vec{K}-\vec{K}_0)\delta(k-k_0)\frac{Y_{lm}(\hat{k})}{k} \\ & \delta^{(3)}(\vec{K}_B-\vec{P}_B)\delta^{(3)}(\vec{K}_C-\vec{P}_C)\delta^{(3)}(\vec{P}_A)\phi_B(\vec{p}_B)\phi_C(\vec{p}_C)\phi_A(\vec{p}_A) \\ & K(|\vec{p}_\mu+\vec{p}_\nu|)\delta^{(3)}(\vec{p}_\delta-(\vec{p}_\alpha-\vec{p}_\mu-\vec{p}_\nu))\delta_{\rho\beta}\delta^{(3)}(\vec{p}_\rho-\vec{p}_\beta) \\ & \frac{1}{2m_\alpha}\left[(\vec{p}_\alpha-\vec{p}_\delta)\cdot\langle\mu\nu|\vec{\sigma}|0\rangle\right]\left[(\vec{p}_\alpha+\vec{p}_\delta)\cdot(\vec{p}_\alpha-\vec{p}_\delta)\right]\delta_{\delta\alpha},\end{aligned} \tag{E.52}$$

that rewriting

$$\begin{aligned}\mathcal{I}^{j^TKj^T,Q^2}_{\text{spin}-\text{space}} =& \frac{1}{\sqrt{1+\delta_{BC}}}\frac{1}{2m_\alpha}\sqrt{\frac{2^7\pi^3}{3}}\int d^3K_Bd^3K_Cd^3p_\delta d^3p_\mu d^3p_\nu d^3p_\alpha d^3p_\beta \\ & \delta^{(3)}(\vec{K}-\vec{K}_0)\delta^{(3)}(\vec{K}_B-\vec{P}_B)\delta^{(3)}(\vec{K}_C-\vec{P}_C)\delta^{(3)}(\vec{P}_A)\frac{\delta(k-k_0)}{k} \\ & \delta^{(3)}(\vec{p}_\delta-(\vec{p}_\alpha-\vec{p}_\mu-\vec{p}_\nu))\frac{K(|\vec{p}_\mu+\vec{p}_\nu|)}{|\vec{p}_\mu+\vec{p}_\nu|^2} \\ & \left\langle\left[[\phi_B(\vec{p}_B)(s_\alpha s_\nu)S_B]\,J_B\,[\phi_C(\vec{p}_C)(s_\mu s_\beta)S_C]\,J_C\right]\,J_{BC}Y_l(\hat{k})\right]\,J_T| \\ & [\mathcal{Y}_1\,(\vec{p}_\alpha+\vec{p}_\delta)\otimes\mathcal{Y}_1\,(\vec{p}_\mu+\vec{p}_\nu)]_0\,|\,[[\phi_A(\vec{p}_A)(s_\alpha s_\beta)S_A]\,J_A\,[\mathcal{Y}_1\,(\vec{p}_\mu+\vec{p}_\nu)\,(s_\mu s_\nu)1]\,0]\,J_A\rangle\,,\end{aligned} \tag{E.53}$$

and decoupling the spin and angular momentum terms following Eq. (E.8) we arrive to

$$\mathcal{I}^{j^TKj^T,Q^2}_{\text{spin}-\text{space}} = \frac{1}{\sqrt{1+\delta_{BC}}}\frac{1}{2m_\alpha}\sqrt{\frac{2^7\pi^3}{3}}\sum_{L_{BC},L,S}\mathcal{J}(A\to BC)\mathcal{E}(A\to BC), \tag{E.54}$$

with $J(A \to BC)$ equal to Eq. (4.19) and

$$\begin{aligned}\mathcal{E}(A \to BC) = \int & d^3K_B d^3K_C d^3p_\alpha d^3p_\beta d^3p_\mu d^3p_\nu d^3p_\delta \\ & \delta^{(3)}(\vec{K} - \vec{K}_0)\delta^{(3)}(\vec{K}_B - \vec{P}_B)\delta^{(3)}(\vec{K}_C - \vec{P}_C)\delta^{(3)}(\vec{P}_A)\frac{\delta(k-k_0)}{k} \\ & \delta^{(3)}(\vec{p}_\delta - (\vec{p}_\alpha - \vec{p}_\mu - \vec{p}_\nu))\frac{K(|\vec{p}_\mu + \vec{p}_\nu|)}{|\vec{p}_\mu + \vec{p}_\nu|^2} \\ & \langle [[\phi_B(\vec{p}_B)\phi_C(\vec{p}_C)]\, L_{BC} Y_l(\hat{k})]\, L|\, [\mathcal{Y}_1(\vec{p}_\alpha + \vec{p}_\delta)\, \mathcal{Y}_1(\vec{p}_\mu + \vec{p}_\nu)]\, 0|\, [\phi_A(\vec{p}_A)\mathcal{Y}_1(\vec{p}_\mu + \vec{p}_\nu)]\, L\rangle\,. \end{aligned} \tag{E.55}$$

We proceed in the same way as in the case of the sKs decay model. However, the terms $[[\mathcal{Y}_1(\vec{p}_\alpha + \vec{p}_\delta)\, \mathcal{Y}_1(\vec{p}_\mu + \vec{p}_\nu)]\, 0]$ and $\mathcal{Y}_1(\vec{p}_\mu + \vec{p}_\nu)$ appear in this case. Therefore we have

$$\begin{aligned}\hat{\mathcal{E}}(A \to BC) = \int & d^3k d^3q d^3P\, \frac{K(P)}{P^2}\, \frac{\delta(k-k_0)}{k^{l+1}} \exp\left[-\frac{1}{2}(Ap_A^2 + Bp_B^2 + Cp_C^2)\right] \\ & \left[[\mathcal{Y}_{L_B}(\vec{p}_B)\mathcal{Y}_{L_C}(\vec{p}_C)]_{L_{BC}}\, \mathcal{Y}_l(\vec{k})\right]_L \left[\mathcal{Y}_1(2\vec{p}_A - \vec{P})\mathcal{Y}_1(\vec{P})\right]_0 \left[\mathcal{Y}_{L_A}(\vec{p}_A)\mathcal{Y}_1(\vec{P})\right]_L, \end{aligned} \tag{E.56}$$

where the only new term is

$$\left[\mathcal{Y}_1(2\vec{p}_A - \vec{P})\mathcal{Y}_1(\vec{P})\right]_0 = 2\sum_{l_1=0}^{1}\sum_{l_2=0}^{1-l_1} C_{l_1}^1 C_{l_2}^{1-l_1} B_{l_1,1}^{1-l_1} x^{l_1} P^{2l_1} \left[\mathcal{Y}_{1-l_1}(\vec{P})\left[\mathcal{Y}_{l_2}(\vec{k})\mathcal{Y}_{1-l_1-l_2}(\vec{q})\right]_{1-l_1}\right]_0, \tag{E.57}$$

reaching the final expression

$$\begin{aligned}\hat{\mathcal{E}}(A \to BC) = {} & 2(4\pi)^2 \int dk dq dP \delta(k-k_0) K(P) e^{-Fk^2 - Dq^2 - \left(\frac{D^2-R^2}{4D}\right)P^2} \\ & \sum_{l_1,\ldots,l_{22}} (-1)^{L_A+L+l_{13}+l_{14}+l_{15}+l_{17}-l_3-l_4-l_{10}} (-i)^{l_{16}+l_{17}} j_{l_{16}}(iGkq) j_{l_{17}}\left[i\left(S - \frac{GR}{2D}\right)kP\right] \\ & \left(\frac{2x+1}{2}\right)^{l_1} x^{l_4} \left(\frac{2x-1}{2}\right)^{l_6} \left(\frac{\omega_\nu}{\omega_{\alpha\nu}}\right)^{l_7} \left(\frac{2x+1}{2}\right)^{l_8} \left(\frac{\omega_\mu}{\omega_{\mu\beta}}\right)^{l_9} C_{l_1}^{L_A} C_{l_2}^{L_A-l_1} C_{l_4}^1 C_{l_5}^{1-l_4} C_{l_6}^{L_B} C_{l_7}^{L_B-l_6} C_{l_8}^{L_C} \\ & C_{l_9}^{L_C-l_8} B_{l_1,1}^{l_3} B_{l_4,1}^{1-l_4} B_{l_6,l_8}^{l_{10}} B_{l_7,l_9}^{l_{12}} B_{L_B-l_6-l_7,L_C-l_8-l_9}^{l_{13}} B_{l_{12},l}^{l_{15}} B_{l_{16},l_{17}}^{l_{18}} B_{l_{17},l_{10}}^{l_{19}} B_{l_{18},l_{15}}^{l_{21}} B_{l_{16},l_{13}}^{l_{22}} B_{1-l_4,l_3}^{l_{19}} B_{l_5,l_2}^{l_{21}} \\ & B_{1-l_4-l_5,L_A-l_1-l_2}^{l_{22}} P^{2+l_1+l_4+l_6+l_8} k^{1+l_2+l_5+l_7+l_9} q^{3+L_A+L_B+L_C-l_1-l_2-l_4-l_5-l_6-l_7-l_8-l_9} \\ & \Pi_{L_A,L_A-l_1,L_B,L_B-l_6,L_C,L_C-l_8,L_{BC},l_3,l_{10},l_{11},l_{11},l_{12},l_{13},l_{14},l_{14},l_{15},l_{18},l_{19},l_{19},l_{20},l_{20},l_{21},l_{21},l_{22},l_{22}} \\ & \begin{Bmatrix} l_1 & L_A-l_1 & L_A \\ L & 1 & l_3 \end{Bmatrix} \begin{Bmatrix} l_{11} & l_{10} & L_{BC} \\ L & l & l_{14} \end{Bmatrix} \begin{Bmatrix} l_{12} & l_{13} & l_{11} \\ l_{14} & l & l_{15} \end{Bmatrix} \begin{Bmatrix} l_{20} & l_{19} & L \\ l_{10} & l_{14} & l_{17} \end{Bmatrix} \begin{Bmatrix} l_{20} & l_{19} & L \\ l_3 & L_A-l_1 & 1-l_4 \end{Bmatrix} \\ & \begin{Bmatrix} l_6 & L_B-l_6 & L_B \\ l_8 & L_C-l_8 & L_C \\ l_{10} & l_{11} & L_{BC} \end{Bmatrix} \begin{Bmatrix} l_7 & L_B-l_6-l_7 & L_B-l_6 \\ l_9 & L_C-l_8-l_9 & L_C-l_8 \\ l_{12} & l_{13} & l_{11} \end{Bmatrix} \begin{Bmatrix} l_{18} & l_{16} & l_{17} \\ l_{15} & l_{13} & l_{14} \\ l_{21} & l_{22} & l_{20} \end{Bmatrix} \begin{Bmatrix} l_5 & 1-l_4-l_5 & 1-l_4 \\ l_2 & L_A-l_1-l_2 & L_A-l_1 \\ l_{21} & l_{22} & l_{20} \end{Bmatrix}, \end{aligned} \tag{E.58}$$

and for the radial integrals one has

$$\begin{aligned}
&\int dkdqdP\delta(k-k_0)K(P)e^{-Fk^2-Dq^2-\left(\frac{D^2-R^2}{4D}\right)P^2}(-i)^{l_{16}+l_{17}}j_{l_{16}}(iGkq)j_{l_{17}}\left[i\left(S-\frac{GR}{2D}\right)kP\right]\times\\
&\times P^{2+l_1+l_4+l_6+l_8}k^{1+l_2+l_5+l_7+l_9}q^{3+L_A+L_B+L_C-l_1-l_2-l_4-l_5-l_6-l_7-l_8-l_9}\\
&=k_0^{1+l_2+l_5+l_7+l_9}e^{-Fk_0^2}\times\\
&\quad\times\int dq\; q^{3+L_A+L_B+L_C-l_1-l_2-l_4-l_5-l_6-l_7-l_8-l_9}i_{l_{16}}(Gk_0q)e^{-Dq^2}\\
&\quad\times\int dPK(P)P^{2+l_1+l_4+l_6+l_8}i_{l_{17}}\left[\left(S-\frac{GR}{2D}\right)k_0P\right]e^{-\left(\frac{D^2-R^2}{4D}\right)P^2}.
\end{aligned}\tag{E.59}$$

E.5 Charge conjugation

The meson state is given by

$$\left|p_{12}JM;LSf_1\bar{f}_2\right\rangle=\sum_{M_LM_S}\langle LM_LSM_S|JM\rangle\,R(p_{12})Y_{LM_L}(\hat{p}_{12})\left|s_1s_2;SM_S\right\rangle a^\dagger_{f_1}(\vec{p}_1)b^\dagger_{f_2}(\vec{p}_2)\left|0\right\rangle,\tag{E.60}$$

where p_{12} is the relative momentum between p_1 and p_2, the momentum of the quark and antiquark, respectively. The C-parity transformation is given by

$$\mathcal{C}\left|p_{12}JM;LSf_1\bar{f}_2\right\rangle=\sum_{M_LM_S}\langle LM_LSM_S|JM\rangle\,R(p_{12})Y_{LM_L}(\hat{p}_{12})\left|s_1s_2;SM_S\right\rangle b^\dagger_{f_1}(\vec{p}_1)a^\dagger_{f_2}(\vec{p}_2)\left|0\right\rangle.\tag{E.61}$$

We can change the order of the particles so

$$\begin{aligned}
Y_{LM_L}(\hat{p}_{12})&=Y_{LM_L}(-\hat{p}_{21})=(-1)^LY_{LM_L}(\hat{p}_{21}),\\
\left|s_1s_2;SM_S\right\rangle&=(-1)^{S-s_1-s_2}\left|s_2s_1;SM_S\right\rangle,\\
b^\dagger_{f_1}(\vec{p}_1)a^\dagger_{f_2}(\vec{p}_2)\left|0\right\rangle&=-a^\dagger_{f_2}(\vec{p}_2)b^\dagger_{f_1}(\vec{p}_1)\left|0\right\rangle,
\end{aligned}\tag{E.62}$$

and arrive to

$$\begin{aligned}
\mathcal{C}\left|p_{12}JM;LSf_1\bar{f}_2\right\rangle=&(-1)^{1+L+S-s_1-s_2}\sum_{M_LM_S}\langle LM_LSM_S|JM\rangle\times\\
&\times R(p_{21})Y_{LM_L}(\hat{p}_{21})\left|s_2s_1;SM_S\right\rangle b^\dagger_{f_2}(\vec{p}_2)a^\dagger_{f_1}(\vec{p}_1)\left|0\right\rangle\\
=&\left|p_{21}JM;LS\bar{f}_2f_1\right\rangle.
\end{aligned}\tag{E.63}$$

If the two flavors are the same $f_1=\bar{f}_2=f$ then

$$\mathcal{C}\left|pJM;LSf\bar{f}\right\rangle=(-1)^{L+S}\left|pJM;LS\bar{f}f\right\rangle,\tag{E.64}$$

since $2s-1$ is even.

The two meson state can be written as follow

$$\begin{aligned}
\left|AB;J_TM_TJ_{AB}l\right\rangle=&\sum_{M_A,M_B,M_{AB},m_l}\langle lm_lJ_{AB}M_{AB}|J_TM_T\rangle\,\langle J_AM_AJ_BM_B|J_{AB}M_{AB}\rangle\times\\
&\times R_{AB}(p_{1234})Y_{lm_l}(\hat{p}_{1234})\left|p_{12}J_AM_A;L_AS_Af_1\bar{f}_2\right\rangle\otimes\left|p_{34}J_BM_B;L_BS_Bf_3\bar{f}_4\right\rangle,
\end{aligned}\tag{E.65}$$

where $p_{1234} = \frac{1}{2}(p_1 + p_2 - p_3 - p_4)$. So C-Parity gives

$$\begin{aligned}\mathcal{C}\left|AB; J_T M_T J_{AB} l\right\rangle = & \sum_{M_A, M_B, M_{AB}, m_l} \left\langle l m_l J_{AB} M_{AB} | J_T M_T \right\rangle \left\langle J_A M_A J_B M_B | J_{AB} M_{AB} \right\rangle \times \\ & \times R_{AB}(p_{1234}) Y_{l m_l}(\hat{p}_{1234}) \times \\ & \times \left(\mathcal{C}\left|p_{12} J_A M_A; L_A S_A f_1 \bar{f}_2\right\rangle\right) \otimes \left(\mathcal{C}\left|p_{34} J_B M_B; L_B S_B f_3 \bar{f}_4\right\rangle\right) \\ = & \sum_{M_A, M_B, M_{AB}, m_l} \left\langle l m_l J_{AB} M_{AB} | J_T M_T \right\rangle \left\langle J_A M_A J_B M_B | J_{AB} M_{AB} \right\rangle \times \\ & \times (-1)^{L_A + S_A + L_B + S_B} R_{AB}(p_{1234}) Y_{l m_l}(\hat{p}_{1234}) \times \\ & \times \left|p_{21} J_A M_A; L_A S_A f_2 \bar{f}_1\right\rangle \otimes \left|p_{43} J_B M_B; L_B S_B f_4 \bar{f}_3\right\rangle . \end{aligned} \tag{E.66}$$

We can exchange the meson states without an additional phase since we need four fermion exchanges, so

$$\begin{aligned}\mathcal{C}\left|AB; J_T M_T J_{AB} l\right\rangle = & \sum_{M_A, M_B, M_{AB}, m_l} \left\langle l m_l J_{AB} M_{AB} | J_T M_T \right\rangle \left\langle J_A M_A J_B M_B | J_{AB} M_{AB} \right\rangle \times \\ & \times (-1)^{L_A + S_A + L_B + S_B} R_{AB}(p_{1234}) Y_{l m_l}(\hat{p}_{1234}) \times \\ & \times \left|p_{43} J_B M_B; L_B S_B f_4 \bar{f}_3\right\rangle \otimes \left|p_{21} J_A M_A; L_A S_A f_2 \bar{f}_1\right\rangle , \end{aligned} \tag{E.67}$$

and now

$$\begin{aligned} R_{AB}(p_{1234}) Y_{l m_l}(\hat{p}_{1234}) &= (-1)^l R_{BA}(p_{4321}) Y_{l m_l}(\hat{p}_{4321}), \\ \left\langle J_A M_A J_B M_B | J_{AB} M_{AB} \right\rangle &= (-1)^{J_{AB} - J_A - J_B} \left\langle J_B M_B J_A M_A | J_{BA} M_{BA} \right\rangle , \end{aligned} \tag{E.68}$$

where $R_{AB} \equiv R_{BA}$, $J_{AB} \equiv J_{BA}$ and $M_{AB} \equiv M_{BA}$, and so

$$\begin{aligned}\mathcal{C}\left|AB; J_T M_T J_{AB} l\right\rangle = & \sum_{M_A, M_B, M_{AB}, m_l} \left\langle l m_l J_{BA} M_{BA} | J_T M_T \right\rangle \left\langle J_B M_B J_A M_A | J_{BA} M_{BA} \right\rangle \times \\ & \times (-1)^{L_A + S_A + L_B + S_B + J_{AB} - J_A - J_B + l} R_{BA}(p_{4321}) Y_{l m_l}(\hat{p}_{4321}) \times \\ & \times \left|p_{43} J_B M_B; L_B S_B f_4 \bar{f}_3\right\rangle \otimes \left|p_{21} J_A M_A; L_A S_A f_2 \bar{f}_1\right\rangle \\ = & (-1)^{L_A + S_A + L_B + S_B + J_{AB} - J_A - J_B + l} \left|BA; J_T M_T J_{BA} l\right\rangle . \end{aligned} \tag{E.69}$$

Notice that in PDG mesons are $q\bar{q}$ but anti-mesons are $\bar{q}q$, so $D(c\bar{n})$ and $\bar{D}(\bar{c}n)$. In this convention the phase does not include $(-1)^{L_A + S_A + L_B + S_B}$. Therefore, for D and D^* in $l = 0$ we have

$$\begin{aligned}\mathcal{C}\left(\frac{1}{\sqrt{2}}(D(c\bar{n})\bar{D}^*(n\bar{c}) - D^*(c\bar{n})\bar{D}(n\bar{c}))\right) &= +\frac{1}{\sqrt{2}}\left(D(c\bar{n})\bar{D}^*(n\bar{c}) - D^*(c\bar{n})\bar{D}(n\bar{c})\right), \\ \mathcal{C}\left(\frac{1}{\sqrt{2}}(D(c\bar{n})\bar{D}^*(\bar{c}n) + D^*(c\bar{n})\bar{D}(\bar{c}n))\right) &= -\frac{1}{\sqrt{2}}\left(D(c\bar{n})\bar{D}^*(\bar{c}n) + D^*(c\bar{n})\bar{D}(\bar{c}n)\right). \end{aligned} \tag{E.70}$$

Appendix F

Matrix elements of weak decays

F.1 Semileptonic decays: $B \to D^{**} l \nu_l$

We are going to study the semileptonic decays of the B (B or B_s) meson into orbitally excited charmed mesons. In the decay we have a $\bar{b} \to \bar{c}$ transition at the quark level and we need to evaluate the hadronic matrix elements of the weak current

$$J_\mu^{bc}(0) = \bar{\psi}_b(0)\gamma_\mu(I - \gamma_5)\psi_c(0). \tag{F.1}$$

Following Ref. [240], the hadronic matrix elements can be parametrized in terms of form factors as

$$\begin{aligned}
&\langle D(0^+), \vec{P}_D | J_\mu^{bc}(0) | B(0^-), \vec{P}_B \rangle = P_\mu F_+(q^2) + q_\mu F_-(q^2), \\
&\langle D(1^+), \lambda \vec{P}_D | J_\mu^{bc}(0) | B(0^-), \vec{P}_B \rangle = \frac{-1}{m_B + m_D} \epsilon_{\mu\nu\alpha\beta} \epsilon_{(\lambda)}^{\nu *}(\vec{P}_D) P^\alpha q^\beta A(q^2) \\
&- i \left\{ (m_B - m_D) \epsilon_{(\lambda)\mu}^*(\vec{P}_D) V_0(q^2) - \frac{P \cdot \epsilon_{(\lambda)}^*(\vec{P}_D)}{m_B + m_D} \left[P_\mu V_+(q^2) + q_\mu V_-(q^2) \right] \right\}, \\
&\langle D(2^+), \lambda \vec{P}_D \left| J_\mu^{bc}(0) \right| B(0^-) \vec{P}_B \rangle = \epsilon_{\mu\nu\alpha\beta} \epsilon_{(\lambda)}^{\nu\delta *}(\vec{P}_D) P_\delta P^\alpha q^\beta T_4(q^2) \\
&- i \left\{ \epsilon_{(\lambda)\mu\delta}^*(\vec{P}_D) P^\delta T_1(q^2) + P^\nu P^\delta \epsilon_{(\lambda)\nu\delta}^*(\vec{P}_D) \left[P_\mu T_2(q^2) + q_\mu T_3(q^2) \right] \right\}.
\end{aligned} \tag{F.2}$$

In the expressions above, $P = P_B + P_D$ and $q = P_B - P_D$, P_B and P_D being the meson four-momenta. The meson masses are m_B and m_D, λ is the spin proyection in the meson center-of-mass, $\epsilon^{\mu\nu\alpha\beta}$ is the fully antisymmetric tensor, for which the convention $\epsilon^{0123} = +1$ is taken, and $\epsilon_{(\lambda)\mu}(\vec{P})$ and $\epsilon_{(\lambda)\mu\nu}(\vec{P})$ are the polarizations of vector and tensor mesons, respectively. The meson states in the Lorentz decompositions of Eq. (F.2) are normalized such that

$$\langle M, \lambda' \vec{P}\,' | M, \lambda \vec{P} \rangle = \delta_{\lambda',\lambda} (2\pi)^3 2 E_M(\vec{P}) \delta(\vec{P}' - \vec{P}), \tag{F.3}$$

where $E_M(\vec{P})$ is the energy of the M meson with three-momentum $\vec{P}$.

The form factors will be evaluated in the center of mass of the 0^- meson, taking $\vec{q}$ in the z-direction, so that $\vec{P}_B = \vec{0}$ and $\vec{P}_D = -\vec{q} = -|\vec{q}|\vec{k}$, with $\vec{k}$ representing the unit vector in the z-direction. We have taken the phases of the states such that all form factors are real. F_+, F_-, A, V_0, V_+, V_- and T_1 are dimensionless, whereas T_2, T_3

and T_4 have dimension of E^{-2}. Defining the vector $V^\mu_\lambda(|\vec{q}|)$ and axial $A^\mu_\lambda(|\vec{q}|)$ matrix elements such that

$$\begin{aligned} V^\mu_\lambda(|\vec{q}|) &= \langle M_F, \lambda - |\vec{q}|\vec{k}| J^{bc\mu}_V(0)|M_I, \vec{0}\rangle \,, \\ A^\mu_\lambda(|\vec{q}|) &= \langle M_F, \lambda - |\vec{q}|\vec{k}| J^{bc\mu}_A(0)|M_I, \vec{0}\rangle \,, \end{aligned} \tag{F.4}$$

we have for a $0^- \to 0^+$ decay, that the form factors are given in terms of vector and axial matrix elements as

$$\begin{aligned} F_+(q^2) &= -\frac{1}{2m_B}\left[A^0(|\vec{q}|) + \frac{A^3(|\vec{q}|)}{|\vec{q}|}(E_D(-\vec{q}) - m_B)\right], \\ F_-(q^2) &= -\frac{1}{2m_B}\left[A^0(|\vec{q}|) + \frac{A^3(|\vec{q}|)}{|\vec{q}|}(E_D(-\vec{q}) + m_B)\right]. \end{aligned} \tag{F.5}$$

In the case of a $0^- \to 1^+$ transition, the corresponding expressions for the form factors are

$$\begin{aligned} A(q^2) &= -\frac{i}{\sqrt{2}}\frac{m_B + m_D}{m_B|\vec{q}|}A^1_{\lambda=-1}(|\vec{q}|), \\ V_+(q^2) &= +i\frac{m_B + m_D}{2m_B}\frac{m_D}{|\vec{q}|m_B}\left\{V^0_{\lambda=0}(|\vec{q}|) - \frac{m_B - E_D(-\vec{q})}{|\vec{q}|}V^3_{\lambda=0}(|\vec{q}|)\right. \\ &\quad \left. +\sqrt{2}\,\frac{m_B E_D(-\vec{q}) - m_D^2}{|\vec{q}|m_D}V^1_{\lambda=-1}(|\vec{q}|)\right\}, \\ V_-(q^2) &= -i\frac{m_B + m_D}{2m_B}\frac{m_D}{|\vec{q}|m_B}\left\{-V^0_{\lambda=0}(|\vec{q}|) - \frac{m_B + E_D(-\vec{q})}{|\vec{q}|}V^3_{\lambda=0}(|\vec{q}|)\right. \\ &\quad \left. +\sqrt{2}\,\frac{m_B E_D(-\vec{q}) + m_D^2}{|\vec{q}|m_D}V^1_{\lambda=-1}(|\vec{q}|)\right\}, \\ V_0(q^2) &= +i\sqrt{2}\,\frac{1}{m_B - m_D}V^1_{\lambda=-1}(|\vec{q}|). \end{aligned} \tag{F.6}$$

Finally, the form factors for a $0^- \to 2^+$ transition are given by the relations

$$\begin{aligned} T_1(q^2) &= -i\frac{2m_D}{m_B|\vec{q}|}A^1_{T\lambda=+1}(|\vec{q}|), \\ T_2(q^2) &= +i\frac{1}{2m_B^3}\left\{-\sqrt{\frac{3}{2}}\frac{m_D^2}{|\vec{q}|^2}A^0_{T\lambda=0}(|\vec{q}|) - \sqrt{\frac{3}{2}}\frac{m_D^2}{|\vec{q}|^3}(E_D(-\vec{q}) - m_B)A^3_{T\lambda=0}(|\vec{q}|)\right. \\ &\quad \left. +\frac{2m_D}{|\vec{q}|}\left(1 - \frac{E_D(-\vec{q})(E_D(-\vec{q}) - m_B)}{|\vec{q}|^2}\right)A^1_{T\lambda=+1}(|\vec{q}|)\right\}, \end{aligned}$$

$$
\begin{aligned}
T_3(q^2) = &+ i\frac{1}{2m_B^3}\Bigg\{ -\sqrt{\frac{3}{2}}\frac{m_D^2}{|\vec{q}|^2}A^0_{T\lambda=0}(|\vec{q}|) - \sqrt{\frac{3}{2}}\frac{m_D^2}{|\vec{q}|^3}(E_D(-\vec{q})+m_B)A^3_{T\lambda=0}(|\vec{q}|) \\
&+ \frac{2m_D}{|\vec{q}|}\left(1 - \frac{E_D(-\vec{q})(E_D(-\vec{q})+m_B)}{|\vec{q}|^2}\right)A^1_{T\lambda=+1}(|\vec{q}|)\Bigg\}, \\
T_4(q^2) = &+ i\frac{m_D}{m_B^2|\vec{q}|^2}V^1_{T\lambda=+1}(|\vec{q}|).
\end{aligned}
\tag{F.7}
$$

The CQM evaluation of the vector and axial matrix elements, $V^\mu_\lambda(|\vec{q}|)$ and $A^\mu_\lambda(|\vec{q}|)$, can be found in the next Section.

For a B meson at rest and neglecting the neutrino mass, we have the double differential decay width [240]

$$
\frac{d^2\Gamma}{dq^2dx_l} = \frac{G_F^2}{64m_B^2}\frac{|V_{bc}|^2}{8\pi^3}\frac{\lambda^{1/2}(q^2,m_B^2,m_D^2)}{2m_B}\frac{q^2-m_l^2}{q^2}\mathcal{H}_{\alpha\beta}(P_B,P_D)\mathcal{L}^{\alpha\beta}(p_l,p_\nu), \tag{F.8}
$$

where x_l is the cosine of the angle between the final meson momentum and the momentum of the final charged lepton measured in the lepton-neutrino center-of-mass frame (CMF). $G_F = 1.16637(1)\times 10^{-5}\,\mathrm{GeV}^{-2}$ is the Fermi constant [78], m_l is the charged lepton mass, $\lambda(a,b,c) = (a+b-c)^2 - 4ab$ and V_{bc} is the bc element of the CKM matrix for which we use $V_{bc} = 0.0413$. $\mathcal{H}_{\alpha\beta}$ and $\mathcal{L}^{\alpha\beta}$ represent the hadron and lepton tensors. P_B, P_D, p_l and p_ν are the meson and lepton momenta.

The quantity $\mathcal{H}_{\alpha\beta}(P_B,P_D)\mathcal{L}^{\alpha\beta}(p_l,p_\nu)$ is a scalar and to evaluate it we have chosen $\vec{P}_D$ along the negative z-axis. This implies also that the CMF of the final leptons moves in the positive z-direction. Furthermore we follow Ref. [241] and introduce helicity components for the hadron and lepton tensors. For that purpose we rewrite

$$
\mathcal{H}_{\alpha\beta}(P_B,P_D)\mathcal{L}^{\alpha\beta}(p_l,p_\nu) = \mathcal{H}^{\sigma\rho}(P_B,P_D)g_{\sigma\alpha}g_{\rho\beta}\mathcal{L}^{\alpha\beta}(p_l,p_\nu), \tag{F.9}
$$

and use

$$
g_{\mu\nu} = \sum_{r=t,\pm1,0} g_{rr}\epsilon_{(r)\mu}(q)\epsilon^*_{(r)\nu}(q), \quad g_{tt} = 1, \quad g_{\pm1,0} = -1, \tag{F.10}
$$

with $\epsilon^\mu_{(t)}(q) = q^\mu/q^2$ and where the $\epsilon_{(r)}(q)$, $r = \pm1,0$ are the polarization vectors for an on-shell vector particle with four-momentum q and helicity r. Defining helicity components for the hadron and lepton tensors as

$$
\begin{aligned}
\mathcal{H}_{rs}(P_B,P_D) &= \epsilon^*_{(r)\sigma}(q)\mathcal{H}^{\sigma\rho}(P_B,P_D)\epsilon_{(s)\rho}(q), \\
\mathcal{L}_{rs}(p_l,p_\nu) &= \epsilon_{(r)\alpha}(q)\mathcal{L}^{\alpha\beta}(p_l,p_\nu)\epsilon^*_{(s)\beta}(q),
\end{aligned}
\tag{F.11}
$$

we have that

$$
\mathcal{H}_{\alpha\beta}(P_B,P_D)\mathcal{L}^{\alpha\beta}(p_l,p_\nu) = \sum_{r=t,\pm1,0}\sum_{s=t,\pm1,0} g_{rr}g_{ss}\mathcal{H}_{rs}(P_B,P_D)\mathcal{L}_{rs}(p_l,p_\nu). \tag{F.12}
$$

The only helicity components of the lepton tensor that we need are the following

$$\begin{aligned}
\mathcal{L}_{tt}(p_l, p_\nu) &= 4\frac{m_l^2(q^2 - m_l^2)}{q^2}, \\
\mathcal{L}_{t0}(p_l, p_\nu) &= \mathcal{L}_{0t}(p_l, p_\nu) = -4x_l\frac{m_l^2(q^2 - m_l^2)}{q^2}, \\
\mathcal{L}_{+1+1}(p_l, p_\nu) &= (q^2 - m_l^2)\left(4(1 \pm x_l) - 2(1 - x_l^2)\frac{q^2 - m_l^2}{q^2}\right), \\
\mathcal{L}_{-1-1}(p_l, p_\nu) &= (q^2 - m_l^2)\left(4(1 \mp x_l) - 2(1 - x_l^2)\frac{q^2 - m_l^2}{q^2}\right), \\
\mathcal{L}_{00}(p_l, p_\nu) &= 4(q^2 - m_l^2)\left(1 - x_l^2\,\frac{q^2 - m_l^2}{q^2}\right),
\end{aligned} \tag{F.13}$$

where $\mp$ signs correspond, respectively, to decays into $l^-\bar{\nu}_l$ and $l^+\nu_l$. As for the nonzero helicity components, $\mathcal{H}_{rs}$, of the hadron tensor

1. Case $0^- \to 0^+$

$$\begin{aligned}
\mathcal{H}_{tt}(P_B, P_D) =& \left[\frac{m_B^2 - m_D^2}{\sqrt{q^2}}F_+(q^2) + \sqrt{q^2}\,F_-(q^2)\right]^2, \\
\mathcal{H}_{t0}(P_B, P_D) =& \mathcal{H}_{0t}(P_B, P_D) = \lambda^{1/2}(q^2, m_B^2, m_D^2)\left[\frac{m_B^2 - m_D^2}{q^2}F_+^2(q^2) + F_+(q^2)F_-(q^2)\right], \\
\mathcal{H}_{00}(P_B, P_D) =& \frac{\lambda(q^2, m_B^2, m_D^2)}{q^2}F_+^2(q^2).
\end{aligned} \tag{F.14}$$

2. Case $0^- \to 1^+$

$$\begin{aligned}
\mathcal{H}_{tt}(P_B, P_D) =& \frac{\lambda(q^2, m_B^2, m_D^2)}{4m_D^2 q^2}\left[(m_B - m_D)(V_0(q^2) - V_+(q^2)) - \frac{q^2}{m_B + m_D}V_-(q^2)\right]^2, \\
\mathcal{H}_{t0}(P_B, P_D) =& \mathcal{H}_{0t}(P_B, P_D) \\
=& \frac{\lambda^{1/2}(q^2, m_B^2, m_D^2)}{2m_D\sqrt{q^2}}\left[(m_B - m_D)(V_0(q^2) - V_+(q^2)) - \frac{q^2}{m_B + m_D}V_-(q^2)\right] \\
&\times\left[(m_B - m_D)\frac{m_B^2 - q^2 - m_D^2}{2m_D\sqrt{q^2}}V_0(q^2) - \frac{\lambda(q^2, m_B^2, m_D^2)}{2m_D\sqrt{q^2}}\frac{V_+(q^2)}{m_B + m_D}\right], \\
\mathcal{H}_{+1+1}(P_B, P_D) =& \left[\frac{\lambda^{1/2}(q^2, m_B^2, m_D^2)}{m_B + m_D}A(q^2) + (m_B - m_D)V_0(q^2)\right]^2, \\
\mathcal{H}_{-1-1}(P_B, P_D) =& \left[-\frac{\lambda^{1/2}(q^2, m_B^2, m_D^2)}{m_B + m_D}A(q^2) + (m_B - m_D)V_0(q^2)\right]^2, \\
\mathcal{H}_{00}(P_B, P_D) =& \left[(m_B - m_D)\frac{m_B^2 - q^2 - m_D^2}{2m_D\sqrt{q^2}}V_0(q^2) - \frac{\lambda(q^2, m_B^2, m_D^2)}{2m_D\sqrt{q^2}}\frac{V_+(q^2)}{m_B + m_D}\right]^2.
\end{aligned} \tag{F.15}$$

3. Case $0^- \to 2^+$

$$\begin{aligned}
\mathcal{H}_{tt}(P_B,P_D) =& \frac{\lambda^2(q^2,m_B^2,m_D^2)}{24m_D^4q^2}\left[T_1(q^2)+(m_B^2-m_D^2)T_2(q^2)+q^2T_3(q^2)\right]^2,\\
\mathcal{H}_{t0}(P_B,P_D) =& \mathcal{H}_{0t}(P_B,P_D) = \frac{\lambda^{3/2}(q^2,m_B^2,m_D^2)}{24m_D^4q^2}\left[T_1(q^2)+(m_B^2-m_D^2)T_2(q^2)+q^2T_3(q^2)\right]\\
&\times\left[(m_B^2-q^2-m_D^2)T_1(q^2)+\lambda(q^2,m_B^2,m_D^2)T_2(q^2)\right],\\
\mathcal{H}_{+1+1}(P_B,P_D) =& \frac{\lambda(q^2,m_B^2,m_D^2)}{8m_D^2}\left[T_1(q^2)-\lambda^{1/2}(q^2,m_B^2,m_D^2)T_4(q^2)\right]^2,\\
\mathcal{H}_{-1-1}(P_B,P_D) =& \frac{\lambda(q^2,m_B^2,m_D^2)}{8m_D^2}\left[T_1(q^2)+\lambda^{1/2}(q^2,m_B^2,m_D^2)T_4(q^2)\right]^2,\\
\mathcal{H}_{00}(P_B,P_D) =& \frac{\lambda(q^2,m_B^2,m_D^2)}{24m_D^4q^2}\left[(m_B^2-q^2-m_D^2)T_1(q^2)+\lambda(q^2,m_B^2,m_D^2)T_2(q^2)\right]^2.
\end{aligned} \tag{F.16}$$

We can now define the combinations [241]

$$\begin{aligned}
H_U &= \mathcal{H}_{+1+1}+\mathcal{H}_{-1-1},\\
H_L &= \mathcal{H}_{00},\\
H_P &= \mathcal{H}_{+1+1}-\mathcal{H}_{-1-1},\\
H_S &= 3\mathcal{H}_{tt},\\
H_{SL} &= \mathcal{H}_{t0},\\
\tilde{H}_J &= \frac{m_l^2}{2q^2}H_J \text{ with } J=U,L,S,SL.
\end{aligned} \tag{F.17}$$

with U, L, P, S and SL representing, respectively, unpolarized-transverse, longitudinal, parity-odd, scalar and scalar-longitudinal interference.

Finally, the double differential decay width is written in terms of the above defined combinations as

$$\begin{aligned}
\frac{d^2\Gamma}{dq^2dx_l} =& \frac{G_F^2}{8\pi^3}|V_{bc}|^2\frac{(q^2-m_l^2)^2}{12m_B^2q^2}\frac{\lambda^{1/2}(q^2,m_B^2,m_D^2)}{2m_B}\left[\frac{3}{8}(1+x_l^2)H_U+\frac{3}{4}(1-x_l^2)H_L\right.\\
&\left.\pm\frac{3}{4}x_lH_P+\frac{3}{4}(1-x_l^2)\tilde{H}_U+\frac{3}{2}x_l^2\tilde{H}_L+\frac{1}{2}\tilde{H}_S+3x_l\tilde{H}_{SL}\right].
\end{aligned} \tag{F.18}$$

Note that for antiparticle decay H_P has the opposite sign to the case of particle decay while all other hadron tensor helicity component combinations defined in Eq. (F.17) do not change. The sign change of H_P compensates the extra sign coming from the lepton tensor. This means that in fact the double differential decay width is the same for $l^-\bar{\nu}_l$ and $l^+\nu_l$. After integration on x_l we have that

$$\frac{d\Gamma}{dq^2} = \frac{G_F^2}{8\pi^3}|V_{bc}|^2\frac{(q^2-m_l^2)^2}{12m_B^2q^2}\frac{\lambda^{1/2}(q^2,m_B^2,m_D^2)}{2m_B}(H_U+H_L+\tilde{H}_U+\tilde{H}_L+\tilde{H}_S), \tag{F.19}$$

and integrating over q^2, we obtain the total decay width that can be written as

$$\Gamma = \Gamma_U+\Gamma_L+\tilde{\Gamma}_U+\tilde{\Gamma}_L+\tilde{\Gamma}_S, \tag{F.20}$$

with Γ_J and $\tilde{\Gamma}_J$ partial helicity widths defined as

$$\Gamma_J = \int dq^2 \frac{G_F^2}{8\pi^3} |V_{bc}|^2 \frac{(q^2 - m_l^2)^2}{12 m_B^2 q^2} \frac{\lambda^{1/2}(q^2, m_B^2, m_D^2)}{2m_B} H_J, \tag{F.21}$$

and similarly for $\tilde{\Gamma}_J$ in terms of $\tilde{H}_J$.

F.1.1 Form factor decomposition of hadronic matrix elements

Here we give general expressions valid for transitions between a pseudoscalar meson M_I at rest with quark content $\bar{q}_{f_1} q_{f_2}$ and a final M_F meson with total angular momentum and parity $J^P = 0^+, 1^+, 2^+$, three-momentum $-|\vec{q}|\vec{k}$, and quark content $\bar{q}_{f_1'} q_{f_2}$. The transition changes the antiquark flavour. Following Ref. [240] we evaluate $V_\lambda^\mu(|\vec{q}|)$ and $A_\lambda^\mu(|\vec{q}|)$ in the CQM through the relations

$$\begin{aligned} V_\lambda^\mu(|\vec{q}|) &= \sqrt{2m_I 2E_F(-\vec{q})}\ {}_{NR}\langle M_F, \lambda - |\vec{q}|\vec{k}| J_V^{bc\mu}(0) | M_I, \vec{0}\rangle_{NR}\,, \\ A_\lambda^\mu(|\vec{q}|) &= \sqrt{2m_I 2E_F(-\vec{q})}\ {}_{NR}\langle M_F, \lambda - |\vec{q}|\vec{k}| J_A^{bc\mu}(0) | M_I, \vec{0}\rangle_{NR}\,. \end{aligned} \tag{F.22}$$

For the different cases under study we have the following

Case $0^- \to 0^+$

$$\begin{aligned} A^0(|\vec{q}|) =& \sqrt{2m_I 2E_F(-\vec{q})} \int d^3p \frac{1}{4\pi|\vec{p}|} \left(\hat{\phi}^{(M(0^+))}_{f_1',f_2}(|\vec{p}|)\right)^* \hat{\phi}^{(M(0^-))}_{f_1,f_2}(|\vec{p} - \frac{m_{f_2}}{m_{f_1'} + m_{f_2}} q\vec{k}|) \\ & \times \sqrt{\frac{\hat{E}_{f_1'}\hat{E}_{f_1}}{4E_{f_1'}E_{f_1}}} \left[\frac{\vec{p}\cdot\left(\frac{m_{f_2}}{m_{f_1'}+m_{f_2}}|\vec{q}|\vec{k} - \vec{p}\right)}{\hat{E}_{f_1}} + \frac{\vec{p}\cdot\left(-\frac{m_{f_1'}}{m_{f_1'}+m_{f_2}}|\vec{q}|\vec{k} - \vec{p}\right)}{\hat{E}_{f_1}} \right], \end{aligned}$$

$$\begin{aligned} A^3(|\vec{q}|) =& \sqrt{2m_I 2E_F(-\vec{q})} \int d^3p \frac{1}{4\pi|\vec{p}|} \left(\hat{\phi}^{(M(0^+))}_{f_1',f_2}(|\vec{p}|)\right)^* \hat{\phi}^{(M(0^-))}_{f_1,f_2}(|\vec{p} - \frac{m_{f_2}}{m_{f_1'} + m_{f_2}} q\vec{k}|) \\ & \times \sqrt{\frac{\hat{E}_{f_1'}\hat{E}_{f_1}}{4E_{f_1'}E_{f_1}}} \Bigg\{ p_z \left[1 - \frac{\left(-\frac{m_{f_1'}}{m_{f_1'}+m_{f_2}}|\vec{q}|\vec{k} - \vec{p}\right)\cdot\left(\frac{m_{f_2}}{m_{f_1'}+m_{f_2}}|\vec{q}|\vec{k} - \vec{p}\right)}{\hat{E}_{f_1'}\hat{E}_{f_1}} \right] \\ & + \frac{1}{\hat{E}_{f_1'}\hat{E}_{f_1}} \left[\left(-\frac{m_{f_1'}}{m_{f_1'}+m_{f_2}}|\vec{q}| - p_z\right) \left[\vec{p}\cdot\left(\frac{m_{f_2}}{m_{f_1'}+m_{f_2}}|\vec{q}|\vec{k} - \vec{p}\right)\right] \right. \\ & \left. + \left(\frac{m_{f_2}}{m_{f_1'}+m_{f_2}}|\vec{q}| - p_z\right) \left[\vec{p}\cdot\left(-\frac{m_{f_1'}}{m_{f_1'}+m_{f_2}}|\vec{q}|\vec{k} - \vec{p}\right)\right] \right] \Bigg\}, \end{aligned} \tag{F.23}$$

where $E_{f_1'}$ and E_{f_1} are shorthand notations for $E_{f_1'}\left(-\frac{m_{f_1'}}{m_{f_1'}+m_{f_2}}|\vec{q}|\vec{k} - \vec{p}\right)$ and $E_{f_1}\left(\frac{m_{f_2}}{m_{f_1'}+m_{f_2}}|\vec{q}|\vec{k} - \vec{p}\right)$ respectively and $\hat{E}_f = E_f + m_f$.

Case $0^- \to 1^+$

Here we have to distinguish two different cases that depend on the total spin S of the quark-antiquark system.

1. Case $S = 0$

$$V_{\lambda=0}^{(1^+,S=0)0}(|\vec{q}|) = -i\sqrt{3}\sqrt{2m_I 2E_F(-\vec{q})}\int d^3p \sqrt{\frac{\hat{E}_{f_1'}\hat{E}_{f_1}}{4E_{f_1'}E_{f_1}}}\frac{1}{4\pi p}\left(\hat{\phi}_{f_1',f_2}^{(M_F(1^+,S=0))}(p)\right)^*$$
$$\times\,\hat{\phi}_{f_1,f_2}^{(M_I(0^-))}(|\vec{p}-\frac{m_{f_2}}{m_{f_1'}+m_{f_2}}|\vec{q}|\vec{k}\,|)\;p_z\left[1+\frac{\left(-\frac{m_{f_1'}}{m_{f_1'}+m_{f_2}}|\vec{q}|\vec{k}-\vec{p}\right)\cdot\left(\frac{m_{f_2}}{m_{f_1'}+m_{f_2}}|\vec{q}|\vec{k}-\vec{p}\right)}{\hat{E}_{f_1'}\hat{E}_{f_1}}\right],$$

$$V_{\lambda=-1}^{(1^+,S=0)1}(|\vec{q}|) = i\sqrt{\frac{3}{2}}\sqrt{2m_I 2E_F(-\vec{q})}\int d^3p \sqrt{\frac{\hat{E}_{f_1'}\hat{E}_{f_1}}{4E_{f_1'}E_{f_1}}}\frac{1}{4\pi p}\left(\hat{\phi}_{f_1',f_2}^{(M_F(1^+,S=0))}(p)\right)^*$$
$$\times\,\hat{\phi}_{f_1,f_2}^{(M_I(0^-))}(|\vec{p}-\frac{m_{f_2}}{m_{f_1'}+m_{f_2}}|\vec{q}|\vec{k}\,|)\;p_x^2\left(\frac{1}{\hat{E}_{f_1}}+\frac{1}{\hat{E}_{f_1'}}\right),$$

$$V_{\lambda=0}^{(1^+,S=0)3}(|\vec{q}|) = -i\sqrt{3}\sqrt{2m_I 2E_F(-\vec{q})}\int d^3p \sqrt{\frac{\hat{E}_{f_1'}\hat{E}_{f_1}}{4E_{f_1'}E_{f_1}}}\frac{1}{4\pi p}\left(\hat{\phi}_{f_1',f_2}^{(M_F(1^+,S=0))}(p)\right)^*$$
$$\times\,\hat{\phi}_{f_1,f_2}^{(M_I(0^-))}(|\vec{p}-\frac{m_{f_2}}{m_{f_1'}+m_{f_2}}|\vec{q}|\vec{k}\,|)\;p_z\left(\frac{\frac{m_{f_2}}{m_{f_1'}+m_{f_2}}|\vec{q}|-p_z}{\hat{E}_{f_1}}-\frac{\frac{m_{f_1'}}{m_{f_1'}+m_{f_2}}|\vec{q}|+p_z}{\hat{E}_{f_1'}}\right),$$

$$A_{\lambda=-1}^{(1^+,S=0)1}(|\vec{q}|) = -i\sqrt{\frac{3}{2}}\sqrt{2m_I 2E_F(-\vec{q})}\int d^3p \sqrt{\frac{\hat{E}_{f_1'}\hat{E}_{f_1}}{4E_{f_1'}E_{f_1}}}\frac{1}{4\pi p}\left(\hat{\phi}_{f_1',f_2}^{(M_F(1^+,S=0))}(p)\right)^*$$
$$\times\,\hat{\phi}_{f_1,f_2}^{(M_I(0^-))}(|\vec{p}-\frac{m_{f_2}}{m_{f_1'}+m_{f_2}}|\vec{q}|\vec{k}\,|)\frac{p_y^2|\vec{q}|}{\hat{E}_{f_1}\hat{E}_{f_1'}}. \tag{F.24}$$

2. Case $S = 1$

$$V_{\lambda=0}^{(1^+,S=1)0}(|\vec{q}|) = i\sqrt{\frac{3}{2}}\sqrt{2m_I 2E_F(-\vec{q})}\int d^3p \sqrt{\frac{\hat{E}_{f_1'}\hat{E}_{f_1}}{4E_{f_1'}E_{f_1}}}\frac{1}{4\pi p}\left(\hat{\phi}_{f_1',f_2}^{(M_F(1^+,S=1))}(p)\right)^*$$
$$\times\,\hat{\phi}_{f_1,f_2}^{(M_I(0^-))}(|\vec{p}-\frac{m_{f_2}}{m_{f_1'}+m_{f_2}}|\vec{q}|\vec{k}\,|)\,\frac{|\vec{q}|(p_z^2-p^2)}{\hat{E}_{f_1'}\hat{E}_{f_1}},$$

$$V^{(1^+,S=1)1}_{\lambda=-1}(|\vec{q}|) = -i\frac{\sqrt{3}}{2}\sqrt{2m_I 2E_F(-\vec{q})}\int d^3p \sqrt{\frac{\hat{E}_{f_1'}\hat{E}_{f_1}}{4E_{f_1'}E_{f_1}}}\frac{1}{4\pi p}\left(\hat{\phi}^{(M_F(1^+,S=1))}_{f_1',f_2}(p)\right)^*$$
$$\times \hat{\phi}^{(M_I(0^-))}_{f_1,f_2}(|\vec{p} - \frac{m_{f_2}}{m_{f_1'}+m_{f_2}}|\vec{q}|\vec{k}\,|)\left(\frac{p_y^2+p_z^2+p_z|\vec{q}|\frac{m_{f_1'}}{m_{f_1'}+m_{f_2}}}{\hat{E}_{f_1'}} - \frac{p_y^2+p_z^2-p_z|\vec{q}|\frac{m_{f_2}}{m_{f_1'}+m_{f_2}}}{\hat{E}_{f_1}}\right),$$

$$V^{(1^+,S=1)3}_{\lambda=0}(|\vec{q}|) = i\sqrt{\frac{3}{2}}\sqrt{2m_I 2E_F(-\vec{q})}\int d^3p \sqrt{\frac{\hat{E}_{f_1'}\hat{E}_{f_1}}{4E_{f_1'}E_{f_1}}}\frac{1}{4\pi p}\left(\hat{\phi}^{(M_F(1^+,S=1))}_{f_1',f_2}(p)\right)^*$$
$$\times \hat{\phi}^{(M_I(0^-))}_{f_1,f_2}(|\vec{p} - \frac{m_{f_2}}{m_{f_1'}+m_{f_2}}|\vec{q}|\vec{k}\,|)\,(p_x^2+p_y^2)\left(\frac{1}{\hat{E}_{f_1}} - \frac{1}{\hat{E}_{f_1'}}\right),$$

$$A^{(1^+,S=1)1}_{\lambda=-1}(|\vec{q}|) = i\frac{\sqrt{3}}{2}\sqrt{2m_I 2E_F(-\vec{q})}$$
$$\times \int d^3p \sqrt{\frac{\hat{E}_{f_1'}\hat{E}_{f_1}}{4E_{f_1'}E_{f_1}}}\frac{1}{4\pi p}\left(\hat{\phi}^{(M_F(1^+,S=1))}_{f_1',f_2}(p)\right)^* \hat{\phi}^{(M_I(0^-))}_{f_1,f_2}(|\vec{p} - \frac{m_{f_2}}{m_{f_1'}+m_{f_2}}|\vec{q}|\vec{k}\,|)$$
$$\times \left\{ p_z \left[1 - \frac{\left(-\frac{m_{f_1'}}{m_{f_1'}+m_{f_2}}|\vec{q}|\vec{k}-\vec{p}\right)\cdot\left(\frac{m_{f_2}}{m_{f_1'}+m_{f_2}}|\vec{q}|\vec{k}-\vec{p}\right)}{\hat{E}_{f_1'}\hat{E}_{f_1}} \right] + \frac{m_{f_2}-m_{f_1'}}{m_{f_1'}+m_{f_2}}\frac{p_x^2|\vec{q}|}{\hat{E}_{f_1'}\hat{E}_{f_1}} \right\}. \tag{F.25}$$

Case $0^- \to 2^+$

Here we have to distinguish between $L = 1$ and $L = 3$.

1. Case $L = 1$

$$V^{(2^+,L=1)1}_{\lambda=+1}(|\vec{q}|) = -i\frac{\sqrt{3}}{2}\sqrt{2m_I 2E_F(-\vec{q})}\int d^3p\sqrt{\frac{\hat{E}_{f_1'}\hat{E}_{f_1}}{4E_{f_1'}E_{f_1}}}\frac{1}{4\pi p}\left(\hat{\phi}^{(M_F(2^+,L=1))}_{f_1',f_2}(p)\right)^*$$
$$\times\hat{\phi}^{(M_I(0^-))}_{f_1,f_2}(|\vec{p}-\frac{m_{f_2}}{m_{f_1'}+m_{f_2}}|\vec{q}|\vec{k}|)\left(\frac{p_y^2-p_z^2-p_z|\vec{q}|\frac{m_{f_1'}}{m_{f_1'}+m_{f_2}}}{\hat{E}_{f_1'}}-\frac{p_y^2-p_z^2+p_z|\vec{q}|\frac{m_{f_2}}{m_{f_1'}+m_{f_2}}}{\hat{E}_{f_1}}\right),$$

$$A^{(2^+,L=1)0}_{\lambda=0}(|\vec{q}|) = -\frac{i}{\sqrt{2}}\sqrt{2m_I 2E_F(-\vec{q})}\int d^3p\sqrt{\frac{\hat{E}_{f_1'}\hat{E}_{f_1}}{4E_{f_1'}E_{f_1}}}\frac{1}{4\pi p}\left(\hat{\phi}^{(M_F(2^+,L=1))}_{f_1',f_2}(p)\right)^*$$
$$\times\hat{\phi}^{(M_I(0^-))}_{f_1,f_2}(|\vec{p}-\frac{m_{f_2}}{m_{f_1'}+m_{f_2}}|\vec{q}|\vec{k}|)\left(\frac{p_x^2+p_y^2-2p_z^2-2p_z|\vec{q}|\frac{m_{f_1'}}{m_{f_1'}+m_{f_2}}}{\hat{E}_{f_1'}}\right.$$
$$\left.+\frac{p_x^2+p_y^2-2p_z^2+2p_z|\vec{q}|\frac{m_{f_2}}{m_{f_1'}+m_{f_2}}}{\hat{E}_{f_1}}\right),$$

$$A^{(2^+,L=1)1}_{\lambda=+1}(|\vec{q}|) = i\frac{\sqrt{3}}{2}\sqrt{2m_I 2E_F(-\vec{q})}\int d^3p\sqrt{\frac{\hat{E}_{f_1'}\hat{E}_{f_1}}{4E_{f_1'}E_{f_1}}}\frac{1}{4\pi p}\left(\hat{\phi}^{(M_F(2^+,L=1))}_{f_1',f_2}(p)\right)^*$$
$$\times\hat{\phi}^{(M_I(0^-))}_{f_1,f_2}(|\vec{p}-\frac{m_{f_2}}{m_{f_1'}+m_{f_2}}|\vec{q}|\vec{k}|)\left\{p_z\left[1-\frac{\left(-\frac{m_{f_1'}}{m_{f_1'}+m_{f_2}}|\vec{q}|\vec{k}-\vec{p}\right)\cdot\left(\frac{m_{f_2}}{m_{f_1'}+m_{f_2}}|\vec{q}|\vec{k}-\vec{p}\right)}{\hat{E}_{f_1'}\hat{E}_{f_1}}\right]\right.$$
$$\left.+\frac{4p_zp_x^2-p_x^2|\vec{q}|\frac{m_{f_2}-m_{f_1'}}{m_{f_1'}+m_{f_2}}}{\hat{E}_{f_1'}\hat{E}_{f_1}}\right\},$$

$$A^{(2^+,L=1)3}_{\lambda=0}(|\vec{q}|) = -i\sqrt{2}\sqrt{2m_I 2E_F(-\vec{q})}\int d^3p\sqrt{\frac{\hat{E}_{f_1'}\hat{E}_{f_1}}{4E_{f_1'}E_{f_1}}}\frac{1}{4\pi p}\left(\hat{\phi}^{(M_F(2^+,L=1))}_{f_1',f_2}(p)\right)^*$$
$$\times\hat{\phi}^{(M_I(0^-))}_{f_1,f_2}(|\vec{p}-\frac{m_{f_2}}{m_{f_1'}+m_{f_2}}|\vec{q}|\vec{k}|)\left\{p_z\left[1-\frac{\left(-\frac{m_{f_1'}}{m_{f_1'}+m_{f_2}}|\vec{q}|\vec{k}-\vec{p}\right)\cdot\left(\frac{m_{f_2}}{m_{f_1'}+m_{f_2}}|\vec{q}|\vec{k}-\vec{p}\right)}{\hat{E}_{f_1'}\hat{E}_{f_1}}\right]\right.$$
$$+\frac{1}{\hat{E}_{f_1'}\hat{E}_{f_1}}\left[2p_z\left(-\frac{m_{f_1'}}{m_{f_1'}+m_{f_2}}|\vec{q}|-p_z\right)\left(\frac{m_{f_2}}{m_{f_1'}+m_{f_2}}|\vec{q}|-p_z\right)\right.$$
$$\left.\left.+(p_x^2+p_y^2)\left(-p_z+\frac{m_{f_2}-m_{f_1'}}{2(m_{f_1'}+m_{f_2})}|\vec{q}|\right)\right]\right\}. \qquad \text{(F.26)}$$

2. Case $L = 3$

$$V^{(2^+,L=3)1}_{\lambda=+1}(|\vec{q}|) = \frac{i}{\sqrt{8}}\sqrt{2m_I 2E_F(-\vec{q})}\int d^3p \sqrt{\frac{\hat{E}_{f_1'}\hat{E}_{f_1}}{4E_{f_1'}E_{f_1}}}\frac{1}{4\pi p^3}\left(\hat{\phi}^{(M(2^+,L=3))}_{f_1',f_2}(p)\right)^*$$
$$\times \hat{\phi}^{(M(0^-))}_{f_1,f_2}(|\vec{p} - \frac{m_{f_2}}{m_{f_1'}+m_{f_2}}|\vec{q}|\vec{k}\,|)\left[\frac{1}{\hat{E}_{f_1}}\left(p^2\Big(2p_y^2 - 3p_z\Big(\frac{m_{f_2}}{m_{f_1'}+m_{f_2}}|\vec{q}| - p_z\Big)\Big)\right.\right.$$
$$\left. + 5p_z\Big(-2p_y^2p_z + \Big(\frac{m_{f_2}}{m_{f_1'}+m_{f_2}}|\vec{q}| - p_z\Big)(p_x^2 - p_y^2 + p_z^2)\Big)\right)$$
$$+ \frac{1}{\hat{E}_{f_1'}}\left(p^2\Big(-2p_y^2 + 3p_z\Big(-\frac{m_{f_1'}}{m_{f_1'}+m_{f_2}}|\vec{q}| - p_z\Big)\Big)\right.$$
$$\left.\left. - 5p_z\Big(-2p_y^2p_z + \Big(-\frac{m_{f_1'}}{m_{f_1'}+m_{f_2}}|\vec{q}| - p_z\Big)(p_x^2 - p_y^2 + p_z^2)\Big)\right)\right],$$

$$A^{(2^+,L=3)0}_{T\lambda=0}(|\vec{q}|) = -i\sqrt{\frac{3}{4}}\sqrt{2m_I 2E_F(-\vec{q})}\int d^3p \sqrt{\frac{\hat{E}_{f_1'}\hat{E}_{f_1}}{4E_{f_1'}E_{f_1}}}\frac{1}{4\pi p}\left(\hat{\phi}^{(M(2^+,L=3)}_{f_1',f_2}(p)\right)^*$$
$$\times \hat{\phi}^{(M(0^-))}_{f_1,f_2}(|\vec{p} - \frac{m_{f_2}}{m_{f_1'}+m_{f_2}}|\vec{q}|\vec{k}\,|)\left[\left(\frac{5p_z^2}{p^2} - 1\right)\left(\frac{p_x^2+p_y^2}{\hat{E}_{f_1}} + \frac{p_x^2+p_y^2}{\hat{E}_{f_1'}}\right),\right.$$
$$\left. - \frac{p_z}{p}\left(\frac{5p_z^2}{p^2} - 3\right)\left(\frac{\frac{m_{f_2}}{m_{f_1'}+m_{f_2}}|\vec{q}| - p_z}{\hat{E}_{f_1}} - \frac{\frac{m_{f_1'}}{m_{f_1'}+m_{f_2}}|\vec{q}| + p_z}{\hat{E}_{f_1'}}\right)\right],$$

$$A^{(2^+,L=3)3}_{\lambda=0}(|\vec{q}|) = -\frac{i}{2}\sqrt{2m_I 2E_F(-\vec{q})}\int d^3p \sqrt{\frac{\hat{E}_{f_1'}\hat{E}_{f_1}}{4E_{f_1'}E_{f_1}}}\frac{1}{4\pi p}\left(\hat{\phi}^{(M(2^+,L=3))}_{f_1',f_2}(p)\right)^*$$
$$\times \hat{\phi}^{(M(0^-))}_{f_1,f_2}(|\vec{p} - \frac{m_{f_2}}{m_{f_1'}+m_{f_2}}|\vec{q}|\vec{k}\,|)\left[(p_x^2+p_y^2)\left(\frac{5p_z^2}{p^2} - 1\right)\left(\frac{\frac{m_{f_2}-m_{f_1'}}{m_{f_1'}+m_{f_2}}|\vec{q}| - 2p_z}{\hat{E}_{f_1}\hat{E}_{f_1'}}\right)\right.$$
$$\left. - p_z\left(\frac{5p_z^2}{p^2} - 3\right)\left(1 - \frac{p_x^2+p_y^2 - \left(-\frac{m_{f_1'}}{m_{f_1'}+m_{f_2}}|\vec{q}| - p_z\right)\left(\frac{m_{f_2}}{m_{f_1'}+m_{f_2}}|\vec{q}| - p_z\right)}{\hat{E}_{f_1}\hat{E}_{f_1'}}\right)\right],$$

$$A^{(2^+,L=3)1}_{\lambda=+1}(|\vec{q}|) = -\frac{i}{\sqrt{8}}\sqrt{2m_I 2E_F(-\vec{q})}\int d^3p\sqrt{\frac{\hat{E}_{f_1'}\hat{E}_{f_1}}{4E_{f_1'}E_{f_1}}}\frac{1}{4\pi p}\left(\hat{\phi}^{(M(2^+,L=3))}_{f_1',f_2}(p)\right)^*$$
$$\times\,\hat{\phi}^{(M(0^-))}_{f_1,f_2}(|\vec{p}-\frac{m_{f_2}}{m_{f_1'}+m_{f_2}}|\vec{q}|\vec{k}\,|)\Bigg[3p_z$$
$$+\,3p_z\frac{p_x^2-p_y^2-\left(-\frac{m_{f_1'}}{m_{f_1'}+m_{f_2}}|\vec{q}|-p_z\right)\left(\frac{m_{f_2}}{m_{f_1'}+m_{f_2}}|\vec{q}|-p_z\right)}{\hat{E}_{f_1}\hat{E}_{f_1'}}$$
$$+\,5p_z\left(\frac{p_x^2}{p^2}+\frac{p_y^2}{p^2}-\frac{p_z^2}{p^2}\right)\left(1+\frac{p_x^2-p_y^2-\left(-\frac{m_{f_1'}}{m_{f_1'}+m_{f_2}}|\vec{q}|-p_z\right)\left(\frac{m_{f_2}}{m_{f_1'}+m_{f_2}}|\vec{q}|-p_z\right)}{\hat{E}_{f_1}\hat{E}_{f_1'}}\right)$$
$$-\,2p_x^2\left(\frac{5p_z^2}{p^2}-1\right)\left(\frac{\frac{m_{f_2}-m_{f_1'}}{m_{f_1'}+m_{f_2}}|\vec{q}|-2p_z}{\hat{E}_{f_1}\hat{E}_{f_1'}}\right)+20\frac{p_zp_x^2p_y^2}{\hat{E}_{f_1}\hat{E}_{f_1'}p^2}\Bigg]. \tag{F.27}$$

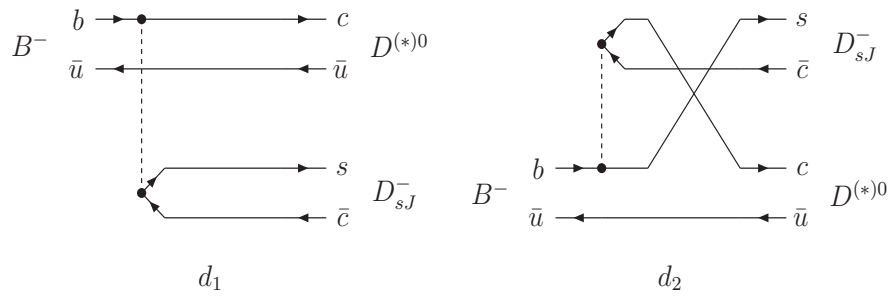

Figure F.1. Diagrammatic representation of B^- decay into $D^{(*)0} D_{sJ}^-$.

F.2 Nonleptonic decays: $B \to D^{(*)} D_{sJ}$

Here we study the nonleptonic decays $B \to D^{(*)} D_{sJ}$ with $D^{(*)}$ the D or D^* mesons, and D_{sJ} the mesons $D_{s0}^*(2317)$, $D_{s1}(2460)$ and $D_{s1}(2536)$. These decay modes involve a $b \to c$ transition at the quark level, governed by the effective Hamiltonian [240, 241, 284]

$$H_{\text{eff}} = \frac{G_F}{\sqrt{2}} \left\{ V_{cb} \left[C_1(\mu)\, Q_1^{cb} + C_2(\mu)\, Q_2^{cb} \right] + h.c. \right\}, \tag{F.28}$$

in which penguin operators have been neglected. In Eq. (F.28), $C_1(\mu)$ and $C_2(\mu)$ are scale-dependent Wilson coefficients, being $\mu \simeq m_b$ the appropriate energy scale in this case. The Q_1^{cb} and Q_2^{cb} are local four-quark operators given by

$$\begin{aligned} Q_1^{cb} &= V_{cs}^* \left[\bar{\psi}_c(0) \gamma_\mu (I - \gamma_5) \psi_b(0) \right] \left[\bar{\psi}_s(0) \gamma^\mu (I - \gamma_5) \psi_c(0) \right], \\ Q_2^{cb} &= V_{cs}^* \left[\bar{\psi}_s(0) \gamma_\mu (I - \gamma_5) \psi_b(0) \right] \left[\bar{\psi}_c(0) \gamma^\mu (I - \gamma_5) \psi_c(0) \right]. \end{aligned} \tag{F.29}$$

We show in Fig. F.1 the schematic representation of the $B^- \to D^{(*)0} D_{sJ}^-$ decay given by the two local four-quark operators, diagram d_1 for Q_1^{cb} and diagram d_2 for Q_2^{cb}. Factorization approximation is implicit in diagram d_1, which amounts to evaluating the hadron matrix element of the effective Hamiltonian as a product of quark-current matrix elements. Fierz reordering of diagram d_2 leads to the same contribution but for a color factor. The full transition amplitude can be evaluated with the Q_1^{cb} part of the Hamiltonian but with an effective coupling given by

$$a_1(\mu) = C_1(\mu) + \frac{1}{N_C}\, C_2(\mu), \tag{F.30}$$

with $N_C = 3$ the number of colors.

The decay width is given by

$$\Gamma = \frac{G_F^2}{16\pi m_B^2} \left| V_{cb} \right|^2 \left| V_{cs} \right|^2 a_1^2 \, \frac{\lambda^{1/2}(m_B^2, m_{D^{(*)}}^2, m_{D_{sJ}}^2)}{2 m_B} \, \mathcal{H}_{\alpha\beta}(P_B, P_{D^{(*)}})\, \hat{\mathcal{H}}^{\alpha\beta}(P_{D_{sJ}}), \tag{F.31}$$

where P_B, $P_{D^{(*)}}$ and $P_{D_{sJ}}$ are the meson momenta. $\mathcal{H}_{\alpha\beta}(P_B, P_{D^{(*)}})$ is the hadron tensor for the $B^- \to D^{(*)0}$ transition and $\hat{\mathcal{H}}^{\alpha\beta}(P_{D_{sJ}})$ is the hadron tensor for the

vacuum $\to D_{sJ}^-$ transition. The latter is

$$\hat{\mathcal{H}}^{\alpha\beta}(P_{D_{sJ}}) = \begin{cases} P^\alpha_{D_{sJ}} P^\beta_{D_{sJ}} f^2_{D_{sJ}} & D_{sJ} \equiv 0^-,\, 0^+ \\ (P^\alpha_{D_{sJ}} P^\beta_{D_{sJ}} - m^2_{D_{sJ}} g^{\alpha\,\beta}) f^2_{D_{sJ}} & D_{sJ} \equiv 1^-,\, 1^+ \end{cases} \tag{F.32}$$

with $f_{D_{sJ}}$ being the D_{sJ} decay constant.

Similarly to the semileptonic case, the product $\mathcal{H}_{\alpha\beta}(P_{B_c}, P_{D^{(*)}})\hat{\mathcal{H}}^{\alpha\beta}(P_{D_{sJ}})$ can be easily written in terms of helicity amplitudes for the $B^- \to D^{(*)}$ transition, so that the width is given as

$$\Gamma = \frac{G_F^2}{16\pi m_B^2} |V_{cb}|^2 |V_{cs}|^2 a_1^2 \, \frac{\lambda^{1/2}(m_B^2, m^2_{D^{(*)}}, m^2_{D_{sJ}})}{2m_B} \, m^2_{D_{sJ}} f^2_{D_{sJ}} \mathcal{H}^{B\to D^{(*)}}_{tt}(m^2_{D_{sJ}}), \tag{F.33}$$

for D_{sJ} a pseudoscalar or scalar meson, and

$$\begin{aligned} \Gamma =& \frac{G_F^2}{16\pi m_B^2} |V_{cb}|^2 |V_{cs}|^2 a_1^2 \, \frac{\lambda^{1/2}(m_B^2, m^2_{D^{(*)}}, m^2_{D_{sJ}})}{2m_B} \, m^2_{D_{sJ}} f^2_{D_{sJ}} \times \\ & \times \left[\mathcal{H}^{B\to D^{(*)}}_{+1+1}(m^2_{D_{sJ}}) + \mathcal{H}^{B\to D^{(*)}}_{-1-1}(m^2_{D_{sJ}}) + \mathcal{H}^{B\to D^{(*)}}_{00}(m^2_{D_{sJ}}) \right], \end{aligned} \tag{F.34}$$

for D_{sJ} a vector or axial-vector meson. The different $\mathcal{H}_{rr}$ are defined above and evaluated in this case at $q^2 = m^2_{D_{sJ}}$.

We are ready to calculate the decay constants that we need to know in the above expressions. In our model, and due to the normalization of our nonrelativistic meson states, the decay constants are given by

$$\begin{aligned} f_{M(0^-)} &= -i\sqrt{\frac{2}{m_{M(0^-)}}} \, \langle 0|J^{f_2 f_1}_{A0}(0)|M(0^-), \vec{0}\rangle \,, \\ f_{M(0^+)} &= +i\sqrt{\frac{2}{m_{M(0^+)}}} \, \langle 0|J^{f_2 f_1}_{V0}(0)|M(0^+), \vec{0}\rangle \,, \\ f_{M(1^-)} &= -\sqrt{\frac{2}{m_{M(1^-)}}} \, \langle 0|J^{f_2 f_1}_{V3}(0)|M(1^-), 0\,\vec{0}\rangle \,, \\ f_{M(1^+)} &= +\sqrt{\frac{2}{m_{M(1^+)}}} \, \langle 0|J^{f_2 f_1}_{A3}(0)|M(1^+), 0\,\vec{0}\rangle \,, \end{aligned} \tag{F.35}$$

for pseudoscalar, scalar, vector and axial-vector mesons, respectively. The correspond-

ing matrix elements are given by

$$\begin{aligned}
\langle 0|J_{A0}^{f_2f_1}(0)|M(0^-),\vec{0}\rangle =& i\frac{\sqrt{3}}{\pi}\int d|\vec{p}|\ |\vec{p}|^2\hat{\phi}_{f_1,f_2}^{(M(0^-))}(|\vec{p}|)\sqrt{\frac{(E_{f_1}(-\vec{p})+m_{f_1})(E_{f_2}(\vec{p})+m_{f_2})}{4E_{f_1}(-\vec{p})E_{f_2}(\vec{p})}}\\
&\times\left[1-\frac{|\vec{p}|^2}{(E_{f_1}(-\vec{p})+m_{f_1})(E_{f_2}(\vec{p})+m_{f_2})}\right],\\
\langle 0|J_{V0}^{f_2f_1}(0)|M(0^+),\vec{0}\rangle =& i\frac{\sqrt{3}}{\pi}\int d|\vec{p}|\,|\vec{p}|^3\hat{\phi}_{f_1,f_2}^{(M(0^+))}(|\vec{p}|)\sqrt{\frac{(E_{f_1}(-\vec{p})+m_{f_1})(E_{f_2}(\vec{p})+m_{f_2})}{4E_{f_1}(-\vec{p})E_{f_2}(\vec{p})}}\\
&\times\left[\frac{1}{E_{f_2}(\vec{p})+m_{f_2}}-\frac{1}{E_{f_1}(-\vec{p})+m_{f_1}}\right],\\
\langle 0|J_{V3}^{f_2f_1}(0)|M(1^-,L=0),0\,\vec{0}\rangle =& -\frac{\sqrt{3}}{\pi}\int d|\vec{p}|\,|\vec{p}|^2\hat{\phi}_{f_1,f_2}^{(M(1^-,L=0))}(|\vec{p}|)\\
&\times\sqrt{\frac{(E_{f_1}(-\vec{p})+m_{f_1})(E_{f_2}(\vec{p})+m_{f_2})}{4E_{f_1}(-\vec{p})E_{f_2}(\vec{p})}}\left(1+\frac{|\vec{p}|^2}{3(E_{f_1}(-\vec{p})+m_{f_1})(E_{f_2}(\vec{p})+m_{f_2})}\right),\\
\langle 0|J_{V3}^{f_2f_1}(0)|M(1^-,L=2,0)\,\vec{0}\rangle =& -\frac{2}{\pi}\sqrt{\frac{2}{3}}\int d|\vec{p}|\,\hat{\phi}_{f_1,f_2}^{(M(1^-,L=2))}(|\vec{p}|)\\
&\times\sqrt{\frac{(E_{f_2}(\vec{p})+m_{f_2})(E_{f_1}(-\vec{p})+m_{f_1})}{4E_{f_1}(-\vec{p})E_{f_2}(\vec{p})}}\frac{|\vec{p}|^4}{(E_{f_2}(\vec{p})+m_{f_2})(E_{f_1}(-\vec{p})+m_{f_1})},\\
\langle 0|J_{A3}^{f_2f_1}(0)|M(1^+,S=0),0\,\vec{0}\rangle =& \frac{1}{\pi}\int d|\vec{p}|\,|\vec{p}|^3\hat{\phi}_{f_1,f_2}^{(M(1^+,S=0))}(|\vec{p}|)\\
&\times\sqrt{\frac{(E_{f_1}(-\vec{p})+m_{f_1})(E_{f_2}(\vec{p})+m_{f_2})}{4E_{f_1}(-\vec{p})E_{f_2}(\vec{p})}}\left[\frac{1}{E_{f_1}(-\vec{p})+m_{f_1}}-\frac{1}{E_{f_2}(\vec{p})+m_{f_2}}\right],\\
\langle 0|J_{A3}^{f_2f_1}(0)|M(1^+,S=1),0\,\vec{0}\rangle =& -\frac{\sqrt{2}}{\pi}\int d|\vec{p}|\,|\vec{p}|^3\hat{\phi}_{f_1,f_2}^{(M(1^+,S=1))}(|\vec{p}|)\\
&\times\sqrt{\frac{(E_{f_1}(-\vec{p})+m_{f_1})(E_{f_2}(\vec{p})+m_{f_2})}{4E_{f_1}(-\vec{p})E_{f_2}(\vec{p})}}\left[\frac{1}{E_{f_1}(-\vec{p})+m_{f_1}}+\frac{1}{E_{f_2}(\vec{p})+m_{f_2}}\right].
\end{aligned}\tag{F.36}$$

For 0^- and 0^+ we have only one possible contribution. In the case of the $J^P = 1^-$ meson we have two contributions coming from the two possible values of the relative angular momentum. For $J^P = 1^+$ states and since C-parity is not well defined in charmed and charmed-strange mesons the wave function is a mixture of $^1P_1$ and $^3P_1$ partial waves and thus there are also two contributions.

Bibliography

[1] M. Gell-Mann, Phys. Lett. **8**, 214 (1964).

[2] G. Zweig, CERN-TH-412, NP-14146 (1964).

[3] J. J. Aubert et al. (E598 Collaboration), Phys. Rev. Lett. **33**, 1404 (1974).

[4] J. E. Augustin et al. (SLAC-SP-017 Collaboration), Phys. Rev. Lett. **33**, 1406 (1974).

[5] S. W. Herb et al., Phys. Rev. Lett. **39**, 252 (1977).

[6] F. Abe et al. (CDF Collaboration), Phys. Rev. Lett. **74**, 2626 (1995).

[7] T. Appelquist and H. D. Politzer, Phys. Rev. Lett. **34**, 43 (1975).

[8] A. De Rújula and S. L. Glashow, Phys. Rev. Lett. **34**, 46 (1975).

[9] T. Appelquist, A. De Rújula, H. D. Politzer, and S. L. Glashow, Phys. Rev. Lett. **34**, 365 (1975).

[10] E. Eichten, K. Gottfried, T. Kinoshita, J. Kogut, K. D. Lane, and T. M. Yan, Phys. Rev. Lett. **34**, 369 (1975), **36**, 1276(E) (1976).

[11] C. Quigg, in *The XVIII Rencontres de la Vallee d'Aoste Conference Proceedings* (2004), FERMILAB-conf-04/033-T, arXiv:hep-ph/0403187v2.

[12] R. Galik, in *The XXIV Physics in Collisions Conference Proceedings* (2004), arXiv:hep-ph/0408190.

[13] N. Brambilla et al., The European Physical Journal C - Particles and Fields **71**, 1 (2011).

[14] K. Seth, in *Journal of Physics: Conference Series* (2005), vol. 9, p. 32.

[15] K. Seth, in *Nuclear Physics B: Proceedings Supplements* (2005), vol. 140, p. 344.

[16] K. Seth et al., in *Nuclear Physics B: Proceedings Supplements* (2006), vol. 152, p. 207.

[17] T. Skwarnicki, in *The 40th Rencontres De Moriond On QCD And High Energy Hadronic Interactions Conference Proceedings* (2005), arXiv:hep-ex/0505050.

[18] E. J. Eichten, K. Lane, and C. Quigg, Phys. Rev. Lett. **89**, 162002 (2002).

[19] D. Boutigny et al., SLAC-R-457 (1995).

[20] J. Haba, Nuclear Instruments and Methods in Physics Research Section A: Accelerators, Spectrometers, Detectors and Associated Equipment **368**, 74 (1995).

[21] M. Ablikim et al., Nuclear Instruments and Methods in Physics Research Section A: Accelerators, Spectrometers, Detectors and Associated Equipment **614**, 345 (2010).

[22] R. Briere, G. Chen, T. Ferguson, G. Tatishvilli, and H. Vogel, CLNS **1**, 1742 (2001).

[23] *LHCb : Technical Proposal*, Tech. Proposal (CERN, Geneva, 1998).

[24] W. Erni et al., arXiv:hep-ex/0903.3905 (2009).

[25] S.-K. Choi et al. (Belle Collaboration), Phys. Rev. Lett. **89**, 102001 (2002).

[26] B. Aubert et al. (BaBar Collaboration), Phys. Rev. Lett. **92**, 142002 (2004).

[27] D. M. Asner et al. (CLEO Collaboration), Phys. Rev. Lett. **92**, 142001 (2004).

[28] A. Tomaradze et al., in *Journal of Physics: Conference Series* (2005), vol. 9, p. 119.

[29] K. Abe et al. (Belle Collaboration), Phys. Rev. Lett. **89**, 142001 (2002).

[30] K. Abe et al. (Belle Collaboration), Phys. Rev. D **70**, 071102 (2004).

[31] P. Pakhlov, in *The 32nd International Conference on High-Energy Physics Proceedings* (2004), arXiv:hep-ex/0412041.

[32] S.-K. Choi et al. (Belle Collaboration), Phys. Rev. Lett. **91**, 262001 (2003).

[33] D. Acosta et al. (CDF II Collaboration), Phys. Rev. Lett. **93**, 072001 (2004).

[34] E. Eichten, K. Gottfried, T. Kinoshita, K. D. Lane, and T. M. Yan, Phys. Rev. D **17**, 3090 (1978).

[35] D. Ebert, R. N. Faustov, and V. O. Galkin, Mod. Phys. Lett. **A20**, 1887 (2005).

[36] B.-Q. Li, C. Meng, and K.-T. Chao, Phys. Rev. D **80**, 014012 (2009).

[37] B. Aubert et al. (BaBar Collaboration), Phys. Rev. Lett. **90**, 242001 (2003).

[38] D. Besson et al. (CLEO Collaboration), Phys. Rev. D **68**, 032002 (2003).

[39] E. S. Swanson, Physics Letters B **582**, 167 (2004).

[40] F. Halzen and A. Martin, *Quarks and leptons* (John Wiley and sons, 1984).

[41] D. Flamm and F. Schöberl, *Introduction to the Quark Model of Elementary Particles: Quantum numbers, gauge theories, and hadron spectroscopy* (Gordon and Breach, 1982).

[42] I. B. Khriplovich, Yad. Fiz. **10**, 409 (1969).

[43] A. Ali, J. Bernstein, and A. Zepeda, Phys. Rev. D **12**, 503 (1975).

[44] V. A. Novikov, L. B. Okun, M. A. Shifman, A. I. Vainshtein, M. B. Voloshin, and V. I. Zakharov, Physics Reports **41**, 1 (1978).

[45] H. D. Politzer, Physics Reports **14**, 129 (1974).

[46] C. Nash, *Relativistic Quantum Fields* (Academic Press, London, 1978).

[47] D. J. Gross and F. Wilczek, Phys. Rev. D **8**, 3633 (1973).

[48] H. D. Politzer, Phys. Rev. Lett. **30**, 1346 (1973).

[49] G. S. Bali, Phys. Rept. **343**, 1 (2001).

[50] C. Bachas, Phys. Rev. **D33**, 2723 (1986).

[51] S. Nussinov, Phys. Rev. Lett. **86**, 4762 (2001).

[52] J. Vijande, F. Fernández, and A. Valcarce, Journal of Physics G: Nuclear and Particle Physics **31**, 481 (2005).

[53] D. I. Dyakonov and V. Y. Petrov, Nuclear Physics B **245**, 259 (1984).

[54] D. I. Dyakonov and V. Y. Petrov, Nuclear Physics B **272**, 457 (1986).

[55] S. Moszkowski, *Nuclear Physics* (Gordon and Breach, New York, 1969).

[56] R. Machleidt, K. Holinde, and C. Elster, Physics Reports **149**, 1 (1987).

[57] M. D. Scadron, Phys. Rev. D **26**, 239 (1982).

[58] A. De Rújula, H. Georgi, and S. L. Glashow, Phys. Rev. D **12**, 147 (1975).

[59] R. K. Bhaduri, L. E. Cohler, and Y. Nogami, Phys. Rev. Lett. **44**, 1369 (1980).

[60] S. Titard and F. J. Ynduráin, Phys. Rev. D **51**, 6348 (1995).

[61] A. M. Badalian and V. L. Morgunov, Phys. Rev. D **60**, 116008 (1999).

[62] A. M. Badalian and B. L. G. Bakker, Phys. Rev. D **62**, 094031 (2000).

[63] D. V. Shirkov and I. L. Solovtsov, Phys. Rev. Lett. **79**, 1209 (1997).

[64] A. M. Badalian and Y. A. Simonov, Yad. Fiz. **60**, 714 (1997).

[65] A. C. Mattingly and P. M. Stevenson, Phys. Rev. D **49**, 437 (1994).

[66] A. M. Badalian and D. S. Kuzmenko, Phys. Rev. D **65**, 016004 (2001).

[67] F. Halzen, C. Olson, M. G. Olsson, and M. L. Stong, Phys. Rev. D **47**, 3013 (1993).

[68] G. S. Bali, H. Neff, T. Düssel, T. Lippert, and K. Schilling (SESAM Collaboration), Phys. Rev. D **71**, 114513 (2005).

[69] N. Brambilla and A. Vairo, in *Nuclear Physics B - Proceedings Supplements* (1998), vol. 64, p. 418, and references therein.

[70] G. S. Bali, K. Schilling, and A. Wachter, Phys. Rev. D **56**, 2566 (1997), and references therein.

[71] N. Isgur, Phys. Rev. D **62**, 014025 (2000).

[72] J. Burger, R. Müller, K. Tragl, and H. M. Hofmann, Nucl. Phys. A **493**, 427 (1989).

[73] C. Semay and B. Silvestre-Brac, Phys. Rev. D **46**, 5177 (1992), and references therein.

[74] M. Kamimura, Phys. Rev. A **38**, 621 (1988).

[75] M. Kamimura, in *Proceedings of the Conference on Muon-Catalyzed Fusion, Sanibel Island, Florida* (1988), p. 330.

[76] E. Hiyama, Y. Kino, and M. Kamimura, Prog. Part. Nucl. Phys. **51**, 223 (2003).

[77] D. V. Bugg, Physics Reports **397**, 257 (2004).

[78] K. Nakamura et al. (PDG2010), Journal of Physics G: Nuclear and Particle Physics **37**, 075021 (2010).

[79] L. Glozman, Physics Reports **444**, 1 (2007).

[80] S. Afonin, Physics Letters B **639**, 258 (2006).

[81] S. Afonin, Int. J. Mod. Phys. A **22**, 4537 (2007).

[82] R. Barbieri and G. Curci, Nucl. Phys. B **154**, 535 (1979).

[83] A. Badalian, A. Veselov, and B. Bakker, Journal of Physics G: Nuclear and Particle Physics **31**, 417 (2005).

[84] K. K. Seth, Phys. Rev. D **72**, 017501 (2005).

[85] S. Uehara et al. (Belle Collaboration), Phys. Rev. Lett. **104**, 092001 (2010).

[86] X. L. Wang et al. (Belle Collaboration), Phys. Rev. Lett. **99**, 142002 (2007).

[87] G. Pakhlova et al. (Belle Collaboration), Phys. Rev. Lett. **101**, 172001 (2008).

[88] S. Uehara et al. (Belle Collaboration), Phys. Rev. Lett. **96**, 082003 (2006).

[89] B. Aubert et al. (BaBar Collaboration), Phys. Rev. Lett. **95**, 142001 (2005).

[90] Q. He et al. (CLEO Collaboration), Phys. Rev. D **74**, 091104 (2006).

[91] C. Z. Yuan et al. (Belle Collaboration), Phys. Rev. Lett. **99**, 182004 (2007).

[92] B. Aubert et al. (BaBar Collaboration), Phys. Rev. Lett. **98**, 212001 (2007).

[93] G. Pakhlova et al. (Belle Collaboration), Phys. Rev. D **77**, 011103 (2008).

[94] B. Aubert et al. (BaBar Collaboration), Phys. Rev. D **76**, 111105 (2007).

[95] E. Eichten, K. Gottfried, T. Kinoshita, K. D. Lane, and T. M. Yan, Phys. Rev. D **21**, 203 (1980).

[96] A. Badalian, B. Ioffe, and A. V. Smilga, Nucl. Phys. **B281**, 85 (1987).

[97] M. Ablikim et al., Physics Letters B **660**, 315 (2008).

[98] T. Barnes, S. Godfrey, and E. S. Swanson, Phys. Rev. D **72**, 054026 (2005).

[99] A. Badalian, B. Bakker, and I. Danilkin, Physics of Atomic Nuclei **72**, 638 (2009).

[100] M. Artuso et al. (CLEO Collaboration), Phys. Rev. D **80**, 112003 (2009).

[101] J. L. Rosner, Phys. Rev. D **78**, 114011 (2008).

[102] H. Mendez et al. (CLEO Collaboration), Phys. Rev. D **78**, 011102 (2008).

[103] R. A. Briere et al. (CLEO Collaboration), Phys. Rev. D **74**, 031106 (2006).

[104] T. E. Coan et al. (CLEO Collaboration), Phys. Rev. Lett. **96**, 162003 (2006).

[105] G. S. Adams et al. (CLEO Collaboration), Phys. Rev. Lett. **101**, 101801 (2008).

[106] E. Glover and A. Morgan, Z. Phys. **C60**, 175 (1993).

[107] A. Ore and J. L. Powell, Phys. Rev. **75**, 1696 (1949).

[108] G. S. Adkins, R. N. Fell, and J. Sapirstein, Phys. Rev. Lett. **84**, 5086 (2000).

[109] A. Burichenko, Physics of Atomic Nuclei **56**, 640 (1993).

[110] G. Adkins, R. Fell, and J. Sapirstein, Annals of Physics **295**, 136 (2002).

[111] B. Aubert et al. (BaBar Collaboration), Phys. Rev. D **79**, 092001 (2009).

[112] E. van Beveren, G. Rupp, and J. Segovia, Phys. Rev. Lett. **105**, 102001 (2010).

[113] H. Nakazawa, in *Nuclear Physics B - Proceedings Supplements* (2008), vol. 181-182, p. 233.

[114] B. Aubert et al. (BaBar Collaboration), Phys. Rev. D **72**, 031101 (2005).

[115] K. Abe et al. (Belle Collaboration), Phys. Rev. Lett. **98**, 082001 (2007).

[116] P. Rubin et al. (CLEO Collaboration), Phys. Rev. D **72**, 092004 (2005).

[117] J. L. Rosner et al. (CLEO Collaboration), Phys. Rev. Lett. **95**, 102003 (2005).

[118] M. Andreotti et al. (Fermilab E835 Collaboration), Phys. Rev. D **72**, 032001 (2005).

[119] S. Dobbs et al. (CLEO Collaboration), Phys. Rev. Lett. **101**, 182003 (2008).

[120] M. Ablikim et al. (BESIII Collaboration), Phys. Rev. Lett. **104**, 132002 (2010), $\Gamma = 0.73 \pm 0.45 \pm 0.28$ and $\mathcal{B} = (54.3 \pm 6.7 \pm 5.2) \times 10^{-2}$.

[121] B. Aubert et al. (BaBar Collaboration), Phys. Rev. D **71**, 071103 (2005).

[122] V. M. Abazov et al. (D0 Collaboration), Phys. Rev. Lett. **93**, 162002 (2004).

[123] K. Abe, arXiv:hep-ex/0505038 (2005).

[124] B. Aubert et al. (BaBar Collaboration), Phys. Rev. D **74**, 071101 (2006).

[125] A. Abulencia et al. (CDF Collaboration), Phys. Rev. Lett. **96**, 102002 (2006).

[126] J. Vijande, E. Weissman, N. Barnea, and A. Valcarce, Phys. Rev. D **76**, 094022 (2007).

[127] E. Hiyama, H. Suganuma, and M. Kamimura, Progress of Theoretical Physics Supplement **168**, 101 (2007).

[128] P. G. Ortega, J. Segovia, D. R. Entem, and F. Fernández, Phys. Rev. D **81**, 054023 (2010).

[129] S.-K. Choi et al. (Belle Collaboration), Phys. Rev. Lett. **94**, 182002 (2005).

[130] B. Aubert et al. (BaBar Collaboration), Phys. Rev. Lett. **101**, 082001 (2008).

[131] J. J. Dudek, R. G. Edwards, and C. E. Thomas, Phys. Rev. D **79**, 094504 (2009).

[132] P. Abreu et al., Physics Letters B **426**, 231 (1998).

[133] P. del Amo Sanchez et al. (BaBar Collaboration), Phys. Rev. D **82**, 111101 (2010).

[134] B. Aubert et al. (BaBar Collaboration), Phys. Rev. Lett. **97**, 222001 (2006).

[135] B. Aubert et al. (BaBar Collaboration), Phys. Rev. D **80**, 092003 (2009).

[136] J. Brodzicka et al. (Belle Collaboration), Phys. Rev. Lett. **100**, 092001 (2008).

[137] A. V. Evdokimov et al. (SELEX Collaboration), Phys. Rev. Lett. **93**, 242001 (2004).

[138] N. Isgur and M. B. Wise, Phys. Rev. Lett. **66**, 1130 (1991).

[139] G. S. Bali, Phys. Rev. D **68**, 071501 (2003).

[140] I. Adachi et al. (Belle Collaboration), Phys. Rev. Lett. **108**, 032001 (2012).

[141] W. R. Innes et al., Phys. Rev. Lett. **39**, 1240 (1977).

[142] K. Han et al., Phys. Rev. Lett. **49**, 1612 (1982).

[143] G. Eigen et al., Phys. Rev. Lett. **49**, 1616 (1982).

[144] C. Klopfenstein et al., Phys. Rev. Lett. **51**, 160 (1983).

[145] F. Pauss et al., Physics Letters B **130**, 439 (1983).

[146] B. Aubert et al. (BaBar Collaboration), Phys. Rev. Lett. **101**, 071801 (2008).

[147] J. P. Lees et al. (BABAR Collaboration), Phys. Rev. D **84**, 072002 (2011).

[148] B. Aubert et al. (BaBar Collaboration), Phys. Rev. Lett. **102**, 012001 (2009).

[149] I. Adachi et al. (Belle Collaboration), Phys. Rev. **D82**, 091106(R) (2010).

[150] D. Besson et al., Phys. Rev. Lett. **54**, 381 (1985).

[151] D. M. J. Lovelock et al., Phys. Rev. Lett. **54**, 377 (1985).

[152] A. Drutskoy et al. (Belle Collaboration), Phys. Rev. D **81**, 112003 (2010).

[153] T. K. Pedlar et al. (CLEO Collaboration), Phys. Rev. Lett. **107**, 041803 (2011).

[154] G. Aad et al. (ATLAS Collaboration), arXiv:hep-ex/1112.5154 (2011).

[155] P. del Amo Sanchez et al. (BaBar Collaboration), Phys. Rev. D **82**, 111102 (2010).

[156] W. Kwong and J. L. Rosner, Phys. Rev. D **38**, 279 (1988).

[157] G. Bonvicini et al. (CLEO Collaboration), Phys. Rev. Lett. **96**, 022002 (2006).

[158] O. Aquines et al. (CLEO Collaboration), Phys. Rev. Lett. **96**, 152001 (2006).

[159] A. Drutskoy et al. (Belle Collaboration), Phys. Rev. D **76**, 012002 (2007).

[160] J. Lee-Franzini et al., Phys. Rev. Lett. **65**, 2947 (1990).

[161] F. Abe et al. (CDF Collaboration), Phys. Rev. Lett. **81**, 2432 (1998).

[162] A. Abulencia et al. (CDF Collaboration), Phys. Rev. Lett. **96**, 082002 (2006).

[163] E. Eichten and F. Feinberg, Phys. Rev. D **23**, 2724 (1981).

[164] A. Barchielli, E. Montaldi, and G. Prosperi, Nuclear Physics B **296**, 625 (1988).

[165] G. S. Bali and P. Boyle, Phys. Rev. D **59**, 114504 (1999).

[166] N. Brambilla and G. Prosperi, Physics Letters B **236**, 69 (1990).

[167] D. Mohler and R. M. Woloshyn, Phys. Rev. D **84**, 054505 (2011).

[168] T. Barnes, F. E. Close, and H. J. Lipkin, Phys. Rev. D **68**, 054006 (2003).

[169] J. Vijande, A. Valcarce, and F. Fernandez, in *AIP Conference Proceedings* (2008), vol. 1030, p. 196.

[170] A. Drutskoy et al. (Belle Collaboration), Phys. Rev. Lett. **94**, 061802 (2005).

[171] O. Lakhina and E. S. Swanson, Physics Letters B **650**, 159 (2007).

[172] S. N. Gupta and S. F. Radford, Phys. Rev. D **24**, 2309 (1981).

[173] S. Godfrey and N. Isgur, Phys. Rev. D **32**, 189 (1985).

[174] A. Galindo and P. Pascual (1990).

[175] E. Ruiz Arriola, A. Calle Cordon, and M. Pavon Valderrama, arXiv:nucl-th/0710.2770 (2007).

[176] M. Pavon Valderrama and E. R. Arriola, Phys. Rev. **C74**, 054001 (2006).

[177] E. R. Arriola and A. C. Cordon, arXiv:cond-matter.other/0912.2658 (2009).

[178] D. R. Entem, E. Ruiz Arriola, M. Pavon Valderrama, and R. Machleidt, Phys. Rev. **C77**, 044006 (2008).

[179] A. Calle Cordon and E. Ruiz Arriola, Phys. Rev. **C81**, 044002 (2010).

[180] M. Pavon Valderrama and E. Ruiz Arriola, Phys. Rev. **C72**, 054002 (2005).

[181] L. Micu, Nucl. Phys. **B10**, 521 (1969).

[182] A. Le Yaouanc, L. Oliver, O. Pène, and J. C. Raynal, Phys. Rev. D **8**, 2223 (1973).

[183] A. Le Yaouanc, L. Oliver, O. Pène, and J.-C. Raynal, Phys. Rev. D **9**, 1415 (1974).

[184] R. Kokoski and N. Isgur, Phys. Rev. D **35**, 907 (1987).

[185] P. Geiger and E. S. Swanson, Phys. Rev. D **50**, 6855 (1994).

[186] E. J. Eichten, K. Lane, and C. Quigg, Phys. Rev. D **73**, 014014 (2006).

[187] E. S. Ackleh, T. Barnes, and E. S. Swanson, Phys. Rev. D **54**, 6811 (1996).

[188] A. L. Yaouanc, L. Oliver, O. Pene, and J.-C. Raynal, Physics Letters B **71**, 397 (1977).

[189] A. L. Yaouanc, L. Oliver, O. Pène, and J. Raynal, Physics Letters B **72**, 57 (1977).

[190] W. Roberts and B. Silvestre-Brac, Phys. Rev. D **57**, 1694 (1998).

[191] S. Okubo, Phys. Lett **5**, 165 (1963).

[192] G. Zweig, CERN-TH-412, NP-8419 (1964).

[193] J. Iizuka, Progress of Theoretical Physics Supplement **37**, 21 (1966).

[194] R. Bonnaz and B. Silvestre-Brac, Few-Body Systems **27**, 163 (1999).

[195] S. Capstick and W. Roberts, Phys. Rev. D **49**, 4570 (1994).

[196] Since the literature is extensive we cite only recent summaries of the $^3P_0$ and related decay models, see H.G. Blundell and S. Godfrey, Phys. Rev. D **53**, 3700 (1996); P.R. Page, Ph.D. thesis, University of Oxford, 1995.

[197] F. E. Close and E. S. Swanson, Phys. Rev. D **72**, 094004 (2005).

[198] B. Aubert, in *33rd International Conference on High-Energy Physics* (2006), arXiv:hep-ex/0607084.

[199] D. Entem, P. Ortega, and F. Fernandez, in *The XIV International Conference on Hadron Spectroscopy* (2011), arXiv:hep-ph/1109.0311.

[200] B. Aubert et al. (BaBar Collaboration), Phys. Rev. D **81**, 092003 (2010).

[201] K. D. Born, E. Laermann, N. Pirch, T. F. Walsh, and P. M. Zerwas, Phys. Rev. D **40**, 1653 (1989).

[202] G. Pakhlova et al. (Belle Collaboration), Phys. Rev. Lett. **98**, 092001 (2007).

[203] E. van Beveren and G. Rupp, arXiv:hep-ph/0904.4351 (2009).

[204] E. van Beveren, X. Liu, R. Coimbra, and G. Rupp, EPL (Europhysics Letters) **85**, 61002 (2009).

[205] D. V. Bugg, Journal of Physics G: Nuclear and Particle Physics **36**, 075002 (2009).

[206] Z. Q. Liu, X. S. Qin, and C. Z. Yuan, Phys. Rev. D **78**, 014032 (2008).

[207] J. Siegrist et al. (MARK I Collaboration), Phys. Rev. Lett. **36**, 700 (1976).

[208] R. Brandelik et al. (DASP Collaboration), Physics Letters B **76**, 361 (1978).

[209] A. Osterheld et al. (Crystall Ball Collaboration) (1986), SLAC-PUB-4160.

[210] J. Z. Bai et al. (BES Collaboration), Phys. Rev. Lett. **88**, 101802 (2002).

[211] G. Pakhlova et al. (Belle Collaboration), Phys. Rev. Lett. **100**, 062001 (2008).

[212] G. Pakhlova et al. (Belle Collaboration), Phys. Rev. D **80**, 091101 (2009).

[213] Gerson, S. Goldhaber, A. Barbaro-Galtieri, et al., *Advances in Particle Physics, vol. 2, p. 197* (Cool, Marshak Eds., 1968).

[214] J. M. Blatt and V. F. Weisskopf, *Theoretical nuclear physics* (Dover Pubns, 1991).

[215] Y.-p. Kuang, Frontiers of Physics in China **1**, 19 (2006).

[216] V. Balagura et al. (Belle Collaboration), Phys. Rev. D **77**, 032001 (2008).

[217] J. Vijande, F. Fernández, and A. Valcarce, Phys. Rev. D **73**, 034002 (2006).

[218] T.-M. Yan, Phys. Rev. D **22**, 1652 (1980).

[219] Y.-P. Kuang and T.-M. Yan, Phys. Rev. D **24**, 2874 (1981).

[220] Y.-P. Kuang, S. F. Tuan, and T.-M. Yan, Phys. Rev. D **37**, 1210 (1988).

[221] Y.-P. Kuang, Y.-P. Yi, and B. Fu, Phys. Rev. D **42**, 2300 (1990).

[222] H.-Y. Zhou and Y.-P. Kuang, Phys. Rev. D **44**, 756 (1991).

[223] L. S. Brown and R. N. Cahn, Phys. Rev. Lett. **35**, 1 (1975).

[224] S. H. H. Tye, Phys. Rev. D **13**, 3416 (1976).

[225] R. C. Giles and S.-H. H. Tye, Phys. Rev. Lett. **37**, 1175 (1976).

[226] R. C. Giles and S.-H. H. Tye, Phys. Rev. D **16**, 1079 (1977).

[227] N. Isgur and J. Paton, Phys. Rev. D **31**, 2910 (1985).

[228] W. Buchmüller and S. H. H. Tye, Phys. Rev. Lett. **44**, 850 (1980).

[229] A. Sokolov et al. (Belle Collaboration), Phys. Rev. D **75**, 071103 (2007).

[230] B. Aubert et al. (BaBar Collaboration), Phys. Rev. Lett. **96**, 232001 (2006).

[231] K.-F. Chen et al. (Belle Collaboration), Phys. Rev. Lett. **100**, 112001 (2008).

[232] A. Ali, C. Hambrock, I. Ahmed, and M. J. Aslam, Physics Letters B **684**, 28 (2010).

[233] A. Ali, C. Hambrock, and M. J. Aslam, Phys. Rev. Lett. **104**, 162001 (2010).

[234] A. Ali, C. Hambrock, and S. Mishima, Phys. Rev. Lett. **106**, 092002 (2011).

[235] D.-Y. Chen, J. He, X.-Q. Li, and X. Liu, Phys. Rev. D **84**, 074006 (2011).

[236] D. Liventsev et al. (Belle Collaboration), Phys. Rev. D **77**, 091503 (2008).

[237] B. Aubert et al. (BaBar Collaboration), Phys. Rev. Lett. **101**, 261802 (2008).

[238] B. Aubert et al. (BaBar Collaboration), Phys. Rev. Lett. **103**, 051803 (2009).

[239] V. M. Abazov et al. (D0 Collaboration), Phys. Rev. Lett. **102**, 051801 (2009).

[240] E. Hernández, J. Nieves, and J. M. Verde-Velasco, Phys. Rev. D **74**, 074008 (2006).

[241] M. A. Ivanov, J. G. Körner, and P. Santorelli, Phys. Rev. D **73**, 054024 (2006).

[242] A. K. Leibovich, Z. Ligeti, I. W. Stewart, and M. B. Wise, Phys. Rev. Lett. **78**, 3995 (1997).

[243] A. K. Leibovich, Z. Ligeti, I. W. Stewart, and M. B. Wise, Phys. Rev. D **57**, 308 (1998).

[244] P. Krokovny et al. (Belle Collaboration), Phys. Rev. Lett. **91**, 262002 (2003).

[245] B. Aubert et al. (BaBar Collaboration), Phys. Rev. D **74**, 091101 (2006).

[246] B. Aubert et al. (BaBar Collaboration), Phys. Rev. D **77**, 011102 (2008).

[247] J. Dalseno et al. (Belle Collaboration), Phys. Rev. D **76**, 072004 (2007).

[248] T. Aushev et al. (Belle Collaboration), Phys. Rev. D **83**, 051102 (2011).

[249] A. L. Yaouanc, L. Oliver, O. Pène, and J.-C. Raynal, Physics Letters B **387**, 582 (1996).

[250] A. Datta and P. O'Donnell, Physics Letters B **572**, 164 (2003).

[251] A. L. Yaouanc, L. Oliver, O. Pène, J.-C. Raynal, and V. Morénas, Physics Letters B **520**, 59 (2001).

[252] P. Colangelo and F. D. Fazio, Physics Letters B **532**, 193 (2002).

[253] P. Colangelo, F. De Fazio, G. Nardulli, N. Paver, and Riazuddin, Phys. Rev. D **60**, 033002 (1999).

[254] Z. Luo and J. L. Rosner, Phys. Rev. D **64**, 094001 (2001).

[255] A. Abd El-Hady, A. Datta, and J. P. Vary, Phys. Rev. D **58**, 014007 (1998).

[256] A. Abd El-Hady, A. Datta, K. S. Gupta, and J. P. Vary, Phys. Rev. D **55**, 6780 (1997).

[257] F. Jugeau, A. Le Yaouanc, L. Oliver, and J.-C. Raynal, Phys. Rev. D **72**, 094010 (2005).

[258] Guo-Li and Wang, Physics Letters B **633**, 492 (2006).

[259] M.B. and Voloshin, Progress in Particle and Nuclear Physics **61**, 455 (2008), ISSN 0146-6410.

[260] D. S. Hwang and D.-W. Kim, Physics Letters B **606**, 116 (2005), ISSN 0370-2693.

[261] H.-Y. Cheng and C.-K. Chua, Phys. Rev. D **74**, 034020 (2006).

[262] B. Silvestre-Brac, private communication.

[263] J. Vijande and A. Valcarce, Physics Letters B **677**, 36 (2009).

[264] D. Barberis et al. (WA102 Collaboration), Physics Letters B **413**, 225 (1997).

[265] M. Sosa et al., Phys. Rev. Lett. **83**, 913 (1999).

[266] F. E. Close and A. Kirk, Z.Phys. **C76**, 469 (1997).

[267] A. Abele et al. (Crystal Barrel Collaboration), Phys.Lett. **B415**, 280 (1997).

[268] A. V. Anisovich, C. A. Baker, C. J. Batty, D. V. Bugg, C. Hodd, H. C. Lu, V. A. Nikonov, A. V. Sarantsev, V. V. Sarantsev, and B. S. Zou, Physics Letters B **491**, 47 (2000).

[269] A. Anisovich, C. Baker, C. Batty, D. Bugg, V. Nikonov, A. Sarantsev, V. Sarantsev, and B. Zou, Physics Letters B **542**, 19 (2002).

[270] P. Boucaud, J. Leroy, A. Yaouanc, J. Micheli, O. Pene, and J. Rodríguez-Quintero, arXiv:hep-ph/1109.1936 (2011).

[271] N. Isgur, R. Kokoski, and J. Paton, Phys. Rev. Lett. **54**, 869 (1985).

[272] B. Aubert et al., Phys. Rev. D **77**, 092002 (2008).

[273] A. Anisovich, C. Baker, C. Batty, D. Bugg, V. Nikonov, A. Sarantsev, V. Sarantsev, and B. Zou, Physics Letters B **517**, 261 (2001).

[274] A. Anisovich, C. Baker, C. Batty, D. Bugg, V. Nikonov, A. Sarantsev, V. Sarantsev, and B. Zou, Physics Letters B **542**, 8 (2002).

[275] C. J. Biddick et al., Phys. Rev. Lett. **38**, 1324 (1977).

[276] R. Barbieri, R. Gatto, R. Kogerler, and Z. Kunszt, Phys. Lett. **B57**, 455 (1975).

[277] D. B. Leinweber, Nucl. Phys. **A470**, 477 (1987).

[278] R. Barbieri, R. Gatto, and R. Kogerler, Physics Letters B **60**, 183 (1976).

[279] R. Barbieri, M. Caffo, R. Gatto, and E. Remiddi, Nuclear Physics B **192**, 61 (1981).

[280] R. Barbieri, G. Curci, E. d' Emilio, and E. Remiddi, Nuclear Physics B **154**, 535 (1979).

[281] W. Kwong, P. B. Mackenzie, R. Rosenfeld, and J. L. Rosner, Phys. Rev. D **37**, 3210 (1988).

[282] W. E. Caswell, G. P. Lepage, and J. Sapirstein, Phys. Rev. Lett. **38**, 488 (1977).

[283] W. Frank, D. J. Land, and R. M. Spector, Rev. Mod. Phys. **43**, 36 (1971).

[284] G. Buchalla, A. J. Buras, and M. E. Lautenbacher, Rev. Mod. Phys. **68**, 1125 (1996).